


Fall 12-20-2019

Computational Studies and Design of PPAR γ and GLUT1 Inhibitors

Suliman Almahmoud
University of Nebraska Medical Center

Follow this and additional works at: <https://digitalcommons.unmc.edu/etd>

 Part of the [Medicinal and Pharmaceutical Chemistry Commons](#), [Medicinal Chemistry and Pharmaceutics Commons](#), and the [Medicinal-Pharmaceutical Chemistry Commons](#)

Recommended Citation

Almahmoud, Suliman, "Computational Studies and Design of PPAR γ and GLUT1 Inhibitors" (2019).
Theses & Dissertations. 401.
<https://digitalcommons.unmc.edu/etd/401>

This Dissertation is brought to you for free and open access by the Graduate Studies at DigitalCommons@UNMC. It has been accepted for inclusion in Theses & Dissertations by an authorized administrator of DigitalCommons@UNMC. For more information, please contact digitalcommons@unmc.edu.

**COMPUTATIONAL STUDIES AND DESIGN OF
PPAR γ AND GLUT1 INHIBITORS**

By

Suliman A Almahmoud

A DISSERTATION

Presented to the Faculty of
the Graduate College of University of Nebraska Medical Center

in Partial Fulfillment of the Requirements

for the Degree of Doctor of Philosophy

Department of Pharmaceutical Sciences

Under the Supervision of Professors

Jonathan L. Vennerstrom, Ph.D.

Haizhen A. Zhong, Ph.D.

University of Nebraska Medical Center

Omaha, Nebraska

October, 2019

TITLE**COMPUTATIONAL STUDIES AND DESIGN OF
PPAR γ AND GLUT1 INHIBITORS****By****Suliman A Almahmoud****SUPERVISORY COMMITTEE****APPROVED****DATE****Jonathan L. Vennerstrom, Ph.D.****October 11th, 2019****Haizhen A. Zhong, Ph.D.****October 11th, 2019****Xiaofang Wang, Ph.D.****October 11th, 2019****Timothy R. McGuire, Pharm.D., FCCP.****October 11th, 2019**

TABLE OF CONTENTS

Acknowledgments.....	VI
Abstract.....	VIII
List of Figures.....	XI
List of Tables	XIV
Chapter 1 Introduction	1
1.1. The Peroxisome Proliferator-Activated Receptors (PPARs)	1
1.2. The Peroxisome Proliferator-Activated Receptor Gamma (PPAR γ).....	2
1.3.The Ligand-Binding Domain (LBD) of PPAR γ	3
1.4. PPAR γ Ligands	10
1.5. Mechanism of Action of PPAR γ Ligands	18
1.6. The Glucose transporters (GLUTs).....	20
1.7. Glucose transporter 1 (GLUT1)	23
1.8. Conformations of GLUT1 Structure	26
1.9. Binding Interaction of GLUT1.....	29
Chapter 2 Molecular Modeling of Allosteric Site of Isoform-Specific Inhibition of the Peroxisome Proliferator-activated Receptor PPAR γ	45
Abstract	45
2.1. Introduction	46

2.2. Computational Methods	48
2.3. Results and Discussion	52
2.4. Conclusion.....	88
Chapter 3 Structure-Based Design of PPAR γ Antagonists as Potential Anti Prostate	
Cancer Agents	93
Abstrac	93
3.1. Introduction	94
3.2. Materials and Methods	98
3.3. Results and Dissection	99
3.4. Conclusion.....	115
Chapter 4 Conformational Studies of Glucose Transporter 1 (GLUT1) as an Anticancer	
Drug Target.....	122
Abstract	121
4.1. Introduction	122
4.2. Results and Discussion.....	126
4.3. Conclusions	161
4.4. Materials and Methods	162
Chapter 5 Ligand-Based Design of GLUT1 Inhibitors as Potential Anti-tumor Agents 177	
Abstract	177
5.1. Introduction	178

5.2. Results and Dissection	181
5.3. Conclusion.....	191
5.4. Materials and Methods	192
Chapter 6 Summary	201
Appendix Molecular Modeling Studies on the Binding Mode of the PD-1/PD-L1 Complex Inhibitors	
1. Introduction:.....	205
2. Results and Discussion:.....	211

ACKNOWLEDGMENTS

I would like first to acknowledge and thank my advisors, Dr. Jonathan L. Vennerstrom and Dr. Haizhen A. Zhong, for their devoted guidance, counseling, and support during my PhD journey. Despite the challenges students may face through this journey, Dr. Jonathan L. Vennerstrom has always been kind, reasonable and supportive. Thanks for the inspiration, critical thinking learning and positive criticism that inspire me to be a good future academic scientist. Truly, he is a scientist whom I am glad and proud of being his mentee. I owe Dr. Haizhen A. Zhong a lot of gratitude for the chance to work in his laboratory and promote my knowledge in computational chemistry. He has always been delighted to elucidate computational chemistry and offer help and suggestions about docking and modeling problem. Working with Dr. Haizhen A. Zhong has enhanced my scope in the field of computational chemistry and fostered my experience.

I would also like to thank my supervisory committee members, Dr. Xiaofang Wang and Dr. Timothy R. McGuire for their time and mentoring throughout my study. I would also like to appreciate their suggestion and assistance through my PhD study. Tremendous thanks to Dr. Corey Hopkins, Dr. Jing Wang, and Dr. Jeremy Jones for their extensive assistance and support. Their extreme help made my thesis more effective and productive.

I would like to thank Dr. Vennerstrom lab members, Dr. James K. Wood, Dr. Yuxiang Dong, Dr. James Hagen, Dr. Jianbo Wu, Dr. Chunkai Wang, and Derek A Leas for their valuable assistance, discussion, and help my science.

I would like to thank the faculty and staff of the University of Nebraska Medical Center and the University of Nebraska at Omaha, especially Renee B Kaszynski, Janine Brooks,

and Cody R Phillips for their extravagant assistance. They always have been there and happy to offer their counseling, help, suggestions.

I am thankful to my Omaha friends who always have helped and supported me during my PhD study. Their love and care have recovered my yearning and homesickness.

Finally, I would like to express my sincere gratitude and thank to my family for continued love, encouragement, patient and support throughout my abroad study. My parents, wife, brothers, and sisters have always believed in me to accomplish what I have set out to achieve. I am grateful to my wife for being a supportive, patient, and loving partner. My heartfelt appreciation to my wife for her extreme help and support. Without her, my life in the United States would not be this easy.

COMPUTATIONAL STUDIES AND DESIGN OF PPAR γ AND GLUT1 INHIBITORS

Suliman A Almahmoud, Ph.D.

University of Nebraska Medical Center, 2019

Advisors: Jonathan L. Vennerstrom, Ph.D., and Haizhen A. Zhong, Ph.D.

The peroxisome proliferator-activated receptor gamma (PPAR γ) is a ligand-dependent transcription factor of nuclear receptor superfamily that controls the expression of a variety of genes involved in fatty acid metabolism, adipogenesis, and insulin sensitivity. PPAR γ is a target for insulin-sensitizing drugs, and plays a significant function in prostate cancer. On the other side, Glucose transporter 1 (GLUT1) is a uniporter protein that facilitates the transport of glucose across the plasma membranes of mammalian cells. GLUT1 is overexpressed in numerous tumors and associated with tumor progression and poor overall survival. Consequently, GLUT1 is a potential target for cancer treatment.

First, PPAR γ antagonists have potent anti-diabetic activity without serious side effects of many of the PPAR γ agonists such as thiazolidinedione (TZD) class. In addition, PPAR γ agonists in cancer model systems have PPAR γ -independent mechanisms, but PPAR γ antagonists have exhibited antiproliferative effects on a broad range of hematopoietic and epithelial cell lines, usually with greater potency than agonists. The

ligand binding domain (LBD) of PPAR γ is large and involves two binding sites: orthosteric and allosteric binding sites. Several co-crystal structure of PPAR γ ligands show two bound molecules, one to the orthosteric pocket and a second bound to the allosteric site. We ran docking studies against the orthosteric and allosteric binding sites to determine the most favorable binding site for PPAR γ antagonists. Our results emphasize that the glide docking performed well in predicting the binding affinity of PPAR γ antagonists, and the allosteric site of PPAR γ is the most favorable binding site for antagonists. Besides, we investigated the ligand-protein interactions for several PPAR γ ligands to explore a structural basis of the binding selectivity of PPAR γ antagonists. Phe282, Arg288, and Lys367 interact with antagonists more than agonists and partial agonists. We fulfilled integrated virtual screening and biological assay for the two binding sites of PPAR γ ; orthosteric and allosteric pockets. Several hits of PPAR γ antagonists showing single digit of micromolar concentration in inhibition of PPAR γ generated from the virtual screening of allosteric pocket.

Second, GLUT1 works through conformational switching from an outward-open (OOP) to an inward-open (IOP) conformation passing through an occluded conformation. It is critical to determine which conformation is preferred by bound ligands because the success of structure-based drug design depends on the appropriate starting conformation of the target protein. To find out the most favorable GLUT 1 conformation for ligand binding, we ran systemic molecular docking studies for different conformations of GLUT1 using known GLUT1 inhibitors. Our data revealed that the IOP is the preferred conformation and that residues Phe291, Phe379, Glu380, Trp388, and Trp412 may play critical roles in ligand binding to GLUT1. To identify new chemotypes targeting GLUT1,

we built a pharmacophore model and searched against an NCI compound database. Sixteen hit molecules with good docking scores were screened for GLUT1 inhibition and antiproliferative activities. From these, we identified that compounds NSC657996, NSC32458, NSC328095 and NSC295720 inhibited the cell viability in a dose-dependent manner and that NSC657996 and NSC328095 are the most potent with less than 10 μ M concentration in the HCT116 colon cancer cell line. Lead compound NSC295720 was a GLUT1 inhibitor.

LIST OF FIGURES

Figure 1.1. The secondary structure of the LBD of PPAR γ in ribbon model.....	5
Figure 1.2. Co-crystal structure of NSI-bound PPAR γ (PDB 2HFP).....	8
Figure 1.3. Crystal structure of PPAR γ bound to Rosiglitazone (PDB 2PRG).	9
Figure 1.4. Chemical Structures of selective TZDs PPAR γ agonists.....	13
Figure 1.5. Chemical Structures of non TZDs PPAR γ agonists.	14
Figure 1.6. Chemical Structures of PPAR γ partial agonists.	15
Figure 1.7. Superimposed ribbon structures of PPAR γ with partial agonists.....	16
Figure 1.8. Chemical Structures of PPAR γ antagonists.	17
Figure 1.9. The secondary Structure of the GLUT1 represented in ribbon model..	22
Figure 1.10. Chemical Structures of GLUT1 inhibitors.	25
Figure 1.11. An overview of working model of GLUT1.....	28
Figure 2.1. Co-crystal structure of NSI-bound PPAR γ (PDB 2HFP).....	51
Figure 2.2. Chemical structures of PPAR γ antagonists.	56
Figure 2.3. Plots of glide docking scores for PPAR γ antagonists.	59
Figure 2.4. The superposition of NSI from the Glide pose and the crystal structure.....	63
Figure 2.5. Chemical structures of PPAR γ partial agonists.....	72
Figure 2.6. Chemical structures of PPAR γ agonists.	74
Figure 2.7. Amino acid frequency of interacting residues at allosteric Binding site.....	77
Figure 2.8. Interactions between PPAR γ and ligands at allosteric binding site	78
Figure 2.9. Amino acid frequency of interacting residues at orthosteric Binding site.	83
Figure 2.10. Interactions between PPAR γ and and ligands at allosteric binding site.....	84

Figure 2.11. Electrostatic surface map of the binding pockets of PPAR γ	87
Figure 3.1. Representative PPAR γ antagonists.....	97
Figure 3.2. The Orthosteric and allosteric sites of PPAR γ	101
Figure 3.3. Chemical structures of seven hit molecules against the orthosteric site.	102
Figure 3.4. Chemical structures of seven hit molecules against the allosteric site.	104
Figure 3.5. The superposition of the Glide pose and the crystal structure (2HFP).....	105
Figure 3.6. PPAR γ inhibition in LCP cells for compounds against the orthosteric site.	108
Figure 3.7. PPAR γ inhibition in LCP cells for compounds against the orthosteric site	109
Figure 3.8. Ligands interactions between ligands and PPAR γ orthosteric site.....	110
Figure 3.9. Ligands interactions between ligands and PPAR γ allosteric site.....	111
Figure 3.10. Ligands interactions between ligands and PPAR γ allosteric site.....	112
Figure 4.1. An overview of working model of GLUT1.....	125
Figure 4.2. Primary sequence alignment of GLUT1, GLUT3, and Xyle.....	128
Figure 4.3. An overview of conformational change of GLUT1.	129
Figure 4.4. The Ramachandran plots for the four homology models.	130
Figure 4.5. Structures of GLUT1 inhibitors (30-44) used in docking studies.	136
Figure 4.6. The superposition of the Glide docked poses and the native conformation.	137
Figure 4.7. Interactions between crystal ligands and glut1 conformation.	149
Figure 4.8. Ligands interactions between 11, 19, 20, 25, and 37 and GLUT1.	150
Figure 4.9. Interacting residues of GLUT1 with inhibitors at different conformations.	151
Figure 4.10. Molecular contact map OF 19 and GLUT1 in different conformations.....	155
Figure 4.11. Electrostatic map between 19 and GLUT1 in different conformations.	157

Figure 4.12. Plots of the predicted versus observed activities pIC ₅₀	159
Figure 5.1. GLUTs Selective Inhibitors Used to build a Pharmacophore Model.....	180
Figure 5.2. Pharmacophore model for GLUTs inhibitors.....	183
Figure 5.3. Chemical structures of sixteen hit molecules.	184
Figure 5.4. The superposition of the Glide pose and the crystal structure of ligand	185
Figure 5.5. Ligands interactions between hit molecules and GLUT1	186
Figure 5.6. FET cells were treated with hit molecules.	190

LIST OF TABLES

Table 2.1. The glide score of PPAR γ antagonists against the allosteric and orthosteric..	57
Table 2.2. Statistical results for the glide score estimation of free energy binding.....	60
Table 2.3. Glide docking scores of drug-like molecules.....	64
Table 2.4. Enrichment factor of the glide docking against PPAR γ at allosteric site.....	68
Table 2.5. Residues Interactions of ligands at allosteric site.....	75
Table 2.6. Residues Interactions of ligands at orthosteric site.....	81
Table 3.1. The molecular weight, glide score, growth inhibition, and residues interactions of compounds resulted from the SBVS against the orthosteric site.....	113
Table 3.2. The molecular weight, glide score, growth inhibition , and residues interactions of compounds resulted from the SBVS against the allosteric site.....	114
Table 4.1. Glide scores of GLUT1 inhibitors against different conformation models..	138
Table 4.2. The average of the mean errors.....	140
Table 4.3. Glide scores of 508 drug-like molecules against the GLUT1.....	141
Table 4.4. The enrichment factors of docking scores for different conformations.....	146
Table 4.5. Residues interaction with different GLUT1 inhibitors.....	152
Table 4.6. The average magnitude of the errors of QSAR model.....	160
Table 5.1. Glide docking scores (kcal/mol) of hit molecules with NSC numbers, logP, and interacting residues of 5EQH.....	187
Table 5.2. IC ₅₀ s of 16 tested compounds against the HCT116 colon cancer cell lines...	189

Chapter 1

Introduction

1.1. The Peroxisome Proliferator-Activated Receptors (PPARs):

The peroxisome proliferator-activated receptors (PPARs) are ligand-inducible transcription factors and members of the nuclear receptor superfamily.^{1, 2, 3} There are three PPARs isotypes: PPAR α (NR1C1), PPAR δ (NR1C2) and PPAR γ (NR1C3).^{1, 2, 3} The PPARs form heterodimers with retinoid X receptor (RXR) which bind to PPAR-responsive regulatory elements (PPREs) in the promoter region of the respective target genes initiating transcription of target genes.^{4,5} The PPARs regulate the expression of several genes involved in abiogenesis, lipid metabolism, inflammation, and maintenance of metabolic homeostasis.^{2, 3, 6} The PPARs are receptors for some dietary fats such as oleic, linoleic and linolenic acids, and diverse endogenous lipid metabolites, including prostaglandin J2, 8S-hydroxyeicosatetraenoic acid, and various oxidized phospholipids can bind to PPARs.^{7, 8}

⁹ The structure of PPARs are similar and consist of different functional domains, including an N-terminal transactivation domain (AF1), a highly conserved DNA-binding domain (DBD) and a C-terminal ligand binding domain (LBD).^{10, 11} The PPARs receptors have a different tissue distribution. PPAR α is mostly expressed in muscles, liver, heart, and kidney.² PPAR δ is amply expressed throughout the body but at low levels in the liver.² The PPAR γ receptor has two isoforms that are expressed from the same gene by utilizing distinct promoters and exons, $\gamma 1$ and $\gamma 2$.² PPAR $\gamma 1$ is expressed in the large intestine, spleen, and mostly in white and brown adipose tissue while PPAR $\gamma 2$ is expressed restricted in adipose tissue.² The PPARs are the significant targets of various synthetic compounds

utilized efficiently in the treatment of diabetes, dyslipidemia, atherosclerosis, colon inflammation, cancer, infertility, and demyelination.^{1, 2}

1.2. The Peroxisome Proliferator-Activated Receptor Gamma (PPAR γ):

The PPAR γ is an essential target of many pharmaceuticals that have produced billions of dollars (USD) for treating insulin resistance and type 2 diabetes, such as thiazolidinedione drugs (TZDs).¹² The function of PPAR γ depends on the formation of heterodimerization with retinoid X receptor α (RXR α) to create a transcription factor that can bind peroxisome proliferator response elements (PPRE) on DNA to initiate transcription of target genes.¹³ The PPAR γ -based gene regulation includes both gene activation and repression events, based on the molecular situation.¹⁴ There are three main mechanisms of modulation of PPAR γ : ligand-independent repression, agonist-dependent activation, and antagonist-dependent repression.⁵ The PPAR γ plays a vital role in controlling adipogenic and lipogenic pathways, and it is the master regulator of adipocyte differentiation.³ The PPAR γ regulates gene networks contributed to glucose homeostasis and insulin sensitivity.^{2, 3} PPAR γ also plays an essential role in inflammation.² It has an important function in different immune cells such as antigen-presenting myeloid dendritic cells and macrophages.² The PPAR γ has been implicated in regulating the pathophysiology of several cancers. The PPAR γ is overexpressed in numerous tumors, including breast, pancreatic, bladder, prostate, and colon.^{15, 16, 17, 18}

The structure PPAR γ has the conserved nuclear receptor domain complex consist of the N-terminal activation function-1 (AF-1) domain, which is a ligand-independent transactivation domain, The DNA-binding domain (DBD) which identifies and binds PPREs within the promoter region of target genes, a flexible hinge region which is a protein

domain required for receptor dimerization, and the C-terminal ligand-binding domain (LBD) which is a ligand-dependent transactivation domain, and it is responsible for ligand binding, dimerization, and transactivation function.¹² The LBD of PPAR γ has been known as the main binding domain for endogenous lipids and regulates the dimerization and the transcriptional activity of PPAR γ .¹⁰ The LBD of PPAR γ has been the primary target for developing therapeutic compounds of PPAR γ such as TZDs.¹⁹

1.3. The Ligand-Binding Domain (LBD) of PPAR γ :

Many structurally-different small molecules interact with PPAR γ through the ligand-binding domain (LBD).¹⁹ The LBD is located in the C-terminal domain of PPAR γ , and it is a ligand-dependent transactivation domain.^{5, 10} The LBD includes activation function 2 (AF-2), which facilitates ligand binding, dimerization, and transactivation functions.²⁰ AF-2 is extraordinarily active and in a balance between many conformations, varying from active to inactive.^{21, 22} Ligand binding induces conformational changes in the AF-2 surface that promote interactions with co-regulators and affect the recruitment of the transcriptional machinery to regulate the downstream of gene expression.^{21, 22} The LBD of PPAR γ can bind multiple domains in PPAR γ and RXR α , forming a non-symmetric complex.²³ In addition, The LBD of PPAR γ interacts with the DNA-binding domain (DBD) to improve response-element (RE) binding.²³ Several endogenous ligands such as prostaglandin J2, 8S-hydroxyeicosatetraenoic acid and many small molecules such as TZDs interact with PPAR γ via the LBD.¹⁹

The crystal structure of LBD of PPAR γ revealed that the LBD of PPAR γ consists of 13 α -helices (H1- H12) and four small β -sheet strands lying between H3 and H6 form a three-layer sandwich fold (Figure 1.1).¹⁰ The structure of LBD of PPAR γ is similar to other

nuclear-receptor, except the structure of LBD of PPAR γ has an extra helix, H2', located between the first β - sheet and H3.¹⁰ In addition, the tertiary position of H2 in PPAR γ is unlike other LBD of nuclear receptors providing more accessible contact with a ligand.¹⁰ The helices H4, H5, H8 are closely located between helices H1, H3, H7, and H10 at the top half of the LBD.¹⁰ The loop between helices H2' and H3 (Ω loop) is thermally mobile loop, which is hard to be observed in crystal structures.¹⁰ The AF-2 is located at the far C terminal of the LBD having three-dimensional (3D) α - helices structure.¹⁰ The AF-2 involves helix H3, H3-4 loop, helix H11, and helix H12.²⁴ The ligand binding site of PPAR γ is a large T-shaped cavity (~ 1.300 Å) extending from the C terminal domain to the β -sheet strands.¹⁰

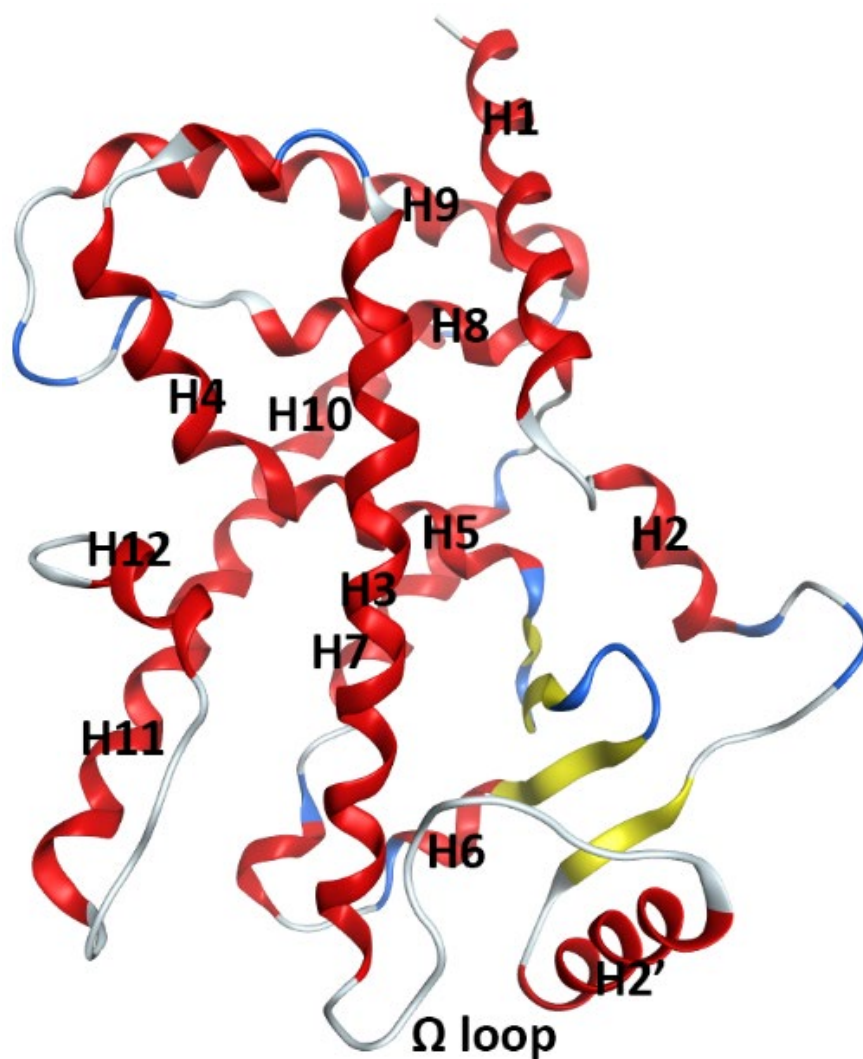


Figure 1.1. The secondary Structure of the LBD of PPAR γ represented in ribbon model.

The ligand binding site is mostly hydrophobic pocket and placed at the bottom half of the LBD.¹⁰ The LBD of PPAR γ has two main ligand-binding sites: orthosteric and allosteric binding sites, each site having different properties and binding preferences.²⁴

The orthosteric site lies from the β -sheet to the far C terminal AF-2 surface which it is perpendicular to the T-shaped cavity, and behind H3 (Figure 1.2).¹⁰ The orthosteric pocket is the canonical binding site for the classic PPAR γ agonists, TZDs.²⁵ The orthosteric pocket involves H3, H5, H11, and 12, which includes various polar residues such as Phe282, Cys285, Ser289, His323, Tyr327, Phe363, Lys367, His449, and Tyr473 (Figure 1.3). The acidic head group of PPAR γ agonist compounds forms hydrogen bonds (H-bonds) with residues Ser289, His323, His449, and Tyr473.^{10, 26} The helix H12 is crucial for ligand binding at the orthosteric site and PPAR function.²⁷ The PPAR γ agonist compounds prompt increases AF-2 stabilization and transcriptional activation by directly binding and stabilizing H12 especially, Tyr473.²⁵

In contrast, several PPAR γ ligands synthesized having the same activity of PPAR γ agonist can bind to an alternate site.²⁴ The PPAR γ ligands binding this alternative site does not compete with endogenous ligand binding at canonical orthosteric pocket so that this binding site can be identified as an allosteric site.²⁴ The allosteric Alternate site binding has three main mechanisms of pharmacological importance. First, two molar equivalents of a PPAR γ ligand can bind to LBD of PPAR γ , one to the canonical orthosteric site and a second to the allosteric site.²⁴ Second, a PPAR γ ligand can bind to allosteric pocket when the canonical orthosteric site is blocked by a covalent irreversible antagonist. Third, a PPAR γ ligand can bind to the allosteric site when the canonical orthosteric pocket is tied with an endogenous covalent ligand.²⁴ The allosteric site extends between H3 and the β -

sheet, which it is parallel to H3 (Figure 1.2).¹⁰ Ligands binding to the allosteric site can also influence PPAR γ structure and function by inducing indirectly AF-2 stabilization and transcriptional activation.¹² The allosteric site surface includes H2', H3, Ω loop, and β -sheets.²⁴

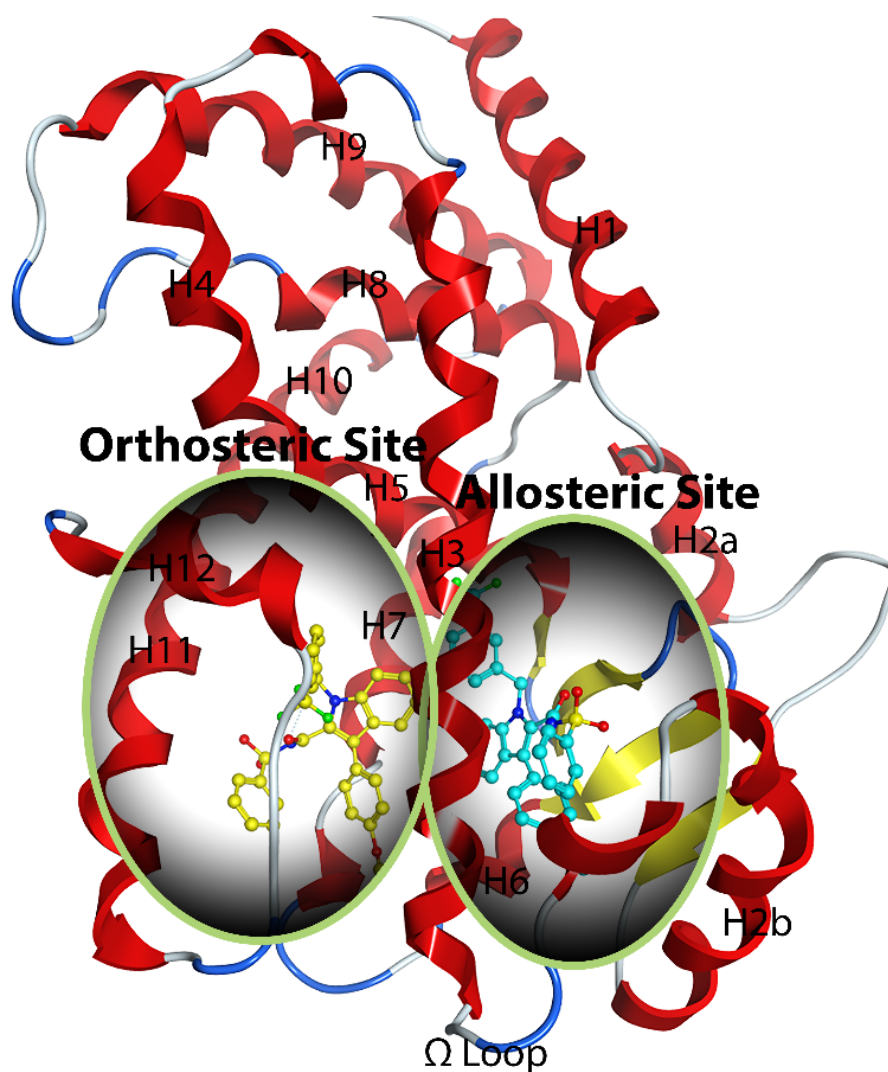


Figure 1.2. Co-crystal structure of NSI-bound PPAR γ (PDB 2HFP) shows two bound NSI molecules, one to the orthosteric pocket and a second bound to the allosteric site.

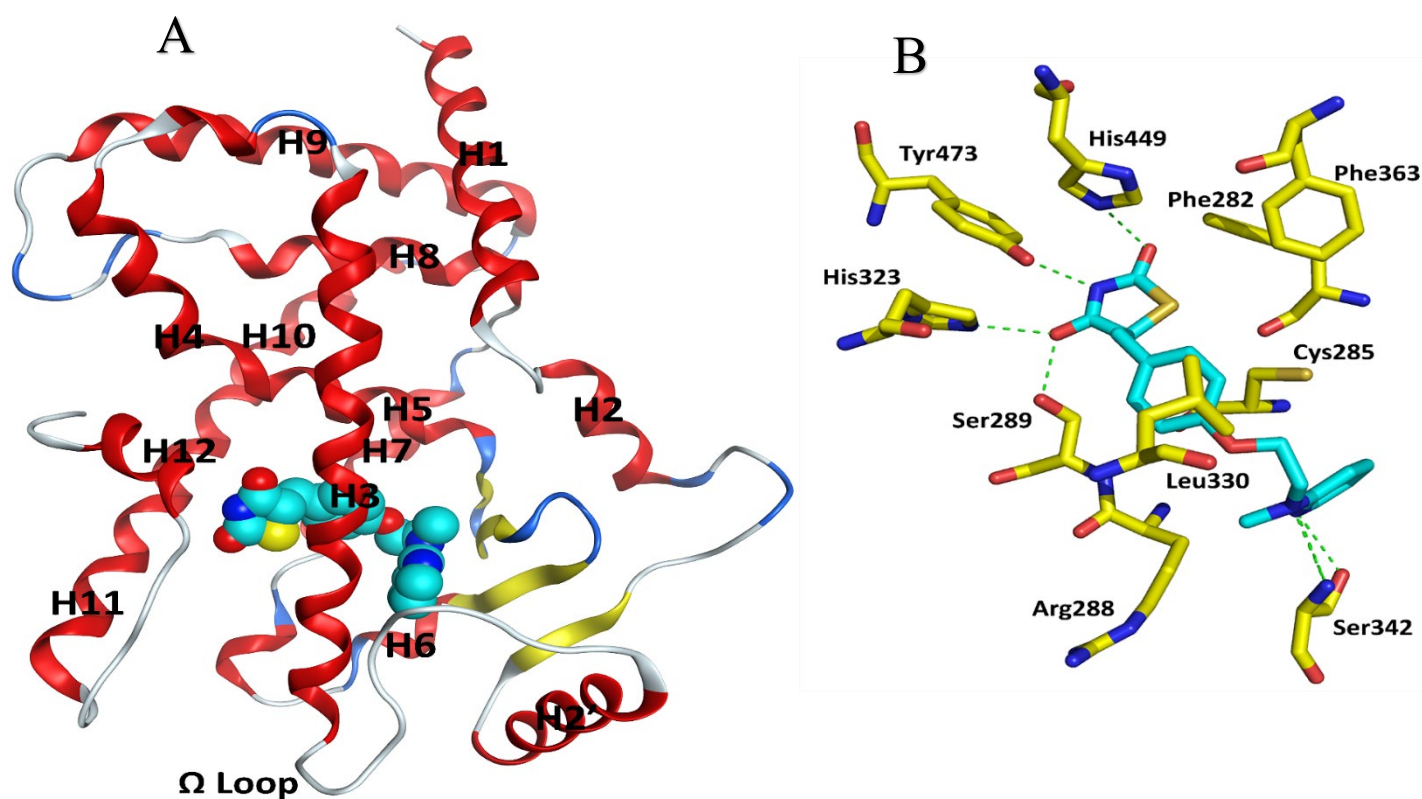


Figure 1.3. (A) Crystal structure of PPAR γ LBD bound to Rosiglitazone (PDB 2PRG).

(B) Binding modes of Rosiglitazone in the orthosteric site of PPAR γ LBD with polar residues for the key interaction.

Hydrophilic residues such as Lys265, Arg288, Ser289, Ser342, and Lys367 are mostly located at the allosteric pocket. Besides, ligands that selectively bind to the allosteric site are possibly exclusive for PPAR γ ligands among other nuclear receptor members.¹²

1.4. PPAR γ Ligands:

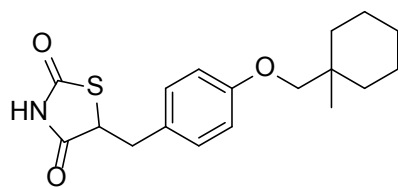
There are several fatty acids and prostanoids are endogenous ligands for PPAR γ . The polyunsaturated fatty acids such as inoleic acid, linolenic acid, arachidonic acid, and eicosapentaenoic acid are the favorable fatty acid agonists for PPAR γ .^{8, 28} The 15-deoxy- $\Delta^{12,14}$ -prostaglandin J₂ (15d-PGJ₂) is also PPAR γ endogenous agonist.^{8, 7} The endogenous ligands have weak PPAR γ agonistic effect at micro molar concentrations.^{29, 30} The TZDs such as ciglitazone, rosiglitazone, pioglitazone, englitazone, and troglitazone were the first small molecules developed as a new class of PPAR γ agonists in the late 1990s (Figure 1.4).¹ They were prepared to improve insulin resistance and antidiabetic activity in patients with type 2 diabetes.¹ Rosiglitazone has a high affinity to PPAR γ , whereas pioglitazone, englitazone, and ciglitazone are less potent PPAR γ ligands.³¹ Troglitazone was the first TZD class got the Food and Drug Administration (FDA) approval for type 2 diabetes in 1997.³² However, it was withdrawn from the US in 2000 due to its severe hepatotoxicity.³² Rosiglitazone and pioglitazone are TZDs, and they are still available in many countries in clinical use in the treatment of type 2 diabetes.³² However, they are associated with numerous undesirable side effects such as fluid retention, heart failure, weight gain, loss of bone mineral density, and cancer.³² Therefore, the use of TZDs is under restrictions now by the FDA.³² Several non-TZD PPAR γ agonists discovered and developed showed a high

affinity to PPAR γ high PPAR γ agonistic effects such as, Farglitazar, MRL-20, and GW1929, GW7845, and GW0207 (Figure 1.5).⁵

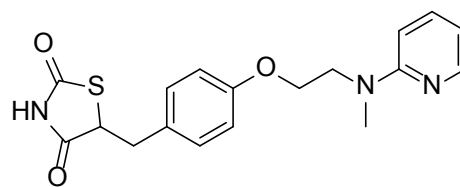
On the other hand, there are several partial PPAR γ agonist molecules such as MRL-24, nTZDpa, SR145, SR147, MBX-102, AMG-131, GW0072, FK614, and SR9034 (Figure 1.6) which partially activate a transcriptional function of a given gene in a wide spectrum of transcriptional activation comparing to full agonists.³³ The partial agonist compounds work as selective PPAR γ modulators (SPPARMs).³³ Therefore, they act as insulin sensitizers and antidiabetic effects as full agonists, and they have lower adverse effects comparing with full PPAR γ agonists.³³ The partial agonist compounds favorably stabilize and interact with the β sheets and H3 than H12 (Figure 1.7).²⁷ Several PPAR γ partial agonists are presently in clinical trials, and none molecule gets the FDA approval yet.³³

In contrast, several PPAR γ antagonist compounds have been identified and prepared to improve the therapeutic index and overcome the undesirable side effects of PPAR γ agonist and partial agonist compounds.^{34, 35} The PPAR γ antagonist compounds exhibited minimum transactivation in PPAR γ . In general, the PPAR γ antagonist compound is defined as a compound has the transactivation efficiency is $\leq 10\%$ of rosiglitazone at 10 μM concentration, and maintain a good affinity for the receptor.³⁴ The PPAR γ antagonist compounds began with covalent PPAR γ antagonists such as GW9662, T0070907, and SR16832 (Figure 1.8), but covalent antagonists are improbable to be designed and developed as therapeutic drugs.^{34 35} However, non-covalent PPAR γ antagonist compounds have prepared and developed, such as SR1664, SR1824, and SR11023 (Figure 1.8).³⁴ The PPAR γ antagonists have strong antidiabetic effects and improve insulin sensitivity. The PPAR γ antagonists showed none of the side effects of TZDs such as fluid retention with

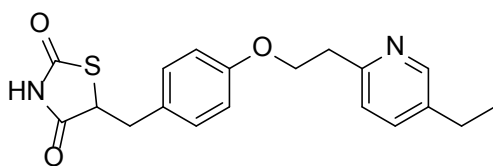
increased risk of weight gain, and loss of bone mineral density.^{36, 37, 38} In addition, the PPAR γ antagonist compounds could inhibit the growth of several tumors such as bladder, breast, pancreatic, and prostate cancer cells.^{15, 16, 17, 18}



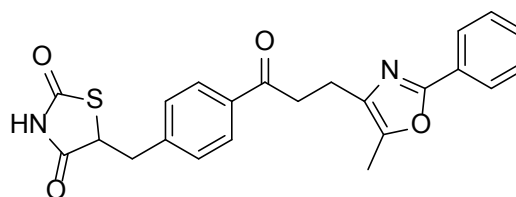
Ciglitazone



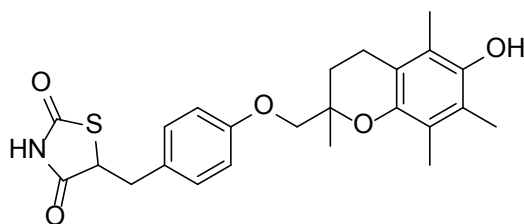
Rosiglitazone



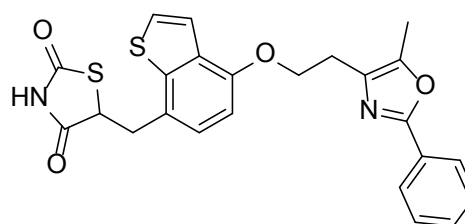
Pioiglitazone



Englitazone

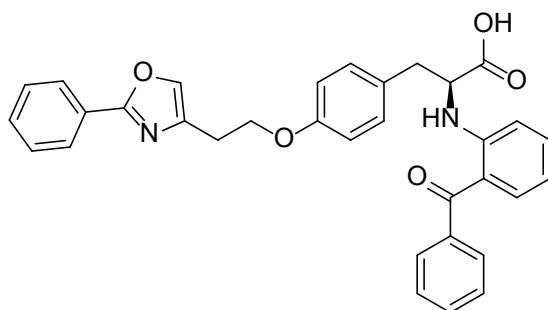


Troglitazone

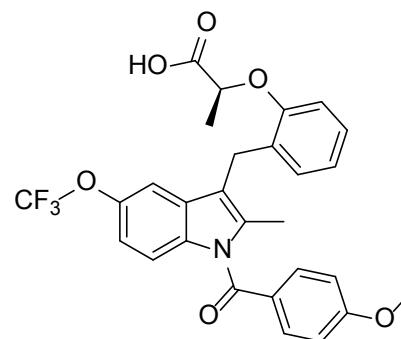


Troglitazone

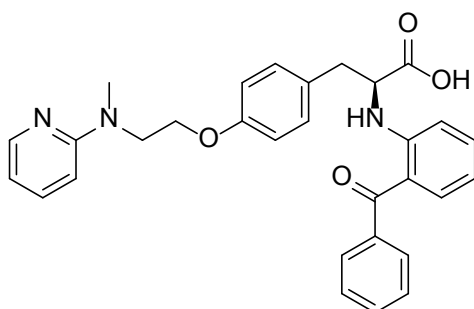
Figure 1.4. Chemical Structures of selective TZDs PPAR γ agonists.



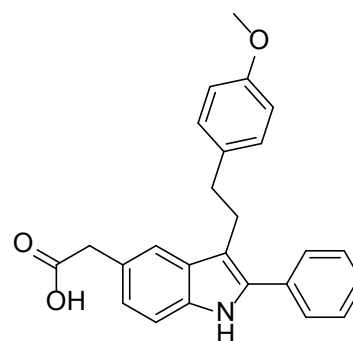
Farglitazar



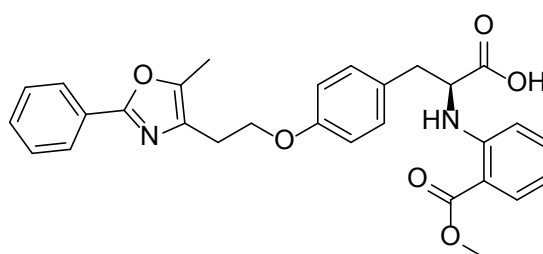
MRL-20



GW1929



GI262570



GW7845

Figure 1.5. Chemical Structures of non TZDs PPAR γ agonists.

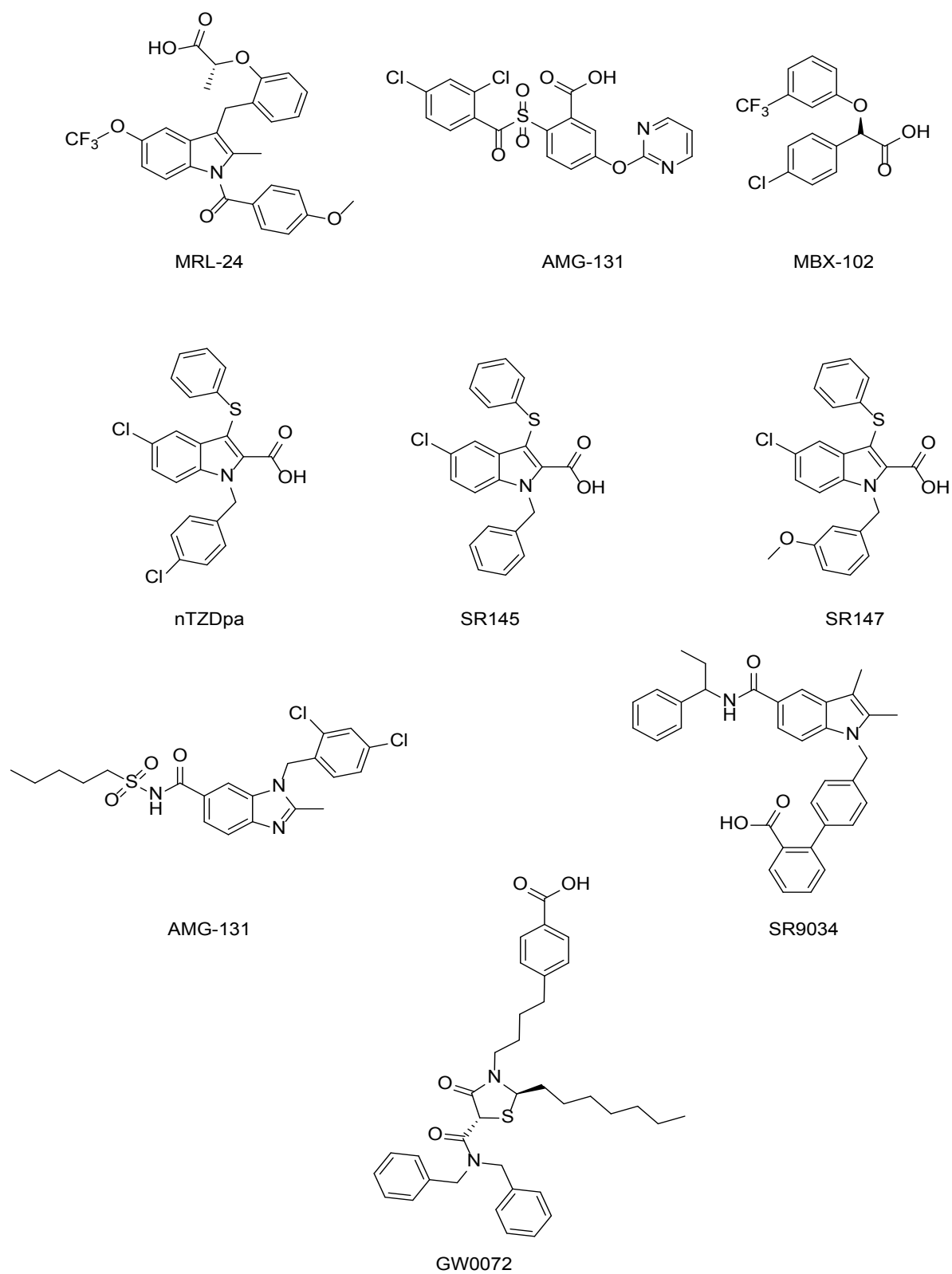


Figure 1.6. Chemical Structures of PPAR γ partial agonists.

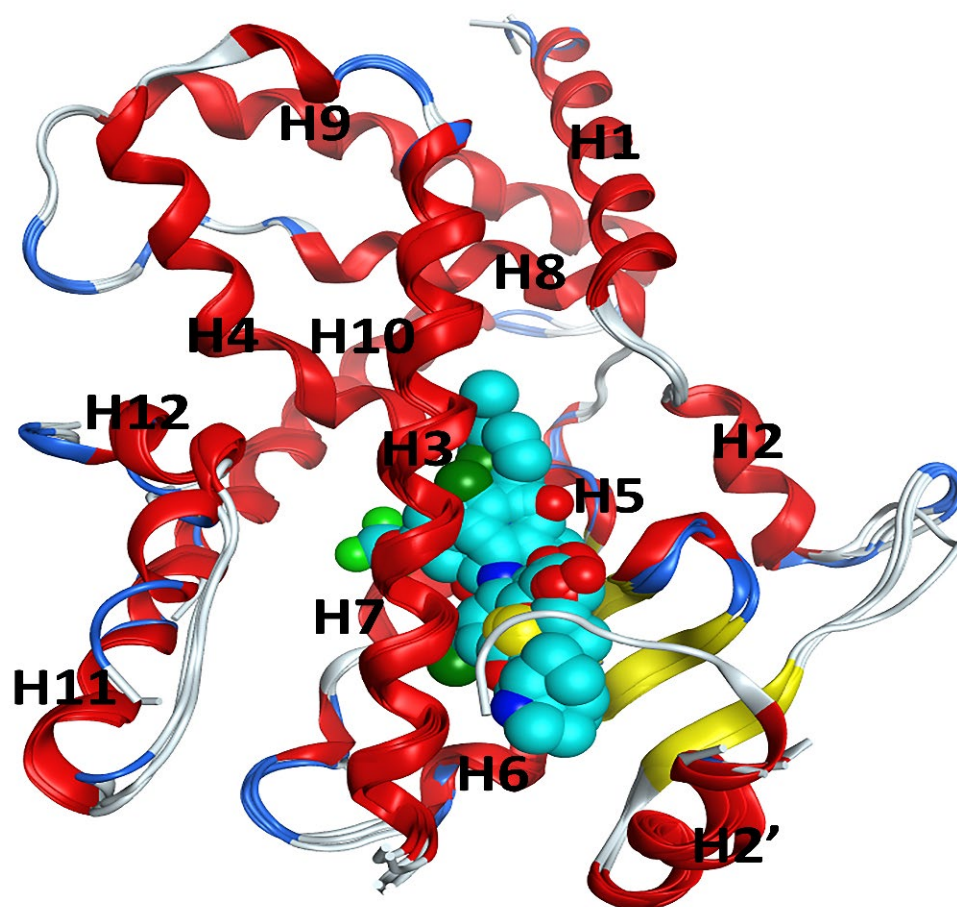
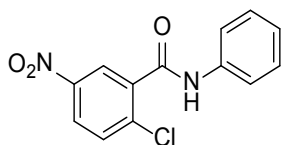
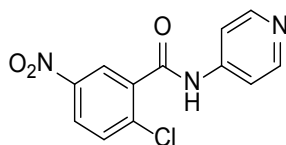


Figure 1.7. Superimposed ribbon structures of PPAR γ with partial agonists.

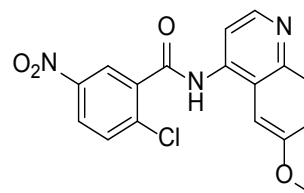
PPAR γ Covalent Antagonists:



GW9662

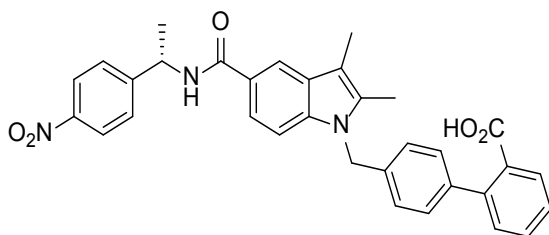


T0070907

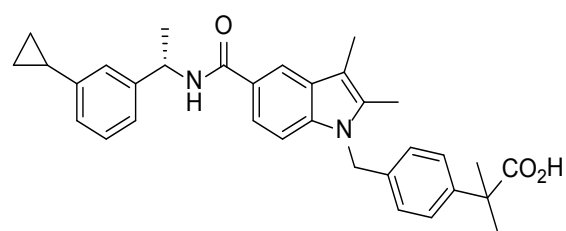


SR16832

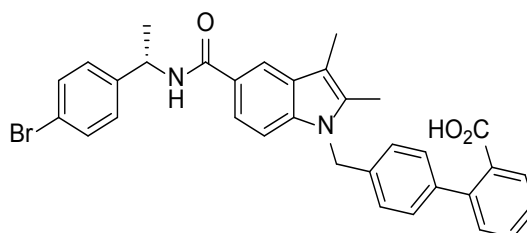
PPAR γ Non Covalent Antagonists



SR1664



SR11023



SR1824

Figure 1.8. Chemical Structures of PPAR γ antagonists.

1.5. Mechanism of Action of PPAR γ Ligands:

The antidiabetic effect of PPAR γ ligands is mostly accomplished by blocking the phosphorylation of PPAR γ by cyclin-dependent kinase 5 (Cdk5) at serine 273 related to obesity.³⁹ The PPAR γ agonists, partial agonist, and antagonists can bind to the LBD of PPAR γ and induce a conformational change of PPAR γ that inhibits the ability of Cdk5 to phosphorylate at serine 273.³⁹ Therefore, the PPAR γ agonists, partial agonist, and antagonists could lower glucose levels and improve insulin sensitivity.³⁹ The PPAR γ full agonists are not required for the strong antidiabetic effect, so the PPAR γ antagonists improved glucose homeostasis and insulin resistance, and they showed none side effects of classical PPAR γ agonists such as TZDs.³⁹

The androgens and the androgen receptor (AR) control the development and growth of prostate cancer.⁴⁰ The suppression of testicular testosterone production was shown to treat prostate cancer.⁴¹ Several AR inhibitors are now approved for the treatment of metastatic prostate cancer.⁴² However, once prostate cancer metastasizes, it eventually develop resistance to AR-targeted therapies.^{43, 44} Many alterations outside of the AR axis have been proposed to contribute to disease initiation and/or progression, including PTEN loss, Nkx3.1 loss, Myc amplification, FOXM1 over-expression, and PI3K/AKT activity, among others.^{45, 46, 47, 48, 49} Recently, the PPAR γ was identified as an oncogene that contributes to prostate cancer development and progression.^{43, 44, 50, 51}

It was originally thought that PPAR γ acted as a tumor suppressor in prostate cancer and that PPAR γ agonists could be used as therapeutics.^{52, 53} However, the PPAR γ agonists were working via PPAR γ -independent mechanisms to inhibit the growth of prostate cancer.^{54, 55} In fact, PPAR γ expression is greater in prostate cancer tissue.^{50, 51, 56} The increased expression of the PPAR γ protein had decreased survival and increased metastases to the lungs and lymph nodes, and positively correlated with prostate cancer.⁵¹ Increased PPAR γ expression in three AR-negative prostate cancer cell lines,

DU-145, PC3, and PC3M, increased cell proliferation and migration.^{44, 51} The siRNA knockdown of PPAR γ and treatment with a PPAR γ antagonist decreased prostate tumor size.⁵¹ Thus, PPAR γ is a novel and important target in prostate cancers. Warfarin inhibited PPAR γ signaling in prostate cancers which lead to the inhibition of prostate cancer growth.^{50, 57} The long-term use of warfarin reduced the risk of prostate cancer.^{50, 57}

1.6. The Glucose transporters (GLUTs):

The Glucose transporters (GLUTs) are members of sugar transporter subfamily of the major facilitator superfamily (MFS), and they are membrane proteins encoded by the solute carrier family genes; SLC2, and SLC5.⁵⁸ The MFS superfamily is one of the most abundant and ubiquitous secondary transporter super families found in bacteria, archaea, and eukarya. The largest family of the MFS is the sugar porter (SP) family.⁵⁹ The GLUTs are facilitative diffusion uniporters of glucose and other monosaccharides from the extracellular matrix (ECM) into cells based on its concentration gradient.⁶⁰ The GLUTs are mainly responsible for the constant uptake of glucose to cells.⁶¹ The GLUTs consist of 14 isoforms and are divided into three classes based on the similarity and identity of the structures and sequences: Class 1 (GLUTs 1–4, and 14), Class 2 (GLUTs 5, 7, 9, and 11), and Class 3 (GLUTs 6, 8, 10, 12, and 13).⁶¹ The expression and distributions GLUTs are different, and they exhibit different transport kinetics, capacity, and substrate selectivity. GLUT1, GLUT2, GLUT3, and GLUT4 are considered the most extensive sugar transporters.⁶¹

The GLUTs have a conserved core fold which consists of 12 transmembrane helices folded into two different domains, the amino and carboxyl terminal domains.⁶² Each domain has six sequential transmembrane helices domain (TMD) that are folded into a pair of ‘3+3’ inverted repeats.⁶³ the amino TMD involves transmembrane helices (TM 1-6), while the carboxyl TMD involves TM7-12.⁶³ The TM7 and TM10 are broken segments, hence termed TM7a/7b and TM10a/10b, respectively (Figure 1.9).⁶³ The GLUTs have the intracellular helical (ICH) domain which involves four short intracellular α -helices (IC1–

4) connect the N-terminal and C-terminal domains, and one short intracellular helix IC5 in the C-terminal domain.⁶³ The C-terminal domain provides the main substrate-binding site for glucose.⁶⁴ The GLUTs transports glucose and several monosaccharides, including galactose, fructose, mannose, xylose, fucose, arabinose, rhamnose, lyxose, altrose, and ribose.^{65, 66}

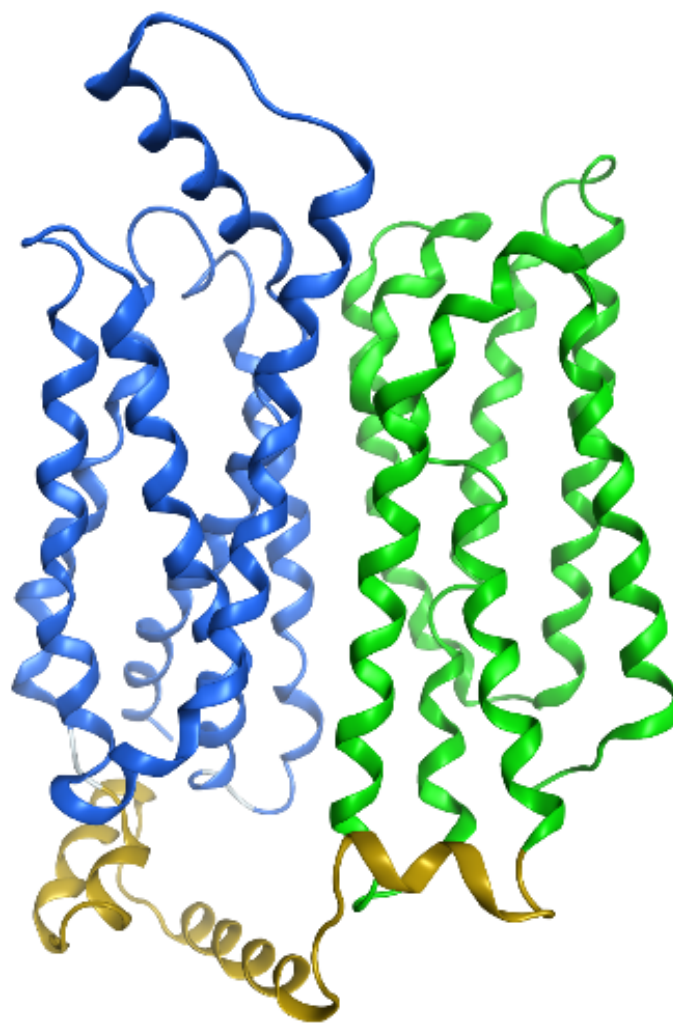


Figure 1.9. The secondary Structure of the GLUT1 represented in ribbon model. The amino TMD is colored blue, the carbonyl TMD is colored green, the ICH are colored yellow.

1.7. Glucose transporter 1 (GLUT1):

The GLUT1 was the first characterized and identified glucose transporters, and it has been a model to recognize and understand the function of glucose transporters.⁶⁷ Cancer cells transport more glucose than normal cells due to their rapid growth and high rate of aerobic glycolysis (Warburg effect).^{68, 69, 70} The high glucose uptake in cancer cells is believed to be related to the upregulated expression of glucose transporter proteins, especially GLUT1. The GLUT proteins have been utilized to be targeted for several anticancer agents by the conjugation the anticancer agents with sugars to improve the delivery and uptake of anticancer agents due to its high expression in tumor cells.⁷¹ The GLUT1 is upregulated in many types of cancers such as brain⁷², breast⁷³, lung⁷⁴, kidney⁷⁵, ovary⁷⁶, prostate,⁷⁷ and colon⁷⁸. In addition, the stimulation of many oncogenes such as KRAS,⁷⁴ BRAF,⁷⁹ c-myc,⁸⁰ and p53,⁸¹ and transcription factors such as hypoxia-inducible factor-1 α (HIF-1)⁸² could upregulate the GLUT1 expression in cancer cells. The positron emission tomography (PET) revealed that the GLUTs are overexpressed on the tumor cells by the high uptake of 2-deoxy-2-[¹⁸F]fluoroglucose, which is a fluorescence glucose analog.⁸³

While GLUT1 is overexpressed in many tumors, it is noted that in the brain, glucose transport is facilitated by both GLUT1 and GLUT3.^{84, 85, 86, 87} Therefore, even though GLUT3 has a greater affinity and higher capacity than GLUT1 in the brain, a potent GLUT1 inhibitor could lead to neurotoxicity. The inhibition of GLUT1 results in a reduction of cancer-cell proliferation and apoptosis.^{88, 89} Several small-molecule inhibitors targeting GLUT1 have been described including resveratrol,⁹⁰ naringenin,⁹¹ phloretin,⁹²

cytochalasin B,⁹³ WZB117,⁹⁴ STF-31,⁹⁵ pyrazolopyrimidines,⁹⁶ phenylalanine amides,⁹³ and (1H-pyrazol-4-yl)quinoline (Figure 1.10).⁹⁷ These compounds showed the anticancer activity against different tumors by their ability to inhibit the glucose uptake and cell proliferation in a dose-dependent manner. All these outcomes emphasize and show the possibility to target and inhibit the GLUT1 protein would be a valid method for cancer treatment.

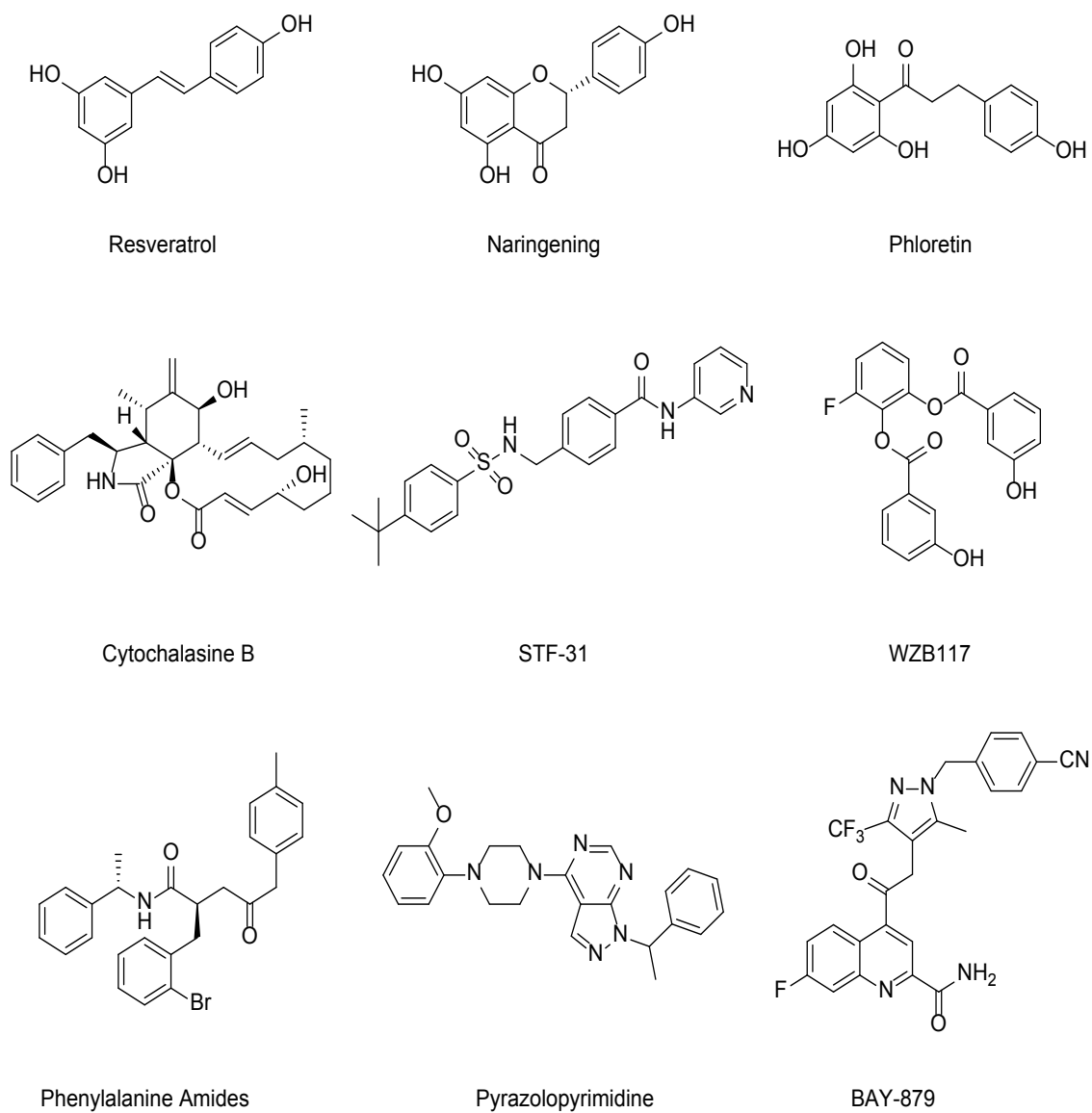


Figure 1.10. Chemical Structures of GLUT1 inhibitors.

1.8. Conformations of GLUT1 Structure:

GLUT1 are uniporters, which transport the substrate across the cell membrane down its concentration by the alternating access mechanism, which involves the “rocker-switch” movement and the “gated pore” mechanisms.^{98,99} GLUT1 transport glucose through alternating access involves substantial conformational change down its concentration gradient⁶⁴. The conformational change is essential to complete a transport cycle⁶⁴. GLUT1 changes from an outward-open conformation (OOP), which opens to the extracellular to take up glucose, to an inward-open conformation (IOP), which allows the release of glucose to the intracellular cytoplasm via partially outward-occluded (POO), outward-occluded (OOC) and partially inward-occluded (PIO) conformations (Figure 1.11)^{63, 64}. Substrate-free GLUT1 structure favors the OOP conformation because of the exuberant interactions between the TMD and the ICH⁶⁴. Once the substrate binds to the C domain of the GLUT1, the binding affinity of the TMD on the extracellular side exceeds the binding affinity of the TMD on the intracellular side, so the transporter shifts to the IOP conformation to release glucose.⁶⁴

Structural studying and analyzing of GLUTs, particularly in complex with ligands, is an essential step for ligands design and optimization. The only crystal structures of human GLUT1 are for the IOP conformation.^{64, 93} However, there are several GLUT1 homologous crystal structures for different conformations. For example, the crystal structures of human glucose transporter 3 (GLUT3), which has an 86% sequence similarity to GLUT1, were obtained for the OOC and OOP conformations.⁶³ The crystal structure of *Escherichia coli* proton: Xylose symporter (Xyle), which has a 49% sequence similarity and 29% sequence identity to GLUT1, were obtained for the POO and PIO conformations.^{100, 101}

The essential amino acids interacting with glucose are conserved between XylE and GLUT1.¹⁰⁰

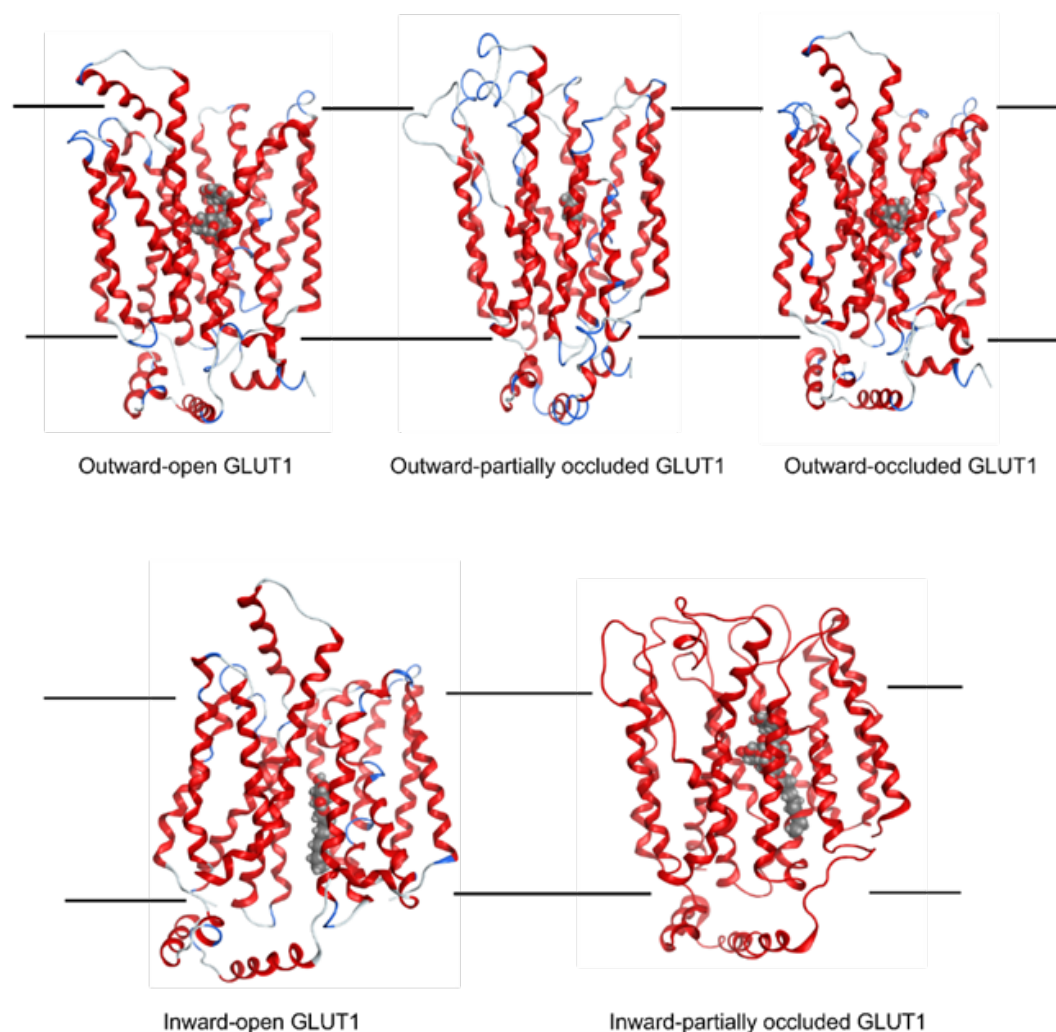


Figure 1.11. An overview of working model of GLUT1: The function of GLUT1 depends on conformational change. The IOP is adopted from PDB ID: 4PYP. The OOP conformation was constructed by homology modeling of PDB ID: 4ZWC; the POO conformation was constructed by homology modeling of PDB ID: 4GBZ; the OOC conformation was constructed by homology modeling of PDB ID: 4ZW9; the Partial inward occluded PIO conformation was constructed by homology modeling of PDB ID: 4JA3.

1.9. Binding Interactions of GLUT1:

The binding site of GLUT1 is predominantly associated with the C domain.⁶⁴ Several amino acids interact with the glucose in different conformations including Gln282, Gln283, Asn288, Asn317, Trp388, Asn411, Trp412, and Asn415^{63 64 100 101}. Most of them are mainly located on TM7 and TM10, which are responsible for alternating access of GLUT1⁶³. Trp388 plays an important role in the alternating access of GLUT1 between the outward open conformation and inward open conformation^{102 103}. Mutation of Trp388 with leucine (W388L) evidently reduce the rate of alternating conformation, and decrease the influx activity of GLUT1^{102, 103}. Trp388 is located in TM10, and it does not expose to the binding site of GLUT1 in OOP.⁹³ While GLUT1 switch to POO and OOC, Trp388 start shifting to the binding site.⁹³ Besides, Trp412, which located in TM11, plays an important role for GLUT1 function.¹⁰⁴ Mutation of Trp412 intensely inhibits the GLUT1 activity.¹⁰⁴ In addition, mutation of Phe379 leads to dropping in glucose transport to less than 25%.¹⁰⁴ Therefore, Phe379, Trp388, and Trp412 play an important role in GLUT1 function and glucose uptake.

References:

1. Willson TM, Brown PJ, Sternbach DD, Henke BR. The PPARs: From orphan receptors to drug discovery. *Journal of medicinal chemistry*. 2000;43(4):527-550. doi: 10.1021/jm990554g.
2. Berger J, Moller DE. The mechanisms of action of PPARs. *Annu Rev Med*. 2002; 53:409-435. doi: 10.1146/annurev.med.53.082901.104018.
3. Ahmadian M, Suh JM, Hah N, et al. PPAR γ signaling and metabolism: The good, the bad and the future. *Nat Med*. 2013;19(5):557-566. doi: 10.1038/nm.3159.
4. Lehrke M, Lazar MA. The many faces of PPARgamma. *Cell*. 2005;123(6):993-999. doi: 10.1016/j.cell.2005.11.026.
5. Sauer S. Ligands for the nuclear peroxisome proliferator-activated receptor gamma. *Trends Pharmacol Sci*. 2015;36(10):688-704. doi: 10.1016/j.tips.2015.06.010.
6. Barish GD, Narkar VA, Evans RM. PPAR delta: A dagger in the heart of the metabolic syndrome. *J. Clin. Invest*. 2006;116(3):590-597. doi: 10.1172/JCI27955.
7. Forman BM, Tontonoz P, Chen J, Brun RP, Spiegelman BM, Evans RM. 15-deoxy-delta 12, 14-prostaglandin J2 is a ligand for the adipocyte determination factor PPAR gamma. *Cell*. 1995;83(5):803-812. doi: 10.1016/0092-8674(95)90193-0.
8. Forman BM, Chen J, Evans RM. The peroxisome proliferator-activated receptors: Ligands and activators. *Ann N Y Acad Sci*. 1996; 804:266-275. doi: 10.1111/j.1749-6632.1996.tb18621.x.

9. Forman BM, Chen J, Evans RM. Hypolipidemic drugs, polyunsaturated fatty acids, and eicosanoids are ligands for peroxisome proliferator-activated receptors alpha and delta. *Proc Natl Acad Sci U S A*. 1997;94(9):4312-4317. doi: 10.1073/pnas.94.9.4312.
10. Nolte RT, Wisely GB, Westin S, et al. Ligand binding and co-activator assembly of the peroxisome proliferator-activated receptor-gamma. *Nature*. 1998;395(6698):137-143. doi: 10.1038/25931.
11. Moore TW, Mayne CG, Katzenellenbogen JA. Minireview: Not picking pockets: Nuclear receptor alternate-site modulators (NRAMs). *Mol Endocrinol*. 2010;24(4):683-695. doi: 10.1210/me.2009-0362.
12. Frkic RL, Marshall AC, Blayo A, et al. PPAR γ in complex with an antagonist and inverse agonist: A tumble and trap mechanism of the activation helix. *iScience*. 2018; 5:69-79. doi: 10.1016/j.isci.2018.06.012.
13. Chandra V, Huang P, Hamuro Y, et al. Structure of the intact PPAR-gamma-RXR-nuclear receptor complex on DNA. *Nature*. 2008;456(7220):350-356. doi: 10.1038/nature07413.
14. Valerio Costa, Maria Assunta Gallo, Francesca Letizia, Marianna Aprile, Amelia Casamassimi, Alfredo Ciccodicola. PPARG: Gene expression regulation and next-generation sequencing for unsolved issues. *PPAR research*. 2010; 2010:1-17. doi: 10.1155/2010/409168.
15. Zaytseva YY, Wallis NK, Southard RC, Kilgore MW. The PPARgamma antagonist T0070907 suppresses breast cancer cell proliferation and motility via both PPARgamma-dependent and -independent mechanisms. *Anticancer Res*. 2011;31(3):813-823.

16. Nakajima A, Tomimoto A, Fujita K, et al. Inhibition of peroxisome proliferator-activated receptor gamma activity suppresses pancreatic cancer cell motility. *Cancer Sci.* 2008;99(10):1892-1900. doi: 10.1111/j.1349-7006.2008.00904.x.
17. Goldstein JT, Berger AC, Shih J, et al. Genomic activation of PPARG reveals a candidate therapeutic axis in bladder cancer. *Cancer Res.* 2017;77(24):6987-6998. doi: 10.1158/0008-5472.CAN-17-1701.
18. Burton JD, Goldenberg DM, Blumenthal RD. Potential of peroxisome proliferator-activated receptor gamma antagonist compounds as therapeutic agents for a wide range of cancer types. *PPAR Res.* 2008; 2008:494161. doi: 10.1155/2008/494161.
19. Mosure SA, Shang J, Eberhardt J, et al. Structural basis of altered potency and efficacy displayed by a major in vivo metabolite of the antidiabetic PPAR γ drug pioglitazone. *J Med Chem.* 2019;62(4):2008-2023. doi: 10.1021/acs.jmedchem.8b01573.
20. W rnmark A, Treuter E, Wright APH, Gustafsson J. Activation functions 1 and 2 of nuclear receptors: Molecular strategies for transcriptional activation. *Mol Endocrinol.* 2003;17(10):1901-1909. <https://academic.oup.com/mend/article/17/10/1901/2747428>. doi: 10.1210/me.2002-0384.
21. Ian M. Chrisman, Michelle D. Nemetchek, Ian Mitchell S. de Vera, et al. Defining a conformational ensemble that directs. *Nat Commun.* 2018;9(1):1-16. <https://www.nature.com/articles/s41467-018-04176-x>. doi: 10.1038/s41467-018-04176-x.
22. Kojetin DJ, Burris TP. Small molecule modulation of nuclear receptor conformational dynamics: Implications for function and drug discovery. *Mol. Pharmacol.* 2013;83(1):1-8. doi: 10.1124/mol.112.079285.

23. Chandra V, Huang P, Hamuro Y, et al. Structure of the intact PPAR- γ -RXR- α nuclear receptor complex on DNA. *Nature*. 2008;456(7220):350-356. doi: 10.1038/nature07413.
24. Hughes TS, Giri PK, de Vera, Ian Mitchell S., et al. An alternate binding site for PPAR γ ligands. *Nat Commun*. 2014; 5:3571. doi: 10.1038/ncomms4571.
25. Brust R, Lin H, Fuhrmann J, Asteian A, Kamenecka TM, Kojetin DJ. Modification of the orthosteric PPAR γ covalent antagonist scaffold yields an improved dual-site allosteric inhibitor. *ACS Chem Biol*. 2017;12(4):969-978. doi: 10.1021/acscchembio.6b01015.
26. Mahindroo N, Huang C, Peng Y, et al. Novel indole-based peroxisome proliferator-activated receptor agonists: Design, SAR, structural biology, and biological activities. *J Med Chem*. 2005;48(26):8194-8208. doi: 10.1021/jm0506930.
27. Bruning JB, Chalmers MJ, Prasad S, et al. Partial agonists activate PPARgamma using a helix 12 independent mechanism. *Structure*. 2007;15(10):1258-1271. doi: 10.1016/j.str.2007.07.014.
28. Poulsen LIC, Siersbæk M, Mandrup S. PPARs: Fatty acid sensors controlling metabolism. *Semin Cell Dev Biol*. 2012;23(6):631-639. doi: 10.1016/j.semcdb.2012.01.003.
29. Lehmann JM, Moore LB, Smith-Oliver TA, Wilkison WO, Willson TM, Kliewer SA. An antidiabetic thiazolidinedione is a high affinity ligand for peroxisome proliferator-activated receptor gamma (PPAR gamma). *J Biol Chem*. 1995;270(22):12953-12956. doi: 10.1074/jbc.270.22.12953.

30. Cho N, Momose Y. Peroxisome proliferator-activated receptor gamma agonists as insulin sensitizers: From the discovery to recent progress. *Curr Top Med Chem.* 2008;8(17):1483-1507.
31. Ye J. Challenges in drug discovery for thiazolidinedione substitute. *Acta Pharmaceutica Sinica B.* 2011;1(3):137-142. doi: 10.1016/j.apsb.2011.06.011.
32. Krische D. The glitazones: Proceed with caution. *West J Emerg Med.* 2000;173(1):54-57. doi: 10.1136/ewjm.173.1.54.
33. Alice J. Kroker, John B. Bruning. Review of the structural and dynamic mechanisms of PPAR γ partial agonism. *PPAR research.* 2015; 2015:816856-15. doi: 10.1155/2015/816856.
34. Asteian A, Blayo A, He Y, et al. Design, synthesis, and biological evaluation of indole biphenylcarboxylic acids as PPAR γ antagonists. *ACS Med Chem Lett.* 2015;6(9):998-1003. doi: 10.1021/acsmchemlett.5b00218.
35. Brust R, Lin H, Fuhrmann J, Asteian A, Kamenecka TM, Kojetin DJ. Modification of the orthosteric PPAR γ covalent antagonist scaffold yields an improved dual-site allosteric inhibitor. *ACS Chem Biol.* 2017;12(4):969-978. doi: 10.1021/acschembio.6b01015.
36. Rubenstrunk A, Hanf R, Hum DW, Fruchart J, Staels B. Safety issues and prospects for future generations of PPAR modulators. *Biochim Biophys Acta.* 2007;1771(8):1065-1081. doi: 10.1016/j.bbalip.2007.02.003.
37. Tang WHW, Maroo A. PPARgamma agonists: Safety issues in heart failure. *Diabetes Obes Metab.* 2007;9(4):447-454. doi: 10.1111/j.1463-1326.2006.00616.x.

38. Kung J, Henry RR. Thiazolidinedione safety. *Expert Opin Drug Saf*. 2012;11(4):565-579. doi: 10.1517/14740338.2012.691963.
39. Choi JH, Banks AS, Estall JL, et al. Anti-diabetic drugs inhibit obesity-linked phosphorylation of PPARgamma by Cdk5. *Nature*. 2010;466(7305):451-456. doi: 10.1038/nature09291.
40. Zhou Y, Bolton EC, Jones JO. Androgens and androgen receptor signaling in prostate tumorigenesis. *J Mol Endocrinol*. 2015;54(1):15. doi: 10.1530/JME-14-0203.
41. Huggins C, Clark PJ. Quantitative studies of prostatic secretion: II. the effect of castration and of estrogen injection on the normal and on the hyperplastic prostate glands of dogs. *J Exp Med*. 1940;72(6):747-762. doi: 10.1084/jem.72.6.747.
42. Friedlander TW, Ryan CJ. Targeting the androgen receptor. *Urol Clin North Am*. 2012;39(4):453-464. doi: 10.1016/j.ucl.2012.07.003.
43. Elix C, Pal SK, Jones JO. The role of peroxisome proliferator-activated receptor gamma in prostate cancer. *Asian J Androl*. 2018;20(3):238-243. doi: 10.4103/aja.aja_15_17.
44. Salgia MM, Elix CC, Pal SK, Jones JO. Different roles of peroxisome proliferator-activated receptor gamma isoforms in prostate cancer. *Am J Clin Exp Urol*. 2019;7(3):98-109.
45. Deocampo ND, Huang H, Tindall DJ. The role of PTEN in the progression and survival of prostate cancer. *Minerva Endocrinol*. 2003;28(2):145-153.

46. Abate-Shen C, Banach-Petrosky WA, Sun X, et al. Nkx3.1; pten mutant mice develop invasive prostate adenocarcinoma and lymph node metastases. *Cancer Res.* 2003;63(14):3886-3890.
47. Ellwood-Yen K, Graeber TG, Wongvipat J, et al. Myc-driven murine prostate cancer shares molecular features with human prostate tumors. *Cancer Cell.* 2003;4(3):223-238.
48. Aytes A, Mitrofanova A, Lefebvre C, et al. Cross-species regulatory network analysis identifies a synergistic interaction between FOXM1 and CENPF that drives prostate cancer malignancy. *Cancer Cell.* 2014;25(5):638-651. doi: 10.1016/j.ccr.2014.03.017.
49. Goldstein AS, Huang J, Guo C, Garraway IP, Witte ON. Identification of a cell of origin for human prostate cancer. *Science.* 2010;329(5991):568-571. doi: 10.1126/science.1189992.
50. Tew BY, Hong TB, Otto-Duessel M, et al. Vitamin K epoxide reductase regulation of androgen receptor activity. *Oncotarget.* 2017;8(8):13818-13831. doi: 10.18632/oncotarget.14639.
51. Ahmad I, Mui E, Galbraith L, et al. Sleeping beauty screen reveals pparg activation in metastatic prostate cancer. *Proc Natl Acad Sci U S A.* 2016;113(29):8290-8295. doi: 10.1073/pnas.1601571113.
52. Kubota T, Koshizuka K, Williamson EA, et al. Ligand for peroxisome proliferator-activated receptor gamma (troglitazone) has potent antitumor effect against human prostate cancer both in vitro and in vivo. *Cancer Res.* 1998;58(15):3344-3352.

53. Mueller E, Smith M, Sarraf P, et al. Effects of ligand activation of peroxisome proliferator-activated receptor gamma in human prostate cancer. *Proc Natl Acad Sci U S A*. 2000;97(20):10990-10995.
54. Shiau C, Yang C, Kulp SK, et al. Thiazolidinediones mediate apoptosis in prostate cancer cells in part through inhibition of bcl-xL/bcl-2 functions independently of PPARgamma. *Cancer Res*. 2005;65(4):1561-1569. doi: 10.1158/0008-5472.CAN-04-1677.
55. Qin L, Gong C, Chen A, et al. Peroxisome proliferator-activated receptor γ agonist rosiglitazone inhibits migration and invasion of prostate cancer cells through inhibition of the CXCR4/CXCL12 axis. *Mol Med Rep*. 2014;10(2):695-700. doi: 10.3892/mmr.2014.2232.
56. Segawa Y, Yoshimura R, Hase T, et al. Expression of peroxisome proliferator-activated receptor (PPAR) in human prostate cancer. *Prostate*. 2002;51(2):108-116. doi: 10.1002/pros.10058.
57. Tagalakis V, Tamim H. The effect of warfarin use on clinical stage and histological grade of prostate cancer. *Pharmacoepidemiol Drug Saf*. 2010;19(5):436-439. doi: 10.1002/pds.1943.
58. Thorens B, Mueckler M. Glucose transporters in the 21st century. *Am J Physiol Endocrinol Metab*. 2010;298(2):141. doi: 10.1152/ajpendo.00712.2009.
59. Quistgaard EM, Low C, Guettou F, Nordlund P. Understanding transport by the major facilitator superfamily. *Nat Rev Mol Cell Biol*. 2016;17(2):123. doi: 10.1038/nrm.2015.25.

60. Cura AJ, Carruthers A. Role of monosaccharide transport proteins in carbohydrate assimilation, distribution, metabolism and homeostasis. *Compr Physiol*. 2012;2(2):863-914. doi: 10.1002/cphy.c110024.
61. Mueckler M, Thorens B. The SLC2 (GLUT) family of membrane transporters. *Mol Aspects Med*. 2013;34(2-3):121-138. doi: 10.1016/j.mam.2012.07.001.
62. Yan N. Structural advances for the major facilitator superfamily (MFS) transporters. *Trends Biochem Sci*. 2013;38(3):151-159.
63. Deng D, Sun P, Yan C, et al. Molecular basis of ligand recognition and transport by glucose transporters. *Nature*. 2015;526(7573):391-396.
64. Deng D, Xu C, Sun P, et al. Crystal structure of the human glucose transporter GLUT1. *Nature*. 2014;510(7503):121-125. doi: 10.1038/nature13306.
65. Rumsey SC, Kwon O, Xu GW, Burant CF, Simpson I, Levine M. Glucose transporter isoforms GLUT1 and GLUT3 transport dehydroascorbic acid. *J Biol Chem*. 1997;272(30):18982-18989. doi: 10.1074/jbc.272.30.18982.
66. Ung PM, Song W, Cheng L, et al. Inhibitor discovery for the human GLUT1 from homology modeling and virtual screening. *ACS Chem Biol*. 2016;11(7):1908-1916. doi: 10.1021/acscchembio.6b00304.
67. Shen Y, Arbman G, Olsson B, Sun X. Overexpression of GLUT1 in colorectal cancer is independently associated with poor prognosis. *Int J Biol Markers*. 2011;26(3):166-172. doi: 10.5301/JBM.2011.8550.

68. Otto W, Wind F, Erwen N. The metabolism of tumors in the body. *J Gen Physiol.* 1927;8(6):519-530.
69. Hanahan D, Weinberg R. Hallmarks of cancer: The next generation. *Cell.* 2011;144(5):646-674. doi: 10.1016/j.cell.2011.02.013.
70. Barron CC, Bilan PJ, Tsakiridis T, Tsiani E. Facilitative glucose transporters: Implications for cancer detection, prognosis and treatment. *Metabolism.* 2015;65(2):124-139. doi: 10.1016/j.metabol.2015.10.007.
71. Calvaresi EC, Hergenrother PJ. Glucose conjugation for the specific targeting and treatment of cancer. *Chem Sci.* 2013;4(6):2319-2333. doi: 10.1039/c3sc22205e.
72. Nishioka T, Oda Y, Seino Y, et al. Distribution of the glucose transporters in human brain tumors. *Cancer Res.* 1992;52(14):3972-3979.
73. Brown RS, Wahl RL. Overexpression of glut-1 glucose transporter in human breast cancer. an immunohistochemical study. *Cancer.* 1993;72(10):2979-2985.
74. Sasaki H, Shitara M, Yokota K, et al. Overexpression of GLUT1 correlates with kras mutations in lung carcinomas. *Mol Med Rep.* 2012;5(3):599-602. doi: 10.3892/mmr.2011.736.
75. Nagase Y, Takata K, Moriyama N, Aso Y, Murakami T, Hirano H. Immunohistochemical localization of glucose transporters in human renal cell carcinoma. *J Urol.* 1995;153(3 Pt 1):798-801.

76. Cai Y, Zhai J, Feng B, Duan X, He X. Expression of glucose transporter protein 1 and p63 in serous ovarian tumor. *J Obstet Gynaecol Res.* 2014;40(7):1925-1930. doi: 10.1111/jog.12447.
77. Reinicke K, Sotomayor P, Cisterna P, Delgado C, Nualart F, Godoy A. Cellular distribution of glut-1 and glut-5 in benign and malignant human prostate tissue. *J Cell Biochem.* 2012;113(2):553-562. doi: 10.1002/jcb.23379.
78. Haber RS, Rathana A, Weiser KR, et al. GLUT1 glucose transporter expression in colorectal carcinoma. *Cancer.* 1998;83(1):34-40. doi: 10.1002/(SICI)1097-0142(19980701)83:13.0.CO;2-E.
79. Sheu JJ, Guan B, Tsai F, et al. Mutant BRAF induces DNA strand breaks, activates DNA damage response pathway, and up-regulates glucose transporter-1 in nontransformed epithelial cells. *Am J Pathol.* 2012;180(3):1179-1188. doi: 10.1016/j.ajpath.2011.11.026.
80. Osthus RC, Shim H, Kim S, et al. Deregulation of glucose transporter 1 and glycolytic gene expression by c-myc. *J Biol Chem.* 2000;275(29):21797-21800. doi: 10.1074/jbc.C000023200.
81. Schwartzberg-Bar-Yoseph F, Armoni M, Karnieli E. The tumor suppressor p53 down-regulates glucose transporters GLUT1 and GLUT4 gene expression. *Cancer Res.* 2004;64(7):2627-2633.
82. Wincewicz A, Sulkowska M, Koda M, Sulkowski S. Clinicopathological significance and linkage of the distribution of HIF-1 α and GLUT-1 in human primary colorectal cancer. *Pathol Oncol Res.* 2007;13(1):15-20.

83. Ong L-, Jin Y, Song I-, Yu S, Zhang K, Chow PKH. 2-[18F]-2-deoxy-D-glucose (FDG) uptake in human tumor cells is related to the expression of GLUT-1 and hexokinase II. *Acta Radiol.* 2008;49(10):1145-1153. doi: 10.1080/02841850802482486.
84. David Z. Gerhart, Margaret A. Broderius, Nancy D. Borson, Lester R. Drewes. Neurons and microvessels express the brain glucose transporter protein GLUT3. *Proc Natl Acad Sci U S A.* 1992;89(2):733-737. doi: 10.1073/pnas.89.2.733.
85. Mantych GJ, James DE, Chung HD, Devaskar SU. Cellular localization and characterization of glut 3 glucose transporter isoform in human brain. *Endocrinology.* 1992;131(3):1270-1278. doi: 10.1210/endo.131.3.1505464.
86. Patching SG. Glucose transporters at the blood-brain barrier: Function, regulation and gateways for drug delivery. *Mol Neurobiol.* 2017;54(2):1046-1077. doi: 10.1007/s12035-015-9672-6.
87. Simpson IA, Dwyer D, Malide D, Moley KH, Travis A, Vannucci SJ. The facilitative glucose transporter GLUT3: 20 years of distinction. *Am J Physiol Endocrinol Metab.* 2008;295(2):242-253. doi: 10.1152/ajpendo.90388.2008.
88. Robey RB, Hay N. Akt, hexokinase, mTOR: Targeting cellular energy metabolism for cancer therapy. *Drug Discov Today Dis, Mech.* 2005;2(2):239-246. doi: 10.1016/j.ddmec.2005.05.021.
89. Xu R, Pelicano H, Zhou Y, et al. Inhibition of glycolysis in cancer cells: A novel strategy to overcome drug resistance associated with mitochondrial respiratory defect and hypoxia. *Cancer Res.* 2005;65(2):613.

90. Salas M, Obando P, Ojeda L, et al. Resolution of the direct interaction with and inhibition of the human GLUT1 hexose transporter by resveratrol from its effect on glucose accumulation. *Am J Physiol , Cell Physiol*. 2013;305(1):90. doi: 10.1152/ajpcell.00387.2012.
91. Martin H, Kornmann F, Fuhrmann GF. The inhibitory effects of flavonoids and antiestrogens on the Glut1 glucose transporter in human erythrocytes. *Chem Biol Interact*. 2003;146(3):225-235.
92. Cho SJ, Moon JS, Lee CM, Choi A M. K., Stout-Delgado HS. Glucose transporter 1–Dependent glycolysis is increased during aging-related lung fibrosis, and phloretin inhibits lung fibrosis. *Am J Respir Cell Mol Biol*. 2017;56(4):521. doi: 10.1165/rcmb.2016-0225OC.
93. Kapoor K, Finer-Moore JS, Pedersen BP, et al. Mechanism of inhibition of human glucose transporter GLUT1 is conserved between cytochalasin B and phenylalanine amides. *Proc Natl Acad Sci U S A*. 2016;113(17):4711-4716.
94. Liu Y, Cao Y, Zhang W, et al. A small-molecule inhibitor of glucose transporter 1 downregulates glycolysis, induces cell-cycle arrest, and inhibits cancer cell growth in vitro and in vivo. *Mol Cancer Ther*. 2012;11(8):1672-1682. doi: 10.1158/1535-7163.MCT-12-0131.
95. Chan DA, Sutphin PD, Nguyen P, et al. Targeting GLUT1 and the warburg effect in renal cell carcinoma by chemical synthetic lethality. *Sci Transl Med*. 2011;3(94):94ra70. doi: 10.1126/scitranslmed.3002394.

96. Siebeneicher H, Bauser M, Buchmann B, et al. Identification of novel GLUT inhibitors. *Bioorg Med Chem Lett*. 2016;26(7):1732-1737.
97. Siebeneicher H, Cleve A, Rehwinkel H, et al. Identification and optimization of the first highly selective GLUT1 inhibitor BAY-876. *ChemMedChem*. 2016;11(20):2261-2271. doi: 10.1002/cmdc.201600276.
98. DeFelice LJ. Transporter structure and mechanism. *Trends In Neurosci*. 2004; 27(6):352–359.
99. Shimamura T, Weyand S, Beckstein O, et al. Molecular basis of alternating access membrane transport by the sodium-hydantoin transporter Mhp1. *Science*. 2010;328(5977):470-473. doi: 10.1126/science.1186303.
100. Sun L, Zeng X, Yan C, et al. Crystal structure of a bacterial homologue of glucose transporters GLUT1-4. *Nature*. 2012;490(7420):361-366. doi: 10.1038/nature11524.
101. Quistgaard EM, Löw C, Moberg P, Trésaugues L, Nordlund P. Structural basis for substrate transport in the GLUT-homology family of monosaccharide transporters. *Nat Struct Mol Biol*. 2013;20(6):766-768.
102. Katagiri H, Asano T, Ishihara H, et al. Role of tryptophan-388 of GLUT1 glucose transporter in glucose-transport activity and photoaffinity-labelling with forskolin. *Biochem J*. 1993;291 (Pt 3):861-867. doi: 10.1042/bj2910861.
103. Kasahara T, Kasahara M. Tryptophan 388 in putative transmembrane segment 10 of the rat glucose transporter Glut1 is essential for glucose transport. *J Biol Chem*. 1998;273(44):29113-29117. doi: 10.1074/jbc.273.44.29113.

104. Garcia JC, Strube M, Leingang K, Keller K, Mueckler MM. Amino acid substitutions at tryptophan 388 and tryptophan 412 of the HepG2 (Glut1) glucose transporter inhibit transport activity and targeting to the plasma membrane in xenopus oocytes. *J Biol Chem.* 1992;267(11):7770-7776.

Chapter 2

Molecular Modeling of Allosteric Site of Isoform-Specific Inhibition of the Peroxisome Proliferator-activated Receptor PPAR γ

Abstract:

Herein we run the docking studies for several antagonists of peroxisome proliferator-activated receptor gamma (PPAR γ), which is a promising target for anticancer, and antidiabetic drug design. The crystal structures of PPAR γ complexed with ligands revealed that PPAR γ ligands can bind alternatively orthosteric or allosteric site. The orthosteric pocket is the favorable binding site for thiazolidinedione (TZD) class of antidiabetic drugs. The glide docking studies performed well in predicting the binding affinity of PPAR γ antagonists, and they are highly related to the allosteric binding site. Our results emphasize that the allosteric site of PPAR γ is the most favorable binding site for antagonists. In addition, the ligand-protein interactions for several PPAR γ antagonists, agonists, and partial agonists were analyzed to define the antagonists binding modes and highlight that very distinct PPAR γ residues interact selectively with antagonists. Phe282, Arg288, and Lys367 interact with antagonists more than agonists and partial agonists at allosteric pocket. In contrast, Phe282, Phe363, Lys367, and His449 interact with antagonists more than agonists and partial agonists at orthosteric pocket. The molecular modeling provides a template to design and develop active and selective therapeutic antagonists against to atherosclerosis, diabetes, obesity, and cancer.

2.1. Introduction:

Peroxisome proliferator-activated receptors (PPARs) are receptors for fatty acids and members of the nuclear receptor superfamily.^{1, 2, 3} PPARs work as ligand activated transcription factors that control gene expression of several biological functions such as lipid and glucose metabolism and cellular differentiation.^{1,2,3} PPAR family involves three isoforms, PPAR α , PPAR γ , and PPAR δ ; each isoform has different tissue distribution, selectivity, and responsiveness to ligands.^{1,4} PPAR γ is an interesting target because of associated with several disorders including atherosclerosis, diabetes, obesity, and cancer.⁵ The thiazolidinedione (TZDs) class of antidiabetic drugs, rosiglitazone and pioglitazone, are classical PPAR γ agonists and they have characterized a significant ligands to treat insulin resistance associated with type 2 diabetes so far.⁶ However, increased PPAR γ expression has been found to control other pathways that could induce cancer development and progression, so PPAR γ antagonists could inhibit the growth of bladder, breast, pancreatic, and prostate cancer cells.^{7, 8, 9, 10} In addition, several PPAR γ antagonists have been showed valuable therapeutic effects in the treatment of obesity with better therapeutic index comparing with PPAR γ agonists.^{11, 12} In fact, PPAR γ antagonists overcome vigorous TZD undesirable side effects such as heart failure, and fluid retention with increased risk of weight gain, loss of bone mineral density.^{11, 12}

PPAR γ forms heterodimerization with retinoid X receptor α (RXR α) to produce a transcription factor which is able to bind peroxisome proliferator response elements (PPRE) on DNA to induce transcription of target genes.¹³ The PPAR γ structure constitutes N-terminal domain which include activation function 1 (AF1) that binds co-regulators, a central zinc-finger domain for DNA binding (DBD); C-terminal domain which include

ligand-binding domain (LBD) and activation function 2 (AF-2) that binds ligands and co-regulators; and a hinge region that connects the LBD and DBD.^{14, 15} The C-terminal domain has a vital function which facilitates ligand binding, dimerization, and transactivation functions.¹⁴ The crystal structure of LBD of PPAR γ consists of 13 α -helices and four β -sheet strands. The LBD of PPAR γ is similar to other nuclear-receptor structures from helix 3 to carboxy-terminal domain, but PPAR γ has an extra helix, H2', located between the first β -sheet and H3.¹⁴ The LBD of PPAR γ is large ($\sim 1,300$ Å), mostly hydrophobic pocket, and T-shaped cavity which expands from β -sheet strands to carboxy-terminal domain.¹⁴ LBD of PPAR γ has two main ligand-binding sites; one lies from the β -sheet to the C-terminal activation function-2 (AF-2) surface which it is perpendicular to the T-shaped cavity, behind H3 (an orthosteric site), while the other one extends between H3 and the β -sheet which it is parallel to H3 (an allosteric site).^{14, 16}

TZDs are PPAR γ agonists that initiate transcription through binding to a canonical orthosteric pocket, and stabilize AF-2 (H11, and H12) which is coactivator interaction surface in the PPAR γ LBD and assists induction of coactivator proteins to PPAR γ target gene promoters, which stimulates chromatin transformation and rises expression of PPAR γ target genes.¹⁷ TZDs generate several interactions with amino acids in H3, H4, H10, and AF-2 which involves various polar residues such as Cys285, Ser289, His323, Tyr327, Lys367, His449, and Tyr473.¹⁴ In contrast, several PPAR γ ligands (agonist, partial agonist, and antagonist) have alternating binding site located between H3 and the β -sheets.¹⁶ PPAR γ ligands binding this alternate site does not compete with endogenous ligand binding canonical orthosteric pocket, so this binding site can be identified as an allosteric site.¹⁶ Ligands binding to the allosteric site can also induce AF-2 stabilization

and transcriptional activation. The allosteric site surface includes: H2', H3, Ω loop, H7, and β -sheets.¹⁶ This site involves several hydrophilic residues such as Glu259, Lys265, His266, Arg288, Ser289, Glu295, Ser342, Glu343, and Lys367. Besides, ligands binding to the allosteric site is possibly exclusive for PPAR γ ligands between other nuclear-receptor members.¹⁵

To define which binding site is the more favorable for PPAR γ antagonists and the structural basis for PPAR γ isoform binding, we run a series of docking studies of testified PPAR γ antagonists with the crystal structures of PPAR γ . In addition, we analyzed the ligand-protein interactions to recognize the restudies which are selective for an interaction with antagonist. We proposed that docking studies based on crystal structures of PPAR γ can provide beneficial understanding for PPAR γ antagonists develop and design. The docking studies showed the allosteric site is more favorable for PPAR γ antagonists binding affinity, so this site can be utilized for PPAR γ antagonists design and develop.

2.2. Computational Methods:

2.2.1 Preparation of Protein Structures:

We downloaded the X-ray crystal structures of PPAR γ wild type complexed with *N*-sulfonyl-2-indole carboxamides (NSI) ligand (PDB ID: 2HFP) (Figure 2.1) from the RCSB Protein Data Bank (<https://www.rcsb.org/structure/2hfp>).¹⁸ 2HFP is a PPAR γ co-crystal with two molecules of NSI bound at different binding site. There are no missing residues in the crystal structure of 2HFP. Straightaway, we used the Protein Preparation Wizard in the Schrödinger software suite for protein structure preparation. The side-chain structures of Gln and Asn were permitted to flip to maximize H-bond interactions through the Protein

Preparation Wizard process. In addition, water molecules in the crystal structure were deleted. Then, the prepared protein was subjected to 500 iterations of energy minimization with backbone atoms being restrained using the OPLS force field in the MacroModel module in the Schrödinger software suite.^{19,20}

2.2.2. Preparation of Ligands:

We collected forty-seventh PPAR γ antagonists (Figure 2.2, Figure 2.4, and Figure 2.5) from different sources^{18, 11 15}, and we built these antagonists based on the template structure of *N*-sulfonyl-2-indole carboxamides (NSI) ligand in 2HFP. Besides, we built several PPAR γ agonists, and partial agonists (Figure 2.2, Figure 2.4, and Figure 2.5) for analyzing the ligand-protein interactions. All PPAR γ ligands were built using the Maestro Build panel and subsequently minimized by the MacroModel program using the OPLS2005 force field. In addition, we downloaded a database of 3D molecules from the National Cancer Institute (NCI),²¹ and then four hundred and twenty-three drug-like molecules were randomly selected from this database to assess the enrichment factor and validate our docking study. The molecules were then subjected to energy minimization using the MacroModel program.

2.2.3. Molecular Docking:

Docking of the antagonists into the orthosteric and allosteric binding sites of PPAR γ was completed using the Schrödinger software suite. We generated two grid files for the crystal structure of 2HFP using the Glide Grid Generation protocol with the bound ligands as centroids, one for orthosteric binding site and the other for allosteric binding site of PPAR γ . All 47 PPAR γ antagonists were docked to each of the two grid files, and we later run docking for the 423 NCI drug-like molecules were docked to the allosteric binding site

of PPAR γ grid file. During the docking process, the scaling factor for receptor van der Waals for the nonpolar atoms was set to 0.8 to allow for some flexibility of the receptor, and the precision was set as extra precision. Besides, all other parameters were used as defaults. The output docking scores were given as extra precision glide scores (XP GScore). The XP GScore is stated in term of a predicated binding affinity as well as a predicated free energy of binding (ΔG_{PRED}). The output ΔG_{PRED} was then related to the experimental ΔG_{EXP} , calculated from the experimental IC_{50} (nM) using the following equation 1²²:

$$\Delta G_{\text{EXP}}(\text{kcal/mol}) = RT \ln (\text{IC}_{50} (\text{nM}) \times 10^{-9})/1000 \quad (1)$$

The Pearson's R (Pearson's correlation coefficient) was estimated using Microsoft Excel and the root-mean-square error and mean-absolute-error were measured from MatLab. Furthermore, we created electrostatic map for the orthosteric binding site of PPAR γ to estimate the electrostatically favored locations of positive, negative and neutral donor locations by using surface and map panel from the molecular operating environment (MOE).²³

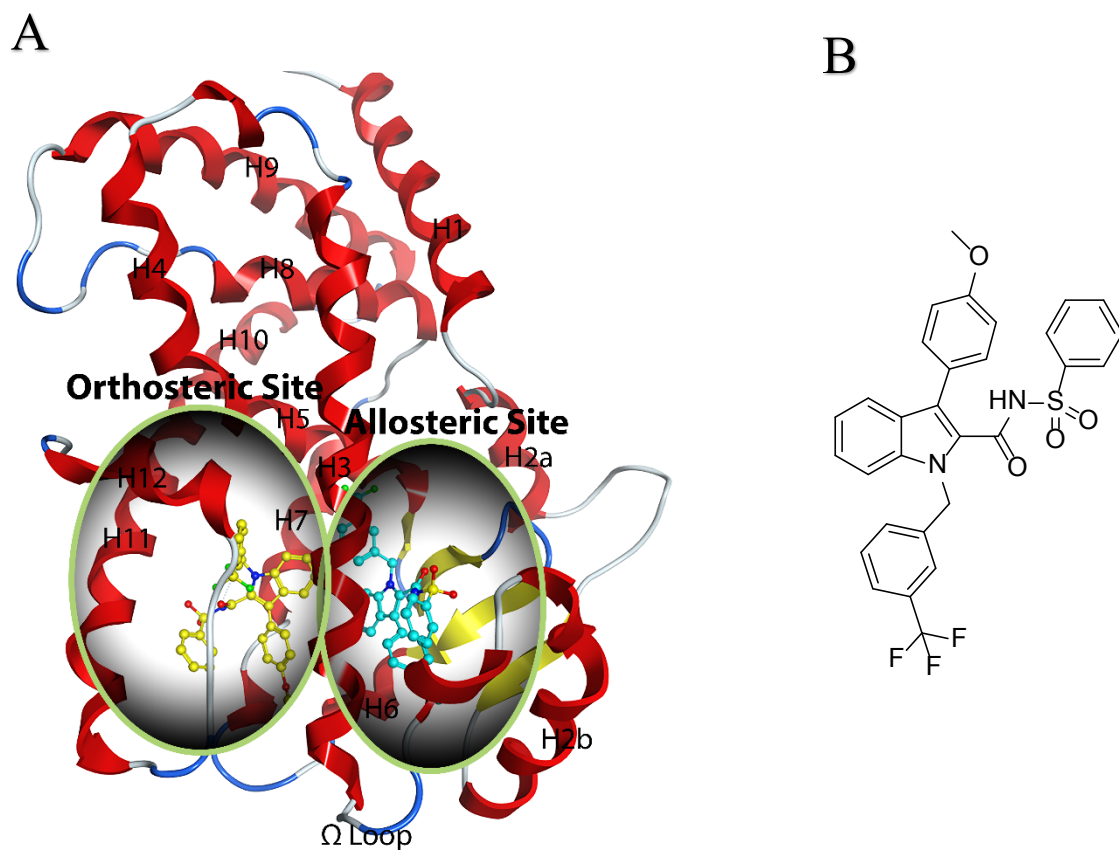


Figure 2.1. Co-crystal structure of NSI-bound PPAR γ (PDB 2HFP) shows two bound NSI molecules, one to the orthosteric pocket and a second bound to the allosteric site (A). Chemical Structure of NSI (B).

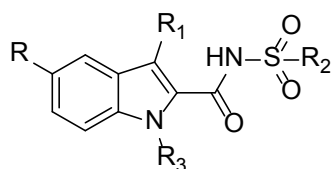
2.3. Results and Discussion:

2.3.1. Glide Docking:

We ran docking experiments of 47 PPAR γ antagonists against (Figure 2.2) the two models of PPAR γ binding sites to evaluate the ΔG_{PRED} alongside the orthosteric and allosteric binding sites of PPAR γ . PPAR γ antagonists docking scores are listed in Table 2.1. The glide docking shows that the glide performance is well in predicting the binding affinity of PPAR γ antagonists at allosteric binding site. The ΔG_{PRED} of PPAR γ antagonists at allosteric binding site of PPAR γ accomplished well in predicting the binding affinity of PPAR γ antagonists, and they show better correlation with the ΔG_{EXP} of PPAR γ antagonists than the ΔG_{PRED} of PPAR γ antagonists at orthosteric binding site of PPAR γ (Figure 2.3). Besides. The Pearson's correlation coefficient at allosteric binding site was 0.80 and the correlation R^2 was 0.64 better than the Pearson's correlation coefficient at orthosteric binding site (0.62) and the correlation R^2 (0.39). In addition, the average of the difference between ΔG_{EXP} and ΔG_{PRED} ($\Delta\Delta G$), the mean of absolute error (MAE), and the root-mean-square (RMS) error for PPAR γ antagonists docked at allosteric binding site of 1.08, 1.10, and 1.29, respectively are lower than respective values at orthosteric binding site (1.50, 1.63, 1.83, respectively) for PPAR γ antagonists (Table 2.2).

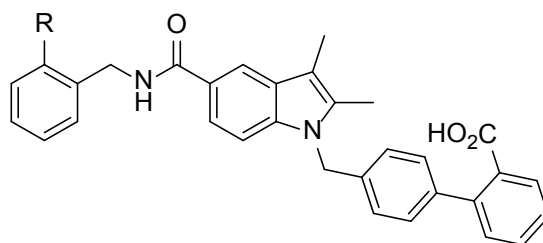
Taken together, our docking results indicate that glide docking is capable of predicting ligands binding affinity in different pocket sites of PPAR γ . The glide docking reveals that the ΔG_{PRED} of PPAR γ antagonists is strongly correlated with the ΔG_{EXP} of PPAR γ antagonists at allosteric binding site. Moreover, the statistical parameters and errors such as Pearson's correlation coefficient, correlation R^2 , $\Delta\Delta G$, MAE, and RMSE of glide docking GD based on estimation of free energy of binding for PPAR γ antagonists at

allosteric binding site much better than at orthosteric binding site. Therefore, the allosteric site of PPAR γ is the most favorable binding site for PPAR γ antagonists.

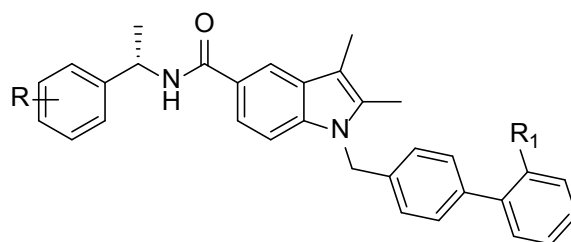


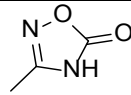
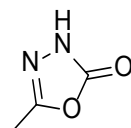
Comp.	R	R ₁	R ₂	R ₃
NSI	H	4-CH ₃ OPh	Ph	3-CF ₃ Bn
1	H	4-CH ₃ OPh	4-F-Ph	3-CF ₃ Bn
2	H	4-CH ₃ OPh	2-CO ₂ MePh	3-CF ₃ Bn
3	H	4-CH ₃ OPh	2-CH ₃ Ph	3-CF ₃ Bn
4	H	4-CH ₃ OPh	Me	3-CF ₃ Bn
5	H	H	Ph	3-CF ₃ Bn
6	H	H	4-F-Ph	3-CF ₃ Bn
7	H	H	4-Cl-Ph	3-CF ₃ Bn
8	H	H	3-CF ₃ -Ph	3-CF ₃ Bn
9	H	H	4-CH ₃ Ph	3-CF ₃ Bn
10	H	H	2-CH ₃ Ph	3-CF ₃ Bn
11	H	H	2-Naphthyl	3-CF ₃ Bn
12	H	H	2-CF ₃ -Ph	3-CF ₃ Bn
13	H	H	2-(5-Chlorothiophene)	3-CF ₃ Bn
14	H	H	Me	3-CF ₃ Bn
15	H	H	4-CF ₃ -Ph	4-CF ₃ Bn
16	H	H	3-CF ₃ -Ph	3-CH ₃ OBn
17	H	H	3-CF ₃ -Ph	3-CF ₃ OBn
18	H	H	3-CF ₃ -Ph	Et
19	H	H	3-CF ₃ -Ph	4-CF ₃ Bn
20	H	H	3-CF ₃ -Ph	3-BnOBn
21	H	H	3-CF ₃ -Ph	Bn
22	H	H	3-CF ₃ -Ph	2,5-DiClBn

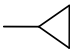
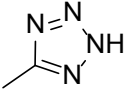
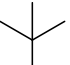
23	H	H	3-CF ₃ -Ph	4- <i>t</i> -BuBn
24	Cl	H	3-CF ₃ -Ph	3-CF ₃ Bn
25	OBn	H	3-CF ₃ -Ph	3-CF ₃ Bn
26	OH	H	3-CF ₃ -Ph	3-CF ₃ Bn



Compound	R	Compound	R	Compound	R
27	CH ₃	28	NH ₂	29	NO ₂



Compound	R	R ₁	Compound	R	R ₁
SR1664	4-NO ₂	COOH	36	3-iPr	
30	3-iPr	COOH	37	3-iPr	

31	3- 	COOH	38	3-iPr	
32	3-tBu	COOH	39	3-iPr	CONHOH
33	4-iPr	COOH	40	3-iPr	CONH ₂
34	4-tBu	COOH	41	3-iPr	CON(CH ₃) ₂
35	3- 	COOH			

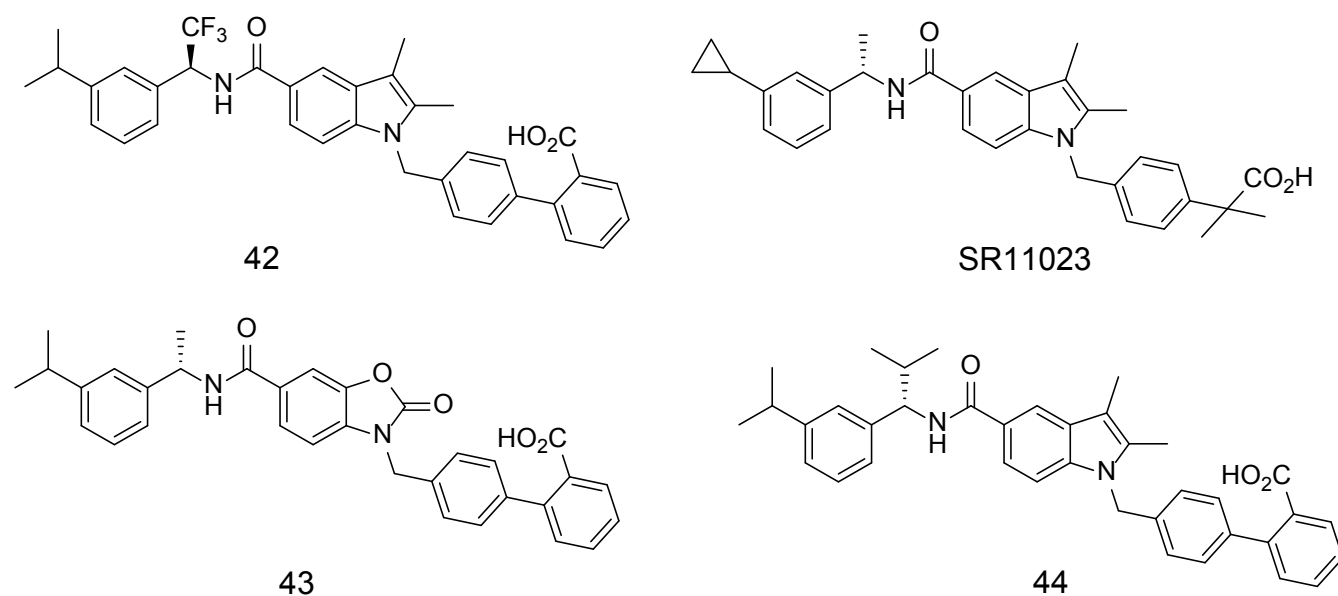


Figure 2.2. Chemical structures of PPAR γ antagonists.

Table 2.1. The glide score of 47 PPAR γ antagonists against the allosteric^a and orthosteric^b binding site of PPAR γ (2HFP).

Compound	IC ₅₀ (nM)	ΔG_{EXP}	XP GScore ^a	XP GScore ^b
NSI	3	-11.63	-12.59	-14.28
SR1664	80	-9.68	-10.31	-10.96
SR11023	108	-9.50	-10.27	-11.85
1	7	-11.12	-12.64	-14.48
2	1	-12.28	-12.75	-11.42
3	7	-11.12	-12.69	-14.14
4	2	-11.87	-11.46	-11.42
5	290	-8.92	-10.33	-10.97
6	720	-8.38	-10.07	-11.63
7	280	-8.94	-10.25	-10.92
8	80	-9.68	-10.78	-10.85
9	290	-8.92	-10.19	-11.07
10	180	-9.20	-10.21	-11.45
11	90	-9.61	-11.14	-11.96
12	80	-9.68	-10.50	-11.02
13	80	-9.68	-10.20	-11.19
14	680	-8.41	-8.93	-9.34
15	700	-8.40	-9.28	-9.90
16	140	-9.35	-9.40	-11.51
17	90	-9.61	-10.74	-10.80
18	2440	-7.66	-7.74	-8.39
19	400	-8.73	-9.94	-10.27
20	50	-9.96	-11.55	-10.55
21	280	-8.94	-9.93	-11.24

^a: Glide Score of PPAR γ antagonists against the allosteric binding site. ^b: Glide Score of PPAR γ antagonists against the orthosteric binding site.

CONTINUED

Compound	IC ₅₀ (nM)	ΔG_{EXP}	XP GScore ^a	XP GScore ^b
22	380	-8.76	-9.74	-11.45
23	330	-8.84	-9.37	-11.19
24	330	-8.84	-9.57	-11.84
25	770	-8.34	-10.89	-10.06
26	540	-8.55	-9.74	-10.15
27	6	-11.22	-11.19	-11.68
28	32	-10.22	-11.42	-11.08
29	24	-10.39	-11.04	-11.17
30	30	-10.26	-12.32	-12.48
31	7	-11.12	-11.54	-11.63
32	5	-11.32	-12.43	-12.25
33	8	-11.05	-11.47	-10.93
34	5	-11.32	-11.84	-11.83
35	17	-10.60	-11.91	-12.73
36	40	-10.09	-11.66	-11.95
37	7	-11.12	-11.07	-11.06
38	22	-10.45	-11.13	-11.32
39	77	-9.70	-12.26	-12.17
40	62	-9.83	-10.68	-11.27
41	148	-9.32	-10.96	-10.66
42	17	-10.60	-13.23	-12.17
43	1100	-8.13	-10.98	-6.61
44	80	-9.68	-11.45	-12.28

^a: Glide Score of PPAR γ antagonists against the allosteric binding site. ^b: Glide Score of PPAR γ antagonists against the orthosteric binding site.

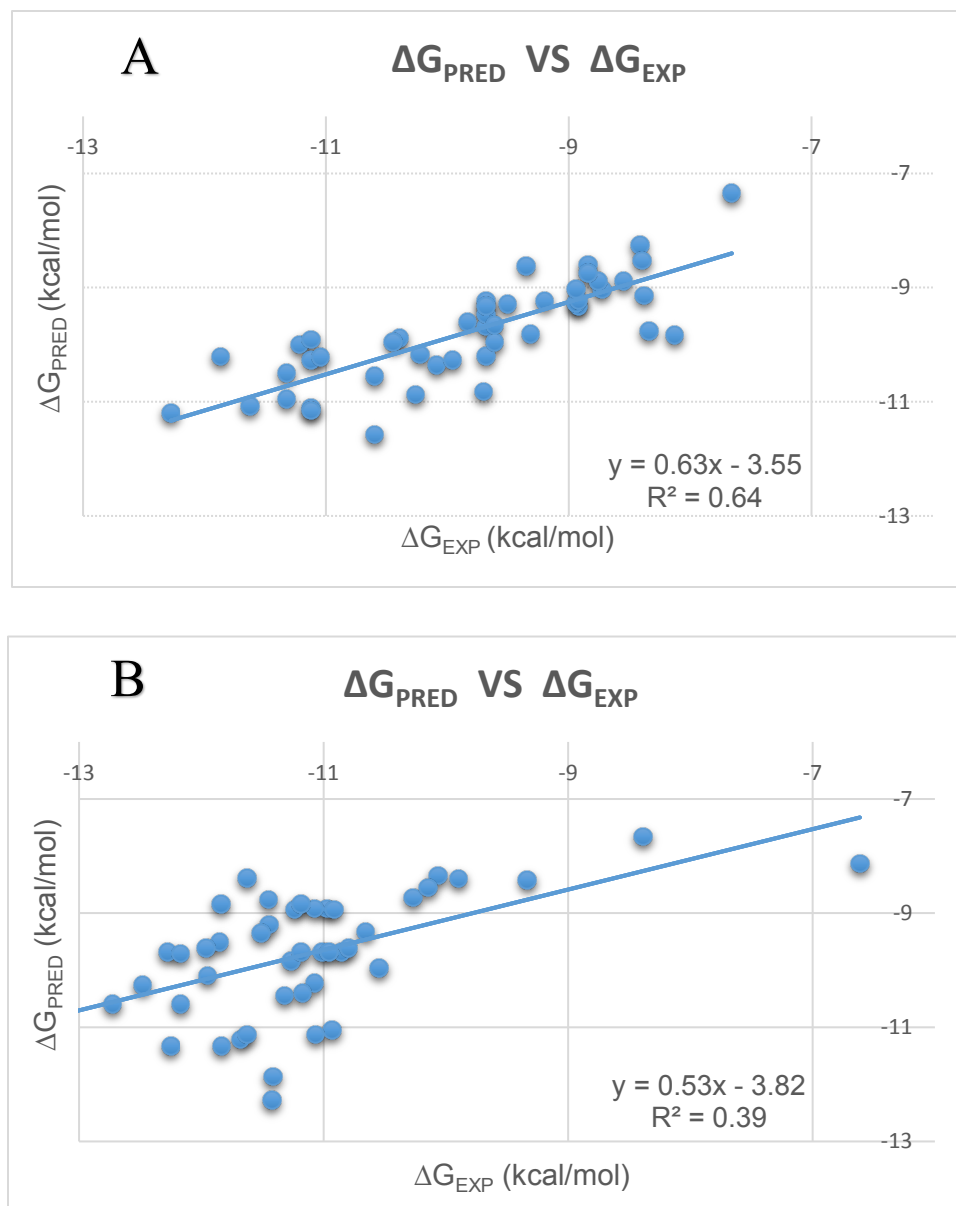


Figure 2.3. Plots of glide docking scores for PPAR γ antagonists against allosteric Binding site (A), and Orthosteric Binding Site (B).

Table 2.2. Statistical results for the glide score estimation of free energy binding for PPAR γ antagonists.

	Allosteric Binding Site	Orthosteric Binding Site
Pearson's R	0.80	0.62
Correlation R^2	0.64	0.39
$\Delta\Delta G$	1.08	1.50
MAE	1.10	1.63
RMSE	1.29	1.83

2.3.2. Validation of the Glide Docking Studies:

We used various methods to validate our docking programs and scoring functions.^{24, 25} One commonly used method is the pose selection whereby docking software are used to re-dock a ligand with a known conformation and orientation, typically from a co-crystal structure, into the binding site. Docking method are considered trustworthy when they are able to generate poses very close to the native conformation, i.e., with low Root Mean Square Deviation (RMSD) value from the known conformation (usually 1.5 or 2 Å depending on ligand size).²⁶ The superposition of the Glide-generated docked pose for NSI and the native conformation in 2HFP (Figure 2.4) revealed that the RMSD between these two poses is 0.22 Å, so the glide docking can successfully generate the native conformation and orientation from crystal structure. This low RMSD value show that GD is able efficiently of finding the innate poses in crystal structures and can be consistently used to define the binding conformations of other ligands. Another validation method is enrichment factor (ER). The ER is a general measurement of the efficiency of a docking program: the higher the ER, the more accurate the docking program.²⁷ The ER measures the concentration of active inhibitors in a specific subset divided ($x\%$) by the concentration of active inhibitors in the database.²⁷ The ER can validate if the docking method will be satisfactorily able identifying active compounds in protein-ligand interactions in PPAR γ by docking a library of 47 PPAR γ antagonists and 423 drug-like compounds against the crystal structure of PPAR γ . Docking of 470 compounds against the PPAR γ (2HFP) model resulted an ER score of 7.02 (Table 3), showing a growth in the chance of finding an active PPAR γ antagonist using glide docking in the top 10% of hits compared to an otherwise random collection. The docking scores of the 423 drug-like compounds against the 2HFP

crystal structure are listed in table 2.3. The efficiency of ER tested by evaluating the hit rate (HR). HR compares the obtained actual EF with desirable ideal EF.²⁸ In our data set, the EF for the ideal case would be 10.00. The HR score of 7.02 for the glide docking indicates that active ligands can be identified using this software (Table 2.4).

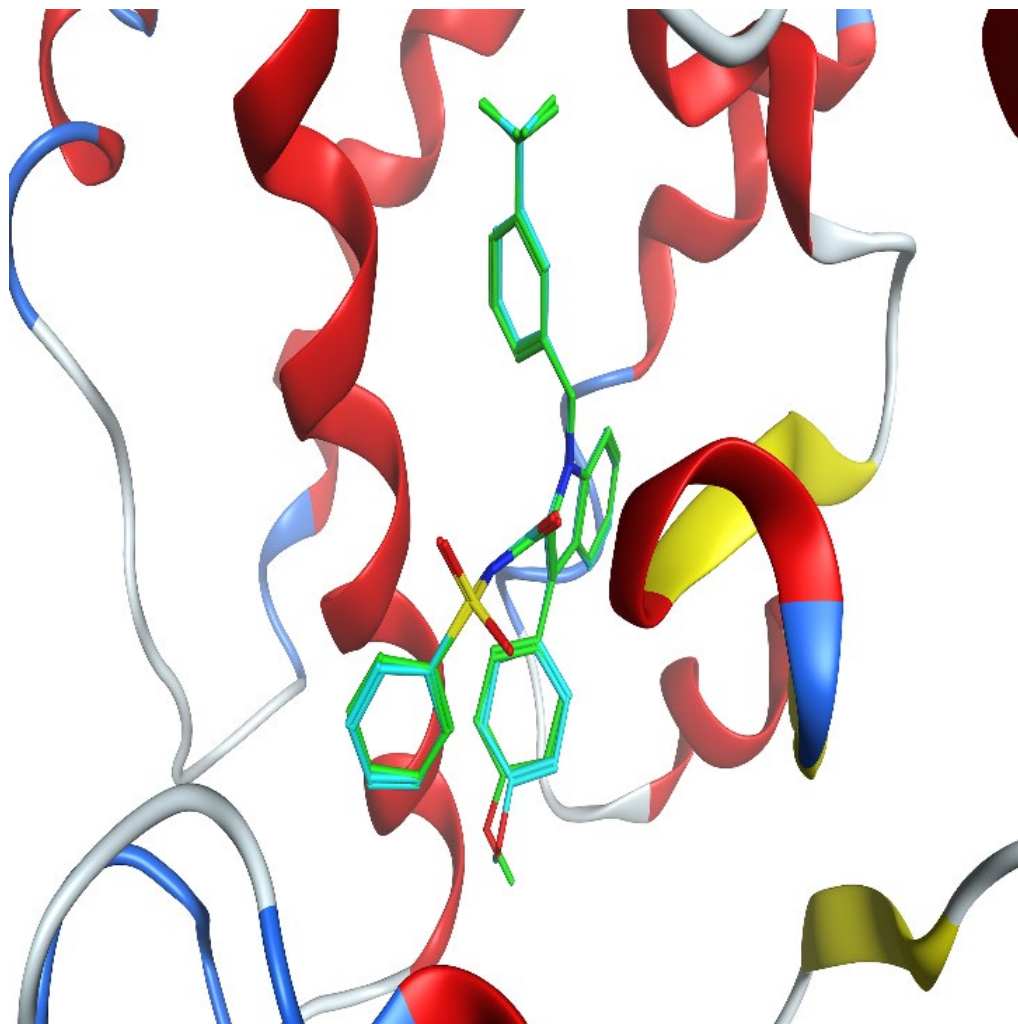


Figure 2.4. The superposition of NSI from the Glide generated pose and the native crystal structure (2HFP). NSI from the Glide generated pose (cyan), and the native crystal structure (green).

Table 2.3. Glide docking scores of drug-like molecules extracted from a NCI database
Against the PPAR γ (2HFP) at allosteric site.

NCI ID	XP GScore	NCI ID	XP GScore	NCI ID	XP GScore	NCI ID	XP GScore
116	-6.57	47742	-8.92	95895	-5.44	130813	-8.28
153	-6.13	48151	-7.65	99547	-8.54	130842	-5.41
3098	-3.65	49628	-6.92	101523	-8.59	131366	-8.68
6918	-5.84	51478	-5.27	101672	-6.10	131367	-8.92
7579	-7.68	52003	-6.80	101793	-8.08	132263	-7.31
8008	-7.78	53199	-5.51	103843	-7.19	132898	-7.22
8490	-5.87	54906	-6.76	105274	-2.80	134118	-6.13
8609	-8.76	56243	-8.84	105337	-6.56	135634	-6.89
8611	-9.12	57034	-10.75	106156	-9.66	135848	-9.42
9011	-4.64	60616	-7.64	106221	-6.73	139461	-7.25
9349	-7.28	62571	-5.89	110347	-8.63	141337	-5.53
10406	-6.33	63837	-7.31	110559	-3.91	142333	-7.60
10671	-9.92	66072	-4.71	111593	-5.81	143351	-7.88
12985	-7.19	69584	-9.17	112828	-7.57	143748	-8.31
13481	-8.36	70824	-6.88	113311	-6.99	144441	-6.86
13843	-8.52	70914	-10.38	113915	-6.69	146005	-5.81
14013	-9.08	70972	-6.44	114133	-6.67	147980	-6.70
15285	-8.80	71012	-5.49	114631	-8.18	148001	-6.77
15903	-6.04	71682	-7.25	114673	-6.33	149543	-5.98
16764	-8.15	71790	-6.86	114819	-7.01	150206	-5.53
16765	-8.15	72559	-8.90	117195	-6.40	150386	-8.82
16768	-9.63	74975	-5.98	117777	-4.40	151215	-7.83
19223	-6.33	77700	-4.04	119707	-7.51	152426	-8.00
21312	-7.07	77720	-6.21	119765	-6.67	155243	-8.07

CONTINUED

24914	-6.17	79023	-9.82	120183	-8.89	156601	-9.99
26870	-8.66	79566	-5.62	122309	-6.98	156773	-7.17
27265	-7.41	81129	-5.22	122514	-6.38	157402	-4.63
30019	-8.80	84538	-7.53	123112	-7.94	157967	-6.14
30967	-8.94	85154	-6.82	123222	-6.57	161387	-7.11
31546	-6.82	85267	-7.91	123247	-5.06	162183	-6.11
33408	-6.04	85410	-6.26	123976	-8.04	162501	-9.45
34567	-7.56	85518	-7.29	124442	-8.51	162765	-6.29
36487	-6.69	85679	-7.80	125281	-7.81	163369	-4.53
36506	-10.26	85740	-5.44	125661	-5.16	164089	-10.94
37117	-7.73	86711	-8.34	126424	-5.30	164113	-5.63
37815	-8.77	88972	-5.92	127678	-8.73	164377	-7.48
39006	-6.08	89808	-8.49	127690	-6.39	164929	-6.86
39612	-8.07	91332	-10.58	128094	-4.94	165995	-5.63
42399	-3.86	91397	-8.77	128583	-6.90	167739	-6.07
44491	-8.35	92204	-7.31	128594	-9.96	167819	-7.97
45093	-5.71	92228	-6.56	130101	-8.92	170757	-7.31
234698	-9.18	341661	-10.03	515421	-6.74	630981	-4.02
240360	-7.78	343544	-8.27	523235	-6.63	632016	-7.68
244974	-8.87	344240	-9.77	527570	-5.76	632242	-7.23
254681	-9.24	345725	-6.28	529321	-8.55	633057	-8.81
269193	-5.06	346878	-7.48	602681	-7.58	633971	-6.54
270150	-7.33	349963	-8.74	603656	-6.02	637660	-5.35
270734	-7.73	350111	-7.52	608550	-6.07	638038	-8.44
273905	-9.93	350986	-6.01	609357	-6.18	639829	-7.75
277480	-6.71	353485	-7.82	609523	-7.09	640341	-8.46
279829	-8.74	356465	-8.40	610540	-6.14	640991	-7.84
281299	-6.16	356785	-6.84	612475	-11.78	640996	-8.47
284669	-6.31	357681	-7.99	612977	-6.44	641217	-7.11

CONTINUED

289626	-8.76	359827	-7.77	613586	-9.79	641250	-9.53
291629	-7.83	363784	-8.54	613748	-9.15	641602	-8.05
292943	-8.22	363918	-7.99	617013	-7.05	642075	-9.13
294866	-6.30	364069	-5.18	618178	-9.15	642305	-9.36
296242	-7.28	364385	-6.65	618443	-8.03	642324	-9.54
298141	-6.91	365357	-9.29	618449	-7.27	643509	-8.32
299208	-6.69	366098	-10.03	618555	-7.66	644965	-8.06
299236	-6.60	367933	-9.70	618660	-6.12	645168	-7.72
300910	-5.19	368279	-9.58	618682	-7.14	645980	-7.98
304891	-8.56	371012	-7.01	618688	-7.39	646474	-8.47
308001	-12.89	371194	-9.22	619196	-8.95	647592	-7.47
309842	-6.26	371488	-6.25	620478	-5.46	648635	-7.81
310324	-7.03	372059	-6.86	622586	-6.06	648639	-6.49
310361	-6.11	372302	-8.31	622958	-7.87	648650	-8.51
310835	-6.76	372523	-6.23	623091	-7.44	648689	-4.84
313957	-7.85	372642	-7.95	623712	-6.35	651331	-2.48
317877	-6.57	374682	-6.69	623768	-8.57	652035	-6.80
318822	-6.85	375722	-8.47	624333	-6.88	652861	-8.23
319112	-6.44	379100	-11.92	624425	-8.16	652900	-7.40
319688	-6.66	379472	-6.59	624454	-8.06	654387	-5.83
320204	-6.91	380509	-6.54	624546	-7.25	655041	-5.69
320212	-7.15	381584	-7.28	624547	-7.74	656455	-7.52
320562	-7.93	400063	-6.50	624548	-6.76	657990	-7.19
320864	-7.16	401688	-7.98	627785	-5.81	658262	-11.55
325304	-10.66	401696	-9.32	627889	-7.93	658994	-9.12
328102	-7.03	401828	-6.81	629819	-11.91	659343	-8.01
331921	-7.88	403031	-4.68	629827	-6.15	661081	-7.54
333346	-5.14	405904	-8.03	630312	-6.25	662564	-5.93
335415	-7.73	406369	-6.67	630321	-7.18	664889	-6.47

CONTINUED

335994	-10.45	408562	-9.79	630373	-9.79	665312	-7.94
337738	-8.06	409253	-6.93	512601	-5.48	666613	-7.16
338540	-8.51	409615	-7.79	514213	-6.78	666714	-7.03
171538	-6.3	210344	-9.86	667386	-6.67	682500	-5.65
172540	-7.21	211226	-8.04	667708	-8.21	682506	-9
172846	-7.5	211831	-7.32	671438	-7.18	683237	-6.63
177363	-7.99	212018	-8.1	672084	-9.87	683711	-5.6
178023	-7.99	212032	-9.16	672293	-6.93	685509	-8.2
178889	-6.78	212112	-5.07	674002	-6.56	685706	-7.53
180617	-7.27	213899	-7.67	674012	-7.49	687105	-5.6
180627	-7.71	215556	-9.97	674612	-6.47	687524	-7.88
180642	-6.9	216451	-7.77	675766	-7.19	687739	-7.86
180648	-7.63	216506	-6.5	675767	-7.98	687869	-8.8
180661	-7.17	216694	-7.7	676464	-6.49	688818	-9.21
190528	-6.8	217080	-7.22	676607	-10.51	690564	-8.85
190748	-6.5	226116	-7.55	677157	-8.56	691348	-7.57
201618	-7.27	226178	-8.16	679497	-8.87	691350	-7.51
201666	-7.58	226517	-9.62	679513	-7.98	691424	-8.98
202677	-7.88	227395	-4.9	680329	-6.28	691578	-6.86
204583	-6.64	230297	-11.56	681170	-7.55	693055	-5.53
204590	-6.52	231315	-9.15	681536	-6.23	693123	-6.76
205546	-7.69	231923	-6.49	681633	-9.27	694919	-6.36
205684	-8.44	232022	-7.76	681958	-8.38	695857	-6.62
205811	-9.58	731365	-7.04	338620	-7.1		

Table 2.4. Enrichment factor of the glide docking against PPAR γ at allosteric site.

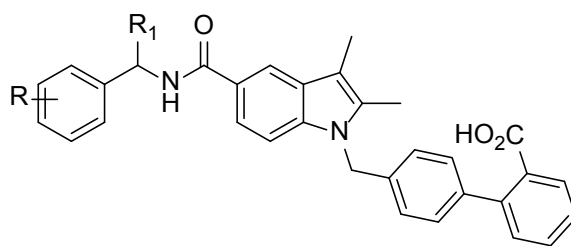
Number of active PPAR γ antagonists	47
Number of total compounds in the database	470
Number of active PPAR γ antagonists in the top 10% subset	33
Enrichment factor (EF) (actual)	7.02
Enrichment factor (EF) (ideal)	10
Hit rate (HR)	70%

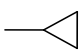
2.3.3. Binding Mode of PPAR γ Ligands at Allosteric Binding Site:

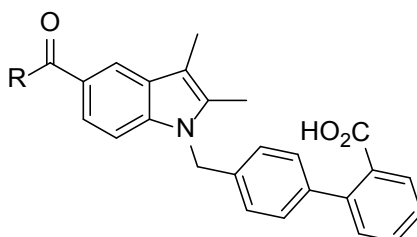
Several PPAR γ antagonists (Figure 2.2), partial agonists (Figure 2.4), and agonists (Figure 2.5) was run in *silico* docking using GD method to identify the binding mechanisms of these compounds, and distinguish the residues that are responsible for antagonists binding or agonists, and partial agonists binding. First, we analyzed the protein-ligand interactions of several PPAR γ ligands at allosteric pocket (Table 2.5). The crystal structure of the PPAR γ /NSI complex at allosteric binding site reveals that residues Lys256 and Ser342 of PPAR γ generate two H-bonds to the NSI ligand. In our docking study, the NSI ligand was docked to PPAR γ and formed two H-bonds with Lys256 and Ser342. This result is compatible with the protein-ligand interactions for the crystal structure of the PPAR γ /NSI complex. The H-bond interactions between PPAR γ ligands and PPAR γ at allosteric binding site show that Lys256 and Ser342 provides H-bonds with the majority of PPAR γ ligands including PPAR γ antagonists, partial agonists, and agonists (Figure2.6). This set of H-bond interactions offers a reasonable explanation for the observation that many PPAR γ ligands are effective against PPAR γ . Arg288 of PPAR γ looks to be important for ligand binding, more so for the PPAR γ antagonists in that this residue affords π -cation interactions with 13 of the 47 antagonists ($\approx 28\%$) for PPAR γ but less than 4 of the 35 partial agonists ($\approx 6\%$), and less than 3 of the 14 agonists ($\approx 14\%$) for the crystal structure of the PPAR γ . In addition, Phe282 and Lys367 of PPAR γ looks to be important for PPAR γ antagonists binding, that Lys367 affords H-bonds or π -cation interactions for with 10 of the 47 antagonists ($\approx 21\%$), and Phe282 create π - π stacking for with 9 of the 47 antagonists ($\approx 19\%$). In contrast, there are less than 4 of the 35 partial agonists ($\approx 6\%$) for Phe282 and ($\approx 8\%$) for Lys367, and less than 3 of the 14 agonists ($\approx 14\%$) for Phe282 and (0%) for

Lys367 (Figure 2.6). In contrast, Ser289 offers H-bonds with 21 of the 35 partial agonists ($\approx 58\%$) for PPAR γ but 8 of the 47 antagonists ($\approx 17\%$). Glu343 forms H-bonds with 5 of the 14 agonists ($\approx 36\%$) but less than 2 of the 47 antagonists ($\approx 2\%$). Taken together, inspection of ligands/ PPAR γ interactions at allosteric pocket shows compounds that are able to form π -cation interactions with Arg288, π - π stacking with Phe282, and H-bonds or π -cation interactions with Lys367 might be attributed to PPAR γ antagonists. Therefore, our docking results suggest that interactions with residues Phe282, Arg288, and Lys367 might be more exploited for specific antagonists design than agonists and partial agonists at allosteric pocket.

The docked pose of NSI and its analogues in the PPAR γ protein at allosteric pocket display that the *N*- sulfonyl carboxamide group of NSI and its analogues localize close to the polar residues of H2', H3, and β -sheet3 of PPAR γ (Figure 2.7), forming favorable two H-bond interactions with Lys256, and Ser342. In addition, the benzyl group of some NSI's analogues attached to the nitrogen atom of the indole can create π -cation interactions with Arg288 of H3 (Figure 2.7). In the other hands, the docked pose of SR1664 and its analogues in the PPAR γ protein at allosteric pocket show that the carboxyl group of SR1664 and its analogues form forming favorable two H-bond interactions with Lys256, and Ser342. In addition, the benzyl group of some SR1664's analogues attached to the carbamoyl form π - π stacking with Phe282 of H3, and favorable H-bond interactions or π -cation interactions with Lys367 of H7.



Compound	R	R ₁	Stereo-chemistry	Compound	R	R ₁	Stereo-chemistry
45	H	H		57	2-Me	Me	S
46	3-Me	H		58	2-Et	Me	S
47	3-OMe	H		59	2-Br	Me	S
48	3-NO ₂	H		60	2-OiPr	Me	S
49	4-Me	H		61	3-Cl	Me	S
50	4-Br	H		62	3-CF ₃	Me	S
51	4-NO ₂	H		63	4-Me	Me	S
SR9034	H	Et	±	64	4-OEt	Me	S
52	H	Et	S	65	3-iPr	H	
53	H	Et	R	66	3-iPr	Et	S
54	4-F	Me	S	67	3-iPr		S
55	4-Br	Me	S	68	3-iPr	nBu	S
56	4-OMe	Me	S	69	3-iPr	iBu	S
				70	3-iPr	Bn	S



Compound	R	Compound	R
71	thiophen-2-ylmethanamine	73	cyclobutanamine
72	diphenylmethanamine	74	cyclohexylmethanamine

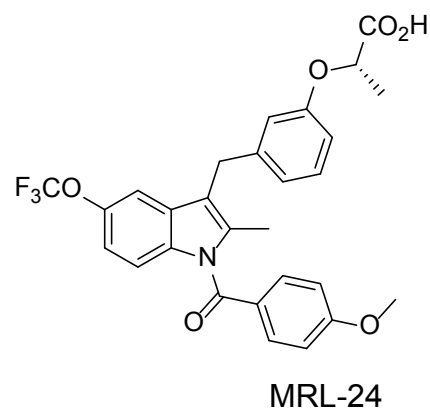
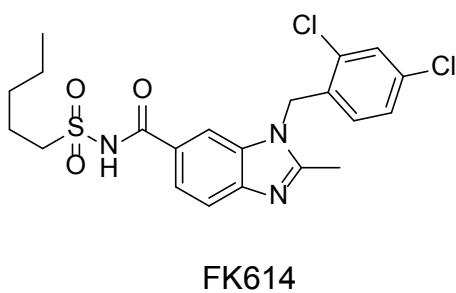
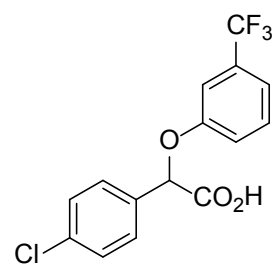
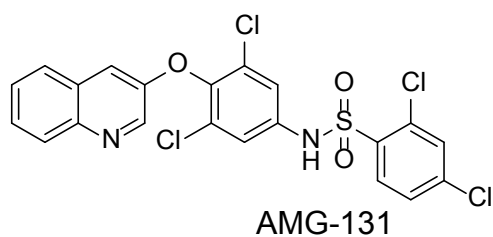
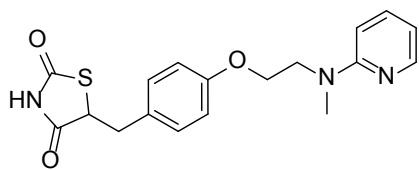
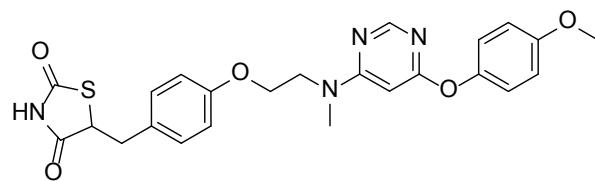


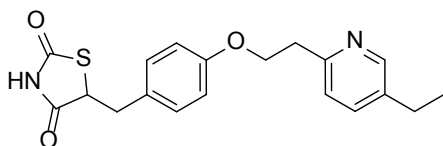
Figure 2.5. Chemical structures of PPAR γ partial agonists.



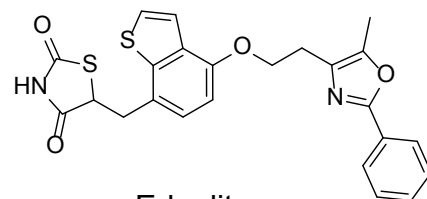
Rosiglitazone



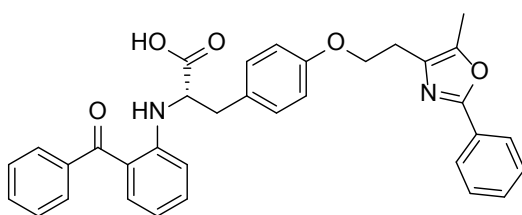
Lobeglitazone



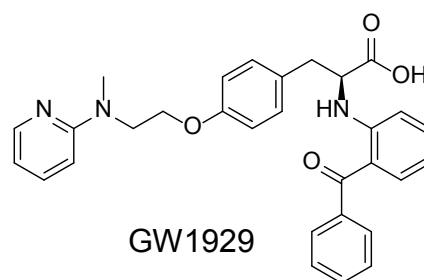
Pioglitazone



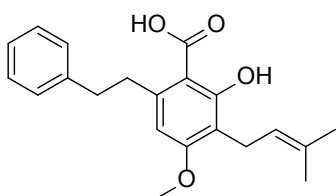
Edaglitazone



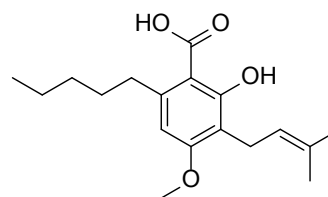
Farglitazar



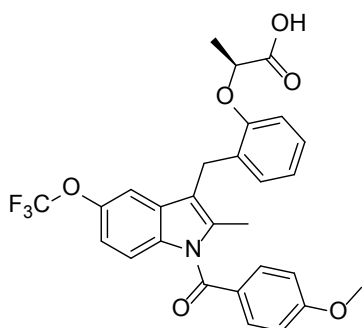
GW1929



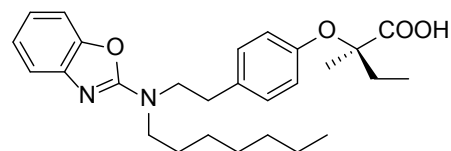
Amrofrutin 1



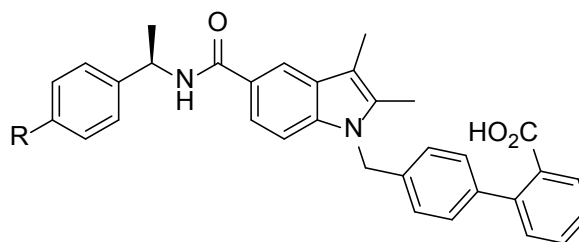
Amrofrutin 2



MRL20



R-1



Compound	R	Compound	R
75	F	77	NO ₂
76	OMe	78	Br

Figure 2.6. Chemical structures of PPAR γ agonists.

Table 2.5. Residues Interactions of ligands at allosteric site:

Antagonists Compound	Interacting Residues	Compound	Interacting Residues
NSI	Lys265, Ser342	22	Lys265, Ser342
SR1664	Lys265, Ser289, Ser342, Lys367	23	Lys265, Arg288, Ser342, Lys367
SR11023	Lys265, Ser289	24	Lys265, Arg288, Ser342
1	Lys265, Ser342	25	Lys265, Arg288, Ser342
2	Lys265, Ser342	26	Lys265, Arg288, Ser342
3	Lys265, Arg288, Ser342	27	Lys265, Ser289, Ser342
4	Lys265, Ser342	28	Lys265, Ser289, Ser342
5	Lys265, Ser342	29	Lys265, Ser289
6	Lys265, Ser342	30	Lys265, Phe282, Ser342, Lys367
7	Lys265, Ser342	31	Lys265, Ser289
8	Lys265, Arg288, Ser342	32	Lys265, Phe282, Ser342, Lys367
9	Lys265, Ser342	33	Lys265, Ser289
10	Lys265, Arg288, Ser342	34	Lys265, Ser289, Ser342, His449
11	Lys265, Arg288, Ser342	35	Lys265, Phe282, Ser342, Lys367, His449
12	Lys265, Ser342	42	Lys265, Phe282, Ser342, Lys367
13	Lys265, Ser342	44	Arg288
14	Lys265, Arg288, Ser342	43	Lys265, Phe282, Ser342, Lys367
15	Lys265, Ser342	36	Lys265, Phe282, Lys367
16	Lys265, Arg288, Ser342	37	Lys265, Ser342
17	Lys265, Ser342	38	Phe282, Lys367
18	Ser342	39	Lys265, Phe282, Lys367
19	Lys265, Arg288, Ser342	40	Lys265, Gly284
20	Lys265, Ser342	41	Phe282
21	Arg288, Ser342, Glu343		

CONTINUED

Agonist Compound	Interacting Residues	Compound	Interacting Residues
LOBEGLITAZONE	NA	75	Lys265, Ser289, Ser342
PIOGLITAZONE	Glu259, Phe282, Gly284	76	Lys265, Ser289, Ser342
EDAGLITAZONE	Leu228	77	Lys265, Ser342
ROSIGLITAZONE	Leu228, Lys265, Glu295, Glu343, Tyr327	78	Lys265, Phe282, Ser342
FARGLITAZAR	Lys265, Ser342	GW1929	Ser342, Glu343
R-1	Lys265, Arg288, Ser342, Glu343, His449	MRL20	Lys265, Ser342
AMROFRUTIN 2	Lys265, Ser342		
AMROFRUTIN 1	Ser342, Glu343		

Partial Agonists			
Compound	Interacting Residues	Compound	Interacting Residues
AMG-131	Phe282, Ser342, Lys367, His449	58	Lys265, Ser342
FK614	Arg288	59	Lys265, Ser289, Ser342
MBX-102	Lys265, Leu340	60	Lys265, Ser289, Ser342
MRL-24	Lys265, Arg288, Ser342, Glu343, Lys367	61	Lys265, Ser289
SR9034	Lys265, Ser289, Ser342	62	Lys265, Ser289, Ser342
45	Lys265, Ser342	63	Lys265, Ser289, Ser342
46	Lys265, Ser289, Ser342	64	Lys265, Ser289
47	Lys265, Ser342	65	Lys265, Ser342
48	Lys265, Ser289	66	Lys265, Ser289
49	Lys265, Ser289	67	Glu343
50	Lys265, Ser289, Ser342	68	Lys265, Ser289
51	Lys265, Ser332, Ser342	69	Lys265, Ser342
52	Lys265, Ser289	70	Lys265, Ser342, Lys367
53	Lys265, Ser289, Ser342	71	Lys265, Ser289, Ser342
54	Lys265, Ser289, Ser342	72	Lys265, Phe282, Ser342
55	Lys265, Ser289, Ser342	73	Lys265, Ser289, Ser342
56	Lys265, Ser342	74	Lys265, Ser289, Ser342
57	Lys265, Ser289, Ser342		

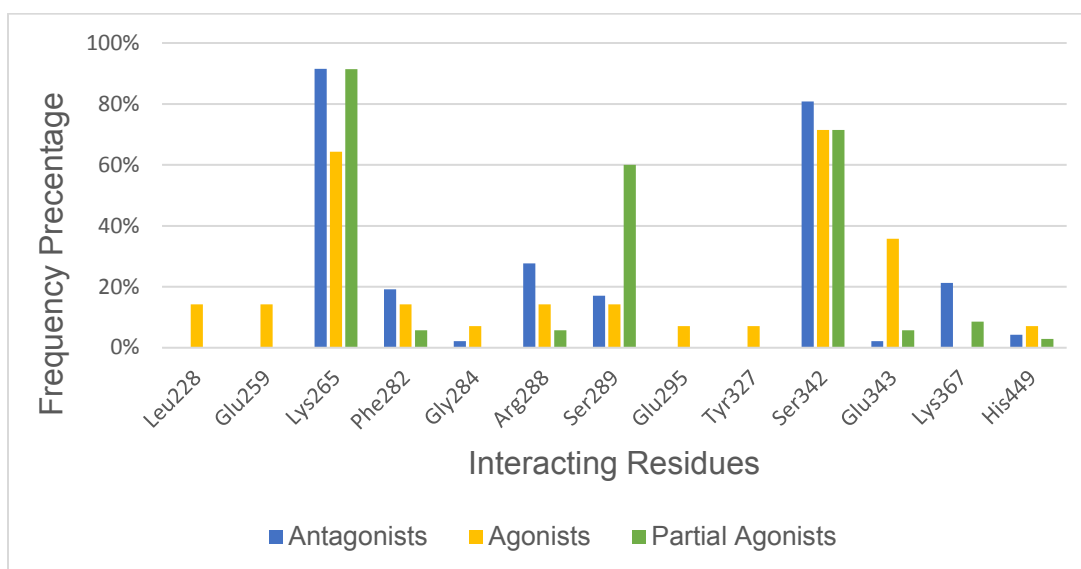


Figure 2.7. Amino acid frequency of interacting residues of various PPAR γ ligands at allosteric Binding site.

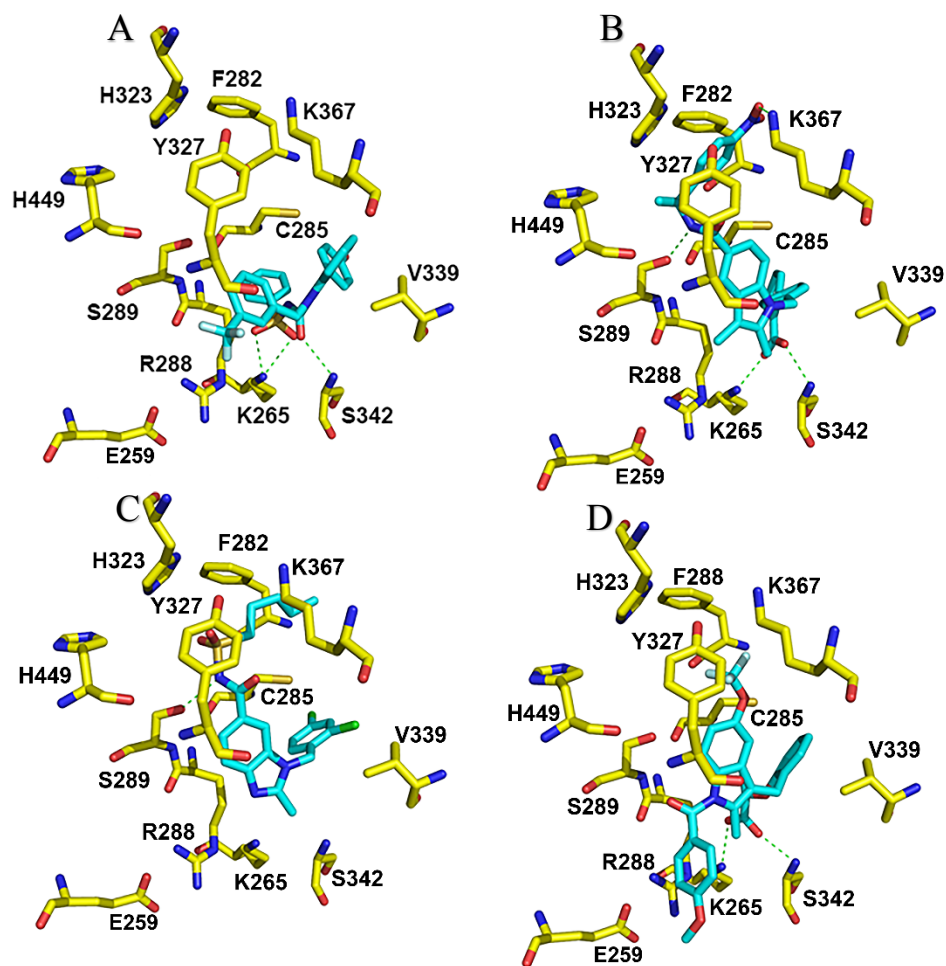


Figure 2.8. Interactions between PPAR γ and NSI (an antagonist) (A), SR1664 (an antagonist) (B), FK614 (a partial agonist) (C), and MRL20 (an agonist) (D) at allosteric binding site. The H-bond interactions are depicted as green dotted lines.

2.3.4. Binding Mode of PPAR γ Ligands at Orthosteric Binding Site:

In contrast, we studied the protein-ligand interactions of PPAR γ ligands at orthosteric pocket (Table 2.6). The crystal structure of the PPAR γ /NSI complex at orthosteric binding site exposes that residues Lys367, and His449 of PPAR γ generate two H-bonds to the NSI. Besides, Phe363, Phe282, and His449 create π - π stacking with the NSI. In our docking study, the NSI was docked to PPAR γ and formed two H-bonds with Lys367, and His449, and π - π stacking with Phe363, Phe282, and His449. This result is also well-matched with the protein-ligand interactions for the crystal structure of the PPAR γ /NSI complex. Phe282 of PPAR γ looks to be important for ligand interactions, especially for the PPAR γ antagonists at orthosteric pocket. Phe282 affords π - π stacking with 22 of the 47 antagonists ($\approx 47\%$) for PPAR γ while 6 of the 36 partial agonists ($\approx 17\%$), and less than 2 of the 14 agonists ($\approx 7\%$) for the crystal structure of the PPAR γ (Figure 2.8). Phe363 of PPAR γ also looks to be important for ligand interactions for the PPAR γ antagonists at orthosteric forming π - π stacking with 9 of the 47 antagonists ($\approx 19\%$) for PPAR γ but less than 2 of the 36 partial agonists ($\approx 3\%$), and of the 14 agonists ($\approx 7\%$) for the crystal structure of the PPAR γ . Besides, His449 can generate π - π stacking with 15 of the 47 antagonists ($\approx 32\%$) for PPAR γ while 3 of the 36 partial agonists ($\approx 8\%$), and less than 3 of the 14 agonists ($\approx 14\%$) for the crystal structure of the PPAR γ . Lys367 forms favorable two H-bond with 20 of the 47 antagonists ($\approx 43\%$) for PPAR γ while less than 5 of the 36 partial agonists ($\approx 11\%$), and of the 14 agonists ($\approx 29\%$) for the crystal structure of the PPAR γ . Taken together, inspection of ligands/ PPAR γ interactions at orthosteric pocket shows compounds which are able to form π - π stacking with Phe282, Phe363, and His449, and H-bonds with Lys367, and His449 might be attributed to PPAR γ antagonists. Therefore, our docking

results suggest that interactions with residues Phe282, Phe363, Lys367, and His449 might be exploited for specific antagonist design than agonists and partial agonists at allosteric pocket.

The docked pose of NSI and its analogues in the PPAR γ protein at orthosteric pocket exhibit that the *N*- sulfonyl carboxamide group of NSI and its analogues is close to the polar residues of H7, and H11 of PPAR γ (Figure 6a), forming favorable two H-bond interactions with Lys367, and His449. In addition, His449 can generate π - π stacking with the benzyl group of some NSI's analogues attached to the nitrogen atom of the indole (Figure 5B). Phe282, and Phe363 induce π - π stacking with phenyl ring attached to indole, and sulfonyl respectively. In the other hands, the docked pose of SR1664 and its analogues in the PPAR γ protein at orthosteric pocket show that the carboxyl group of SR1664 and its analogues form forming favorable two H-bond interactions with Lys256, and Ser342. In addition, the benzyl group of some SR1664's analogues attached to the carbamoyl form π - π stacking with Phe282 of H3, and favorable H-bond interactions with Lys367 of H7. Ser289 in H3 can also form favorable H-bond interactions with the nitrogen atom of the amide group.

Table 2.6. Residues Interactions of ligands at orthosteric site.

Antagonists Compound	Interacting Residues	Compound	Interacting Residues
NSI	Phe282, Phe363, Lys367, His449	22	Phe282, Phe363, Lys367
SR1664	Lys265, Ser289, Ser342, Lys367	23	Phe363
SR11023	Lys265, Ser289, Ser342	24	Phe282, Lys367, His449
1	Phe282, Phe363, Lys367, His449	25	Phe363
2	Phe282, His449	26	Phe282, Lys367
3	Phe282, Phe363, His449	27	Lys265, Ser289, Ser342
4	Lys367, His449	28	Lys265, Ser342
5	Lys367	29	Lys265, Ser289, Ser342
6	His449	30	Lys265, Ser289, Ser342
7	Phe282, Lys367, His449	31	Lys265, Phe282, Ser342
8	Phe282, Lys367, His449	32	Lys265, Phe282, Ser342
9	Phe282, His449	33	Lys265
10	Phe363, Lys367, His449	34	Lys265, Phe282, Ser289, Ser342
11	Phe282, Lys367	35	Lys265, Ser342, Tyr473
12	Lys367	42	Lys265
13	Lys367, His449	44	Lys265
14	Phe282, Lys367, His449	43	NA
15	Phe282, Lys367, His449	36	Lys265, Ser342
16	Phe282, Phe363, Lys367	37	Lys265, Phe282
17	Phe282, Lys367	38	Lys265
18	Phe282, Lys367	39	Lys265, Ser342
19	Phe282, Lys367	40	Lys265, Glu291
20	NA	41	Lys265, Gly284, Tyr327
21	Phe282, Phe363, Lys367		

Agonists Compound	Interacting Residues	Compound	Interacting Residues
LOBEGLITAZONE	Leu228, Phe282	75	Lys265, Ser289, Ser342
PIOGLITAZONE	Leu228, Ser289, Tyr327, Glu343	76	Lys265, Ser342
EDAGLITAZONE	Leu228	77	Lys265, Leu340, Ser342
ROSIGLITAZONE	Leu228, Ser289, Tyr327, Glu343	78	Lys265, Ser342
FARGLITAZAR	Lys265, Ser342	GW1929	Phe363, Lys367
R-1	Lys265, Ser342	MRL20	His323
AMROFRUTIN 2	Lys367, His449		
AMROFRUTIN 1	Lys367		

Partial Agonists Compound	Interacting Residues	Compound	Interacting Residues
AMG-131	Phe282, Ser342, Lys367	58	Lys265, Ser289, Ser342
FK614	Phe282, Lys367, His449	59	Lys265, Ser289, Ser342
MBX-102	Phe282, Phe363, Lys367, His449	60	Lys265, Ser342
MRL-24	Phe282, Arg288, Glu343, His449	61	Lys265, Ser289, Ser342
SR9034	Lys265, Ser289, Ser342	62	Lys265, Ser289, Ser342
45	Lys265, Ser289, Ser342	63	Lys265, Ser289, Ser342
46	Lys265, Ser342	64	Lys265, Ser289
47	Lys265, Ser342	65	Lys265, Ser342
48	Lys265, Ser342	66	Lys265, Ser289, Ser342
49	Lys265, Ser342	67	Lys265, Ser289, Ser342
50	Lys265, Ser342	68	Lys265
51	Lys265, Ser342	69	Lys265
52	Lys265, Ser289, Ser342	70	Lys265
53	Lys265, Ser289, Ser342	71	Lys265, Ser289, Ser342
54	Lys265, Ser289, Ser342	72	Lys265, Phe282, Ser342
55	Lys265, Ser342	73	Lys265, Ser289, Ser342
56	Lys265, Ser289, Ser342	74	Arg288
57	Lys265, Ser289, Ser342		

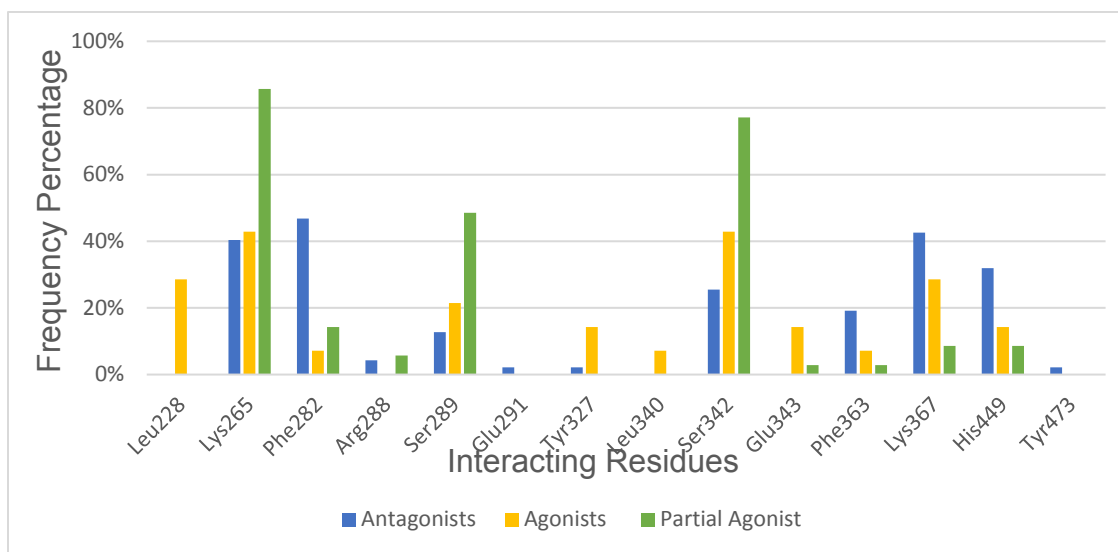


Figure 2.9. Amino acid frequency of interacting residues of various PPAR γ ligands at orthosteric Binding site.

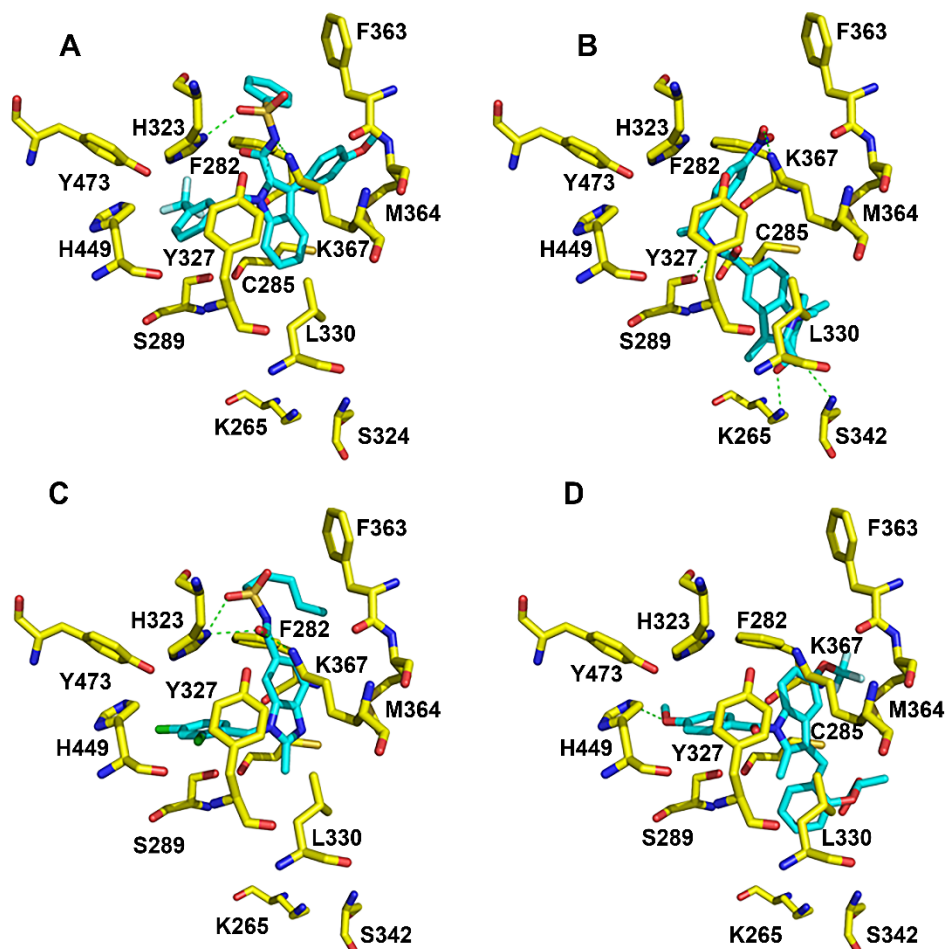


Figure 2.10. Interactions between PPAR γ and NSI (an antagonist) (A), SR1664 (an antagonist) (B), FK614 (a partial agonist) (C), and MRL20 (an agonist) (D) at allosteric binding site. The H-bond interactions are depicted as green dotted lines.

2.3.5. The electrostatic map of PPAR γ Binding Sites:

The electrostatic map of PPAR γ protein at allosteric pocket displays that the side chain amino group of Lys265, and the backbone amide of Ser342 were situated toward the ligand binding site and served as an H-bond acceptor for ligands. The electrostatic maps surrounding Lys265, Ser342 for the three proteins PPAR γ ligands at allosteric pocket are very similar; these residues contribute to H-bond interactions with PPAR γ ligands. This reveals a rational clarification that several PPAR γ ligands form H-bonds with Lys265, and Ser342 of the PPAR γ at allosteric pocket. This shows that the allosteric pocket of PPAR γ protein adopts a considerably activation binding site for PPAR γ ligands (Figure 2.10). The more noticeable difference among the PPAR γ ligands at allosteric pocket lies in Arg288; it is located deeper in the binding pocket in the allosteric pocket of PPAR γ protein. Arg288 forms favorable π -cation interactions with antagonists, an observation consistent with our docking results. The noteworthy residue in the PPAR γ protein at allosteric pocket is Lys367. Because the side-chain structure is extended, and Lys367 located far from the binding pocket (Figure 11C), which it is less likely to interact with ligands. This explains why there are only SR1664 and its analogues form H-bonds with Lys367 of PPAR γ at allosteric pocket (Table 4). In addition, Phe282 is able to form π - π stacking with PPAR γ ligands and mainly with PPAR γ antagonists through its benzyl ring. In contrast, the electrostatic map of PPAR γ protein at orthosteric pocket shows that the side chain amino group of Lys367 served as H-bond donors for ligands, and the nitrogen of imidazole side chain of His449 were situated toward the ligand-binding site and served as H-bond acceptors for ligands (Figure 11C). Besides, the imidazole side chain of His449 is close to (≈ 3.50 Å) the benzyl group of some NSI's analogues attached to the nitrogen atom of the

indole, and it is able to generate π – π stacking. Phe282 and Phe363 enclose the phenyl group attached to the sulphonyl.

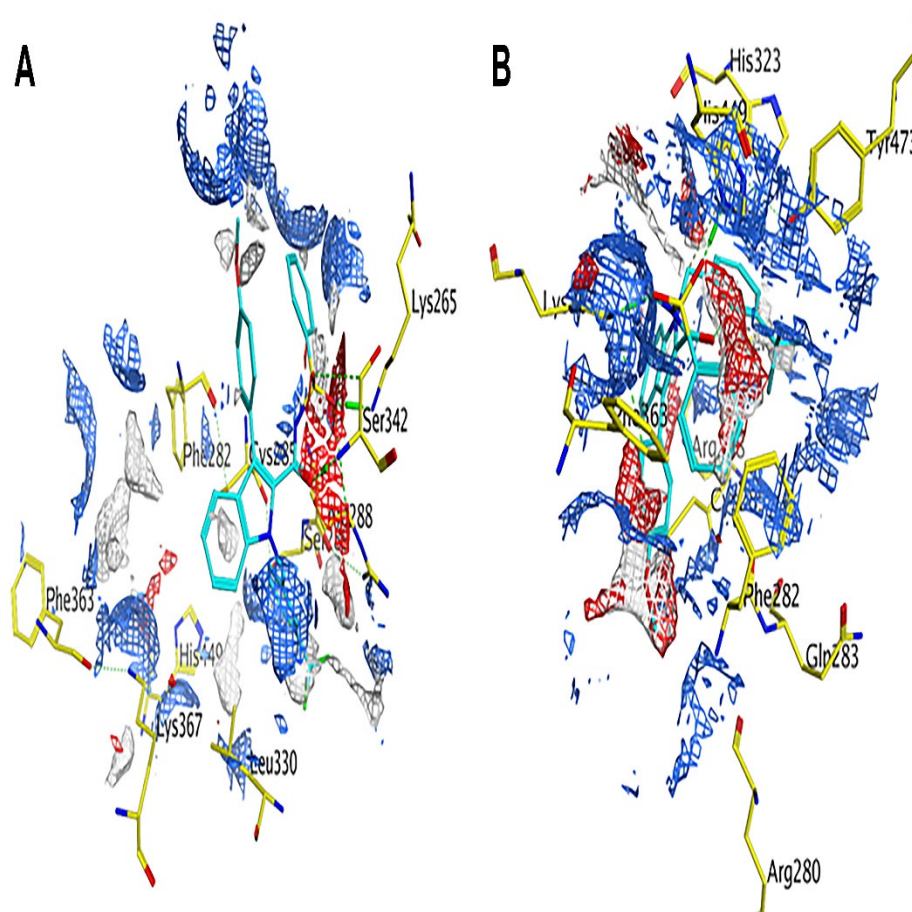


Figure 2.11. Electrostatic surface map of the binding pockets of PPAR γ . The hydrophobic region is depicted as white; H-bond acceptor as red; and H-bond donor, as blue. (A) Allosteric Binding site. (B) Orthosteric Binding Site.

2.4. Conclusion:

PPAR γ is an attractive target for drug discovery and development. PPAR γ antagonists have showed antitumor activity against different tumors. Furthermore, PPAR γ antagonists have showed better treatment of obesity and diabetic than PPAR γ agonists. The crystal structures PPAR γ complexed with antagonists revealed that antagonists can occupy the two binding sites, orthosteric pocket, and allosteric pocket. Docking of PPAR γ antagonists efficaciously similar to the experimentally observed binding affinity. Docking studies PPAR γ shows that the experimental binding affinity of PPAR γ antagonists more correlated to allosteric binding site than the orthosteric binding site. In addition, the statistical parameters of docking scores at allosteric pocket better than orthosteric pocket. Therefore, the allosteric site looks like the most favorable binding site for PPAR γ antagonists. Inspection of ligand/ PPAR γ interactions at allosteric binding site shows that the PPAR γ antagonists seems to require an interaction with residues Phe282, Arg288, and Lys367 more than agonists or partial agonists. In contrast, PPAR γ ligands interactions at orthosteric binding site reveals that the PPAR γ antagonists are able to interact with residues Phe282, Phe363, Lys367, and His449 more than agonists or partial agonists. This study improves the thoughtful of the PPAR γ binding site, which assists in the design and optimization of more specific PPAR γ antagonists.

References:

1. Rosen ED, Spiegelman BM. Molecular regulation of adipogenesis. *Annu Rev Cell Dev Biol.* 2000;16(1):145-171.
2. Maglich JM, Sluder A, Guan X, et al. Comparison of complete nuclear receptor sets from the human, caenorhabditis elegans and drosophila genomes. *Genome Biol.* 2001;2(8).
3. Evans RM. The steroid and thyroid hormone receptor superfamily. *Science.* 1988;240(4854):889-895.
4. Willson TM, Brown PJ, Sternbach DD, Henke BR. The PPARs: From orphan receptors to drug discovery. *J Med Chem.* 2000;43(4):527-550.
5. Rosen ED, Spiegelman BM. PPARgamma: A nuclear regulator of metabolism, differentiation, and cell growth. *J Biol Chem.* 2001;276(41):37731-37734.
6. Wagstaff AJ, Goa KL. Rosiglitazone: A review of its use in the management of type 2 diabetes mellitus. *Drugs.* 2002;62(12):1805-1837.
7. Goldstein JT, Berger AC, Shih J, et al. Genomic activation of PPAR γ reveals a candidate therapeutic axis in bladder cancer. *Cancer Res.* 2017;77(24):6987-6998.
8. Zaytseva YY, Wallis NK, Southard RC, Kilgore MW. The PPARgamma antagonist T0070907 suppresses breast cancer cell proliferation and motility via both PPARgamma-dependent and -independent mechanisms. *Anticancer Res.* 2011;31(3):813-823.
9. Nakajima A, Tomimoto A, Fujita K, et al. Inhibition of peroxisome proliferator-activated receptor gamma activity suppresses pancreatic cancer cell motility. *Cancer Sci.* 2008;99(10):1892-1900.

10. Burton JD, Goldenberg DM, Blumenthal RD. Potential of peroxisome proliferator-activated receptor gamma antagonist compounds as therapeutic agents for a wide range of cancer types. *PPAR Res.* 2008;2008:494161.
11. Asteian A, Blayo A, He Y, et al. Design, synthesis, and biological evaluation of indole biphenylcarboxylic acids as PPAR γ antagonists. *ACS Med Chem Lett.* 2015;6(9):998-1003.
12. Choi JH, Banks AS, Kamenecka TM, et al. Antidiabetic actions of a non-agonist PPAR γ ligand blocking Cdk5-mediated phosphorylation. *Nature.* 2011;477(7365):477-481.
13. Chandra V, Huang P, Hamuro Y, et al. Structure of the intact PPAR- γ -RXR- α nuclear receptor complex on DNA. *Nature.* 2008;456(7220):350-356.
14. Nolte RT, Wisely GB, Westin S, et al. Ligand binding and co-activator assembly of the peroxisome proliferator-activated receptor-gamma. *Nature.* 1998;395(6698):137-143.
15. Frkic RL, Marshall AC, Blayo A, et al. PPAR γ in complex with an antagonist and inverse agonist: A tumble and trap mechanism of the activation helix. *iScience.* 2018;5:69-79.
16. Hughes TS, Giri PK, de Vera, Ian Mitchell S, et al. An alternate binding site for PPAR γ ligands. *Nature Commun.* 2014;5(1):3571.
17. Brust R, Lin H, Fuhrmann J, Asteian A, Kamenecka TM, Kojetin DJ. Modification of the orthosteric PPAR γ covalent antagonist scaffold yields an improved dual-site allosteric inhibitor. *ACS Chem Biol.* 2017;12(4):969-978.
18. Hopkins CR, O'Neil SV, Laufersweiler MC, et al. Design and synthesis of novel N-sulfonyl-2-indole carboxamides as potent PPAR- γ binding agents with potential

application to the treatment of osteoporosis. *Bioorg. Med. Chem. Lett.* 2006;16(21):5659-5663.

19. Sastry GM, Adzhigirey M, Day T, Annabhimoju R, Sherman W. Protein and ligand preparation: Parameters, protocols, and influence on virtual screening enrichments. *J Comput Aided Mol Des.* 2013;27(3):221-234. Accessed Mar 10, 2019. doi: 10.1007/s10822-013-9644-8.

20. Schrödinger, LLC, New York, NY, 2019. Schrödinger suite 2019-1 protein preparation wizard.

21. NCI open database compounds, release 3; national cancer institute, national institutes of health: Bethesda, MD, Sept. 2003. available online at: [Http://Cactus.nci.nih.gov/download/nci](http://Cactus.nci.nih.gov/download/nci)

22. Zhong HA, Santos EM, Vasileiou C, Zheng Z, Geiger JH, Borhan B, Merz KM Jr. Free-energy-based protein design: Re-engineering cellular retinoic acid binding protein II assisted by the moveable-type approach. *J Am Chem Soc.* 2018;140(10):3483-3486.

23. The molecular operating EnVironment (MOE); *Chemical Computing Group Inc.:Montreal, Quebec, Canada, 2009.*

24. Cole JC, Murray CW, Nissink JWM, Taylor RD, Taylor R. Comparing protein-ligand docking programs is difficult. *Proteins.* 2005;60(3):325-332.

25. Jain AN. Bias, reporting, and sharing: Computational evaluations of docking methods. *J Comput Aided Mol Des.* 2008;22(3-4):201-212.

26. Hevener KE, Zhao W, Ball DM, et al. Validation of molecular docking programs for virtual screening against dihydropteroate synthase. *J Chem Inf Model.* 2009;49(2):444-460.

27. Bender A, Glen RC. A discussion of measures of enrichment in virtual screening: Comparing the information content of descriptors with increasing levels of sophistication. *J Chem Inf Model*. 2005;45(5):1369-1375.
28. Bissantz C, Folkers G, Rognan D. Protein-based virtual screening of chemical databases. 1. evaluation of different docking/scoring combinations. *J Med Chem*. 2000;43(25):4759-4767.

Chapter 3

Structure-Based Design of PPAR γ Antagonists as Potential Anti Prostate Cancer Agents

ABSTRACT:

The peroxisome proliferator-activated receptor gamma is (PPAR γ) recently identified as an oncogene and it plays a key role in prostate cancer (PC) development and progression. PPAR γ antagonists contributed to the inhibition of PC cell growth. We describe a structure-based approach that led to the discovery of a series of novel hits for PPAR γ antagonists. We fulfilled integrated virtual screening and biological assay for the two binding sites of PPAR γ ; orthosteric and allosteric pockets. Several hits of PPAR γ antagonists showing single digit of micro molar concentration in inhibition of PPAR γ generated from the virtual screening of allosteric pocket. The docking studies showed that compounds have more ligand protein interactions at allosteric pocket. Arg288, Lys367, and His449 are significant residues to be targeted by PPAR γ antagonists. The allosteric site showed that it is the most favorable binding for the PPAR γ antagonists.

3.1. Introduction:

Prostate cancer (PC) is the second most diagnosed cancer and sixth leading cause of cancer mortality in men in the world.¹ The androgens and the androgen receptor (AR) control the development and growth of PC². Several agents targeting AR signaling have improved and approved for the treatment of metastatic PC.³ PC metastasis is still irremediable and develops resistance to AR-targeted therapies.⁴ Several molecular pathways have been suggested to overcome PC, including phosphatase and tensin homolog (PTEN) loss, NK3 homeobox 1 (Nkx3.1) loss, Myc amplification, Forkhead box protein M1 (FoxM1) overexpression, and phosphoinositide 3-kinase/AKT serine/threonine kinase 1 (PI3K/AKT) activity.^{5,6,7,8,9} The peroxisome proliferator-activated receptor gamma (PPAR γ) have recently identified as an oncogene that contributes to PC development and progression.^{10,11,12} PPAR γ is a ligand-dependent transcription factor belonging to the nuclear hormone receptor superfamily.¹³ PPAR γ is known to play a prominent role in adipocyte differentiation, the inflammatory response, lipid metabolism, and peripheral glucose utilization.⁴

PPAR γ was originally thought that PPAR γ acted as a tumor suppressor in PC, and PPAR γ agonists could be used as therapeutics for PC.^{14,15,16,17} However, further analysis clearly demonstrated that the inhibition of PC growth were working via PPAR γ -independent mechanisms.^{18,19,20} In fact, PPAR γ is recently defined as an oncogene in PC, and PPAR γ expression is greater in PC.^{11,12,21,22} PPAR γ expression increases with stage and grade of PC, and PPAR γ positively correlated with PC grade.^{11,12,21,22} Three AR-negative PC cell lines: DU-145, PC3, and PC3M were revealed that the overexpression of PPAR γ prompted cell proliferation, migration levels and metastases to the lungs and lymph

nodes.¹¹ The siRNA knockdown of PPAR γ and treatment with a PPAR γ antagonist reduced the tumor size of PC.^{10,11} Besides, Warfarin which inhibited PPAR γ signaling in PC cells leading to an inhibition of AR signaling and the inhibition of PC cell growth.¹⁰ Thus, PPAR γ is a novel and important target in PC. Therefore, there is an urgent need to develop novel, potent PPAR γ antagonists for treatment and prevention of PC and other diseases.

PPAR γ is a nuclear receptor and a ligand-dependent transcription factor.²³ The endogenous lipids and synthetic small molecule ligands bind PPAR γ and regulate the transcriptional activity of PPAR γ through the C-terminal ligand-binding domain (LBD).²⁴ The LBD of PPAR γ is big ($>1200 \text{ \AA}^3$), and there are three binding area within distinct regions of the LBD.²⁵ The thiazolidinedione drugs (TZDs) are high-affinity synthetic PPAR γ agonists, and they are commonly used as insulin sensitizers in patients with type II diabetes.⁴ TZDs binds to the canonical orthosteric pocket of PPAR γ , and stabilize the activation function 2 (AF-2).²⁶ The AF-2 involves helix 3, helix 5, and the critical helix 12.²⁷ In contrast, several PPAR γ ligands have alternating binding site located between H3 and the β -sheets and does not compete with endogenous ligand binding the canonical orthosteric pocket, so this binding site can be identified as an allosteric site.²⁸ The allosteric site surface includes H2', H3, Ω loop, H7, and β -sheets.²⁸ While hundreds of PPAR γ agonists and partial agonist have been developed, only a handful of pure antagonists have been developed. GW9662 and T0070907 have similar structures, and they are both covalent modifiers of target proteins and have never been developed clinically (Figure 3.1).^{29,30} Several reversible PPAR γ antagonists have been developed, but this class of molecules do not have good drug-like properties (Figure 1).^{31,32}

Here, we used computational and experimental approach to find novel hits of PPAR γ antagonists. We performed a comprehensive structure based virtual screening (SBVS) comparison between the orthosteric and allosteric sites of PPAR γ to find out the most favorable binding site for PPAR γ antagonists. The identified hit molecules then were tested for their ability to suppress PPAR γ activation in a cell-based assay. We identified regions of the PPAR γ protein that can be targeted to design PPAR γ antagonists. Besides, we discuss the potential ligand protein interactions of PPAR γ antagonists for drug development and optimization. This comparison revealed a probable basis for the design and development of PPAR γ antagonists. Our docking results provide an important structural insight to the identification and development of several novel PPAR γ antagonists with potencies in the single-digit micromolar range.

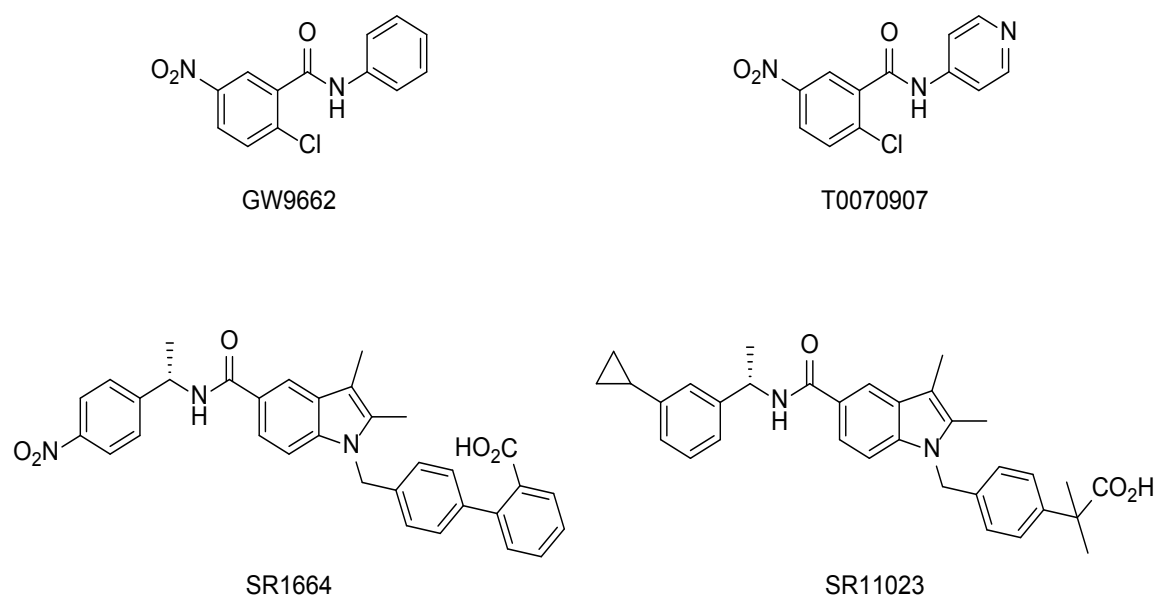


Figure 3.1. Representative PPAR γ antagonists.

3.2. Materials and Methods:

3.2.1. Virtual screening and molecular modeling:

A database of 260,071 molecules was downloaded from the National Cancer Institute (NCI), then the energy was minimized using MMFF94X force field in Molecular Operating Environment (MOE) software.^{33,34,35} In this study, we used Glide Dock in the Maestro 11.2 for ligand docking to PPAR γ (PDB ID: 2HFP) as a target protein.^{36,37} Then, two grid files was generated by the Glide Grid Generation panel with the bound ligands as the centroid of the protein binding pocket for the orthosteric and allosteric sites of PPAR γ .³⁶ The site of the bound ligand (NSI) in the crystal structure 2HFP was defined as the centroid. Then, all compounds were docked with the precision and ligand sampling were set to extra-precision (XP) method, and all other parameters were used as defaults.³⁶ The binding affinity of the various conformation of PPAR γ /ligand complexes was evaluated by the Glide scores. The protein/ligand interactions was created by using the Pymol software.³⁸

3.2.2. Cell lines and culture conditions:

LNCaP cells (ATCC) were maintained in phenol red-free RPMI 1640 supplemented with 10% FBS and antibiotics. LNCaP cells stably expressing AR and PPAR γ were generated through the transfection of fluorescent and HA-tagged AR and PPAR γ (clone HsCD00455985).

3.2.3. Transfection and transcriptional assays:

LNCaP cells were transfected using Lipofectamine Plus (Thermofisher) with PPAR response element (PPRE) driven firefly luciferase and pRL-SV40 (Promega) as a control. Cells were transferred to a 96-well plate 24 hours after transfection and treated with vehicle, pioglitazone (pio) or the selected compounds in quadruplicate. Luciferase activity

was assayed 24 hours after treatment using the dual-luciferase reporter assay system (Promega) and the renilla-normalized firefly luciferase activity was reported. IC_{50s} were determined by linear regression. Student's t-tests (two-sided and equal variance) were performed to determine differences from pio-induced full activity ($p < 0.05$ indicated by an asterisk.)

3.3. Results and Dissection:

To identify compounds that can repress the PPAR γ -controlled gene expression, we carried out docking studies against the crystal structure of PPAR γ (PDB ID: 2HFP).³⁷ This crystal structure has two ligands occupied two different binding sites of PPAR γ , the orthosteric and allosteric pockets, forming a 1:2 complex within the crystal (Figure 3.2). We performed SBVS to the both binding site of PPAR γ . A database of 260,071 molecules was downloaded from the National Cancer Institute (NCI), then it was filtered according to the Lipinski's rule of five by the logP ($\log P < 5$), and molecular weight ($MW < 500$) yielding 33,778 drug-like molecules.³⁹ 500 compounds were randomly selected from this database based on their availability from commercial sources and were then screened and docked through the orthosteric and allosteric pockets. There are some compounds have molecular weight over 500 because they look like a dimer. The docked results of the top-scored were chosen as potential PPAR γ antagonists based on their glide docking sources. The Glide docking scores of these compounds were the minimum docking scores. The more minimum docking scores of a compound is the more favorable binding affinity of the complex compounds.⁴⁰ Seven compounds were identified from the SBVS against the orthosteric site of PPAR γ and they were selected for biological testing for further evaluation (Figure 3.3). In contrast, seventeen compounds were identified from the SBVS

against the allosteric site of PPAR γ and they were selected for biological testing too for further evaluation (Figure 3.4). The glide docking results of PPAR γ antagonists against the orthosteric and allosteric pockets are listed in Table 3.1, and 3.2 respectively.

The pose selection method was performed to validate the glide docking method.⁴¹ This is a standard method which have been used by comparing the docked pose of a ligand with the co-crystal structure of the ligand. A pose with an RMSD < 2.0 Å is considered to be good.⁴¹ The superposition of the Glide-generated docked pose, and the native conformation in the co-crystal structure (PDB ID: 2HFP) for compound NSI (Figure 3.5) showed that the RMSD values between these two poses is 0.24 Å for the orthosteric pocket and 0.37 Å for the allosteric pocket (Figure 5). These RMSD values indicate that the glide docking can successfully predict ligand-binding conformations and it is able to successfully reproduce the native conformation.

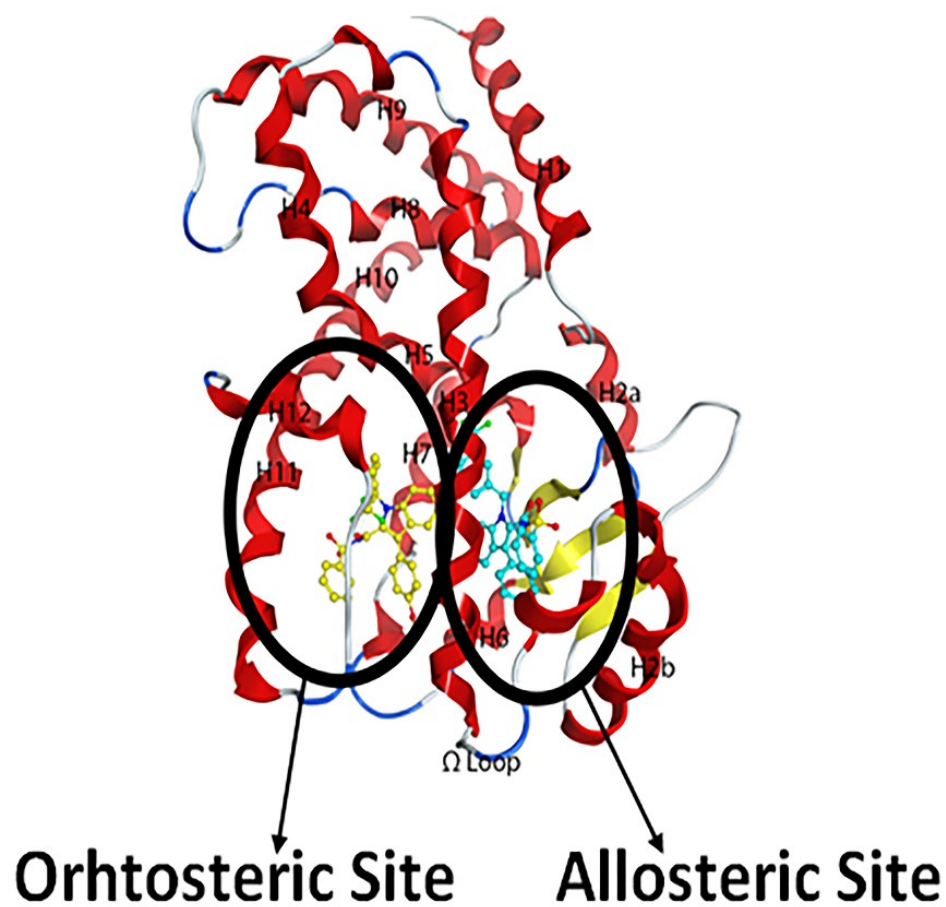


Figure 3.2. The Orthosteric and allosteric sites of PPAR γ . The Co-crystal structure of NSI-bound PPAR γ (PDB 2HFP) shows two bound NSI molecules, one to the orthosteric pocket and a second bound to the allosteric site.

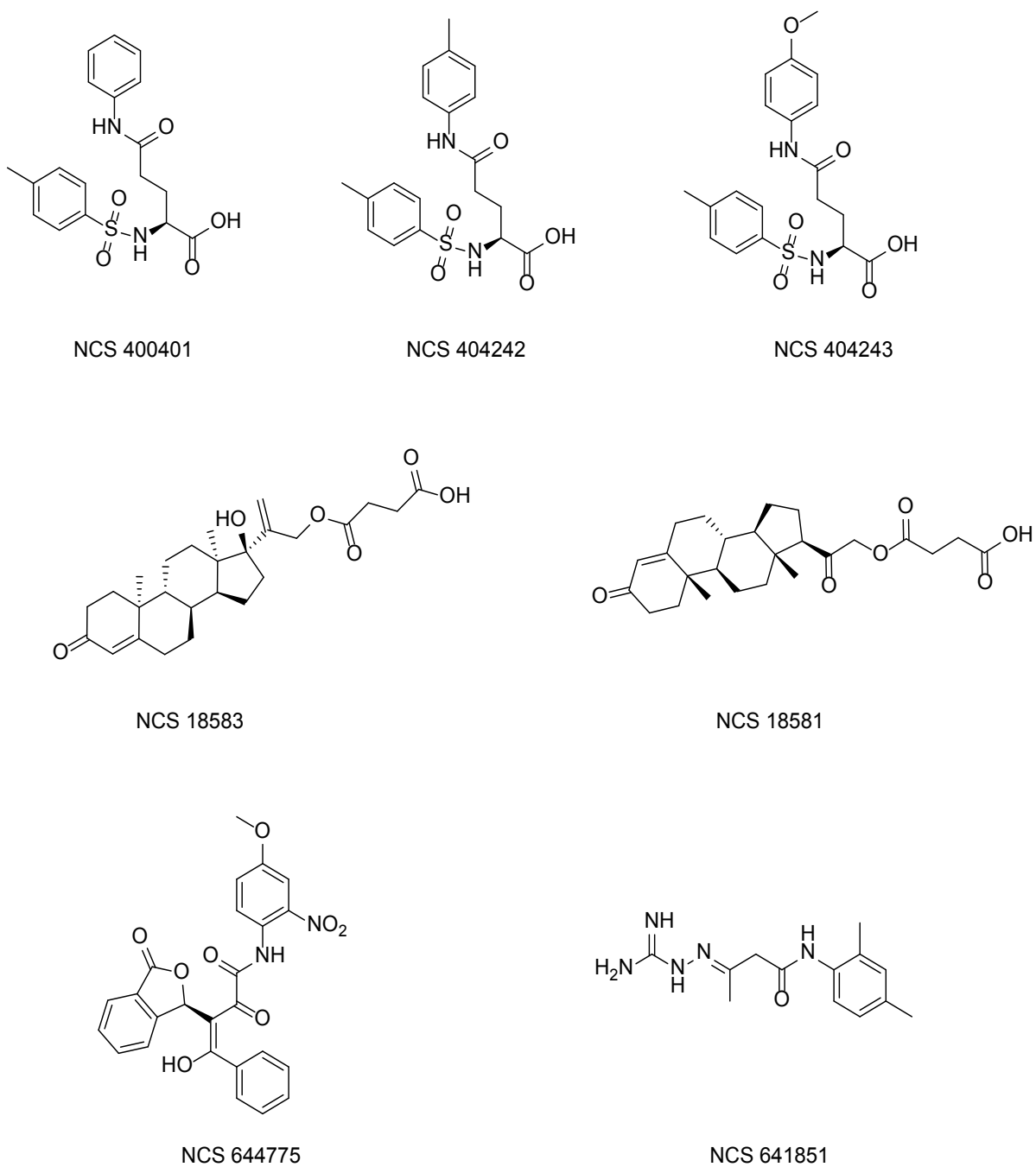
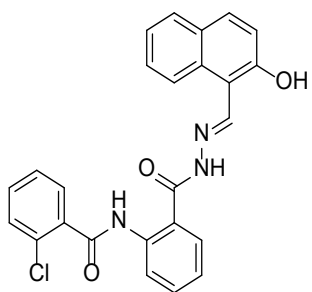
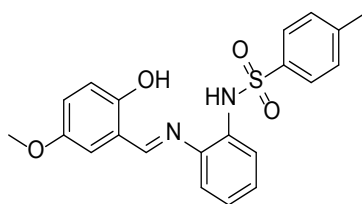


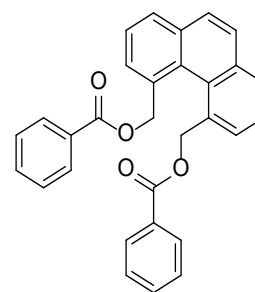
Figure 3.3. Chemical structures of seven hit molecules resulted from the SBVS against the orthosteric site.



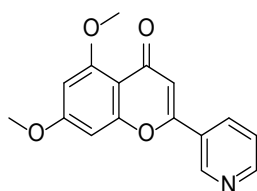
NCS 215556



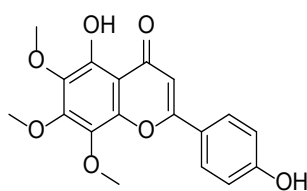
NCS 120176



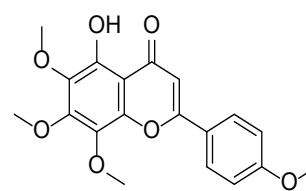
NCS 408562



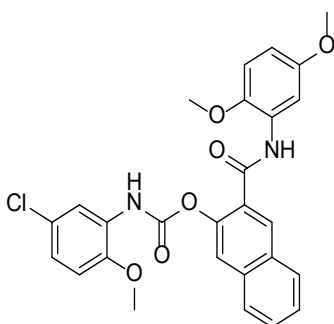
NCS 51349



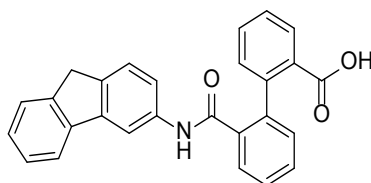
NCS 79093



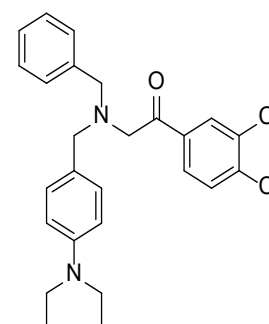
NCS 79323



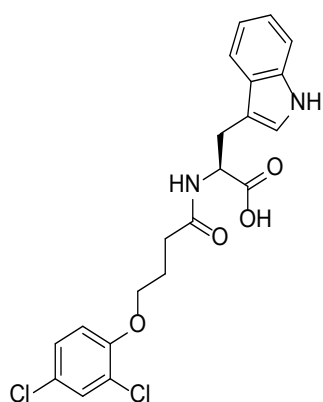
NCS 205811



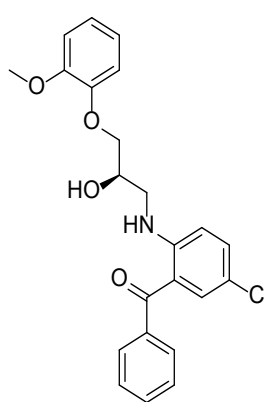
NCS 128594



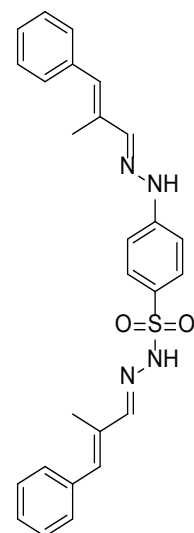
NCS 10671



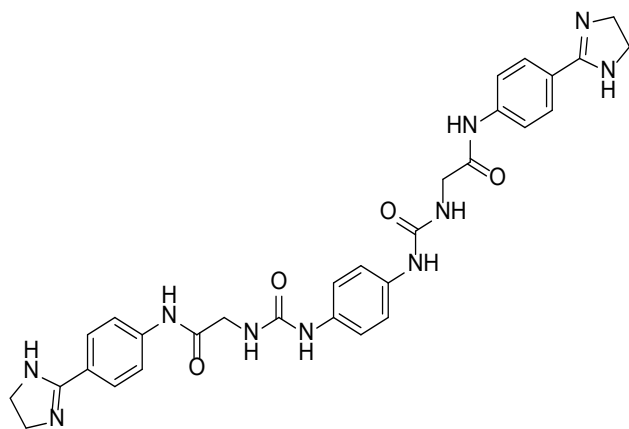
NCS 16768



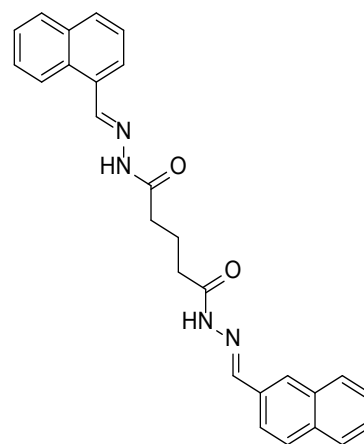
NCS 366098



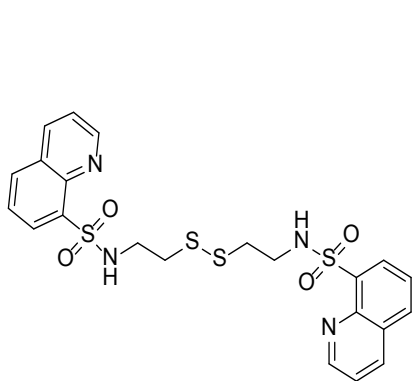
NCS 70914



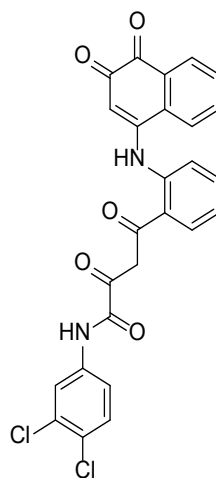
NCS 79023



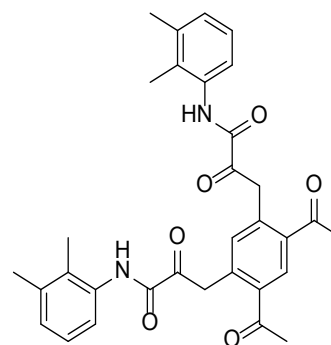
NCS 106156



NCS 273905



NCS 641250



NCS 658262

Figure 3.4. Chemical structures of seven hit molecules resulted from the SBVS against the allosteric site.

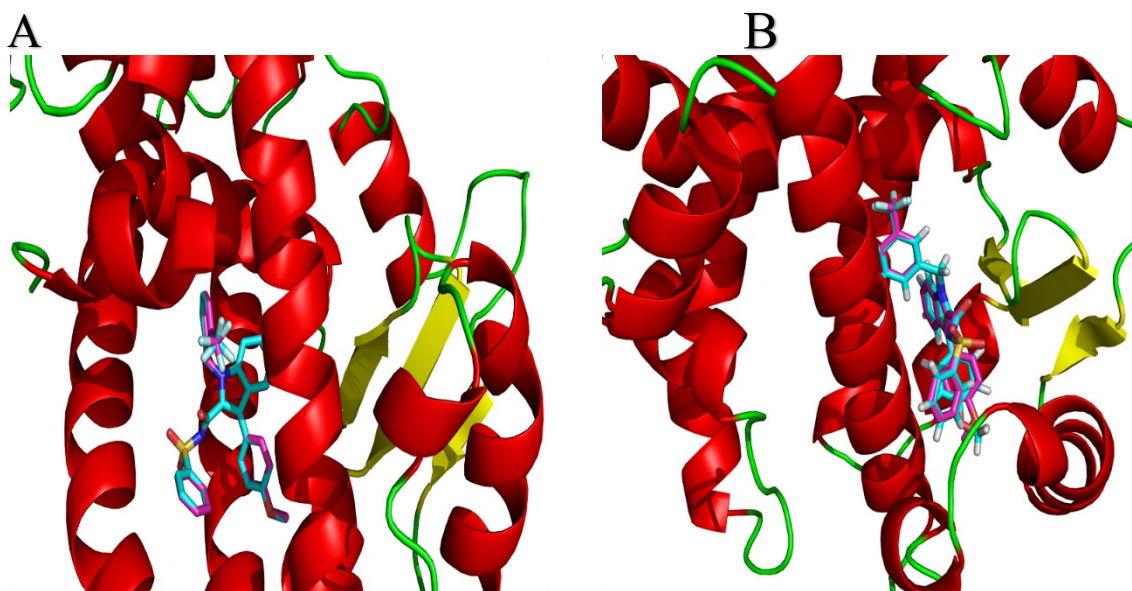


Figure 3.5. The superposition of the Glide generated pose and the native ligands of the crystal structure (2HFP). The RMSD between these two conformations is 0.24 Å for orthosteric site (A) and 0.37 Å for allosteric site (B).

The top-scored compounds were then tested for their ability to inhibit PPAR γ in a luciferase reporter assay. Cells transfected with PPAR-responsive and control reporters were treated with the agonist pioglitazone (pio) and the selected compounds overnight. The following day, the luciferase activities were determined. We found that three compounds resulted from the SBVS against the orthosteric site inhibited the PPAR γ activity with IC_{50s} in the high micro molar range (Table 3.1). 641851, 404243, 400401 all had better responses to increasing doses, allowing for an accurate measurement of IC_{50s} (Figure 3.6). Although these antagonists are not potent, this work is an important first step in the rational design of PPAR γ antagonists.

In contrast, we found that many of the compounds resulted from the SBVS against the allosteric site inhibited PPAR γ activity in the micro molar range (Table 3.2). Indeed, the potency of these compounds is in single-digit micro molar range with IC_{50s} less than 10 μ M. Among the most potent, with IC_{50s} less than 3 μ M, were compounds 51349, 79023, 215556, and 273905 (Figure 3.7). Although the newly identified antagonists are not quite as potent as some existing molecules, this work demonstrates the strong SAR of a novel class of PPAR γ antagonists and is a great starting point for the rational design of even more potent PPAR γ antagonists. These results demonstrate the utility of SBVS against the allosteric site in discovering novel chemical hits that would unlikely to be discovered otherwise.

To explore the structural basis of small molecules antagonists targeting of the PPAR γ , we further completed docking studies for the orthosteric and allosteric binding site residues to determine the binding mode of PPAR γ antagonists. Therefore, we studied the docking poses of these top-ranking compounds to analyze the ligands protein interactions of PPAR γ

antagonists. We found that 641851, 404243, 400401 resulted from the SBVS against the orthosteric site had similar interactions with PPAR γ . They all had $\pi - \pi$ stacking with Phe363 and His449 (Figure 3.8). The potency of 400401 toward PPAR γ might be attributed to their ability to form $\pi - \pi$ stacking with Tyr327. In contrast, compounds resulted from the SBVS against the allosteric site had more interactions with PPAR γ . We divided the newly identified hits from the SBVS against the allosteric site into the following two groups based on their ligand protein interactions. Group one involves 16768, 51349, 120176, 205811 formed H-bonds and π -cation interaction with Ser342 and Arg288, respectively (Figure 3.9). A ligand interaction to Arg288 is a significant interaction for PPAR γ antagonists.⁴² On other side, we found that 128594, 366098, 408562, and 10671 formed H-bonds and $\pi - \pi$ stacking with Lys367 and His449, respectively (Figure 3.10). Ligand hydrogen bonding with Lys367 could be an important interaction for PPAR γ antagonists. Therefore, to design PPAR γ antagonists, it is essential to maintain the critical H-bonds interaction to Arg288, Ser342, Lys367, and His449 at allosteric site of PPAR γ .

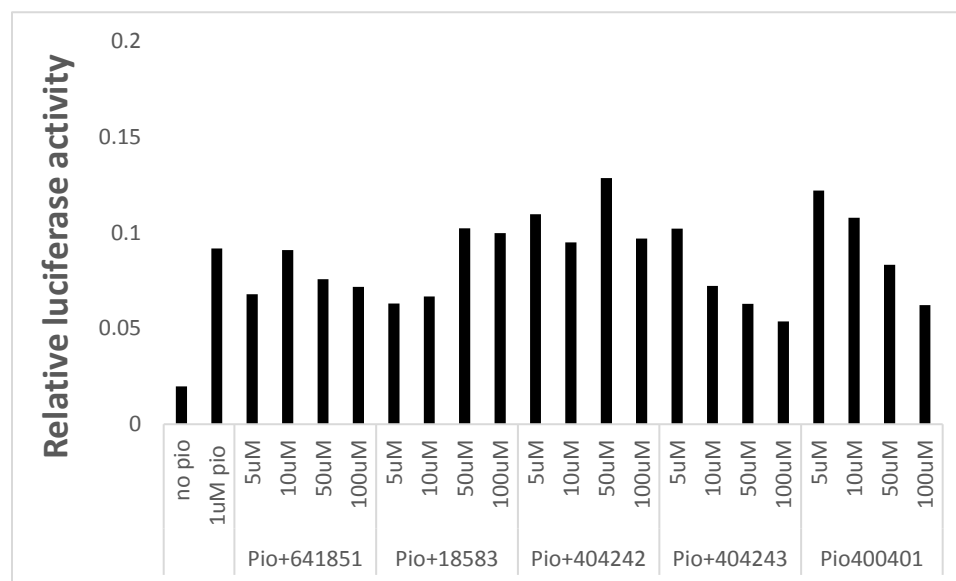


Figure 3.6. Effects of PPAR γ inhibition in LCP cells for compounds resulted from the SBVS against the orthosteric site. Cells were transfected with PPRELuc + pRL SV40 and treated as indicated. The following day, relative luciferase activity was measured. PPAR γ activity was stimulated by pio, and inhibited by compounds in LCP cells (*P<0.05 difference from Pio treated cells).

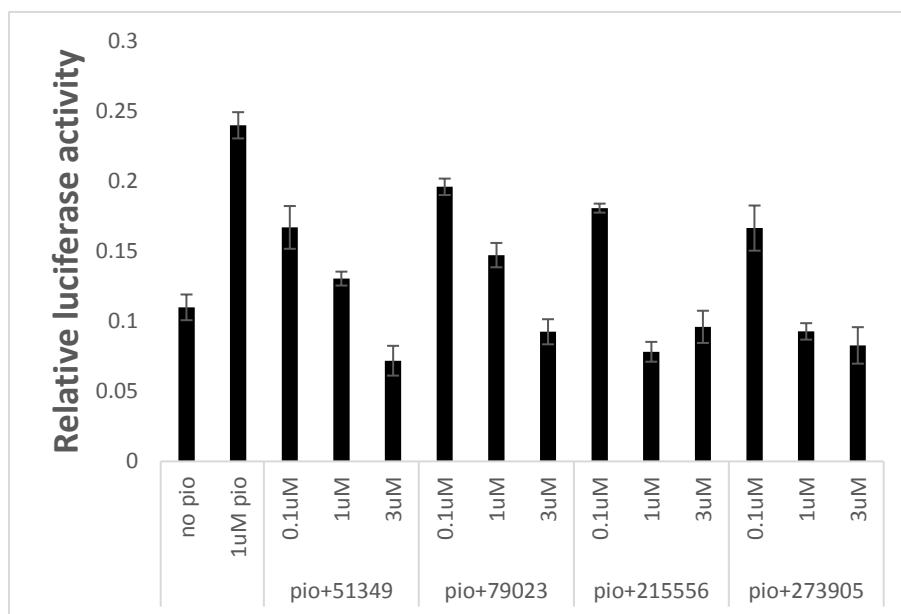


Figure 3.7. Effects of PPAR γ inhibition in LCP cells for compounds resulted from the SBVS against the orthosteric site. Cells were transfected with PPRELuc + pRL SV40 and treated as indicated. The following day, relative luciferase activity was measured. PPAR γ activity was stimulated by pio, and inhibited by compounds in LCP cells (*P<0.05 difference from Pio treated cells).

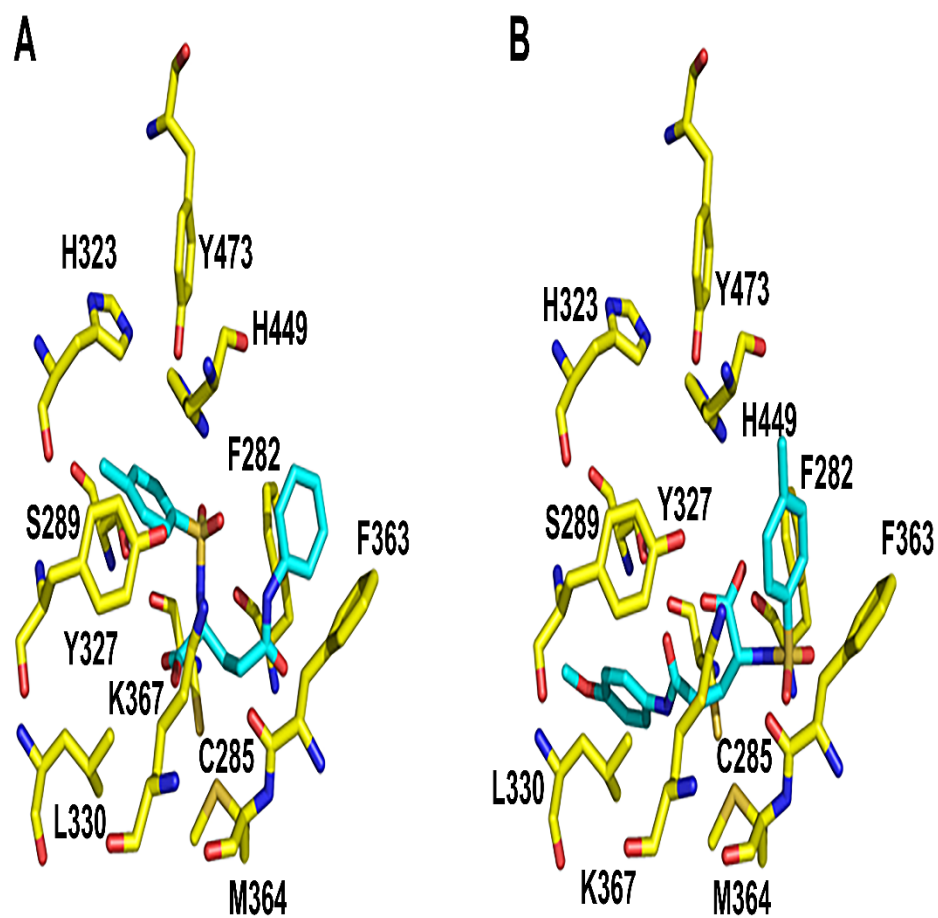


Figure 3.8. Ligands interactions between compounds resulted from the SBVS against the orthosteric site and PPAR γ for 400401 (A), and 404243 (B).

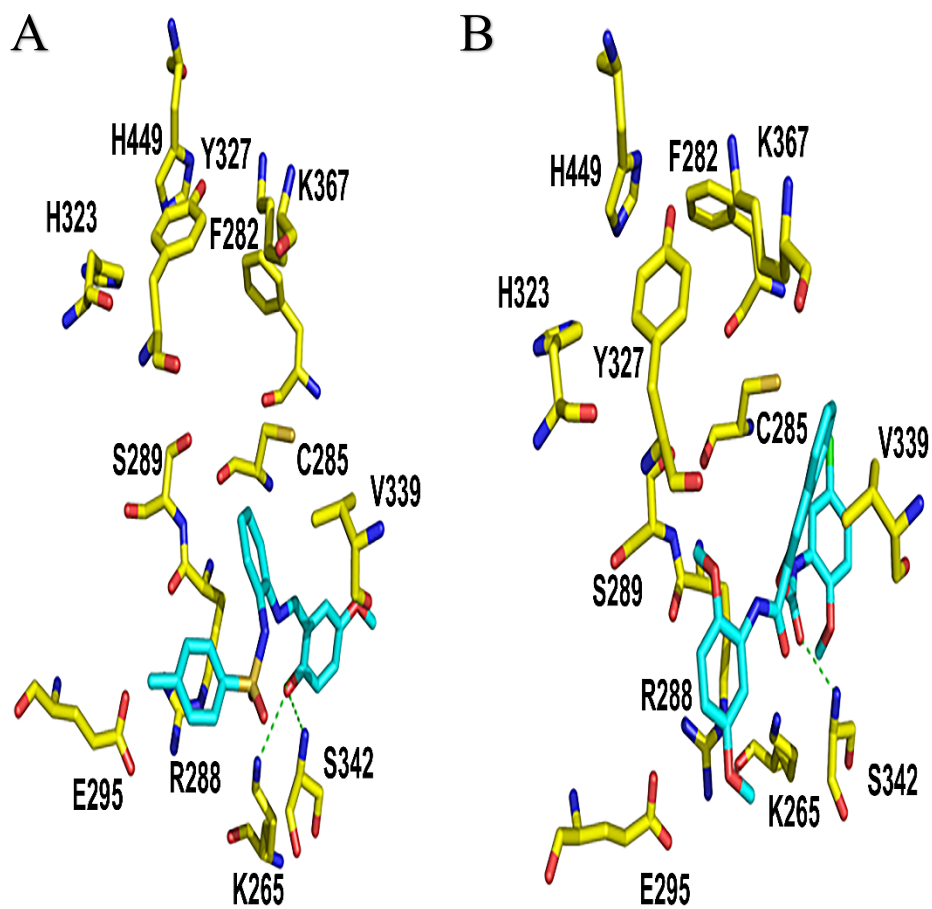


Figure 3.9. Ligands interactions between compounds resulted from the SBVS against the allosteric site and PPAR γ for group 1, 120176 (A), and 205811 (B). The H-bond interactions are shown as green dotted lines.

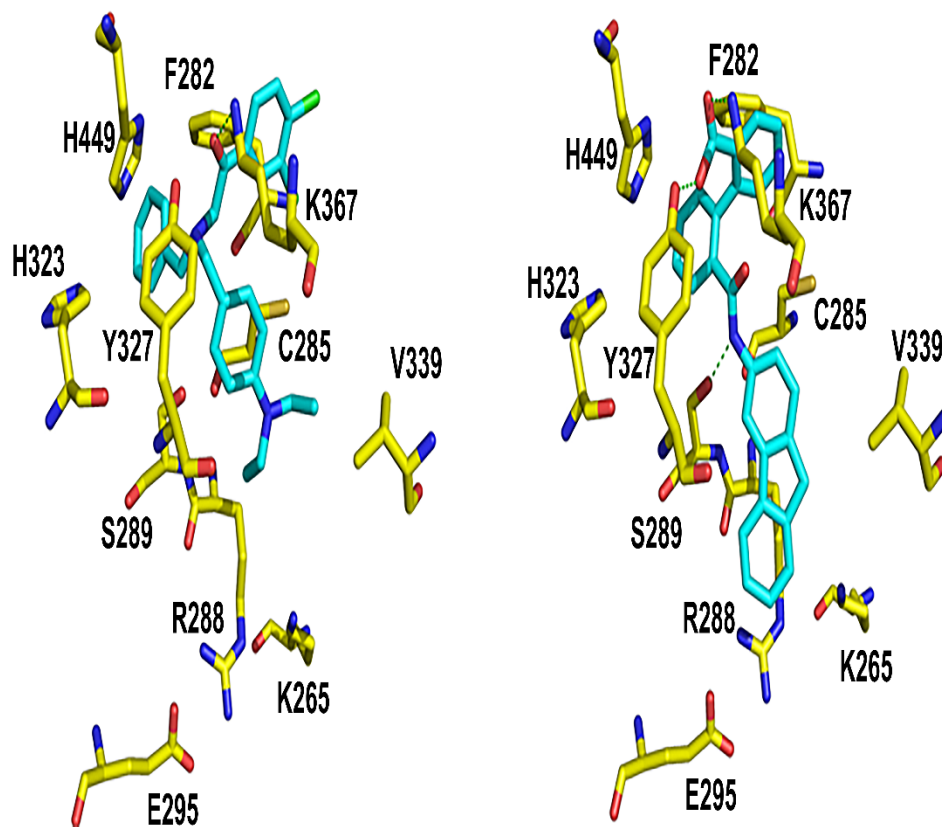


Figure 3.10. Ligands interactions between compounds resulted from the SBVS against the allosteric site and PPAR γ for group 2, 10671 (A), and 128594 (B). The H-bond interactions are shown as green dotted lines.

Table 3.1. The molecular weight, glide score, growth inhibition of LCP cells, and residues interactions of compounds resulted from the SBVS against the orthosteric site.

Compound	Mw (g/mol)	XP Gscore	IC ₅₀ (μM)	Residue Interactions
400401	376.43	-8.60	140.01	Tyr327, Phe363, His449
404243	406.45	-8.70	274.99	Phe363, His449
641851	261.33	-7.24	179.51	Phe363, His449

Table 3.2. The molecular weight, glide score, growth inhibition of LCP cells, and residues interactions of compounds resulted from the SBVS against the allosteric site.

Compound	Mw (g/mol)	XP Gscore	IC50 (uM)	Residue Interactions
10671	455.43	-9.92	4.46	Lys367, His449
16768	435.31	-9.63	2.41	Ser342, Ser289, Arg288
51349	283.28	-8.5	1.12	Leu228, Glu343, Arg288
70914	534.68	-10.38	2.27	Phe282
79023	596.65	-9.82	1.64	Gln271, Ser289, Ser342
79093	358.35	-8.31	5.39	Ser342, Glu343
79323	344.32	-8.88	2.47	Leu228
106156	436.51	-9.66	2.12	Phe282, Ser289
120176	396.46	-8.05	2.30	Lys265, Ser342, Arg288
128594	405.45	-9.96	3.53	Ser289, Lys367, His449
205811	506.94	-9.58	8.72	Ser342, Arg288
215556	443.89	-9.97	1.68	No Interactions
273905	534.68	-9.93	1.50	Phe282, Arg288
366098	411.88	-10.03	2.35	Ser289, Lys367
408562	446.50	-9.79	5.40	Lys367, His449
641250	507.33	-9.53	2.75	Leu228, Arg288
658262	541.60	-11.55	2.58	Arg288, Ser289, Tyr327, Ser342, Glu343

3.4. Conclusion:

The PPAR γ is an oncogene protein that prompt PC growth and progress. PPAR γ is a novel and important target in PC. PPAR γ antagonist decreased tumor size. The identification of hit compounds is an important step in the development of PPAR γ antagonists. PPAR γ has two binding sites: orthosteric and allosteric sites. Here, we used an integrated computational and experimental approach against the crystal structures of PPAR γ which is a PPAR γ model that has two molar equivalents of a ligand binding at different sites. We then performed SBVS of small molecule libraries against the two binding sites followed by experimental testing to discover new hits of PPAR γ antagonists. Compounds, which were identified as PPAR γ antagonists, resulted from SBVS against the allosteric site much more and more potent than compounds were resulted from SBVS against the orthosteric site. Structural analysis of the two binding sites of PPAR γ showed that the allosteric site has more ligand protein interactions with the compounds. Inspection of ligand/PPAR γ interactions showed that a ligand form H-bonds to PPAR γ through the residues: Arg288, and Lys367 would be PPAR γ antagonists. This study improves the understanding of the PPAR γ binding site, which supports in the design and optimization of more specific PPAR γ antagonists. Next, we will effort on the design and synthesis and optimized of derivatives of selected hits to develop lead candidates as PPAR γ antagonists for the treatment of PC and other solid tumors.

References:

1. Siegel RL, Miller KD, Jemal A. Cancer statistics, 2015. *CA Cancer J Clin.* 2015;65(1):5-29.
2. Zhou Y, Bolton EC, Jones JO. Androgens and androgen receptor signaling in prostate tumorigenesis. *J Mol Endocrinol.* 2015;54(1):15.
3. Friedlander TW, Ryan CJ. Targeting the androgen receptor. *Urol Clin North Am.* 2012;39(4):453-464.
4. Elix C, Pal SK, Jones JO. The role of peroxisome proliferator-activated receptor gamma in prostate cancer. *Asian J Androl.* 2018;20(3):238-243.
5. Deocampo ND, Huang H, Tindall DJ. The role of PTEN in the progression and survival of prostate cancer. *Minerva Endocrinol.* 2003;28(2):145-153.
6. Abate-Shen C, Banach-Petrosky WA, Sun X, et al. Nkx3.1; pten mutant mice develop invasive prostate adenocarcinoma and lymph node metastases. *Cancer Res.* 2003;63(14):3886-3890.
7. Ellwood-Yen K, Graeber TG, Wongvipat J, et al. Myc-driven murine prostate cancer shares molecular features with human prostate tumors. *Cancer Cell.* 2003;4(3):223-238.
8. Aytes A, Mitrofanova A, Lefebvre C, et al. Cross-species regulatory network analysis identifies a synergistic interaction between FOXM1 and CENPF that drives prostate cancer malignancy. *Cancer Cell.* 2014;25(5):638-651.
9. Goldstein AS, Huang J, Guo C, Garraway IP, Witte ON. Identification of a cell of origin for human prostate cancer. *Science.* 2010;329(5991):568-571.
10. Tew BY, Hong TB, Otto-Duessel M, et al. Vitamin K epoxide reductase regulation of androgen receptor activity. *Oncotarget.* 2017;8(8):13818-13831.

11. Ahmad I, Mui E, Galbraith L, et al. Sleeping beauty screen reveals pparg activation in metastatic prostate cancer. *Proc Natl Acad Sci U S A*. 2016;113(29):8290-8295.
12. Salgia MM, Elix CC, Pal SK, Jones JO. Different roles of peroxisome proliferator-activated receptor gamma isoforms in prostate cancer. *Am J Clin Exp Urol*. 2019;7(3):98-109.
13. Rosen ED, Spiegelman BM. PPARgamma: A nuclear regulator of metabolism, differentiation, and cell growth. *J Biol Chem*. 2001;276(41):37731-37734.
14. Butler R, Mitchell SH, Tindall DJ, Young CY. Nonapoptotic cell death associated with S-phase arrest of prostate cancer cells via the peroxisome proliferator-activated receptor gamma ligand, 15-deoxy-delta12,14-prostaglandin J2. *Cell Growth Differ*. 2000;11(1):49-61.
15. Hisatake JI, Ikezoe T, Carey M, Holden S, Tomoyasu S, Koeffler HP. Down-regulation of prostate-specific antigen expression by ligands for peroxisome proliferator-activated receptor gamma in human prostate cancer. *Cancer Res*. 2000;60(19):5494-5498.
16. Kubota T, Koshizuka K, Williamson EA, et al. Ligand for peroxisome proliferator-activated receptor gamma (troglitazone) has potent antitumor effect against human prostate cancer both in vitro and in vivo. *Cancer Res*. 1998;58(15):3344-3352.
17. Mueller E, Smith M, Sarraf P, et al. Effects of ligand activation of peroxisome proliferator-activated receptor gamma in human prostate cancer. *Proc Natl Acad Sci U S A*. 2000;97(20):10990-10995.
18. Qin L, Gong C, Chen A, et al. Peroxisome proliferator-activated receptor γ agonist rosiglitazone inhibits migration and invasion of prostate cancer cells through inhibition of the CXCR4/CXCL12 axis. *Mol Med Rep*. 2014;10(2):695-700.

19. Shiao C, Yang C, Kulp SK, et al. Thiazolidinediones mediate apoptosis in prostate cancer cells in part through inhibition of bcl-xL/bcl-2 functions independently of PPARgamma. *Cancer Res.* 2005;65(4):1561-1569.
20. Yang C, Wang Y, Wei S, et al. Peroxisome proliferator-activated receptor gamma-independent suppression of androgen receptor expression by troglitazone mechanism and pharmacologic exploitation. *Cancer Res.* 2007;67(7):3229-3238.
21. Rogenhofer S, Ellinger J, Kahl P, et al. Enhanced expression of peroxisome proliferator-activated receptor gamma (PPAR- γ) in advanced prostate cancer. *Anticancer Res.* 2012;32(8):3479-3483.
22. Segawa Y, Yoshimura R, Hase T, et al. Expression of peroxisome proliferator-activated receptor (PPAR) in human prostate cancer. *Prostate.* 2002;51(2):108-116.
23. Meinke PT, Wood HB, Szewczyk JW. Nuclear hormone receptor modulators for the treatment of diabetes and dyslipidemia. *Annu. Rep. Med. Chem.* 2006; 41, 99–126.
24. Mosure SA, Shang J, Eberhardt J, et al. Structural basis of altered potency and efficacy displayed by a major in vivo metabolite of the antidiabetic PPAR γ drug pioglitazone. *J Med Chem.* 2019;62(4):2008-2023.
25. Kroker AJ, Bruning JB. Review of the structural and dynamic mechanisms of PPAR γ partial agonism. *PPAR Res.* 2015;2015:816856.
26. Brust R, Lin H, Fuhrmann J, Asteian A, Kamenecka TM, Kojetin DJ. Modification of the orthosteric PPAR γ covalent antagonist scaffold yields an improved dual-site allosteric inhibitor. *ACS Chem Biol.* 2017;12(4):969-978.
27. Brust R, Shang J, Fuhrmann J, et al. A structural mechanism for directing corepressor-selective inverse agonism of PPAR γ . *Nat Commun.* 2018;9(1):4687.

28. Hughes TS, Giri PK, de Vera, Ian Mitchell S., et al. An alternate binding site for PPAR γ ligands. *Nat Commun.* 2014;5:3571.
29. Seargent JM, Yates EA, Gill JH. GW9662, a potent antagonist of PPARgamma, inhibits growth of breast tumour cells and promotes the anticancer effects of the PPARgamma agonist rosiglitazone, independently of PPARgamma activation. *Br J Pharmacol.* 2004;143(8):933-937.
30. Wright HM, Clish CB, Mikami T, et al. A synthetic antagonist for the peroxisome proliferator-activated receptor gamma inhibits adipocyte differentiation. *J Biol Chem.* 2000;275(3):1873-1877.
31. Asteian A, Blayo A, He Y, et al. Design, synthesis, and biological evaluation of indole biphenylcarboxylic acids as PPAR γ antagonists. *ACS Med Chem Lett.* 2015;6(9):998-1003.
32. Zheng J, Corzo C, Chang MR, et al. Chemical crosslinking mass spectrometry reveals the conformational landscape of the activation helix of PPAR γ ; a model for ligand-dependent antagonism. *Structure.* 2018;26(11):143-1439.e6.
33. NCI open database compounds, release 3; national cancer institute national institutes of health: Bethesda, MD, sep 2003).
34. Halgren TA. Merck molecular force field. I. basis, form, scope, parameterization, and performance of MMFF94. *J. Comput. Chem.* 1996;17(5-6):490-519.
35. The molecular operating Environment (MOE); *Chemical Computing Group Inc.:Montreal, Quebec, Canada, 2009.*
36. Protein preparation wizard, maestro, MacroModel, and glide; *Schrödinger, LLC: Portland, OR, 2009.*

37. Hopkins CR, O'Neil SV, Laufersweiler MC, et al. Design and synthesis of novel N-sulfonyl-2-indole carboxamides as potent PPAR- γ binding agents with potential application to the treatment of osteoporosis. *Bioorg Med Chem Lett*. 2006;16(21):5659-5663.
38. DeLano WL. The PyMOL molecular graphics system. *The PyMOL Molecular Graphics System; DeLano Scientific: San Carlos, CA, 2002. 2009.*
39. Lipinski CA, Lombardo F, Dominy BW, Feeney PJ. Experimental and computational approaches to estimate solubility and permeability in drug discovery and development settings. *Adv Drug Deliv Rev*. 2001;46(1-3):3-26.
40. Sabbah DA, Vennerstrom JL, Zhong H. Docking studies on isoform-specific inhibition of phosphoinositide-3-kinases. *J Chem Inf Model*. 2010;50(10):1887-1898.
41. Hevener KE, Zhao W, Ball DM, et al. Validation of molecular docking programs for virtual screening against dihydropteroate synthase. *J Chem Inf Model*. 2009;49(2):444-460.
42. Brust R, Shang J, Fuhrmann J, et al. A structural mechanism for directing corepressor-selective inverse agonism of PPAR γ . *Nat Commun*. 2018;9(1):4687.

Chapter 4

Conformational Studies of Glucose Transporter 1 (GLUT1) as an Anticancer Drug Target

Abstract:

Glucose transporter 1 (GLUT1) is a facilitative glucose transporter overexpressed in various types of tumors; thus, it has been considered as an important target for cancer therapy. GLUT1 works through conformational switching from an outward-open (OOP) to an inward-open (IOP) conformation passing through an occluded conformation. It is critical to determine which conformation is preferred by bound ligands because the success of structure-based drug design depends on the appropriate starting conformation of the target protein. To find out the most favorable GLUT 1 conformation for ligand binding, we ran systemic molecular docking studies for different conformations of GLUT1 using known GLUT1 inhibitors. Our data revealed that the IOP is the preferred conformation and that residues Phe291, Phe379, Glu380, Trp388, and Trp412 may play critical roles in ligand binding to GLUT1. Our data suggests that conformational differences in these five amino acids in the different conformers of GLUT1 may be used to design ligands that inhibit GLUT1.

4.1. Introduction:

Glucose transporter 1 (GLUT1) is a membrane protein encoded by the solute carrier family 2A1 (SLC2A1) genes¹. GLUT1 is a member of sugar transporter subfamily of the major facilitator superfamily (MFS)². GLUT1 has a conserved core fold that consists of 12 transmembrane helices folded into two distinguishing domains, the amino (N) and carboxyl (C) terminal domains³. Each domain has six sequential transmembrane helices (TMs) that are folded into a pair of '3+3 inverted repeats.³ TM7 and TM10 are broken segments, hence termed TM7a/7b and TM10a/10b, respectively⁴. Four short intracellular α -helices (IC1–4) connect the N-terminal and C-terminal domains.⁴ The C domain provides the main substrate-binding site for glucose⁵. GLUT1 transports monosaccharides including d-glucose and d-galactose, but does not transport fructose^{6 7}. GLUT1 is expressed in diverse tissues with distinct kinetic behavior and different substrate affinity⁸.

Cancer cells transport more glucose than normal cells due to their rapid growth and high rate of aerobic glycolysis, a phenomenon called the Warburg effect^{9 10 11}. GLUT1 is upregulated in many cancers such as brain¹², breast¹³, lung¹⁴, kidney¹⁵, ovary¹⁶, prostate¹⁷, and colon¹⁸. In addition, stimulation of oncogenes like such as KRAS¹⁴, BRAF¹⁹, c-myc²⁰, and p53²¹, and transcription factors such as hypoxia-inducible factor-1 α (HIF-1)²² upregulate GLUT1 expression. GLUT1 inhibition results in reduction of cancer-cell proliferation and apoptosis^{23 24}. While GLUT1 is overexpressed in many tumors, we note that in the brain, glucose transport is facilitated by both GLUT1 and GLUT3^{25 26 27 28}. However, GLUT3 has greater affinity for glucose and higher capacity than GLUT1 in the brain (Km for d-glucose of 3.4 mM for GLUT1, and Km for 2-deoxy-glucose of 5 and 1.4 mM for GLUT1 and GLUT3, respectively)^{26 27}. A ligand selectively bound to GLUT1

rather than GLUT3 would be able to spare the GLUT3 inhibition and, thus, would minimize the potential neurotoxicity due to GLUT inhibition. Several small molecule GLUT1 inhibitors and chemotypes have been described including resveratrol²⁹, naringenin³⁰, phloretin³¹, cytochalasin B³², WZB117³³, STF-31³⁴, pyrazolopyrimidines³⁵, phenylalanine amides³², and (1H-pyrazol-4-yl)quinoline³⁶.

GLUT1 transports substrates by the alternating access mechanism (Figure 4.1), which involves the “rocker-switch” movement and the “gated pore” mechanisms^{37 38}. GLUT1 changes from an outward-open (OOP) conformation, which opens to the extracellular to take up glucose, to an inward-open (IOP) conformation, which allows the release of glucose to the intracellular cytoplasm via intermediate outward-occluded (OOC) and partially inward-occluded (PIO) conformations^{39 40 41 42}. Substrate-free GLUT1 favors the OOP conformation⁵. Once the substrate binds to the C domain of the GLUT1, the transporter shifts to the IOP conformation to release glucose⁵.

The only crystal structures of human GLUT1 are for the IOP conformation^{5 32}. Since only the IOP conformation is available for the human GLUT1 protein, we built homology models for other conformations using GLUT1 homologous crystal structures that have already adopted the needed conformations. For example, crystal structures of human glucose transporter 3 (GLUT3), which has an 86% sequence similarity to GLUT1, were obtained for the OOC and OOP conformations⁴. The crystal structure of *Escherichia coli* proton: Xylose symporter (Xyle), which has a 63% sequence similarity to GLUT1, were obtained for the PIO and inward-occluded (IOC) conformations^{43 44}. The essential amino acids interacting with glucose are conserved between Xyle and GLUT1⁴³.

It is critical to determine which conformation is preferred by bound ligands because the success of structure-based drug design depends on the appropriate starting conformation of the target protein. To identify the most favorable conformation for GLUT1 inhibitor binding, and to determine important amino residues that may be responsible for ligand interactions, we ran a series of docking studies of reported GLUT1 inhibitors against GLUT1 in different conformations: Outward-open (the OOP), partially outward occluded (POO), outward occluded (OOC), inward-open (IOP), and partially inward occluded (PIO) conformations. The docking scores and the enrichment factor (EF) as well as the ligand protein interactions suggested that the GLUT1 prefers the IOP conformation for ligand binding.

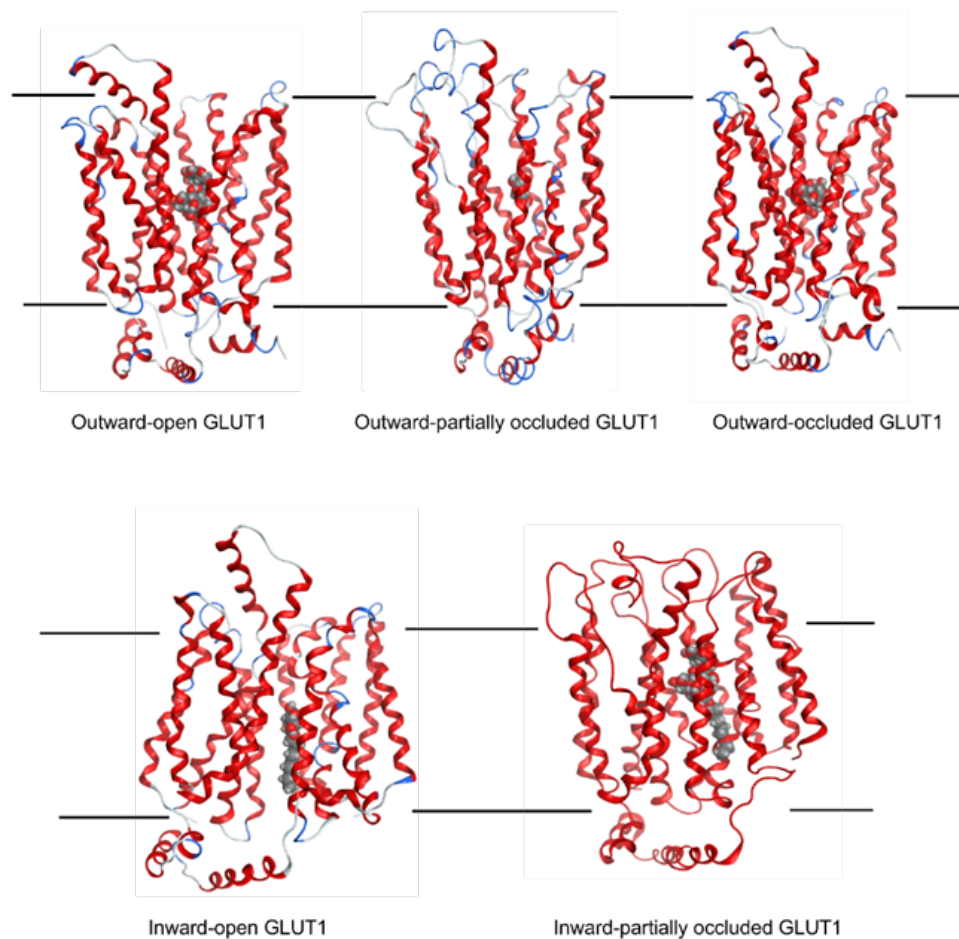


Figure 4. 1. An overview of working model of GLUT1: The function of GLUT1 depends on conformational change. The IOP is adopted from PDB ID: 4PYP. The OOP conformation was constructed by homology modeling of PDB ID: 4ZWC; the POO conformation was constructed by homology modeling of PDB ID: 4GBZ; the OOC conformation was constructed by homology modeling of PDB ID: 4ZW9; the Partial inward occluded PIO conformation was constructed by homology modeling of PDB ID: 4JA3.

4.2. Results and Discussion:

4.2.1. Homology Modeling of GLUT1:

The only crystal structures described for GLUT1 (PDB ID: 4PYP, 5EQG, 5EQH, and 5EQI) are for the IOP^{5 32}. The OOP, OOC, POO, and PIO conformations for GLUT1 have not yet been identified by X-ray crystallographic structures; hence, we constructed these models through homology modeling. The amino acid residue alignment of GLUT1 with GLUT3 and Xyle proteins showed that they have largely conserved glucose-binding residues and the highly conserved residues between these three proteins are highlighted in yellow (Figure 4.2). GLUT1 has 66% sequence identity and 80% similarity with GLUT3; GLUT1 has 29% sequence identity and 49% similarity with Xyle⁴³. The OOP and OOC were built through homology modeling by using the crystal structures of human GLUT3 (PDB ID: 4ZWC, and 4ZW9)⁴ as templates. Bacterial Xyle, a GLUT1 homology model (PDB: 4GBZ) was used to model the POO conformation⁴³, and the template (PDB: 4JA3) was used to build the PIO conformation⁴⁴. Structural alignment of GLUT1 to different homolog models shows that most of the secondary structures are conserved between these models and that the orientation of the folds differs, resulting in the OOP, POO, OOC, PIO, and IOP conformations (Figure 4.1).

Homology modeling is one of the most successful methods to build and predict the tertiary structure of a protein that has not been defined⁴⁵. Homology modeling depends on sequence alignment of proteins. If the sequences of two proteins are similar, they will have comparable tertiary structure folding⁴⁵. Amino acid residue alignment of GLUT1 with GLUT3 and Xyle proteins exhibited that they have notable conserved residues in the

sequences, especially at the glucose binding site residues (Figure 4.2). GLUT1 has high sequence identity (66%) and similarity (80%) with GLUT3, and GLUT1 has sequence identity (29%) and similarity (49%) with Xyle⁴³. The accuracy of the models was evaluated by comparing the backbone atoms of the homology modeling and the X-ray template and measuring the root mean-square deviation (RMSD) between the backbone atoms of the homology modeling and the template after superposition. The RMSDs were 0.59, 0.56, 1.27, and 1.49 Å for the conformations OOP, OOC, POO, and PIO, respectively (Figure 4.3). The low RMSDs (0.55–1.49 Å, less than the threshold of 2 Å) indicates that these homology models are reliable.

In addition, the backbone structures of the homology models of GLUT1 were evaluated by the Ramachandran's plots assessment (Figure 4.4). The OOP model had 90%, 10%, and 0.50% of the residues, respectively, assigned as the “most favored”, “additionally allowed”, and “generously allowed” regions. Moreover, no residue was found in the “disallowed” region. The OOC model had 90%, 9%, and 1% in the three “allowed” regions, and only two residues (0.50%) were in the “disallowed” region (Tyr52 and Gln469). The POO model had had 79%, 16%, and 3% in the three “allowed” regions, and five residues (1.3%) were in the “disallowed” region (Val39, Ile128, Gln305, Tyr308, and Ser365), while the PIO had 78%, 18%, and 3% in the three “allowed” regions, and six residues (1.6%) were in the “disallowed” region (Leu115, Ile259, Tyr268, Val307, Tyr308, and Trp363). The residues in the disallowed regions are not involved in the glucose binding site. Thus, both the RMSD values and the Ramachandran's plots assessment confirm that these homology models of hGLUT1 should be useful for ligand docking.

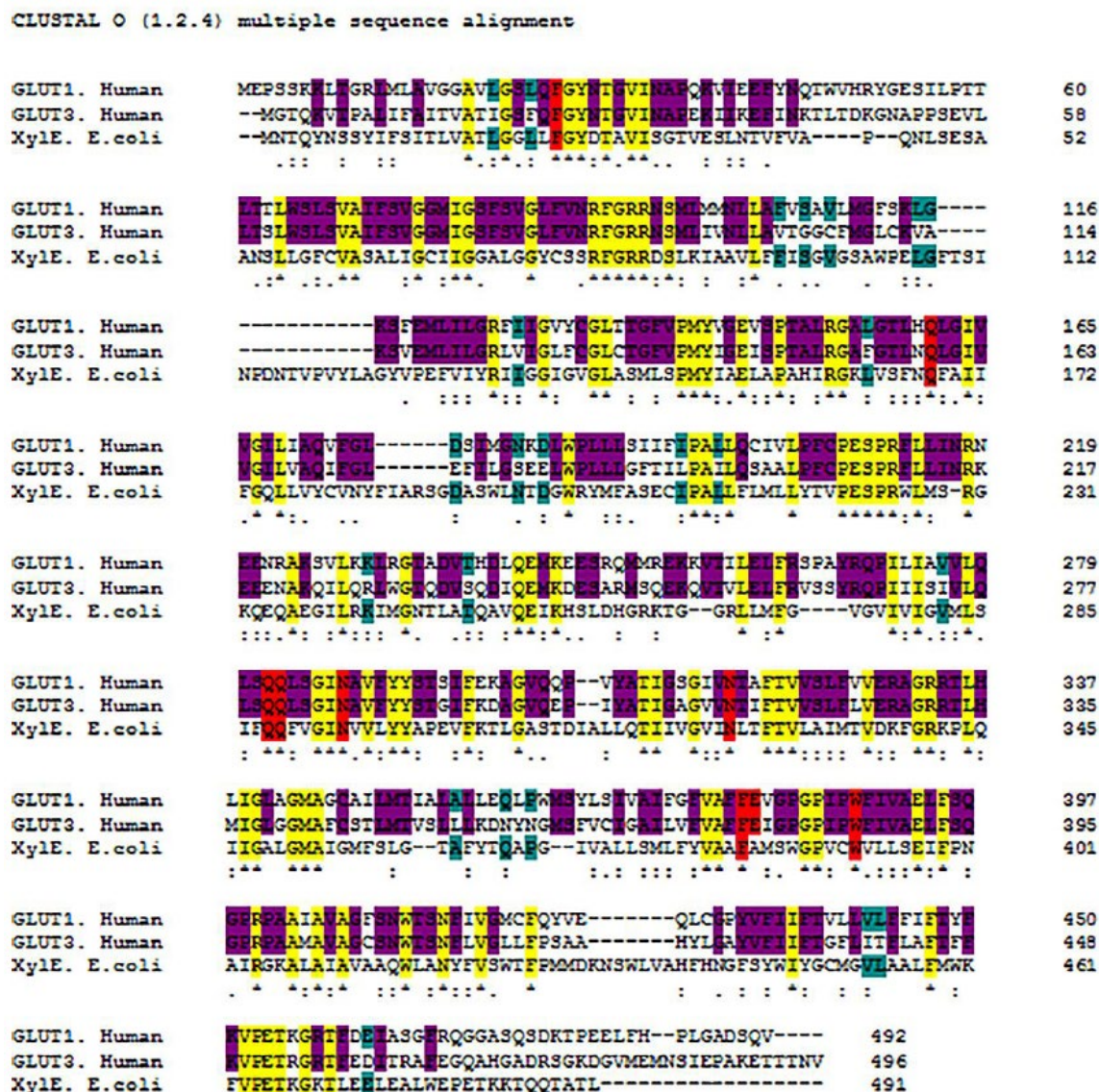


Figure 4. 2. Primary sequence alignment of GLUT1, GLUT3, and XylE: Invariant and highly conserved residues between GLUT1, GLUT3, and XylE are highlighted yellow; conserved residues between GLUT1 and GLUT3 are highlighted violet; conserved residues between GLUT1 and XylE are highlighted teal. The amino acid residues that are bonded to D-glucose are highlighted red. The human GLUT3 were used to build the homology modeling of OOP and OOC conformations, while bacterial XylE were used to build the homology modeling of POO and PIO conformations.

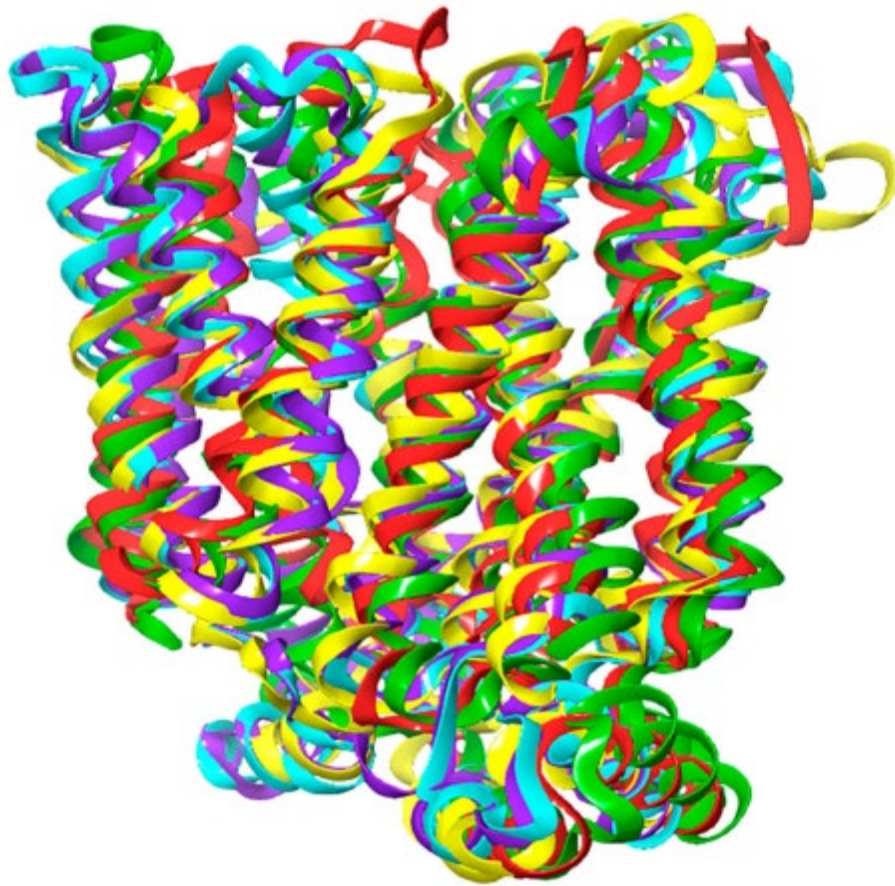


Figure 4. 3. An overview of working model of GLUT1: The function of GLUT1 depends on conformational change. The inward-open (IOP) conformation, green, was adopted from PDB ID: 5EQG; the outward-open (OOP) conformation, cyan, was constructed by homology modeling of PDB ID: 4ZWC; the partially outward occluded (POO) conformation, yellow, was constructed by homology modeling of PDB ID: 4GBZ; the outward-occluded (OOC) conformation, violet, was constructed by homology modeling of PDB ID: 4ZW9; the partially inward occluded (PIO) conformation, red, was constructed by homology modeling of PDB ID: 4JA3.

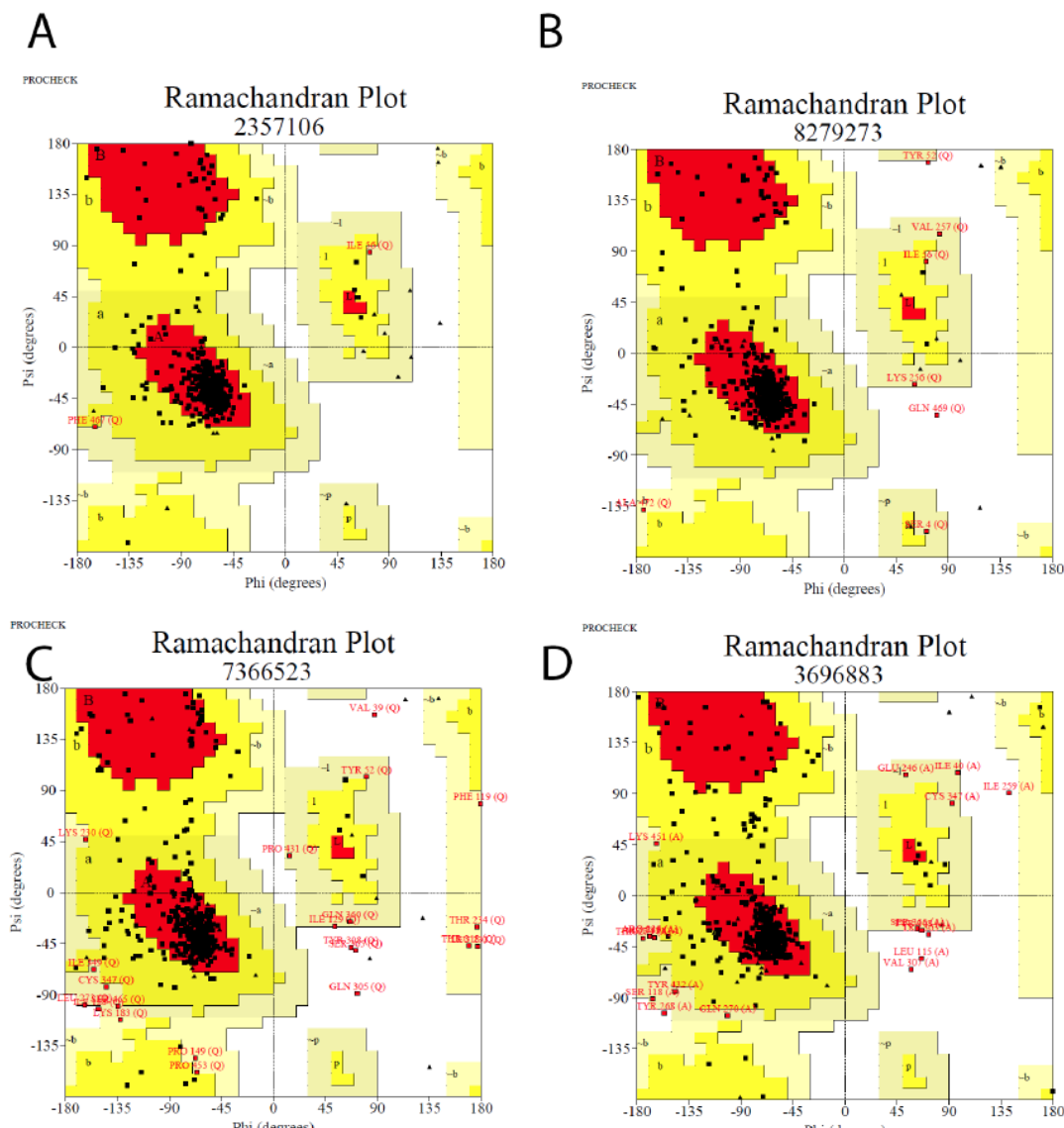


Figure 4. 4. The Ramachandran plots for the four homology models and the number of residues in the disallowed regions:(A) OOP conformation (4ZWC model: zero residues in disallowed regions); (B) OOC conformation (4ZW9 model: Only 2 out of 404 residues (0.5%) in the disallowed regions: Tyr52 and Gln469); (C) POO conformation (4GBZ model: 5 out of 398 residues (1.3%) in the disallowed regions: Val39, Ile128, Gln305, Tyr308, and Ser365); (D) PIO conformation (4JA3 model: 6 out of 383 residues (1.6%) in the disallowed regions: Leu115, Ile259, Tyr268, Val307, Tyr308, and Trp363).

4.2.2. Docking Scores and Validation:

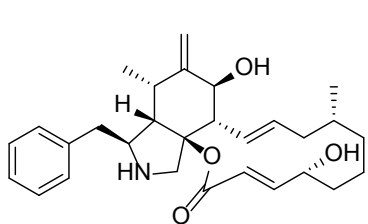
To identify amino acids that are essential for ligand binding, we performed docking studies with 44 GLUT1 inhibitors [32,36] (Figures 4.5). To evaluate the accuracy of the Glide Dock, we first assessed the similarities between the docked poses and original conformations in the crystal structures. The root mean square deviation (RMSD) between the docked poses and the native conformations found in the crystal structures is used to measure the effectiveness of a docking program. A pose with an RMSD $< 2.0 \text{ \AA}$ is considered to be good⁴⁶. The superposition of the Glide generated docked poses of ligands and the native conformation in the crystal structure (Figure 4.6) show that the Glide program accurately identified the native conformation and, thus, can be reliably used to identify the binding conformations of other ligands. The RMSD between two poses for 5RE in 5EQG, 5RF in 5EQH, 5RH in 5EQI, MAL in 4ZWC, BGC in 4GBZ, GLC in 4ZW9, and BGC in 4ZW9 were 1.62, 1.49, 1.09, 0.14, 0.61, 0.94, and 0.06 \AA , respectively. These data validate the accuracy of Glide Dock for this study.

The docking of GLUT1 inhibitors to the conformational models of GLUT1 (Table 4.1) reveal that Glide scores are close to the experimental free energies (ΔG_{exp}) where ΔG_{exp} was approximated as ($\Delta G_{\text{exp}} = RT \ln IC_{50}$) for the IOP conformation. In the IOP conformation, the difference between ΔG_{exp} and Glide scores for the majority of GLUT1 inhibitors was less than 2 kcal/mol. The mean errors ($\Delta \Delta G$) (Table 4.2) between ΔG_{exp} and Glide scores (ΔG_{pred}) was -0.97 kcal/mol , which is lower than ± 1.00 for the IOP conformation. The predicted docking scores for many compounds were very close to those obtained from the experiments. For instance, the $\Delta \Delta G$ for cytochalasin B was only 0.10 kcal/mol (Table 4.1). The $\Delta \Delta G$ for the IOP model was listed in Table 4.1. The $\Delta \Delta G$ for

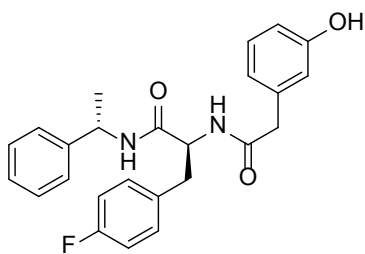
POO, OOP, and PIO were -1.37 , -1.44 , and -1.14 kcal/mol, respectively. The mean absolute error (MAE), which is the mean absolute value of $\Delta\Delta G$, was the lowest for the IOP conformation. The MAE for the IOP conformation was the lowest 1.45 kcal/mol, while the MAE for POO, OOP, and PIO was 1.75, 1.82, and 1.68 kcal/mol, respectively. In addition, the root mean square error (RMSE) (Table 4.2) for the IOP was the lowest at 1.79, whereas RMSE for POO, OOP, and PIO was 2.07, 2.05, and 1.92, respectively. Finally, there were no Glide scores from the OOC. In sum, these data suggest that the IOP is the most favorable conformation for ligand binding.

In addition to the statistical results between ΔG_{exp} and Glide scores, the enrichment factor (EF) is another very valuable approach to measure the accuracy of a docking program; the higher the EF, the more accurate the docking model⁴⁷. To evaluate the EF values, we obtained 508 drug-like molecules from the NCI database (Table 4.3) and docked these molecules along with GLUT1 inhibitors to all GLUT1 conformations. EF is the ratio between the percentage of active ligands in the particular subset and the percentage in the total database⁴⁷. We obtained the highest EF values for the IOP conformation (Table 4.4), further confirming that IOP is the preferred conformation for ligand binding since it recognizes the largest number of active inhibitors. We calculated the EFs based on the top 1%, 5%, or 10%; all three cases show that IOP has the best EFs. The OOP conformer and the PIO conformer also show good EF values, suggesting that ligands may be able to bind to these conformations as well. However, the partial outward open (POO) conformation had very low EF values. The EF for best case scenario, which all active molecules are identified in the top percentage poses, is 13.44. The EF of 10.45 in the IOP suggests that

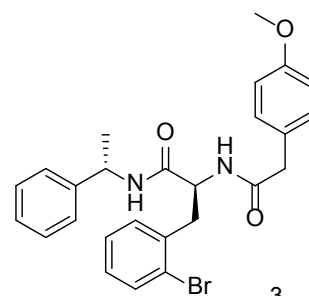
this model is the most ideal one among all studied conformations as the EF is the closest to the ideal EF.



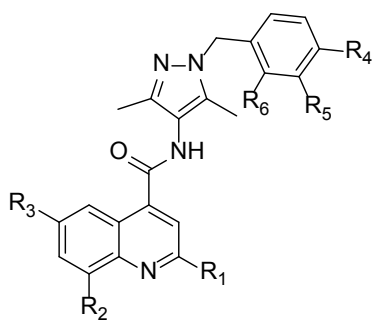
Cytochalasin B 1



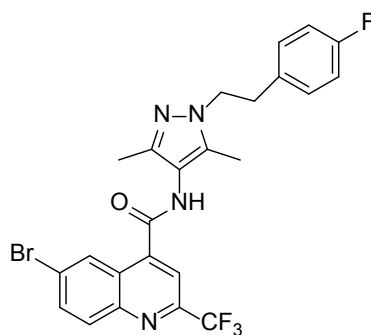
2



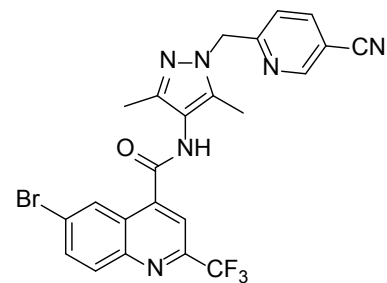
3



4 - 8

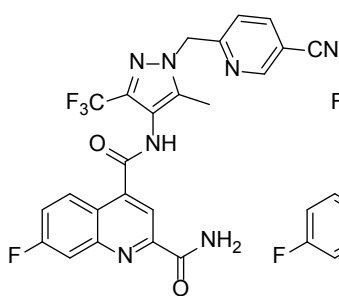


9

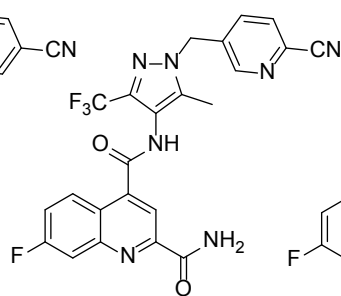


10

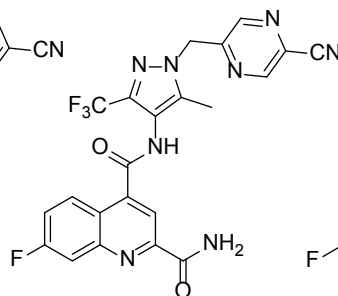
Compd	R ₁	R ₂	R ₃	R ₄	R ₅	R ₆
4		*-Me	*-Me	*-F	*-H	*-H
5	*-CF ₃	*-H	*-Br	*-F	*-H	*-H
6	*-CF ₃	*-H	*-Br	*-CN	*-H	*-H
7	*-CF ₃	*-H	*-Br	*-CN	*-F	*-H
8	*-CF ₃	*-H	*-Br	*-CN	*-H	*-F



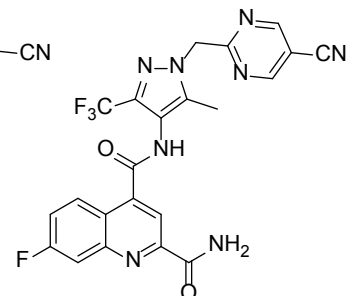
11



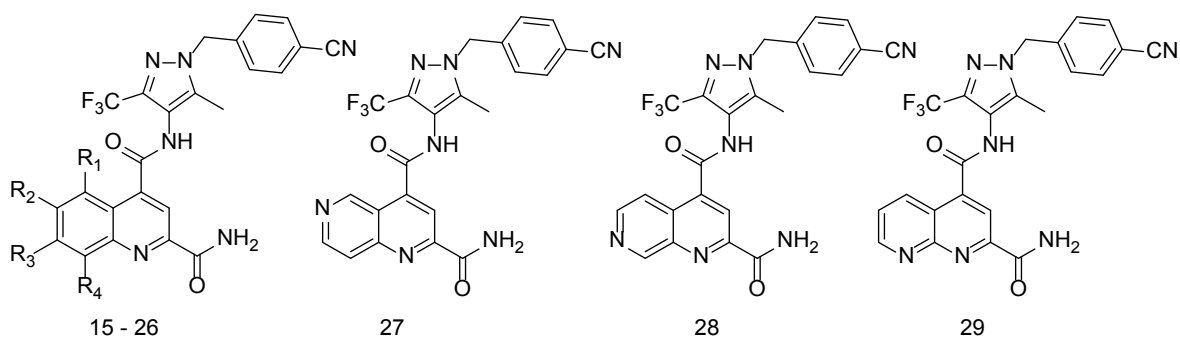
12



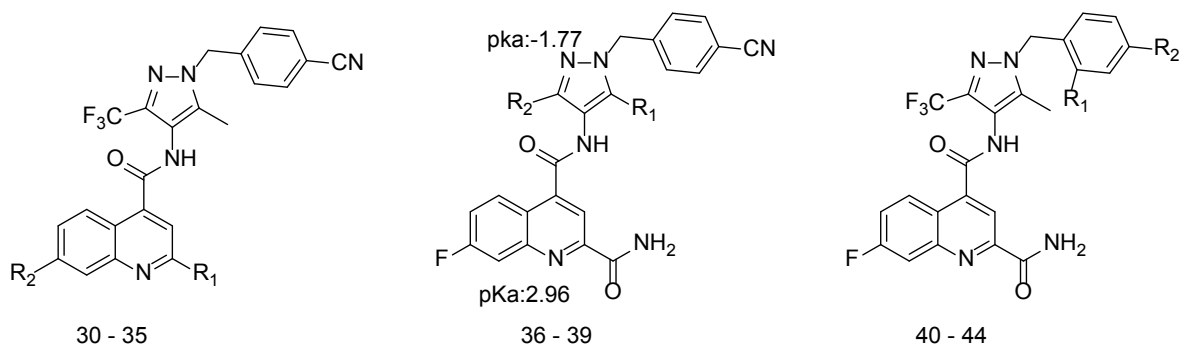
13



14



Compd	R ₁	R ₂	R ₃	R ₄	Compd	R ₁	R ₂	R ₃	R ₄
15	*-H	*-H	*-H	*-H	21	*-H	*-H	*-Me	*-H
16	*-F	*-H	*-H	*-H	22	*-H	*-H	*-OMe	*-H
17	*-H	*-F	*-H	*-H	23	*-H	*-H	*-H	*-F
18	*-H	*-Me	*-H	*-H	24	*-H	*-H	*-H	*-Cl
19	*-H	*-OMe	*-H	*-H	25	*-F	*-H	*-F	*-H
20	*-H	*-H	*-F	*-H	26	*-H	*-F	*-F	*-H



Compd	R ₁	R ₂	Compd	R ₁	R ₂
30		*-H	37	*-H	*-Me
31		*-H	38	*-Me	*-H
32		*-H	39	*-Me	
33		*-H	40	*-CN	*-H

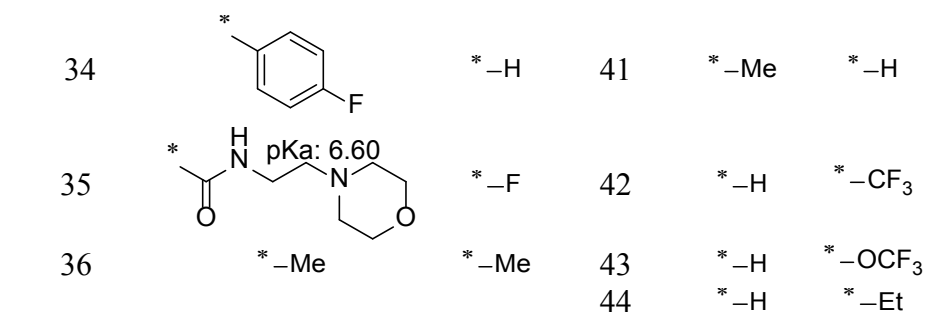


Figure 4. 5. Structures of GLUT1 inhibitors (30-44) used in docking studies.

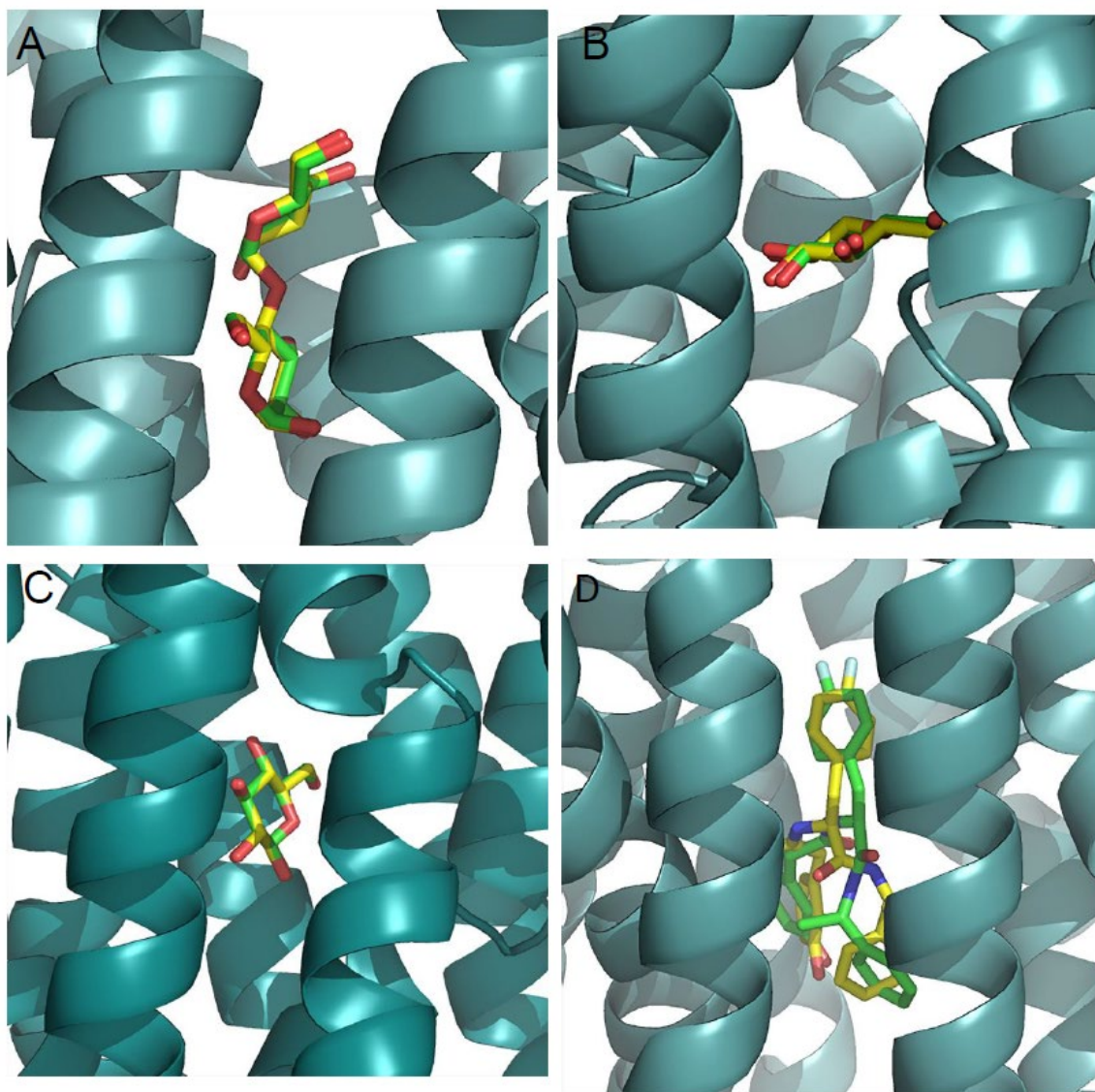


Figure 4. 6. The superposition of the Glide generated docked poses and the native conformation of ligand in the crystal structure: A) MAL in 4ZWC, B) BGC in 4GBZ, C) BGC in 4ZW9, D) 5RE in 5EQG. Color code: Yellow, the ligand in the crystal structure; green, the ligand from Glide generated poses. The RMSD between two poses for MAL in 4ZWC, BGC in 4GBZ, BGC in 4ZW9, and 5RE in 5EQG is 0.14, 0.61, 0.06, and 1.62 Å, respectively.

Table 4. 1. Glide scores (Kcal/mol) of GLUT1 inhibitors against different conformation models of GLUT1: 5EQG (IOP); HM_4GBZ (POO); HM_4ZWC (OOP); and HM_4JA3 (PIO).

Compd	IC ₅₀ (uM) ^a	ΔG_{exp} ^b	5EQG	HM_4GBZ	HM_4ZWC	HM_4JA3
1	0.11	-9.49	-9.39	NA ^c	-5.84	NA ^c
2	0.267	-8.97	-10.61	-11.63	-11.11	-10.53
3	0.14	-9.35	-11.54	-9.46	-10.26	-10.84
4	0.11	-9.49	-9.53	-9.05	-8.88	-6.64
5	0.006	-11.22	-9.39	-7.22	-7.71	-7.96
6	0.004	-11.46	-9.24	-7.45	-9.11	-8.23
7	0.003	-11.63	-9.45	-9.77	-10.23	-8.49
8	0.008	-11.05	-9.68	-9.61	-10.16	-8.35
9	0.087	-9.63	-9.43	-7.39	-8.75	-8.73
10	0.002	-11.87	-9.24	-8.83	-8.10	-8.17
11	0.004	-11.46	-10.62	-10.34	-9.01	-10.23
12	0.032	-10.22	-10.30	-9.93	-8.74	-10.12
13	0.005	-11.32	-10.96	-9.36	-9.18	-9.68
14	0.026	-10.35	-10.38	-8.99	-9.10	-9.42
15	0.006	-11.22	-9.49	-9.47	-9.17	-9.49
16	0.003	-11.63	-11.47	-10.22	-9.26	-9.34
17	0.005	-11.32	-9.34	-10.36	-9.51	-10.99
18	0.007	-11.12	-10.29	-10.88	-9.02	-9.32
19	0.0003	-12.99	-9.61	-10.91	-9.77	-10.78
20	0.002	-11.87	-9.70	-9.71	-9.51	-10.44
21	0.008	-11.05	-8.92	-10.95	-10.03	-9.78
22	0.024	-10.39	-9.52	-9.12	-9.72	-11.13
23	0.005	-11.32	-10.32	-10.24	-9.84	-10.00
24	0.003	-11.63	-10.34	-10.94	-9.96	-9.68
25	0.0005	-12.69	-11.37	-10.46	-9.04	-10.77
26	0.002	-11.87	-7.42	-10.11	-9.39	-11.14
27	0.014	-10.71	-10.82	-10.20	-10.56	-9.65

28	0.01	-10.91	-10.49	-9.20	-9.42	-9.88
29	0.045	-10.02	-9.33	-10.25	-9.61	-9.26
30	0.004	-11.46	-9.48	-10.02	-10.45	-10.28
31	0.76	-8.35	-9.12	-4.47	-9.53	-8.30
32	0.007	-11.12	-9.25	-9.83	-9.23	-10.18
33	0.074	-9.73	-9.54	-5.26	-10.13	-10.32
34	0.92	-8.23	-10.62	-9.99	-9.42	-10.60
35	0.34	-8.82	-11.77	-12.23	-11.43	-12.81
36	0.0009	-12.34	-9.02	-9.99	-9.18	-9.65
37	0.003	-11.63	-9.70	-9.75	-9.53	-8.38
38	0.007	-11.12	-8.89	-9.81	-8.92	-9.61
39	0.007	-11.12	-10.36	-9.83	-8.64	-9.40
40	0.003	-11.63	-9.45	-9.84	-10.10	-10.28
41	0.007	-11.12	-10.09	-8.71	-10.13	-9.73
42	0.009	-10.98	-11.28	-10.07	-10.32	-10.81
43	0.005	-11.32	-10.58	-9.91	-10.01	-9.84
44	0.0009	-12.34	-9.59	-9.20	-9.38	-10.89

Note: ^a The IC₅₀ were obtained from Reference 39, and 40. ^b ΔG_{exp} was calculated as $RT \ln IC_{50}$ where R: Universal gas constant (1.987 cal/mol.K), T: Temperature in Kelvin (298.15 K). ^c The ligand does not fit well to the generated Glide file.

Table 4. 2.The average of the mean errors between experimental free energy (ΔG_{exp}) and predicted free energy for different models: 5EQG (IOP); HM_4GBZ (POO); HM_4ZWC (OOP); and HM_4JA3 (PIO).

	5EQG (IOP)	4GBZ (POO)	4ZWC (OOP)	4JA3 (PIO)
$\Delta\Delta G$	-0.97	-1.37	-1.44	-1.16
MAE	1.45	1.75	1.82	1.66
RMSE	1.79	2.07	2.05	1.92

Table 4. 3. Glide scores of 508 drug-like molecules against the GLUT1 IOP conformation.

NCS Title	Glide Score	NCS Title	Glide Score	NCS Title	Glide Score	NCS Title	Glide Score
451	-3.873	76604	-4.336	194897	-5.433	611435	-8.255
1282	-6.413	76808	-7.643	195326	-6.453	611913	-10.207
1439	-4.227	76925	-7.133	201533	-7.244	613729	-8.14
1642	-5.464	77128	-5.198	202825	-5.252	615396	-7.67
1971	-7.39	77739	-7.642	203330	-5.558	615397	-8.353
3248	-2.655	79245	-8.839	204342	-6.704	617827	-4.404
3581	-9.254	79575	-6.506	204799	-9.066	618430	-8.198
3604	-6.474	81217	-5.357	205707	-7.787	618508	-9.099
3609	-3.837	81336	-4.566	207116	-5.409	619691	-9.732
4092	-2.982	81767	-6.761	208702	-6.595	620117	-6.249
4863	-6.921	82222	-8.339	208881	-3.392	620148	-9.922
5037	-3.623	86416	-7.947	211578	-8.428	620280	-8.225
5317	-5.354	92983	-4.829	212090	-7.858	622374	-7.742
5431	-3.497	93303	-7.837	212139	-6.878	622562	-7.489
6846	-8.354	93438	-6.207	213630	-8.539	623439	-5.991
7796	-9.607	93714	-5.258	215613	-6.592	623762	-7.567
8218	-5.058	93929	-5.088	216752	-7.675	623898	-7.348
8588	-8.165	95384	-5.466	217039	-3.418	626384	-8.544
9430	-4.876	95570	-6.671	220094	-5.586	626940	-7.37
9489	-4.749	95791	-6.404	220240	-4.614	630876	-7.396
10080	-5.552	96341	-8.957	222625	-5.57	631647	-4.989
10752	-8.41	96992	-7.229	222790	-4.028	633214	-5.674
11429	-6.697	97507	-2.741	226089	-5.275	634581	-4.59
13036	-8.21	98375	-5.546	229350	-4.7	634627	-7.156
13141	-5.575	100941	-6.797	229647	-5.245	636507	-9.912
13961	-4.936	102391	-7.71	231557	-4.931	636881	-7.444
13997	-5.003	102541	-4.347	236249	-6.968	637401	-7.348
14001	-6.007	103747	-4.501	241598	-7.575	641124	-7.748
15330	-5.14	105534	-7.356	243021	-7.968	641190	-8.224
15440	-6.291	106060	-8.192	244299	-2.431	641860	-7.262
16766	-10.046	106310	-6.252	245089	-4.55	644223	-9.246
16886	-4.84	107092	-6.443	245146	-7.174	645810	-7.249
17233	-3.73	107109	-4.602	248531	-9.012	645901	-8.09
17461	-5.956	107160	-8.707	249213	-4.935	646436	-7.012
17682	-4.041	108078	-6.405	250686	-10.463	646652	-7.907
17823	-4.747	108395	-7.277	251159	-6.049	647155	-8.86
19082	-4.604	108611	-7.299	260419	-6.255	647621	-7.581
19676	-5.691	109297	-6.869	264255	-9.231	648213	-7.361

19929	-5.156	110619	-6.644	264430	-4.989	648842	-9.067
20654	-4.884	110651	-9.085	265436	-7.42	649595	-5.748
21347	-7.813	110770	-7.359	267447	-6.956	650736	-7.849
21468	-4.848	111712	-8.327	268719	-4.982	652037	-7.732
21770	-6.202	111724	-5.616	270703	-6.266	652117	-7.327
21941	-5.01	112430	-6.638	271266	-5.934	652910	-7.9
22940	-8.785	113532	-5.241	276740	-8.007	652938	-9.281
23086	-6.681	114477	-5.964	278073	-5.953	653492	-5.888
23458	-7.639	114640	-6.082	283482	-7.285	653956	-7.227
23538	-4.636	115165	-8.206	284220	-5.503	654111	-4.627
23700	-4.658	115221	-4.203	284670	-6.757	655335	-7.327
24991	-4.78	115615	-6.806	286671	-7.312	657952	-7.786
25039	-6.275	115932	-6.911	286710	-7.136	657983	-7.574
26460	-3.62	116803	-3.909	287491	-8.624	658812	-8.309
26836	-7.015	117260	-6.192	287993	-4.439	659307	-8.055
26960	-5.55	117379	-4.896	289365	-6.377	660842	-6.791
27907	-8.106	118712	-7.416	290094	-10.025	661173	-6.658
28401	-7.327	119498	-5.081	290494	-8.608	661954	-7.626
29324	-7.836	119542	-5.498	291066	-5.726	662770	-5.732
29874	-5.403	120511	-5.572	291572	-8.339	664213	-9.352
30159	-6.362	122582	-7.64	293788	-4.928	665489	-8.854
30215	-4.025	122619	-2.924	294379	-4.106	666377	-7.761
32052	-8.323	123133	-3.17	294992	-8.329	666861	-7.5
32568	-8.177	123278	-4.729	297929	-6.375	669315	-9.568
33614	-7.738	123820	-6.011	299964	-9.223	671104	-9.276
33632	-4.201	124206	-8.455	300236	-4.443	671327	-7.92
33634	-5.652	124616	-5.677	300908	-5.744	671802	-8.209
33698	-4.559	125017	-8.328	301466	-2.996	672556	-6.313
35498	-6.365	125376	-5.984	305213	-7.513	675799	-8.283
36819	-10.133	125563	-8.905	306131	-7.985	676446	-8.728
37853	-5.397	125618	-7.725	306778	-5.384	677448	-9.409
41519	-6.725	126880	-7.123	308800	-7.223	677792	-9.071
41633	-6.033	128910	-4.525	312029	-6.553	679560	-5.866
41814	-6.735	131082	-6.077	312610	-7.416	679577	-4.884
42019	-5.812	131164	-5.144	319030	-7.34	683715	-4.869
42597	-6.194	131287	-5.344	332690	-6.458	686789	-5.412
42740	-5.45	132945	-6.831	338058	-7.571	687820	-8.18
43063	-6.254	134178	-8.908	338186	-4.371	687853	-8.375
43639	-4.168	135021	-7.466	338531	-8.441	688729	-7.174
44348	-4.783	135066	-8.671	338574	-5.474	689594	-5.103
45766	-4.564	135311	-5.919	338604	-5.329	690572	-5.547
47429	-5.592	137412	-5.275	338623	-6.875	691569	-7.634
48174	-5.181	137505	-4.964	338627	-6.405	691849	-8.709

CONTINUED

49499	-8.107	139207	-8.346	344016	-8.089	692611	-5.82
49745	-6.402	140053	-8.907	345395	-7.311	693633	-6.141
51876	-6.03	140382	-5.726	346098	-6.434	696124	-9.281
52216	-3.921	141876	-4.713	352267	-8.091	697931	-9.113
52479	-6.426	142200	-7.269	355186	-10.336	698074	-7.522
53077	-5.706	142555	-8.379	356130	-6.998	698559	-5.309
53284	-5.223	143308	-7.863	356486	-6.496	699123	-6.562
53466	-6.044	143989	-5.357	357566	-6.611	703459	-7.339
53806	-5.63	145881	-5.164	362252	-4.929	703889	-8.367
53880	-5.454	147640	-6.422	363847	-2.987	704117	-4.31
54427	-9.253	148291	-8.393	364027	-6.257	708438	-5.699
55495	-5.542	149692	-6.317	364095	-4.929	708967	-6.923
56629	-6.838	150016	-4.771	364720	-7.067	709508	-6.795
57381	-6.074	150158	-6.961	367101	-7.838	714085	-8.228
57543	-3.072	151034	-6.601	368255	-8.255	714378	-7.249
58322	-8.723	151087	-7.556	372636	-8.08	715654	-8.604
58812	-3.608	151259	-5.509	372663	-3.917	716023	-4.277
58894	-6.522	151736	-7.105	372778	-8.555	716062	-9.053
59022	-4.885	152426	-7.784	374153	-2.617	719712	-7.447
60443	-6.719	152647	-7.731	382808	-8.786	720995	-8.626
60806	-6.769	154776	-6.229	382958	-10.624	724571	-6.661
62525	-7.98	156773	-8.563	402506	-5.26	724869	-6.906
62992	-4.386	158180	-6.024	403474	-6.841	725149	-9.189
63031	-4.387	160062	-7.281	404215	-8.188	726399	-8.402
63486	-7.476	160173	-4.926	404221	-4.446	726406	-9.176
65372	-9.392	162174	-4.675	404935	-4.211	726719	-6.941
65988	-4.171	162275	-5.077	406312	-4.306	727512	-9.435
66471	-9.569	162289	-4.709	406401	-5.075	727978	-10.419
66524	-4.754	163853	-4.545	406476	-3.607	728240	-10.543
66596	-5.113	164081	-8.689	408503	-7.797	729188	-7.389
67195	-3.594	167493	-4.489	408859	-5.866	730571	-7.933
67458	-5.462	167911	-4.692	409231	-6.293	730774	-8.501
67470	-7.888	169683	-7.57	409518	-6.651	731659	-8.504
67854	-6.018	169879	-5.098	508388	-3.955	732842	-8.313
68482	-5.439	171178	-4.717	511710	-4.255	733410	-7.218
70306	-5.684	171545	-9.257	512733	-9.2	734148	-7.154
70656	-4.039	171619	-4.324	515544	-6.457	740535	-7.664
70958	-6.681	172291	-6.217	515547	-7.301	740617	-8.264
71385	-2.858	172636	-7.434	516423	-6.185	743490	-7.926
72069	-4.947	173085	-7.405	522167	-5.008	744263	-7.799
72797	-8.747	173346	-4.103	523371	-4.576	744479	-4.436
73945	-3.568	173353	-4.604	526972	-5.464	745068	-7.698
74632	-4.639	173742	-3.931	606256	-9.268	746579	-7.658

CONTINUED

75421	-4.902	179467	-11.576	608686	-7.499	748262	-8.274
75952	-11.169	179618	-4.76	608833	-6.896	748543	-7.607
76503	-6.905	185315	-6.97	610980	-7.464	748706	-8.022

Table 4. 4. The enrichment factors of docking scores for different conformations: The ideal enrichment factor (EF) in this case equals 13.44.

Model	EF (1%)	EF (5%)	EF (10%)
5EQG	10.45	8.51	7.76
4GBZ	4.24	3.30	4.63
4ZWC	8.35	8.05	7.06
4JA3	6.37	8.02	6.72

4.2.3. Binding Interaction of GLUT1 Inhibitors:

As the validity of Glide dock was confirmed, the protein–ligand interactions for the docked poses could then be identified. The homology model of the OOP reveals that one of glucose substructures of maltose forms five H-bonds with four polar residues of GLUT1: Gln161 (2 H-bonds), Gln282, Gln283, and Asn317. In the OOC, β -glucose forms five H-bonds with Gln161, Gln282, Gln283, Asn317, and Trp388. In POO, β -glucose and α -glucose form seven H-bonds with residues: Gln283 (3 H-bonds), Asn288 (2 H-bonds), Asn317, and Trp388. In the IOP conformation, the small molecules interact with Trp388. Our docking studies were in good agreement with the crystal structures of different conformations of GLUT1 (Figure 4.7).

Trp388 plays an important role in the access of GLUT1 between the OOP conformation and the IOP conformations^{32 48}. Mutation of Trp388 with Leu (W388L) evidently reduced the rate of conformation interchange, consequently decreasing the glucose influx activity⁴⁸. Therefore, an inhibitor that can bind with Trp388 is able to prevent the rotation of Trp388 into the binding site and inhibit glucose uptake. In addition, Trp412 and Phe379 play important roles for the glucose transport function of GLUT1^{49 50}. Therefore, Phe379, Trp388, and Trp412 have important roles in GLUT1 function and glucose uptake. We investigated the interacting residues for ligand binding in different conformations. The protein–ligand interactions between GLUT1 inhibitors and the four GLUT1 models are listed in Table 4.5. Table 4.5 shows that the majority of GLUT1 inhibitors form H-bonds with Trp388 and π – π stacking via residues Phe379 and Trp412 in the IOP conformation. The inhibitors are able to bind with Phe379, Trp388, and Trp412 once the GLUT1 is in the IOP conformation

because these residues are exposed to the IOP binding site (Figure 4.8). In the OOP and POO conformations, inhibitors do not interact with Trp388 because the indole ring of Trp388 in the OOP is unreachable⁴³². In the PIO conformation, inhibitors have H-bond interactions with Trp388, but are not able to interact with Phe379 and Trp412. To visualize the important binding residues that interact with ligands, we numerated the number of occurrences that such residues interacted with ligands and presented this frequency in Figure 4.9. Figure 4.9 shows that Trp388, Phe379, Glu380, and Trp412 are responsible for ligand-binding to the IOP conformation. Finally, no ligand is well fit to the OOC conformation in the grid generated in Glide.

In addition, Phe291 and Glu380, which are highly accessible in the binding site in the IOP conformation (Figure 4.8), may be important residues for ligand interactions, as illustrated in Figure 7. Many GLUT1 inhibitors form H-bonds with Glu380 and π - π stacking interactions with Phe291. Moreover, some ligands have interactions with Phe26 (π - π stacking) and His160 (H-bonds) of GLUT1 (Table 4.5 and Figure 4.9), suggesting a possible role for these two residues in GLUT1 binding. These residues may be future targets for site-directed mutagenesis to define their role in GLUT1 function and glucose uptake. In contrast, the number of ligand interactions with these residues is low in the OOP, POO, and PIO conformations.

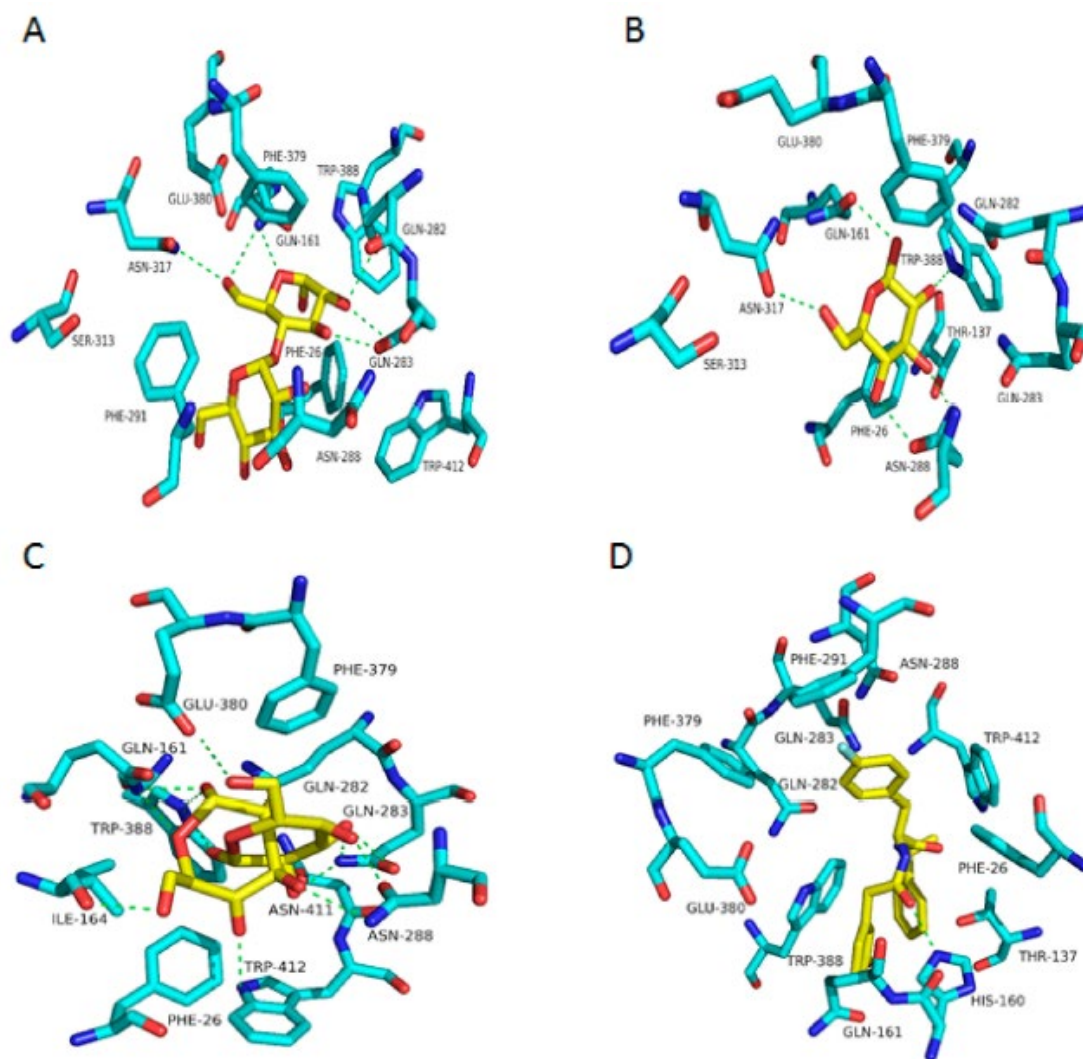


Figure 4. 7. Interactions between crystal ligands and their conformation: The H-bond interactions are shown as green dotted lines. (A) Interaction between MAL and GLUT1 in the OOP. (B) Interaction between BGC and GLUT1 in the POO. (C) Interaction between BGC, GLC, and GLUT1 in the OOC. (D) Interaction between 5RE and GLUT1 in the IOP.

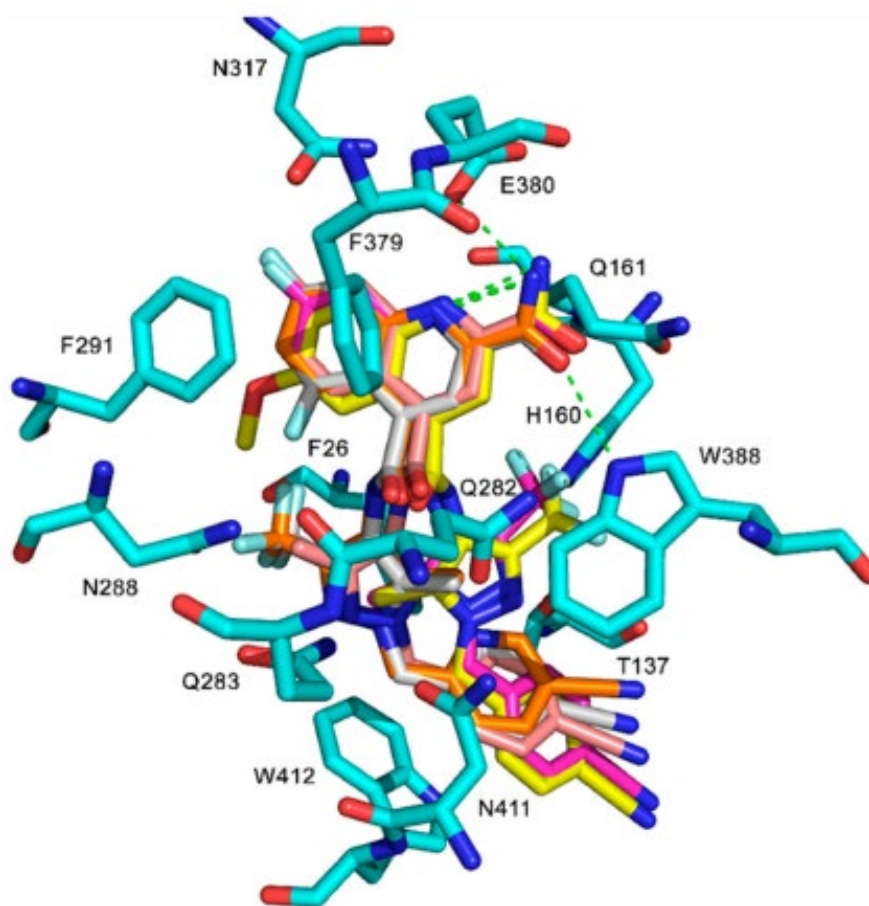


Figure 4. 8. Ligands interactions between 11, 19, 20, 25, and 37 and GLUT1: The H-bond interactions are shown as green dotted lines, and the π - π stacking interaction are shown as chocolate dotted lines. Ligands color code: 11: Carbons, gray; oxygen, red; nitrogen, blue; fluoro, cyan; 19: Carbons, yellow; oxygen, red; nitrogen, blue; fluoro, cyan; 20: Carbons, magenta; oxygen, red; nitrogen, blue; fluoro, cyan; 25: Carbons, orange; oxygen, red; nitrogen, blue; fluoro, cyan; 37: Carbons, tint; oxygen, red; nitrogen, blue; fluoro, cyan. Amino acids residues color codes: Carbons, green; oxygen, red; nitrogen, blue.

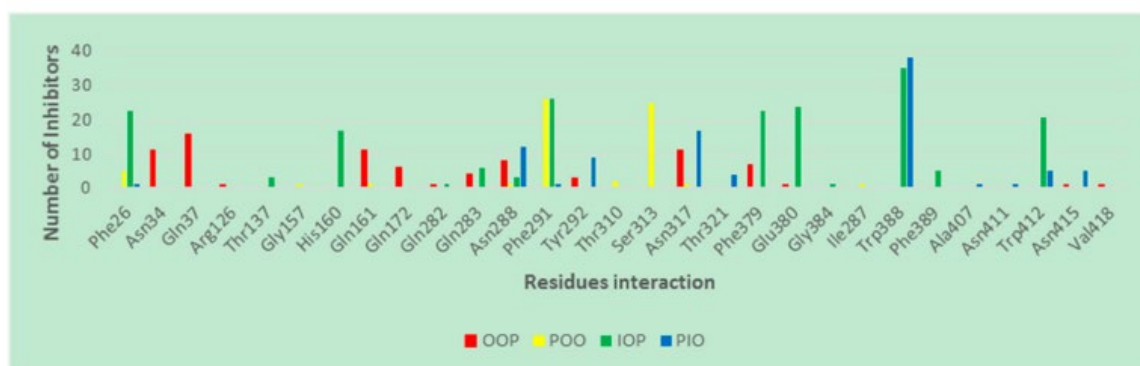


Figure 4. 9. Interacting residues of GLUT1 with inhibitors at different GLUT1 conformations.

Table 4. 5. Residues interaction with different GLUT1 inhibitors: 5EQG: Inward-open conformation; HM_4GBZ: Outward-partially occluded conformation; HM_4ZWC: Outward-open conformation; HM_4JA3: Inward-partially occluded conformation. NA: No interaction was found between the ligand and the GLUT1.

Compd	5EQG	HM_4GBZ	HM_4ZWC	HM_4JA3
1	Thr137, His160, Gln282, Gln283, Trp388, Gly384	NA ^a	Asn34, Gln283, Asn288, Asn415	NA ^a
2	His160, Trp388	Gly157, Gln161	Asn317, Phe379, Glu380	Asn288, Asn317, Asn411
3	His160, Trp388	Phe291, Asn317	Gln161	Trp388
4	Phe26, His160, Phe379, Trp388	Phe26, Phe291	NA ^a	Phe26, Trp388
5	Phe26, His160, Phe389	Phe26	NA ^a	Trp412
6	His160, Trp388	Phe291	NA ^a	Trp388, Trp412
7	His160, Phe379	Phe291	Gln161, Phe379	Trp388
8	His160, Phe379	Phe291	Gln161, Phe379	Trp388
9	Asn288, Trp388	Phe291	NA ^a	Phe291, Trp388, Trp412
10	His160, Phe389	Phe291	Asn34, Asn288	Trp388
11	Phe26, Phe291, Phe379, Glu380, Trp388, Trp412	Ser313	Gln37, Gln282, Gln283, Asn288	Asn288, Asn317, Thr321, Trp388
12	Glu380, Trp388, Trp412	Ser313	Gln37, Gln161	Tyr292, Trp388
13	Phe26, Phe291, Phe379, Glu380, Trp388, Trp412	Ser313	Gln161, Gln172	Tyr292, Trp388
14	Phe26, Phe291, Phe379, Glu380, Trp388, Trp412	Ser313	Gln161, Gln172	Asn288, Asn317, Trp388
15	Phe379, Glu380, Trp388, Trp412	Ser313	Gln37	Trp388, Trp412
16	Phe26, Phe291, Phe379, Glu380, Trp388, Trp412	Ser313	Asn34, Gln37, Gln161, Tyr292	Asn288, Trp388
17	Phe26, Phe379, Glu380, Trp388, Trp412	Ser313	Tyr292, Val418	Trp388, Asn415
18	Phe26, Phe291, Phe379, Glu380, Trp388, Trp412	Ser313	Gln172, Asn288	Tyr292, Trp388
19	Phe26, Phe379, Glu380, Trp388, Trp412	Phe291, Ser313	Gln37	Tyr292, Trp388, Asn415
20	Phe379, Glu380, Trp388, Trp412	Ser313	Gln37, Arg126	Trp388, Asn415
21	Phe26, His160, Trp388, Phe389	Phe291	Asn34, Asn317	Asn288, Asn317, Trp388
22	Phe26, Trp388	Ser313	Asn34, Asn317	Tyr292, Trp388, Asn415

23	Phe26, Phe291, Phe379, Glu380, Trp388, Trp412	Ser313	Asn317	Tyr292, Trp388
24	Glu380, Trp388	Phe26, Ser313	Gln37, Asn317	Asn288, Trp388
25	Phe26, Phe291, Phe379, Glu380, Trp388, Trp412	Ile287, Phe291	Gln37, Gln283	Asn317, Trp388
26	Phe26, Phe379, Glu380, Trp388, Trp412	NA ^a	Gln172, Asn288	Asn317, Trp388, Asn415
27	Phe26, Phe291, Phe379, Glu380, Trp388, Trp412	Thr310, Ser313	Asn317	Asn288, Trp388
28	Phe26, Phe291, Phe379, Glu380, Trp388, Trp412	Thr310, Ser313	Asn317	Tyr292, Trp388
29	Phe26, Phe379, Glu380, Trp388, Trp412	Ser313	Gln37, Gln161, Asn317, Phe379	NA ^a
30	His160, Phe389	Ser313	Asn34	Asn317
31	Phe26, His160	Phe291	Gln161, Asn288, Phe379	Trp388, Trp412
32	Phe26, His160, Trp388	Phe291	Gln37, Gln161, Asn288, Phe379	Asn288, Asn317, Trp388
33	His160, Trp388	Phe291	Gln37, Tyr292, Asn317	Asn317, Trp388
34	Phe26, His160, Trp388, Phe389	Phe26	NA ^a	Asn317, Trp388
35	Phe379, Glu380, Trp388, Trp412	Ser313	Asn34, Gln37, Asn317	Asn288, Asn317, Trp388
36	Phe379, Glu380, Trp388	Ser313	Gln37	Asn288, Asn317, Trp388
37	Phe26, Phe291, Phe379, Glu380, Trp388, Trp412	Phe291, Ser313	Gln37, Gln161, Phe379	Tyr292, Trp388
38	Phe291, Phe379, Glu380, Trp388	Ser313	Asn34, Gln172	Tyr292, Phe379, Trp388
39	His160, Gln283, Asn288	Ser313	Gln283	Ala407
40	Ser80, Thr137, Asn288	NA ^a	Asn34, Asn288, Asn317, Asn415	Asn317, Glu380, Trp388
41	Phe26, Thr137, His160	Phe26, Asn288	Asn34, Gln172	Asn317, Trp388
42	Glu380, Trp388, Trp412	Ser313	Gln37	Asn288, Asn317, Thr321, Trp388
43	Phe379, Glu380, Trp388, Trp412	Ser313	Gln37	Asn288, Asn317, Thr321, Trp388
44	Phe26, Glu380, Trp388, Trp412	Ser313	Asn34	Asn317, Thr321, Trp388

^aNA: No interaction were found between the ligand and the GLUT1.

The contact interaction map for the very potent compound 19 identifies residues that may be exposed selectively in the IOP conformation (Figure 4.10). In our docking study, the interactions surrounding inhibitors for the different conformations of GLUT1 are dissimilar. The obvious distinction among the different GLUT1 conformations is the rotation of Trp388 around the binding site. In the IOP conformation, Trp388 is close to the ligands and more likely to interact and form H-bonds. In addition, Phe379 and Trp412 in the IOP conformation are readily accessible for ligand interactions. In contrast, Phe379, Trp388, and Trp412 in the OOP and POO conformations are away from the binding site and, thus, unable to participate in ligand binding interactions. Trp388 in the PIO conformation almost starts to drift away from the binding site whereas Phe379 and Trp412 are far from the binding site. In our docking study, the contact interaction map in the IOP conformation showed that complex of transmembrane helices (TMs) TM5, TM7, TM10, and TM11 surround the ligand while in the IPO conformation the ligand is mostly surrounded by TM7, TM10, and TM11. In contrast, the ligand is bounded by TM1, TM5, and TM7 in the OOP conformation and TM5, TM7, TM8, and TM10 in the OOC conformation (Figure 4.10).

Moreover, the contact interaction of the IOP conformation reveals hydrophobic and polar residues in the binding site sharing hydrogen bonds and π - π stacking with the inhibitor. Furthermore, the TM10 is exposed in the active site and can interact with inhibitors for binding in the IOP conformation. This explains why inhibitors interact with Phe379, Trp388, and Trp412 mainly in IOP conformation, and this provides a rational clarification that the IOP conformation is favorable for productive binding interactions.

Figure 4. 10. Molecular contact map between 19 and GLUT1 in different conformations: The H-bond interactions are shown as green dotted lines. (A) The OOP conformation. (B) The POO conformation. (C) The IOP conformation. (D) The PIO conformation.

The electrostatic map of GLUT1 reveals that the most prominent difference between the various protein conformations lies in Trp388; the nitrogen atom of indole ring of Trp388 is located toward the binding site and functions as an H-bond donor to an inhibitor in the IOP conformation. The carboxyl group of residue Glu380 serves as H-bond donor to the amide functional group of compound 19 (Figure 4.11) whereas these two H-bonds are absent in other conformations. The Trp388 in the PIO conformation mostly starts to flip out the binding site, and this makes Trp388 less likely to form H-bond with the ligands. However, the Trp388 in the OOP and POO conformations is distant and unlikely to interact with inhibitors. This suggests that the indole ring of Trp388 is important for IOP selective binding. In addition, in the IOP conformation, Phe291, Phe379, Glu380, and Trp412 play important roles in ligand binding by forming π - π stacking and favorable H-bond interactions with inhibitors. We conclude that inhibitors interact with Trp388 and Glu380 via H-bonds, and with Phe291, Phe379, and Trp412 by π - π stacking in the IOP conformation.

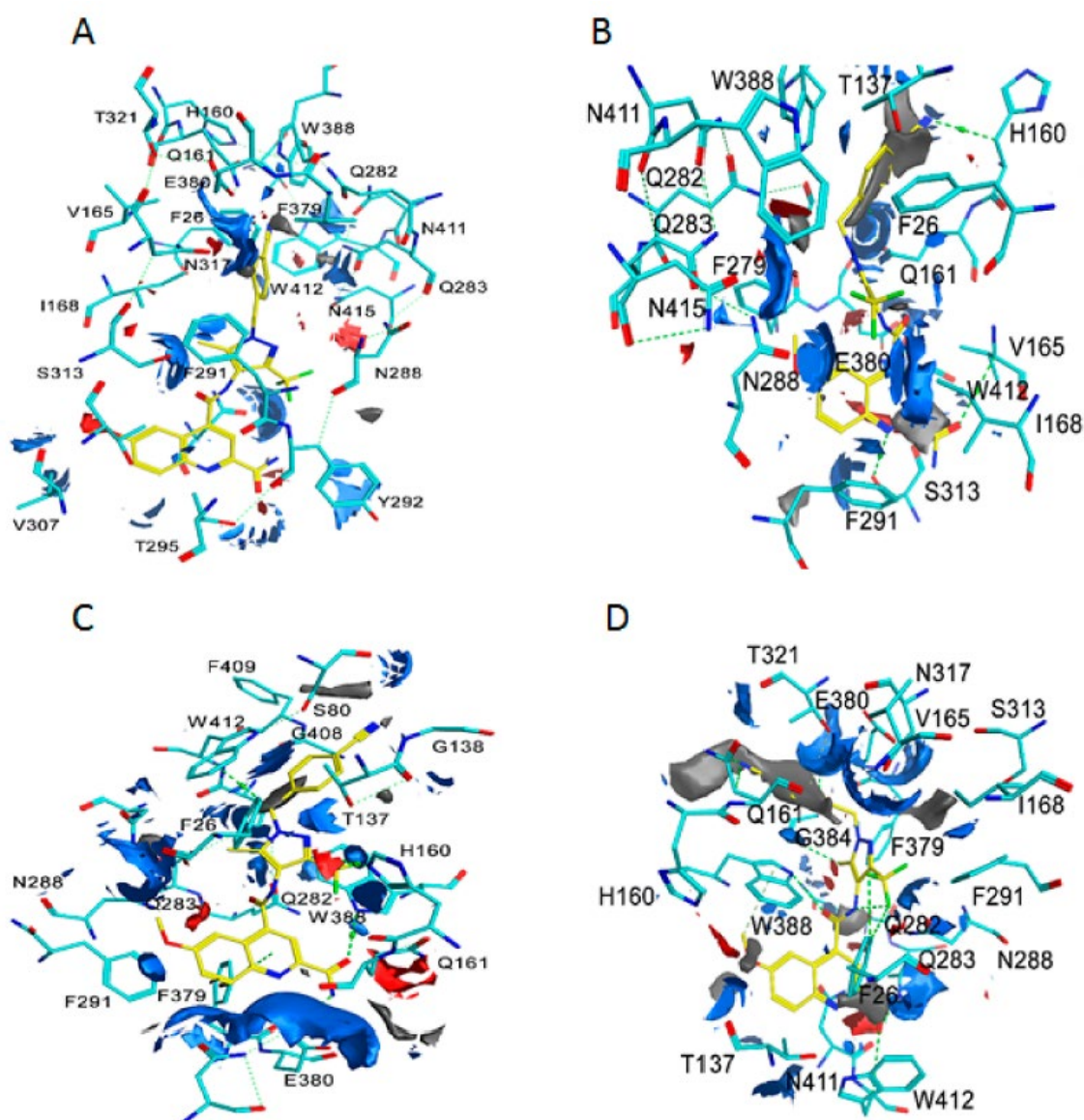


Figure 4. 11. Electrostatic map between 19 and GLUT1 in different conformations: The H-bond interactions are shown as green dotted blue. (A) The OOP conformation. (B) The POO conformation. (C) The IOP conformation. (D) The PIO conformation.

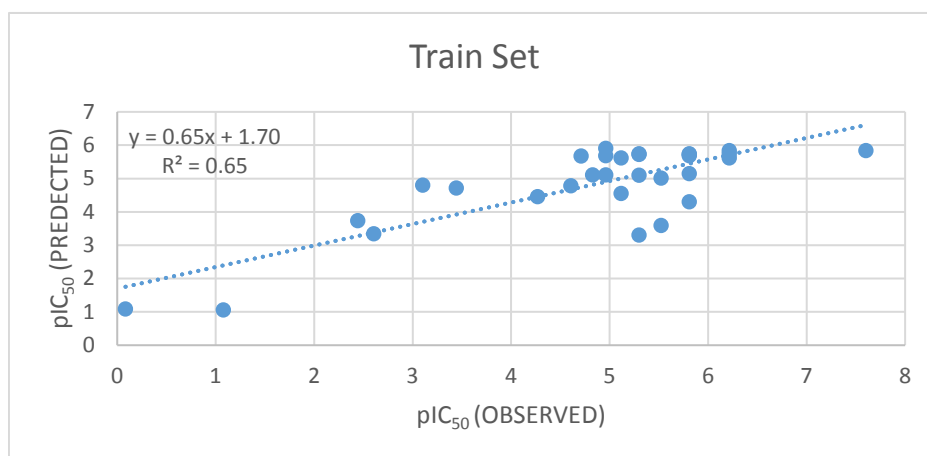
4.2.4. QSAR Model of GLUT1 Inhibitors:

To assess what properties of a ligand are required for potent binding to GLUT1, we applied QSAR analysis to the (1H-pyrazol-4-yl)quinoline inhibitors. We randomly divided 41 inhibitors into a training set of 30 molecules and a test set of 11 inhibitors. We identified partition coefficient (logP) and the steric factor SMR (molecular refractivity, a description of the volume, or size of a compound) to be important for ligand binding (Equation 1).

$$\text{pIC}_{50} = -0.42 \cdot \log P^2 + 2.86 \cdot \log P - 1.47 \cdot \text{SMR} + 18.79 \quad (1)$$

Equation 1 indicates that the inhibitory activity (pIC_{50} , more potent compounds have smaller IC_{50} s, larger $-\log \text{IC}_{50}$, i.e., larger pIC_{50} means more potent compound.) is negatively related to SMR and positively related to $\log P$ before it reaches an optimal $\log P$ ($\log P_{\text{opt}} = 3.75$). This suggests that decreasing the size of molecules while maintaining a $\log P$ close to 3.75 would likely improve Glut1 inhibitory potency. The Pearson's correlation (Pearson R) for training set (0.80) and test set (0.89) are high, and the R^2 values are high for the training set (0.65) and test set (0.80) which Equation 1 results in a predictive linear relationship between the predicted pIC_{50} and the experimental pIC_{50} (Figure 4.12). The mean absolute error (MAE) and the root-mean-square errors (RMSE) in training and test sets was less than two units (Table 4.6). Hence, the QSAR model should be useful for GLUT1 inhibitor optimization.

A



B

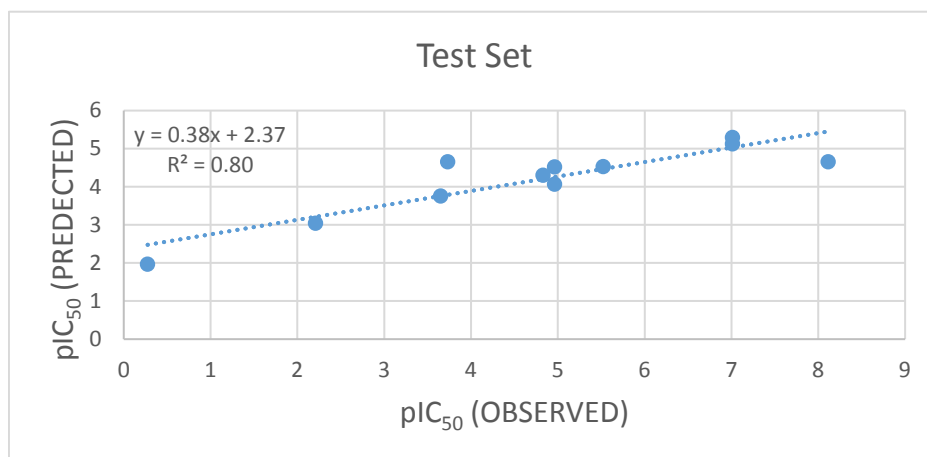


Figure 4. 12. Plots of the predicted versus observed activities pIC₅₀: A) Train set. B) Test Set.

Table 4. 6. The average magnitude of the errors of QSAR model.

	Train Set	Test Set
Pearson R	0.80	0.89
Correlation R²	0.65	0.80
MAE	0.72	1.22
RMSE	0.93	1.55

4.3. Conclusions:

In summary, protein–ligand dockings on different GLUT1 conformations suggest three significant outcomes: First, the docking scores suggested that the IOP conformation would be preferred for ligand binding. Besides, the MAE and RMSE for each conformation in comparison to experimental observations IC₅₀ of ligands also confirm this conclusion. Second, enrichment factor (EF) calculation from docking studies further confirms that the Glide dock program is able to distinguish the real inhibitors from drug-like molecules with best results in the IOP conformation. Third, residues Trp388, Glu380, Phe379, and Trp412 are important for the IOP conformation selective binding. Taken together, all these results support the conclusion that the IOP conformation is the most recognized conformation for ligand interaction and, thus, should be used for future molecule design targeting GLUT1.

4.4. Materials and Methods:

Only wild type (WT)-human GLUT1 (hGLUT1) inward-open (IOP) conformation has been resolved in X-ray crystal structures (PDB: 4PYP, 5EQG, 5EQH, and 5EQI)^{5 32}. For other unavailable human model proteins, we used the following homology modeling method to build various types of conformations. Several atoms structures of GLUTs have been resolved with different conformational states and/or different subtypes. Bacterial GLUTs homologous such as the d-xylose:H1 symporter from *Escherichia coli* (Xyle) in partial outward occluded (POO) conformation (PDB: 4GBY, 4GBZ, and 4GC0)⁴³; and partial inward occluded (PIO) conformations (PDB: 4JA3)⁴⁴; and the GLUT1 homologs of the lactose permease of *Escherichia coli* (LacY)⁵¹, and the glucose:H1 symporter from *Staphylococcus epidermidis* (GlcP)⁵². The hGLUT3 outward-open (OOP) and outward-occluded (OOC) conformations were identified with X-ray structures with PDB IDs of 4ZWC and 4ZW9, respectively⁴. The essential amino acids for the interacting with glucose are invariant between Xyle and GLUT1⁴³. Therefore, the hGLUT3 and the Xyle are GLUT1 homologs and they can be an appropriate template to build respective conformational states of hGLUT1.

4.3.1. Homology Modeling and Preparation of Model Proteins:

We used five structures of several conformations for GLUT1 for docking studies. For the IOP conformation, we downloaded and utilized the X-ray crystal structures of hGLUT1 (PDB ID:5EQG), which bound to phenylalanine amide compound (5RE)³² from the RCSB Protein Data Bank at <http://www.rcsb.org/pdb/>. No hGLUT1 X-ray structures have been reported yet for the OOP, POO, OOC, and PIO conformations. Thus, homology

model techniques were employed. Strong homology was identified between hGLUT3 and hGLUT1, and Xyle and hGLUT1 by ProBiS-CHARMMing⁵³. Structural alignment between these three proteins using the Clustalo program⁵⁴ (Version: 1.2.4) further confirmed the structural homology between them. The following protein templates were used to build different conformational states: hGLUT3 (PDB ID: 4ZW9, and 4ZWC)⁴ for the OOC and OOP conformations; Xyle (PDB ID: 4GBZ, and 4JA3)^{43 44} for the POO and PIO conformations. The ligand (β -NG) was adopted from (PDB ID: 4PYP)⁵ as a ligand for 4JA3 homology model. There are four regions of missing residues in the crystal structure of 4JA3: Region 1 (Lys265–Val275), region 2 (Phe304–Ala309), region 3 (Ile398–Lys406), and region 4 (Trp434–Phe439). The missing residues were constructed by using loop modeler on MOE [55] within root mean square deviation (RMSD) limit = 0.5 Å. The template for region 1 and region 3 was selected from (PDB ID: 3TZY.A)⁵⁶ and (PDB ID: 3RE4.A)⁵⁷, respectively. The templates for region 2 and region 4 were built by de novo method. The rebuilt residues that were missing and its surrounding residues underwent energy minimization to minimize steric repulsion. In addition, all these protein structures were subjected to automated structure preparation to fix issues found in crystallographic structure such as replacing missing protein sections, optimization of the hydrogen bonding network, and allowing protonation be assigned to charged residues and allowing the flipping side chains of Asn, Gln, His in MOE to maximize H-bond interactions. Also, they were subjected to energy minimization using the Amber14:EHT⁵⁸ force field in MOE, followed by protein preparation using the Protein Preparation Wizard in the Schrödinger software to allow the side-chain of residues of Asn and Gln to move to make the most favorable H-bond interactions. Then, they were subjected to energy minimization with

protein backbone by using the OPLS3 force field in the MacroModel module in the Maestro 11.2⁵⁹. The stereochemical quality of homology modeling was evaluated by the Ramachandran's plot assessment. The Ramachandran's plot assessment was measured Procheck⁶⁰.

4.3.2. Ligands Sources, Preparation, and Docking:

The small molecules (Figures 2–5) were built using MOE build panel and subjected to energy minimization using the MMFF94x force field in MOE using the MMFF force field partial charges. In addition, they were minimized by using the OPLS3 force field of the MacroModel program using the OPLS3 force field partial charges. All ligands were subject to pKa calculations using the Epik program in the Schrödinger software. The Epik calculations in the Maestro 11.2 showed that the pKa of all nitrogen atoms in these ligands are less than 7, suggesting that under the pH = 7 condition, all nitrogen shall remain deprotonated, i.e., neutral. A database of 260,071 ligands was taken from the National Cancer Institute database⁶¹ and further filtered by the logP ($\log P < 5$), and molecular weight ($MW < 500$) set by the Lipinski's rule of five (RO5)⁶². To expedite the docking and to define enrich factors, we randomly selected 508 drug-like molecules from this database after the filtration of RO5. These 508 molecules were minimized using the OPLS3 force field and the OPLS3 partial charges using the MacroModel program.

Commonly used software for ligand-protein docking include the Surflex docking module in Sybyl^{63 64}, and the Schrödinger Glide Dock program^{64 65}. In this study for ligand docking to GLUT1, we used Glide Dock in the Maestro 11.2 with the different conformations of GLUT1 (5EQG, HM_4ZW9, HM_4ZWC, HM_4GBZ, and HM_4JA3) as target proteins. First, crystallographic water and 1-Oleoyl-R-glycerol (OLC) molecules

were deleted from 4ZW9, 4ZWC, and 4GBZ. Hydrogen atoms were added to both the protein and the ligand. Then, five grid files for 5EQG, 4ZW9, 4ZWC, 4GBZ, and 4JA3 were created by the Glide Grid Generation panel [59] with the bound ligands as the centroid of the protein binding pocket. The site of the bound ligands in the crystal structure 5EQG was defined as the centroid; and for the homology models, all four homology models were structurally aligned to 5EQG and, thus, the 5EQG-bound ligand was adopted as bound ligand for those four homology models and used as a centroid to define binding pockets for those four homology models. Then, all GLUT1 inhibitors were docked with the precision and ligand sampling were set to extra-precision (XP) method to generate each of the five grid files. All other parameters were used as defaults. In addition, 508 drug-like molecules were also docked to the different conformations of GLUT1 (5EQG, 4ZW9, 4ZWC, 4GBZ, and 4JA3). The binding affinity of the various conformation of GLUT1/ligand complexes was evaluated by the Glide scores. The protein/ligand interactions and contact interaction were created by using the Maestro 11.2. The electrostatic map was generated by using the MOE. The frequency of residues interacting with ligands was made using Excel.

4.3.3. QSAR Model of GLUT1 Inhibitors:

To create the physicochemical factors, we constructed the 3D models of all molecules in MOE. The physicochemical parameters such as the logarithm of partition coefficient (logP), and structure molar refractivity (SMR) were calculated by using MOE. The activity data were established as $\text{pIC}_{50} = -\log \text{IC}_{50}$. Subsequently, all physicochemical parameters being assigned, all compounds were divided into a training set and a test set after all physicochemical parameters being generated. Correlations

between the physicochemical parameters and the pIC₅₀ were calculated using the Partial Least Squares Fit (PLS) method⁶⁶. To examine the QSAR models, the resulting QSAR models from the train set were employed to predict the activity data of the molecules in the test set.

References:

1. Mueckler, M.; Thorens, B. The SLC2 (GLUT) family of membrane transporters. *Mol. Asp. Med.* 2013, 34, 121–138.
2. Pao, S.S.; Paulsen, I.T.; Saier, M.H., Jr. Major facilitator superfamily. *Microbiol. Mol. Biol. Rev.* 1998, 62, 1–34.
3. Yan, N. Structural advances for the major facilitator superfamily (MFS) transporters. *Trends Biochem. Sci.* 2013, 38, 151–159.
4. Deng, D.; Sun, P.; Yan, C.; Ke, M.; Jiang, X.; Xiong, L.; Ren, W.; Hirata, K.; Yamamoto, M.; Fan, S.; et al. Molecular basis of ligand recognition and transport by glucose transporters. *Nature* 2015, 526, 391–396.
5. Deng, D.; Xu, C.; Sun, P.; Wu, J.; Yan, C.; Hu, M.; Yan, N. Crystal structure of the human glucose transporter GLUT1. *Nature* 2014, 510, 121–125.
6. Rumsey, S.C.; Kwon, O.; Xu, G.W.; Burant, C.F.; Simpson, I.; Levine, M. Glucose transporter isoforms GLUT1 and GLUT3 transport dehydroascorbic acid. *J. Biol. Chem.* 1997, 272, 18982–18989.
7. Ung, P.M.; Song, W.; Cheng, L.; Zhao, X.; Hu, H.; Chen, L.; Schlessinger, A. Inhibitor Discovery for the Human GLUT1 from Homology Modeling and Virtual Screening. *ACS Chem. Biol.* 2016, 11, 1908–1916.
8. Zhao, F.Q.; Keating, A.F. Functional properties and genomics of glucose transporters. *Curr. Genom.* 2007, 8, 113–128.

9. Warburg, O.; Wind, F.; Negelein, E. The metabolism of tumors in the body. *J. Gen. Physiol.* 1927, 8, 519–530.
10. Hanahan, D.; Weinberg, R.A. Hallmarks of cancer: The next generation. *Cell.* 2011, 144, 646–674.
11. Barron, C.C.; Bilan, P.J.; Tsakiridis, T.; Tsiani, E. Facilitative glucose transporters: Implications for cancer detection, prognosis and treatment. *Metabolism.* 2015, 65, 124–139.
12. Nishioka, T.; Oda, Y.; Seino, Y.; Yamamoto, T.; Inagaki, N.; Yano, H.; Imura, H.; Shigemoto, R.; Kikuchi, H. Distribution of the glucose transporters in human brain tumors. *Cancer Res.* 1992, 52, 3972–3979.
13. Brown, R.S.; Wahl, R.L. Overexpression of Glut-1 glucose transporter in human breast cancer. An immunohistochemical study. *Cancer.* 1993, 72, 2979–2985.
14. Sasaki, H.; Shitara, M.; Yokota, K.; Hikosaka, Y.; Moriyama, S.; Yano, M.; Fujii, Y. Overexpression of GLUT1 correlates with kras mutations in lung carcinomas. *Mol. Med. Rep.* 2012, 5, 599–602.
15. Nagase, Y.; Takata, K.; Moriyama, N.; Aso, Y.; Murakami, T.; Hirano, H. Immunohistochemical localization of glucose transporters in human renal cell carcinoma. *J. Urol.* 1995, 153, 798–801.
16. Cai, Y.; Zhai, J.J.; Feng, B.B.; Duan, X.Z.; He, X.J. Expression of glucose transporter protein 1 and p63 in serous ovarian tumor. *J. Obstet. Gynaecol. Res.* 2014, 40, 1925–1930.

17. Reinicke, K.; Sotomayor, P.; Cisterna, P.; Delgado, C.; Nualart, F.; Godoy, A. Cellular distribution of Glut-1 and Glut-5 in benign and malignant human prostate tissue. *J. Cell. Biochem.* 2012, 113, 553–562.
18. Shen, Y.; Arbman, G.; Olsson, B.; Sun, X.F. Overexpression of GLUT1 in colorectal cancer is independently associated with poor prognosis. *Int. J. Biol. Markers.* 2011, 26, 166–172.
19. Sheu, J.J.; Guan, B.; Tsai, F.J.; Hsiao, E.Y.-T.; Chen, C.-M.; Seruca, R.; Wang, T.-L.; Shih, I.-M. Mutant BRAF induces DNA strand breaks, activates DNA damage response pathway, and up-regulates glucose transporter-1 in nontransformed epithelial cells. *Am. J. Pathol.* 2012, 180, 1179–1188.
20. Osthus, R.C.; Shim, H.; Kim, S.; Li, Q.; Reddy, R.; Mukherjee, M.; Xu, Y.; Wonsey, D.; Lee, L.A.; Dang, C.V. Deregulation of glucose transporter 1 and glycolytic gene expression by c-myc. *J. Biol. Chem.* 2000, 275, 21797–21800.
21. Schwartzenberg-Bar-Yoseph, F.; Armoni, M.; Karnieli, E. The tumor suppressor p53 down-regulates glucose transporters GLUT1 and GLUT4 gene expression. *Cancer Res.* 2004, 64, 2627–2633.
22. Wincewicz, A.; Sulkowska, M.; Koda, M.; Sulkowski, S. Clinicopathological significance and linkage of the distribution of HIF-1alpha and GLUT-1 in human primary colorectal cancer. *Pathol. Oncol. Res.* 2007, 13, 15–20.
23. Robey, R.B.; Hay, N. Akt, hexokinase, mTOR: Targeting cellular energy metabolism for cancer therapy. *Drug Discov. Today Dis. Mech.* 2005, 2, 239–246.

24. Xu, R.H.; Pelicano, H.; Zhou, Y.; Carew, J.S.; Feng, L.; Bhalla, K.N.; Keating, M.J.; Huang, P. Inhibition of glycolysis in cancer cells: A novel strategy to overcome drug resistance associated with mitochondrial respiratory defect and hypoxia. *Cancer Res.* 2005, 65, 613–621.
25. Gerhart, D.Z.; Broderius, M.A.; Borson, N.D.; Drewes, L.R. Neurons and microvessels express the brain glucose transporter protein GLUT3. *Proc. Natl. Acad. Sci. USA.* 1992, 89, 733–737.
26. Mantych, G.J.; James, D.E.; Chung, H.D.; Devaskar, S.U. Cellular localization and characterization of glut 3 glucose transporter isoform in human brain. *Endocrinology.* 1992, 131, 1270–1278.
27. Patching, S.G. Glucose transporters at the blood-brain barrier: Function, regulation and gateways for drug delivery. *Mol. Neurobiol.* 2017, 54, 1046–1077.
28. Simpson, I.A.; Dwyer, D.; Malide, D.; Moley, K.H.; Travis, A.; Vannucci, S.J. The facilitative glucose transporter GLUT3: 20 years of distinction. *Am. J. Physiol. Endocrinol. Metab.* 2008, 295, E242–E253.
29. Salas, M.; Obando, P.; Ojeda, L.; Ojeda, P.; Pérez, A.; Vargas-Urbe, M.; I Rivas, C.; Vera, J.C.; Reyes, A.M. Resolution of the direct interaction with and inhibition of the human GLUT1 hexose transporter by resveratrol from its effect on glucose accumulation. *Am. J. Physiol. Cell Physiol.* 2013, 305, C90–C99.
30. Martin, H.J.; Kornmann, F.; Fuhrmann, G.F. The inhibitory effects of flavonoids and antiestrogens on the Glut1 glucose transporter in human erythrocytes. *Chem. Biol. Interact.* 2003, 146, 225–235.

31. Cho, S.J.; Moon, J.S.; Lee, C.M.; Choi, A.M.; Stout-Delgado, H.W. Glucose Transporter 1-Dependent Glycolysis Is Increased during Aging-Related Lung Fibrosis, and Phloretin Inhibits Lung Fibrosis. *Am. J. Respir. Cell Mol. Biol.* 2017, 56, 521–531.
32. Kapoor, K.; Finer-Moore, J.S.; Pedersen, B.P.; Caboni, L.; Waight, A.; Hillig, R.C.; Bringmann, P.; Heisler, I.; Müller, T.; Siebeneicher, H.; et al. Mechanism of inhibition of human glucose transporter GLUT1 is conserved between cytochalasin B and phenylalanine amides. *Proc. Natl. Acad. Sci. USA.* 2016, 113, 4711–4716.
33. Liu, Y.; Cao, Y.; Zhang, W.; Bergmeier, S.; Qian, Y.; Akbar, H.; Colvin, R.; Ding, J.; Tong, L.; Wu, S.; et al. A small-molecule inhibitor of glucose transporter 1 downregulates glycolysis, induces cell-cycle arrest, and inhibits cancer cell growth In Vitro and In Vivo. *Mol. Cancer Ther.* 2012, 11, 1672–1682.
34. Chan, D.A.; Sutphin, P.D.; Nguyen, P.; Turcotte, S.; Lai, E.W.; Banh, A.; Reynolds, G.E.; Chi, J.-T.; Wu, J.; Solow-Cordero, D.E.; et al. Targeting GLUT1 and the warburg effect in renal cell carcinoma by chemical synthetic lethality. *Sci. Transl. Med.* 2011, 3, 94ra70.
35. Siebeneicher, H.; Bauser, M.; Buchmann, B.; Heisler, I.; Müller, T.; Neuhaus, R.; Rehwinkel, H.; Telser, J.; Zorn, L. Identification of novel GLUT inhibitors. *Bioorg. Med. Chem. Lett.* 2016, 26, 1732–1737.
36. Siebeneicher, H.; Cleve, A.; Rehwinkel, H.; Neuhaus, R.; Heisler, I.; Müller, T.; Bauser, M.; Buchmann, B. Identification and optimization of the first highly selective GLUT1 inhibitor BAY-876. *ChemMedChem.* 2016, 11, 2261–2271.

37. DeFelice, L.J. Transporter structure and mechanism. *Trends Neurosci.* 2004, 27, 352–359.
38. Shimamura, T.; Weyand, S.; Beckstein, O.; Rutherford, N.G.; Hadden, J.M.; Sharples, D.; Sansom, M.S.P.; Iwata, S.; Henderson, P.J.F.; Cameron, A.D.; et al. Molecular basis of alternating access membrane transport by the sodium-hydantoin transporter Mhp1. *Science* 2010, 328, 470–473.
39. Wisedchaisri, G.; Park, M.S.; Iadanza, M.G.; Zheng, H.; Gonen, T. Proton-coupled sugar transport in the prototypical major facilitator superfamily protein Xyle. *Nat. Commun.* 2014, 5, 4521.
40. Radestock, S.; Forrest, L.R. The alternating-access mechanism of MFS transporters arises from inverted-topology repeats. *J. Mol. Biol.* 2011, 407, 698–715.
41. Majumdar, D.S.; Smirnova, I.; Kasho, V.; Nir, E.; Kong, X.; Weiss, S.; Kaback, H.R. Single-molecule FRET reveals sugar-induced conformational dynamics in LacY. *Proc. Natl. Acad. Sci. USA* 2007, 104, 12640–12645.
42. Smirnova, I.; Kasho, V.; Kaback, H.R. Lactose permease and the alternating access mechanism. *Biochemistry*. 2011, 50, 9684–9693.
43. Sun, L.; Zeng, X.; Yan, C.; Sun, X.; Gong, X.; Rao, Y.; Yan, N. Crystal structure of a bacterial homologue of glucose transporters GLUT1-4. *Nature*. 2012, 490, 361–366.
44. Quistgaard, E.M.; Löw, C.; Moberg, P.; Trésaugues, L.; Nordlund, P. Structural basis for substrate transport in the GLUT-homology family of monosaccharide transporters. *Nat. Struct. Mol. Biol.* 2013, 20, 766–768.

45. Schmidt, T.; Bergner, A.; Schwede, T. Modelling three-dimensional protein structures for applications in drug design. *Drug Discov. Today*. 2014, 19, 890–897.
46. Hevener, K.E.; Zhao, W.; Ball, D.M.; Babaoglu, K.; Qi, J.; White, S.W.; Lee, R.E. Validation of molecular docking programs for virtual screening against dihydropteroate synthase. *J. Chem. Inf. Model*. 2009, 49, 444–460.
47. Bender, A.; Glen, R.C. A discussion of measures of enrichment in virtual screening: Comparing the information content of descriptors with increasing levels of sophistication. *J. Chem. Inf. Model*. 2005, 45, 1369–1375.
48. Katagiri, H.; Asano, T.; Ishihara, H.; Lin, J.L.; Inukai, K.; Shanahan, M.F.; Tsukuda, K.; Kikuchi, M.; Yazaki, Y.; Oka, Y. Role of tryptophan-388 of GLUT1 glucose transporter in glucose-transport activity and photoaffinity-labelling with forskolin. *Biochem. J*. 1993, 291, 861–867.
49. Garcia, J.C.; Strube, M.; Leingang, K.; Keller, K.; Mueckler, M.M. Amino acid substitutions at tryptophan 388 and tryptophan 412 of the HepG2 (Glut1) glucose transporter inhibit transport activity and targeting to the plasma membrane in xenopus oocytes. *J. Biol. Chem*. 1992, 267, 7770–7776.
50. Kasahara, T.; Kasahara, M. Tryptophan 388 in putative transmembrane segment 10 of the rat glucose transporter Glut1 is essential for glucose transport. *J. Biol. Chem*. 1998, 273, 29113–29117. [CrossRef]
51. Kumar, H.; Kasho, V.; Smirnova, I.; Finer-Moore, J.S.; Kaback, H.R.; Stroud, R.M. Structure of sugar-bound LacY. *Proc. Natl. Acad. Sci. USA*. 2014, 111, 1784–1788.

52. Iancu, C.V.; Zmoon, J.; Woo, S.B.; Aleshin, A.; Choe, J. Crystal structure of a glucose/H⁺ symporter and its mechanism of action. *Proc. Natl. Acad. Sci. USA*. 2013, 110, 17862–17867.
53. Lešnik, S.; Miller, B.T.; Štular, T.; Woodcock, H.L.; Brooks, B.R.; Janežič, D.; Konec, J. ProBiS-CHARMMing: Web interface for prediction and optimization of ligands in protein binding sites. *J. Chem. Inf. Model.* 2015, 55, 2308–2314.
54. Thompson, J.D.; Higgins, D.G.; Gibson, T.J. CLUSTAL W: Improving the sensitivity of progressive multiple sequence alignment through sequence weighting, position-specific gap penalties and weight matrix choice. *Nucleic Acids Res.* 1994, 22, 4673–4680.
55. The Molecular Operating Environment (MOE). Chemical Computing Group Inc.: Montreal, QC, Canada, 2018.
56. Bergeret, F.; Gavalda, S.; Chalut, C.; Malaga, W.; Quémard, A.; Pedelacq, J.-D.; Daffé, M.; Guilhot, C.; Mourey, L.; Bon, C. Biochemical and structural study of the atypical acyltransferase domain from the mycobacterial polyketide synthase Pks13. *J. Biol. Chem.* 2012, 287, 33675–33690.
57. Kiburu, I.N.; LaRonde-LeBlanc, N. Interaction of Rio1 kinase with toyocamycin reveals a conformational switch that controls oligomeric state and catalytic activity. *PLoS ONE*. 2012, 7, e37371.
58. Case, D.A.; Darden, T.A.; Cheatham, T.E., III; Simmerling, C.L.; Wang, J.; Duke, R.E.; Luo, R.; Walker, R.C.; Zhang, W.; Merz, K.M.; et al. Amber 14; *University of California: San Francisco, CA, USA*, 2014.

59. Schrödinger Suite 2019-1. Protein Preparation Wizard, Maestro, MacroModel, LigPrep, EPik, Glide Grid Generation, and Glide; Schrödinger, LLC: New York, NY, USA, 2019.
60. Laskowski, R.A.; MacArthur, M.W.; Moss, D.S.; Thornton, J.M. PROCHECK: A program to check the stereochemical quality of protein structures. *J. Appl. Crystallogr.* 1993, 26, 283–291.
61. NCI Open Database Compounds, Release 3; National Cancer Institute, National Institutes of Health: Available online: <http://Cactus.Nci.Nih.Gov/Download/Nci> (accessed on 18 August 2008).
62. Lipinski, C.A.; Lombardo, F.; Dominy, B.W.; Feeney, P.J. Experimental and computational approaches to estimate solubility and permeability in drug discovery and development settings. *Adv. Drug Deliv. Rev.* 2001, 46, 3–26.
63. Guariento, S.; Bruno, O.; Fossa, P.; Cichero, E. New insights into PDE4B inhibitor selectivity: CoMFA analyses and molecular docking studies. *Mol. Divers.* 2016, 20, 77–92.
64. Franchini, S.; Manasieva, L.I.; Sorbi, C.; Battisti, U.M.; Fossa, P.; Cichero, E.; Denora, N.; Iacobazzi, R.M.; Cilia, A.; Pirona, L.; et al. Synthesis, biological evaluation and molecular modeling of 1-oxa-4-thiaspiro- and 1,4-dithiaspiro [4.5] decane derivatives as potent and selective 5-HT_{1A} receptor agonists. *Eur. J. Med. Chem.* 2017, 125, 435–452.
65. Sabbah, D.A.; Zhong, H.A. Modeling the protonation states of β -secretase binding pocket by molecular dynamics simulations and docking studies. *J. Mol. Graph. Model.* 2016, 68, 206–215.

66. Sabbah, D.A.; Vennerstrom, J.L.; Zhong, H. Docking studies on isoform-specific inhibition of phosphoinositide-3-kinases. *J. Chem. Inf. Model.* 2010, 50, 1887–1898.
67. Wold S, Sjöström M, Eriksson L. PLS-regression: A basic tool of chemometrics. *Chemo. Metrics. Intel. Lab. Sys.* 2001;58(2):109-130.
68. Almahmoud, S.; Wang, X.; Vennerstrom, J. L.; Zhong, H. A. Conformational studies of glucose transporter 1 (GLUT1) as an anticancer drug target. *Molecules.* 2019, 24(11). E2159.

Chapter 5

Ligand-Based Design of GLUT1 Inhibitors as Potential Anti-tumor Agents

ABSTRACT:

Glucose transporters (GLUTs) regulate glucose uptake and are often overexpressed in several human tumors. To identify new chemotypes targeting GLUT1, we built a pharmacophore model and searched against an NCI compound database. Sixteen hit molecules with good docking scores were screened for GLUT1 inhibition and antiproliferative activities. From these, we identified that compounds 2, 5, 6 and 13 inhibited the cell viability in a dose-dependent manner and that 2 and 6 are the most potent with less than 10 μ M concentration in the HCT116 colon cancer cell line. Lead compound 13 (NSC295720) was a GLUT1 inhibitor. Docking studies show that GLUT1 residues Phe291, Phe379, Glu380, Trp388, and Trp412 were important for inhibitor binding.

5.1. Introduction:

Glucose is an important energy source for several biological functions, including cell proliferation, and motility.¹⁻² Glucose transporters (GLUTs) regulate cellular glucose uptake and help maintain proper glucose concentration in various tissues.³ The GLUTs are membrane proteins encoded by the solute carrier transporter family, SLC2, and SLC5 genes.³⁻⁴ Cancer cells transport more glucose than normal cells due to their rapid growth and high rate of aerobic glycolysis (Warburg effect).⁵⁻⁷ Glucose transport 1 (GLUT1) is upregulated in many types of cancers such as breast, lung, prostate, and colon.⁸⁻¹¹ In addition, stimulation of oncogenes such as KRAS, BRAF, c-Myc, and p53, and transcription factors such as hypoxia-inducible factor-1a (HIF-1) upregulate the GLUT1 expression.^{9,12-15}

A specific antibody targeting GLUT1 reduced glucose uptake, induced apoptosis in lung and breast cancer cells, and improved the activity of anticancer drugs such as cisplatin, paclitaxel and gefitinib.¹⁶ Glucose transport in the brain is facilitated by both GLUT1 and GLUT3.¹⁷⁻¹⁸ In the brain, GLUT3 has greater affinity and higher capacity than GLUT1.¹⁷⁻²⁰ Therefore, GLUT-1-selective ligands would minimize potential neurotoxicity. Several small molecule GLUT inhibitors including resveratrol, naringenin, phloretin, cytochalasin B, WZB117, STF-31, pyrazolopyrimidines, phenylalanine amides, and (1H-pyrazol-4-yl)quinolone inhibit cell proliferation and induce apoptosis of cancer cells.²¹⁻²⁸ Most of these inhibitors, however, are unlikely to have high selectivity for GLUT-1.

GLUT1 transports substrates through the alternating access mechanism, which involves substantial conformational change across the cell membrane.²⁹⁻³⁰ GLUTs conformation changes from an outward-facing conformation (open to the extracellular) to an inward-

facing conformation (open to the intracellular) to deliver glucose through the cell membrane passing through an intermediate state in which the GLUTs conformation is occluded.³⁰ The substrate-free GLUT protein favors the outward-open conformation.³⁰ Once the substrate binds to the C domain of the GLUT1, the GLUT1 shifts to the inward-open conformation to release glucose.³⁰ Our docking study on different conformations of GLUT1 also confirmed that the inward-open conformation is the most favorable ligand binding site.³¹

In this paper, we explored a lead generation technique for identification of GLUT1 inhibitors by ligand-based pharmacophore modeling. We developed a 3D pharmacophore model that was formed from known GLUT1 inhibitors reported in the literature (Figure 5.1).^{24,27-28} To identify potential hit molecules, we searched the generated pharmacophore model against a National Cancer Institute (NCI) database. Our results led to the identification of four compounds that inhibited glucose uptake and decreased growth of colon cancer cells in vitro.

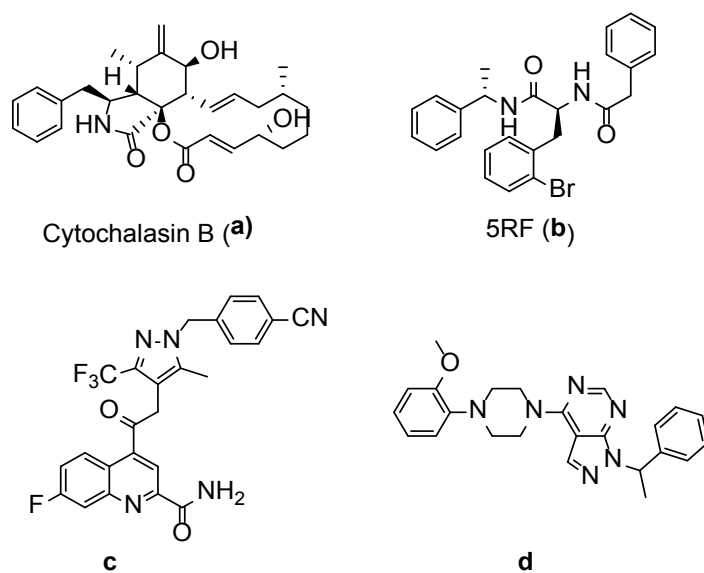


Figure 5.1. GLUTs Selective Inhibitors Used to build a Pharmacophore Model.

5.2. Results and Dissection:

We created a 3D pharmacophore model in MOE based on structures of known GLUT1 inhibitors (Figure 5.1). The selection of these compounds to build a pharmacophore for potential GLUT1 inhibitors was based on their high potency and structural diversity. The MOE software Pharmacophore modeling module³² allowed the superposition of compounds b-d to compound a and thus generated a 3D pharmacophore model composed of one aromatic group (F1), one hydrophobic group (F2), an aromatic ring/hydrophobic (F3), and one hydrogen bond donor (F4, Don) (Figure 5.2). Using this 3D pharmacophore model we performed a virtual screen of the NCI compound database. 1,469 compounds were found to satisfy the 3D pharmacophore and were reported as hits to identify novel GLUT inhibitors. Figure 2 showed the pharmacophore that was built based on compounds a-d (Figure 5.2). Hit molecules 6 and 13 were able to fit into three out of four pharmacophoric points (Figure 5.2).

We then carried out docking studies of all 1,469 molecules that satisfied the pharmacophore model. Those with good docking scores and availability from the NCI were considered as lead molecules for further testing. Our previous study showed that the inward-open conformation of GLUT1 proteins is the most favorable conformation for ligand binding.³¹ The inward-open conformation crystal structures for GLUT1 are PDB ID: 4PYP, 5EQG, 5EQH, and 5EQI.^{24,30} We used 5EQH as a model protein because the bound ligand was one of the potent molecules used to build the pharmacophore model. From this docking of 1,469 NCI compounds, 16 top-ranking compounds were chosen as lead molecules with GLUT1 inhibition potential based on their glide docking scores and the availability from NCI. The glide docking scores against the inward-open GLUT1 are

listed in Table 1. All 16 hit molecules also had better Glide docking scores than glucose, the natural GLUT1 substrate. The structures of the 16 compounds are given in Figure 5.3.

The validation of the glide docking method was performed by the pose selection method.³³ This is a standard method used by comparing the docked pose of a ligand with the cocrystal structure of the ligand. A pose with an RMSD < 2.0 Å is considered to be good.³³ The superposition of the Glide-generated docked pose, and the native conformation in the cocrystal structure (PDB ID: 5EQH) for compound 5RF (the ligand bound to 5EQH, Figure 5.4) showed that the RMSD between these two poses is 1.34 Å. This indicates that the glide docking can successfully predict ligand-binding conformations.

We also investigated ligand-protein interactions of the 16 top-ranking compounds to analyze their binding modes. Phe379, Trp388, and Trp412 play essential roles in GLUT1 function and glucose uptake.^{34-36,24} Gln282, Gln283, Asn288, Phe291, Asn317, and Glu380 are also important residues for glucose binding.^{31,37} Notably, our analysis showed that the 16 top-ranking compounds were able to bind to these reported residues. Our glide docking results of the 16 top-ranking compounds against the inward-open GLUT1 conformation revealed that all compounds bound to the glucose binding site of GLUT1, and the most frequently observed interacting residues were Thr137, Gln282, Phe291, Phe379, Glu380, Trp388, and Trp412 for their role in providing H-bonds or $\pi - \pi$ stacking interactions (Table 5.1). Hit compounds **2**, **6**, **13**, and **5** were able to create $\pi - \pi$ stacking interactions with Phe291, and Phe379, Trp388, and Trp412 and H-bonds with Thr137 of GLUT1 (Figure 5.5). This suggests that Thr137 may be a significant residue for ligand binding. Taken together, the docking scores and ligand-protein interactions of the 16 top-ranking compounds suggest that these compounds may be potential GLUT1 inhibitors.

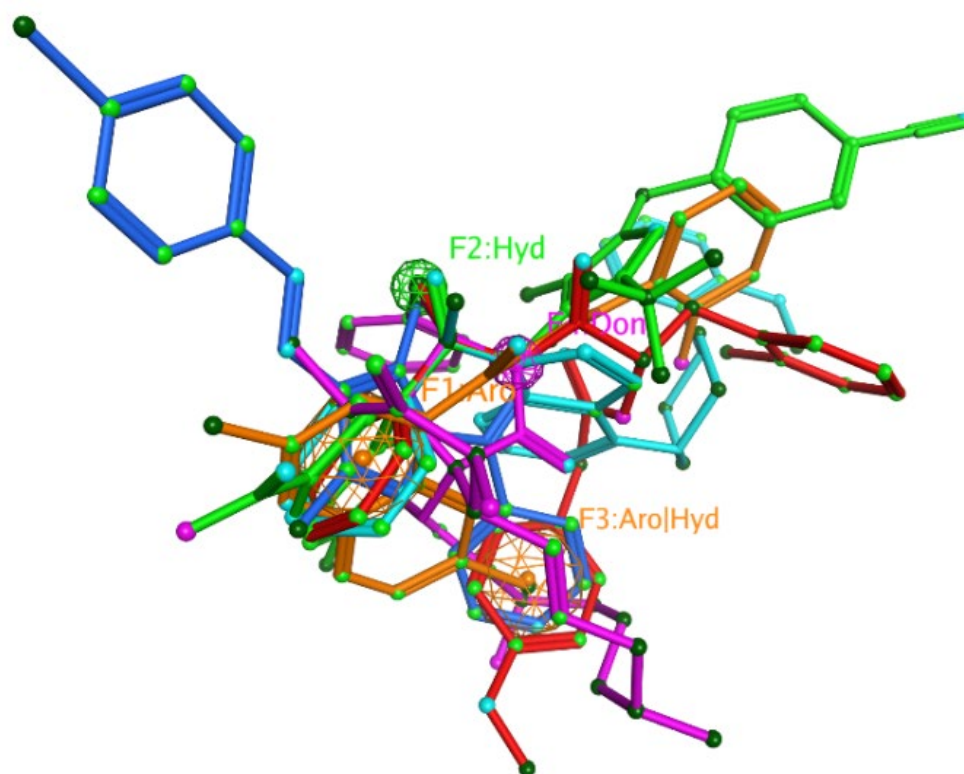


Figure 5.2. Pharmacophore model for GLUTs inhibitors. Color code: Cytochalasin B (a), magenta; 5RF (b), red; Compound c, green; Compound d, cyan; hit molecules NSC328095 (6), orange; and NSC295720 (13), blue. Aro: aromatic rings; Don: H-bond donor; Hyd: hydrophobic groups.

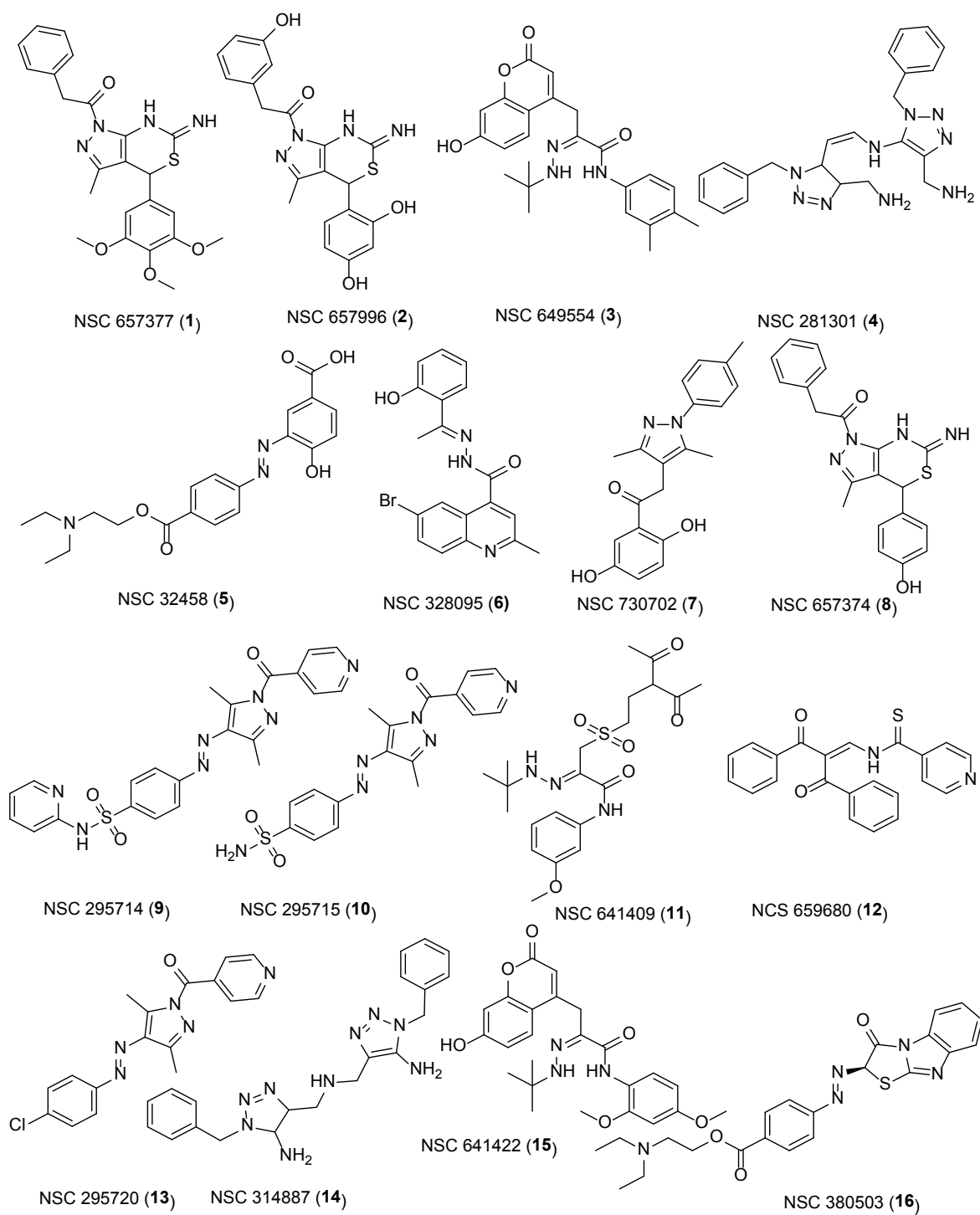


Figure 5.3. Chemical structures of sixteen hit molecules.

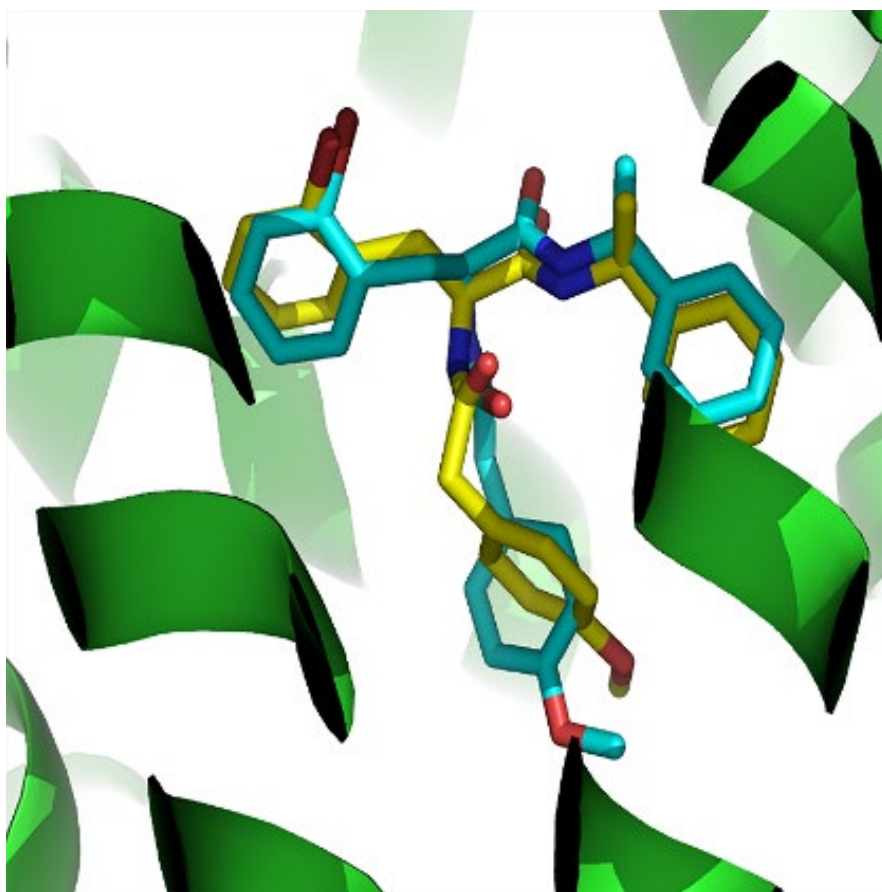


Figure 5.4. The superposition of the Glide generated pose and the native ligand of the crystal structure (5EQH). The RMSD between these two conformations is 1.34 Å.

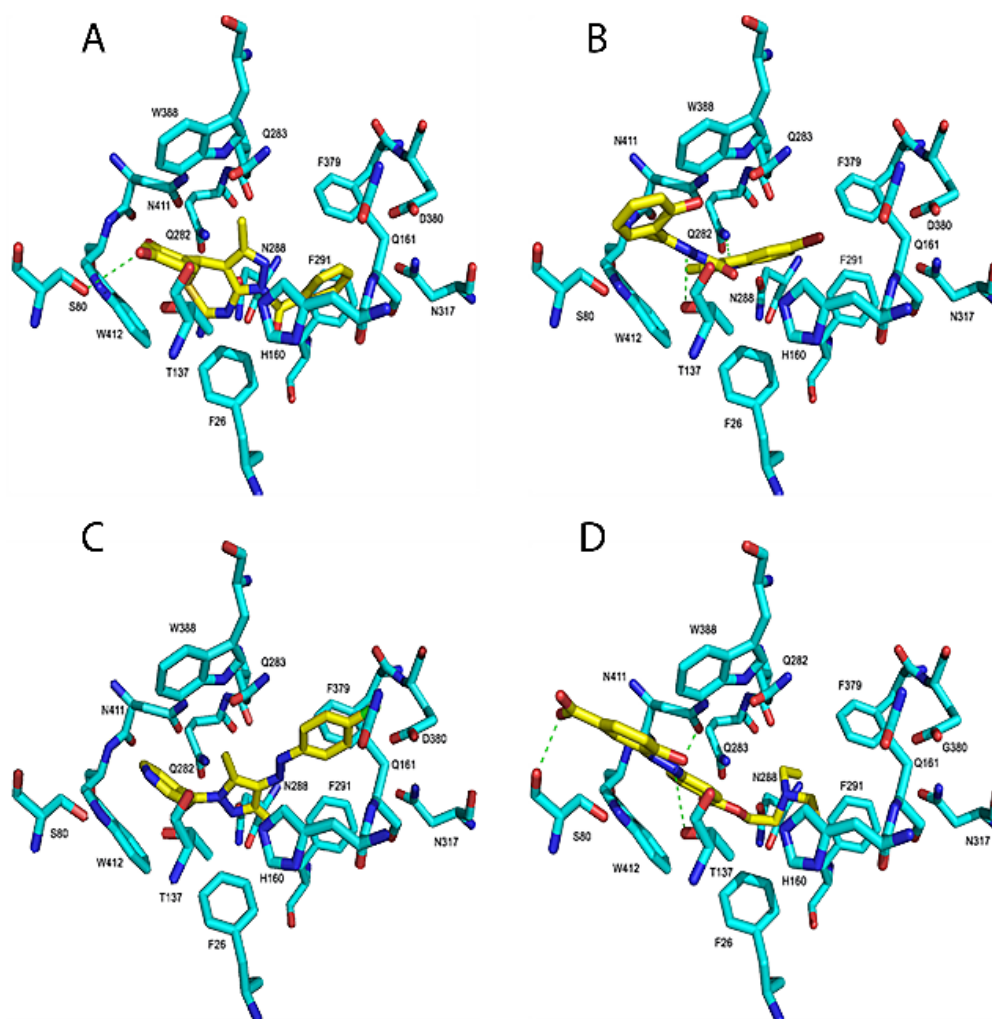


Figure 5.5. Ligands interactions between 2 (A), 6 (B), 13 (C), and 5 (D) and GLUT1: The H-bond interactions are shown as green dotted lines.

Table 5.1. Glide docking scores (kcal/mol) of hit molecules with NSC numbers, logP, and interacting residues of 5EQH.

NSC# (Comp#)	logP	XP GScore	Interacting residues
657377 (1)	4.45	-7.54	Phe291, Phe379, Trp388, Trp412
657996 (2)	4.03	-8.78	Ser80, Phe291, Phe379, Trp388, Trp413
649554 (3)	4.53	-7.85	Glu380, Trp388, Trp412
281301 (4)	0.75	-8.47	Phe291, Phe379, Trp388, Trp412
32458 (5)	3.82	-9.48	Ser80, Thr137, Trp388, Asn411, Trp412
328095 (6)	4.64	-8.14	Thr137, Gln282, Trp388, Trp412
730702 (7)	3.37	-7.00	Phe379, Glu380, Trp388, Trp412
657374 (8)	4.7	-7.85	Asn288, Glu380, Trp388, Trp412
295714 (9)	3.04	-7.63	Phe291, Phe379, Trp388, Trp412
295715 (10)	1.54	-6.66	Phe379, Trp388, Trp412
641409 (11)	1.18	-7.46	Trp388, Trp412
659680 (12)	2.31	-8.12	Phe379, Trp388, Trp412
295720 (13)	3.71	-6.3	Phe291, Phe379, Trp388, Trp412
314887 (14)	1.08	-7.08	Phe379, Trp388, Trp412
641422 (15)	3.85	-7.14	Glu380, Trp388
380503 (16)	4.27	-8.59	Thr137, Trp388, Asn411, Trp412
β -D-glucose		-5.96	
α -D-glucose		-5.91	

In order to evaluate the antiproliferative activities of the 16 potential lead compounds, we assessed the growth inhibition of these candidates in the highly malignant HCT116 colon cancer cell line³⁸. Compounds 2 and 6 were the most potent with IC₅₀ values <10 μ M followed by 13 with an IC₅₀ value of 56 μ M. Compounds 1, 3, 5, 10, and 16 had IC₅₀ values ranging from 250 and 660 μ M whereas the remaining compounds were inactive (Table 5.2). Compounds 2, 5, 6 and 13 inhibited cell viability of the HCT116 colon cancer cell lines in a dose-dependent manner.

We next determined whether the cell viability inhibition by lead compounds 2, 5, 6, and 13 was mediated through inhibition of GLUT1. We tested GLUT1 specificity in the presence of mitochondrial electron transport inhibitor rotenone using methods published previously.³⁹⁻⁴¹ Rotenone inhibits ATP production through mitochondrial respiration; therefore in co-incubations of the compounds with rotenone, cells would produce ATP only through glycolysis which is linked with glucose uptake. These data showed that 13 significantly decreased ATP levels in the presence of rotenone (Figure 5.6), suggesting that this compound specifically inhibits glucose uptake, leading to reduced glycolysis. Taken together, these results indicate that 13 is a specific GLUT1 inhibitor.

Table 5.2.IC₅₀s of 16 tested compounds against the HCT116 colon cancer cell lines.

NSC#	IC ₅₀ (μM)	NSC#	IC ₅₀ (μM)
657377 (1)	450	295714 (9)	inactive
657996 (2)	4.9	295715 (10)	660
649554 (3)	560	641409 (11)	inactive
281301 (4)	inactive	659680 (12)	inactive
32458 (5)	250	295720 (13)	56
328095 (6)	9.1	314887 (14)	inactive
730702 (7)	inactive	641422 (15)	inactive
657374 (8)	inactive	380503 (16)	260

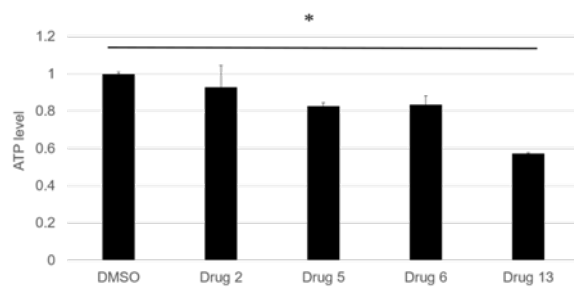


Figure 5.6. FET cells were treated with hit molecules 2, 5, 6 and 13 in the presence of rotenone (1 μ M) for 1 hour and ATP level was measured by Cell Titer-Glo® Luminescent Cell Viability Assay Kit. The experiment was repeated twice. * $P < 0.1$.

5.3. Conclusion:

Pharmacophore modeling and database searching identified 16 hit compounds. The ability to generate π - π stacking with Phe291, and Phe379, Trp388, and Trp412 and form H-bonds with Thr137 may be responsible for the binding of these hit molecules to GLUT1. Two of these inhibited the HCT116 colon cancer cell line at low micromolar concentrations. One compound (13) was a GLUT1 inhibitor.

5.4. Materials and Methods:

5.4.1 Three-Dimensional (3D) Pharmacophore Model Design and Virtual screening:

The Computational pharmacophore generation was carried out using Molecular Operating Environment (MOE).⁴³ The 3D structures of the known GLUTs inhibitors from literature (Figure 1) were built and energy minimized using MMFF94X force field⁴⁴ in MOE software based on the 5RH ligand in the crystal structure 5EQH. The 3D pharmacophore was generated by the flexible superimposition of the 3D model of GLUTs inhibitors, and identification of the 3D features that they shared. Then, the 3D pharmacophore model was applied in the design of novel GLUTs inhibitors according to the Pharmacophore Query module in MOE. A database of 260,071 molecules was downloaded from the National Cancer Institute (NCI),⁴⁵ then it was filtered according to the Lipinski's rule of five by the logP ($\log P < 5$), and molecular weight ($MW < 500$)⁴⁶, yielding 33,778 drug-like molecules.

A pharmacophore search against this database of 33,778 molecules resulted in 1,469 hit molecules that fit the pharmacophore model. To help narrow down the number of hit molecules that we will use for the biological test, we docked all these 1,469 molecules to the GLUT1 5EQH ligand binding site using the procedure established in our previous studies.^{47 48} In this study, Glide Dock⁴⁹ in the Maestro 11.2 were performed for ligands docking against inward-open conformations of GLUT1 (PDB ID: 5EQH) which has been prepared using the Protein Preparation Wizard module followed by energy optimization using the MacroModel in the Schrödinger software suite with the OPLS force field. Then,

a grid file for was generated by the Glide Grid Generation panel with the bound ligand (5RF) as the centroid of the minimized protein. Then, all compounds were docked to the grid file with ligand sampling being set to extra-precision (XP) method, and all other parameters were used as defaults. The binding affinity of the various conformation of GLUT1/ligand complexes was evaluated by the Glide scores. The protein/ligand interactions was created by using the Pymol software.⁵⁰

5.4.2. Cell Viability Assay:

Human colon cancer cell lines HCT116 and FET were maintained in McCoy's 5A medium (Sigma, St Louis, MO, USA) with 10 ng/ml epidermal growth factor (EGF), 20 µg/ml insulin and 4 µg/ml transferrin. Cells were culture at 37°C in a humidified incubator with 6% CO₂. HCT116 cells were seeded into 96-well plates at a density of 6000 cells per well, and treated with compounds for 72 hours. Cells were stained for 2 hours with alamar blue reagent (Bio-rad). The OD at 570 nm and 630nm were read on an ELx808 Absorbance Microplate Reader (BioTek, Winooski, VT, USA). Cell viability was calculated as a ratio of OD values of drug-treated samples to those of controls.

5.4.3. GLUT1 specificity assay:

To test the specificity of GLUTs inhibitors, colon carcinoma cell line FET were seeded in 96 plates at a density of 20000 cells per well. The cells were then cultured overnight in glucose free media. After 16 hours, the cells were incubated with 0.1M glucose with or without compounds in the presence of 1 µM rotenone for 60 min. The Cell Titer-Glo® Luminescent Cell Viability Assay from Promega was then used to measure ATP levels. Statistical analyses were performed using Student's t-test.

REFERENCES:

1. Maher, F.;Vannucci, S. J.; Simpson, I. A. Glucose transporter proteins in brain. *FASEB J.*1994, 8, 1003-1011.
2. Navale, A. M.;Paranjape, A. N. Glucose transporters: Physiological and pathological roles. *Biophys. Rev.*2016, 8, 5-9.
3. Mueckler, M.;Thorens, B. The SLC2 (GLUT) family of membrane transporters. *Mol. Aspects. Med.*2013, 34, 121-138.
4. Thorens, B.;Mueckler, M. Glucose transporters in the 21st century. *Am. J. Physiol. Endocrinol. Metab.*2010, 298, E141-145.
5. Warburg, O.; Wind, F.; Negelein, E. The metabolism of tumors in the body. *J. Gen. Physiol.*1927, 8, 519–530.
6. Hanahan, D.; Weinberg, R. Hallmarks of cancer: The next generation. *Cell.* 2011, 144, 646-674.
7. Barron, C. C.;Bilan, P. J.; Tsakiridis, T.;Tsiani, E. Facilitative glucose transporters: Implications for cancer detection, prognosis and treatment. *Metab. Clin. Exp.*2016, 65, 124-139.
8. Brown, R. S.; Wahl, R. L. Overexpression of glut-1 glucose transporter in human breast cancer. An immunohistochemical study. *Cancer.* 1993, 72, 2979-2985.
9. Sasaki, H.; Shitara, M.; Yokota, K.; et al. Overexpression of GLUT1 correlates with kras mutations in lung carcinomas. *Mol. Med. Rep.* 2012, 5, 599-602.

10. Reinicke, K.; Sotomayor, P.; Cisterna, P.; Delgado, C.; Nualart, F.; Godoy, A. Cellular distribution of glut-1 and glut-5 in benign and malignant human prostate tissue. *J. Cell. Biochem.* 2012, 113, 553-562.
11. Shen, Y.; Arbman, G.; Olsson, B.; Sun, X. Overexpression of GLUT1 in colorectal cancer is independently associated with poor prognosis. *Int. J. Biol. Markers.* 2011, 26, 166-172.
12. Sheu, J. J.; Guan, B.; Tsai, F. J.; et al. Mutant BRAF induces DNA strand breaks, activates DNA damage response pathway, and up-regulates glucose transporter-1 in nontransformed epithelial cells. *Am. J. Pathol.* 2012, 180, 1179-1188.
13. Osthus, R. C.; Shim, H.; Kim, S.; et al. Deregulation of glucose transporter 1 and glycolytic gene expression by c-myc. *J. Biol. Chem.* 2000, 275, 21797-21800.
14. Schwartzberg-Bar-Yoseph, F.; Armoni, M.; Karnieli, E. The tumor suppressor p53 down-regulates glucose transporters GLUT1 and GLUT4 gene expression. *Cancer Res.* 2004, 64, 2627-2633.
15. Wincewicz, A.; Sulkowska, M.; Koda, M.; Sulkowski, S. Clinicopathological significance and linkage of the distribution of HIF-1 α and GLUT-1 in human primary colorectal cancer. *Pathol. Oncol. Res.* 2007, 13, 15-20.
16. Rastogi, S.; Banerjee, S.; Chellappan, S.; Simon, G. R. Glut-1 antibodies induce growth arrest and apoptosis in human cancer cell lines. *Cancer Lett.* 2007, 257, 244-251.

17. Mantych, G. J.; James, D. E.; Chung, H. D.; Devaskar, S. U. Cellular localization and characterization of glut 3 glucose transporter isoform in human brain. *Endocrinology*. 1992, 131, 1270-1278.
18. Patching, S. G. Glucose transporters at the blood-brain barrier: Function, regulation and gateways for drug delivery. *Mol. Neurobiol.* 2017, 54, 1046-1077.
19. Simpson, I. A.; Dwyer, D.; Malide, D.; Moley, K. H.; Travis, A.; Vannucci, S. J. The facilitative glucose transporter GLUT3: 20 years of distinction. *Am. J. Physiol. Endocrinol. Metab.* 2008, 295, E242-253.
20. Gerhart, D. Z.; Broderius, M. A.; Borson, N. D.; Drewes, L. R. Neurons and microvessels express the brain glucose transporter protein GLUT3. *Proc. Natl. Acad. Sci. U.S.A.* 1992, 89, 733-737.
21. Salas, M.; Obando, P.; Ojeda, L.; et al. Resolution of the direct interaction with and inhibition of the human GLUT1 hexose transporter by resveratrol from its effect on glucose accumulation. *Am. J. Physiol. Cell. Physiol.* 2013, 305, C90-99.
22. Martin, H.; Kornmann, F.; Fuhrmann, G. F. The inhibitory effects of flavonoids and antiestrogens on the Glut1 glucose transporter in human erythrocytes. *Chem. Biol. Interact.* 2003, 146, 225-235.
23. Cho, S. J.; Moon, J.; Lee, C.; Choi, A. M. K.; Stout-Delgado, H. W. Glucose transporter 1-dependent glycolysis is increased during aging-related lung fibrosis, and phloretin inhibits lung fibrosis. *Am. J. Respir. Cell. Mol. Biol.* 2017, 56, 521-531.

24. Kapoor, K.; Finer-Moore, J. S.; Pedersen, B. P.; et al. Mechanism of inhibition of human glucose transporter GLUT1 is conserved between cytochalasin B and phenylalanine amides. *Proc. Natl. Acad. Sci. U.S.A.* 2016, 113, 4711-4716.
25. Liu, Y.; Cao, Y.; Zhang, W.; et al. A small-molecule inhibitor of glucose transporter 1 downregulates glycolysis, induces cell-cycle arrest, and inhibits cancer cell growth in vitro and in vivo. *Mol. Cancer Ther.* 2012, 11, 1672-1682.
26. Chan, D. A.; Sutphin, P. D.; Nguyen, P.; et al. Targeting GLUT1 and the warburg effect in renal cell carcinoma by chemical synthetic lethality. *Sci. Transl. Med.* 2011, 3(94), 94ra70.
27. Siebeneicher, H.; Bauser, M.; Buchmann, B.; et al. Identification of novel GLUT inhibitors. *Bioorg. Med. Chem. Lett.* 2016, 26, 1732-1737.
28. Siebeneicher, H.; Cleve, A.; Rehwinkel, H.; et al. Identification and optimization of the first highly selective GLUT1 inhibitor BAY-876. *ChemMedChem.* 2016, 11, 2261-2271.
29. Pao, S. S.; Paulsen, I. T.; Saier, M. H. Major facilitator superfamily. *Microbiol. Mol. Biol. Rev.* 1998, 62, 1-34.
30. Deng, D.; Xu, C.; Sun, P.; et al. Crystal structure of the human glucose transporter GLUT1. *Nature.* 2014, 510, 121-125.
31. Almahmoud, S.; Wang, X.; Vennerstrom, J. L.; Zhong, H. A. Conformational studies of glucose transporter 1 (GLUT1) as an anticancer drug target. *Molecules.* 2019, 24(11), E2159.

32. The Molecular Operating Environment (MOE). Chemical Computing Group Inc.: Montreal, QC, Canada, 2018.
33. Hevener, K. E.; Zhao, W.; Ball, D. M.; et al. Validation of molecular docking programs for virtual screening against dihydropteroate synthase. *J. Chem. Inf. Model.* 2009, 49, 444-460.
34. Kasahara, T.; Kasahara, M. Tryptophan 388 in putative transmembrane segment 10 of the rat glucose transporter Glut1 is essential for glucose transport. *J. Biol. Chem.* 1998, 273, 29113-29117.
35. Garcia, J. C.; Strube, M.; Leingang, K.; Keller, K.; Mueckler, M. M. Amino acid substitutions at tryptophan 388 and tryptophan 412 of the HepG2 (Glut1) glucose transporter inhibit transport activity and targeting to the plasma membrane in xenopus oocytes. *J. Biol. Chem.* 1992, 267, 7770-7776.
36. Katagiri, H.; Asano, T.; Ishihara, H.; et al. Role of tryptophan-388 of GLUT1 glucose transporter in glucose-transport activity and photoaffinity-labelling with forskolin. *Biochem. J.* 1993, 291, 861-867.
37. Deng, D.; Xu, C.; Sun, P.; et al. Crystal structure of the human glucose transporter GLUT1. *Nature.* 2014, 510, 121-125.
38. Brattain, M. G.; Levine, A. E.; Chakrabarty, S.; Yeoman, L. C.; Willson, J. K.; Long, B. Heterogeneity of human colon carcinoma. *Cancer Metastasis Rev.* 1984, 3, 177-191.

39. Li, N.; Ragheb, K.; Lawler, G.; et al. Mitochondrial complex I inhibitor rotenone induces apoptosis through enhancing mitochondrial reactive oxygen species production. *J. Biol. Chem.* 2003, 278, 8516-8525.
40. Gielisch, I.; Meierhofer, D. Metabolome and proteome profiling of complex I deficiency induced by rotenone. *J. Proteome. Res.* 2015, 14, 224-235.
41. Lindahl, P. E.; Oberg, K. E. The effect of rotenone on respiration and its point of attack. *Exp. Cell Res.* 1961, 23, 228-237.
42. Zhao, Y.; Wieman, H. L.; Jacobs, S. R.; Rathmell, J. C. Mechanisms and methods in glucose metabolism and cell death. *Methods Enzymol.* 2008, 442, 439-457.
43. The Molecular Operating Environment (MOE). Chemical Computing Group Inc.: Montreal, QC, Canada, 2018.
44. Halgren, T. A. Merck molecular force field. I. basis, form, scope, parameterization, and performance of MMFF94. *J. Comput. Chem.* 1996, 17, 490-519.
45. NCI open database compounds, release 3; National Cancer Institute, National Institutes of Health: Bethesda, MD, Sept. 2003. Available online at: [Http://Cactus.nci.nih.gov/download/nci](http://Cactus.nci.nih.gov/download/nci) (accessed Aug 18, 2008).
46. Lipinski, C. A.; Lombardo, F.; Dominy, B. W.; Feeney, P. J. Experimental and computational approaches to estimate solubility and permeability in drug discovery and development settings. *Adv Drug Deliv Rev.* 2001, 46, 3-26.
47. Sabbah, D. A.; Vennerstrom, J. L.; Zhong, H. Docking studies on isoform-specific inhibition of phosphoinositide-3-kinases. *J. Chem. Inf. Model.* 2010, 50, 1887-1198.

48. Almahmoud, S.; Wang, X.; Vennerstrom, J. L.; Zhong, H. A. Conformational studies of glucose transporter 1 (GLUT1) as an anticancer drug target. *Molecules*. 2019, 24(11). E2159.
49. Schrödinger, LLC, New York, NY, 2019. Schrödinger suite 2019-1 protein preparation wizard, Glide Dock, Macromodel.
50. DeLano WL. The PyMOL molecular graphics system. The PyMOL Molecular Graphics System; DeLano Scientific: San Carlos, CA, 2002. 2009.

Chapter 6

Summary

PPAR γ is an essential target of many pharmaceuticals that have produced billions of dollars (USD) for treating insulin resistance and type 2 diabetes, such as thiazolidinedione drugs (TZDs). PPAR γ has a vital role in controlling adipogenic, lipogenic pathways, glucose homeostasis and insulin sensitivity, inflammation. PPAR γ is overexpressed in numerous tumors, including breast, pancreatic, bladder, prostate, and colon. The LBD of PPAR γ is a large T-shaped cavity (~ 1.300 Å), and it is mostly hydrophobic pocket. The LBD of PPAR γ has two main ligand-binding sites: orthosteric and allosteric binding sites, each site having different properties and binding preferences. PPAR γ antagonists improved glucose homeostasis, insulin resistance, no side effects of classical PPAR γ agonists such as TZDs. The overexpression of PPAR γ decreased survival of prostate cancer and increased metastases to the lungs and lymph nodes, and positively correlated with prostate cancer. Therefore, there is an urgent need to develop novel, potent PPAR γ antagonists. On the other hands, The GLUT1 was the first characterized and identified glucose transporters. Cancer cells transport more glucose than normal cells due to their rapid growth and high rate of aerobic glycolysis (Warburg effect). The GLUT1 is upregulated in many types of cancers such as brain, breast, lung, kidney, ovary, prostate, and colon. GLUT1 transport glucose through alternating access, which involves substantial conformational change down its concentration gradient. GLUT1 changes from an outward-open conformation (OOP), which opens to the extracellular to take up glucose, to an inward-open conformation (IOP), which allows the release of

glucose to the intracellular cytoplasm via partially outward-occluded (POO), outward-occluded (OOC) and partially inward-occluded (PIO) conformations. Several small molecule GLUTs inhibitors and chemotypes have been described including resveratrol, naringenin, phloretin, cytochalasin B, WZB117, STF-31, pyrazolopyrimidines, phenylalanine amides, and (1H-pyrazol-4-yl)quinoline. Most of these inhibitors violate drug-like properties and could be toxic, so small molecules targeting GLUTs are still required as lead compounds for future drug discovery.

In Chapter 2, The crystal structures of PPAR γ complexed with antagonists revealed that antagonists can occupy the two binding sites, orthosteric pocket, and allosteric pocket. Docking studies PPAR γ shows that the experimental binding affinity of PPAR γ antagonists more correlated to allosteric binding site than the orthosteric binding site. In addition, the statistical parameters of docking scores at allosteric pocket better than orthosteric pocket. Therefore, the allosteric site looks like the most favorable binding site for PPAR γ antagonists. Inspection of ligand/ PPAR γ interactions at allosteric binding site shows that the PPAR γ antagonists seems to require an interaction with residues Phe282, Arg288, and Lys367 more than agonists or partial agonists. This study improves the thoughtful of the PPAR γ binding site, which assists in the design and optimization of more specific PPAR γ antagonists. In future studies, we plan to run docking studies against the crystal structure of PPAR α , PPAR γ , PPAR δ , estrogen receptor α (ER α), and estrogen receptor β (ER β) bound to antagonists to which helps in the design and optimization of more specific inhibitors for the PPAR γ . Besides, we will investigate the ligand protein interactions to define the most selective residues, which can be targeted by a molecule during the design and optimization of more specific inhibitors for the PPAR γ .

In chapter 3, PPAR γ is a novel and important target in prostate cancer. PPAR γ antagonist decreased tumor size. The identification of hit compounds is an important step in the development of PPAR γ antagonists. We used an integrated computational and experimental approach against the crystal structure of PPAR γ , which is a PPAR γ model that has two molar equivalents of a ligand binding at different sites. We then performed structure based virtual screening of small molecule libraries against the two binding sites followed by experimental testing to discover new hits of PPAR γ antagonists. Compounds resulted from structure based virtual screening against the allosteric site are more potent than the orthosteric site. Structural analysis of the two binding sites of PPAR γ showed that the allosteric site has more ligand protein interactions with the compounds. Arg288 and Lys367 would be PPAR γ antagonists. This study improves the understanding of the PPAR γ binding site, which supports in the design and optimization of more specific PPAR γ antagonists. Next, we will effort on the design and synthesis and optimized of derivatives of selected hits to develop lead candidates as PPAR γ antagonists for the treatment of prostate cancer and other solid tumors.

In chapter 4, the protein–ligand dockings on different GLUT1 conformations suggest three significant outcomes: First, the docking scores suggested that the IOP conformation would be preferred for ligand binding. Besides, the MAE and RMSE for each conformation in comparison to experimental observations IC₅₀ of ligands also confirm that the IOP conformation would be preferred for ligand binding. Second, enrichment factor (EF) calculation from docking studies is a method to validate the docking study, and it further confirms that the Glide dock program is able to distinguish the real inhibitors from drug-like molecules with best results in the IOP conformation. Third, residues

Trp388, Glu380, Phe379, and Trp412 are important for the IOP conformation selective binding. Taken together, all these results support the conclusion that the IOP conformation is the most recognized conformation for ligand interaction and, thus, it should be used for future molecule design targeting GLUT1. In future studies, we will run docking studies against other GLUTs isoforms such as GLUT2, GLUT3, and GLUT4 to help in the design and optimization of more specific inhibitors for the GLUT1. Besides, we will investigate the ligand protein interactions to define the most selective residues, which can be targeted by a molecule during the design and optimization of more specific inhibitors for the GLUT1.

In Chapter 5, Pharmacophore modeling and database searching identified 16 hit compounds. The ability to generate π - π stacking with Phe291, and Phe379, Trp388, and Trp412 and form H-bonds with Thr137 may be responsible for the binding of these hit molecules to GLUT1. NSC657996 and NSC328095 inhibited the HCT116 colon cancer cell line at low micromolar concentrations. Besides, NSC295720 was a GLUT1 inhibitor. Next, we will evaluate the NSC657996, NSC328095, and NSC295720 against a panel of GLUTs isoforms to investigate their selectivity. Future hit identification could involve fingerprint-based similarity searching.

Appendix

Molecular Modeling Studies on the Binding Mode of the PD-1/PD-L1

Complex Inhibitors

1. Introduction:

Immune checkpoints (ICPs) are paramount regulators of the immune system, and they can differentiate between the healthy and foreign cells and prevent activation of immune cells.¹⁻³ Cancer cells can evade immune system control by overexpressing inhibitory ICPs.⁴⁻⁷ There are several co-inhibitory ICPs such as T-lymphocyte-associated protein 4 (CTLA-4), and programmed cell death protein 1 (PD-1) / programmed cell death ligand 1 (PD-L1), which inhibit T cell activation by different mechanisms.⁸⁻¹⁰ Several antibodies targeting CTLA-4 or PD-1/PD-L1 revealed encouraging clinical results.¹¹⁻¹² Monoclonal antibodies (mAbs) against PD-1 pathway show significant tumor treatment benefit, and they were considered a better option than mAbs targeting CTLA-4.¹³⁻¹⁵ Several successful mAbs targeting the PD1/PD-L1 pathway for treatment of various tumors have been approved. These approved mAbs included nivolumab and pembrolizumab.¹⁵⁻¹⁷ The activity of mAbs against PD1/PD-L1 checkpoints led to accelerated approval of nivolumab and pembrolizumab by regulatory bodies in 2014.^{5,14}

PD-1 is a type I transmembrane immune-inhibitory protein that is expressed on activated CD4⁺ and CD8⁺ T cells, natural killer T (NKT) cells, B cells, activated monocytes, and dendritic cells (DCs).¹⁸⁻¹⁹ PD-1 and its ligands control the activity and tolerance of T cells, and immune-mediated tissue damage.¹⁹⁻²⁰ PD-1 has two ligands: PD-L1 and PD-L2; PD-L1 is expressed broadly and upregulated on activated T cells, B cells,

myeloid, and dendritic cells, while PD-L2 is expressed only in activated dendritic cells and some macrophages.^{9,21} In normal conditions, PD-1/PD-Ls pathways play an essential function in maintaining immune homeostasis and avoiding autoimmunity by the inhibition of T cell activation.²²⁻²⁴ In cancer cells, the PD-1/PD-L1 interaction has a crucial role in tumor immune resistance.²⁵⁻²⁶ The binding of the PD-1/PD-L1 complex inhibits T-lymphocyte proliferation, the release of cytokines, and induces apoptosis of T cells.²⁷⁻²⁸ PD-L1 is overexpressed in several tumors such as lymphoma, melanoma, lung, breast cancer, glioblastoma, ovarian, kidney tumors, and bladder cancers.²⁹⁻³⁴ Blocking of the PD-1/PD-L1 complex interaction would promote the reactivation and revival of exhausted T cell phenotype which would normalize and stimulate the antitumor response of T cells.²⁸ PD-1/PD-L1 complex inhibitors represent a new type of immunotherapy drugs which could afford new treatment for various kinds of cancers.³⁵⁻³⁷ There are four therapeutic mAbs against PD-1/PD-L1 immune checkpoint proteins (nivolumab and pembrolizumab targeting PD-1; atezolizumab and avelumab binding to PD-L1) have been approved by the US FDA. These mAbs are used to treat prepared against metastatic melanoma, non-small-cell lung cancer (NSCLC), renal cell carcinoma, head and neck squamous cell cancer (HNSCC), and bladder cancer.

However, the occurrence of immune-mediated adverse effects has been observed in some patients receiving the immune checkpoint inhibition (ICI) by mAbs. The side effects can be colitis, autoimmune hepatitis, endocrine or neurological disorders.³⁸ A study shows that 44.4% of patients with pre-existing AID experienced immune-related adverse event (irAE) whereas only 23.8% were observed with irAE in those without pre-existing AID.³⁹ In addition, a rapid worsening of the disease upon treatment with ICIs have been

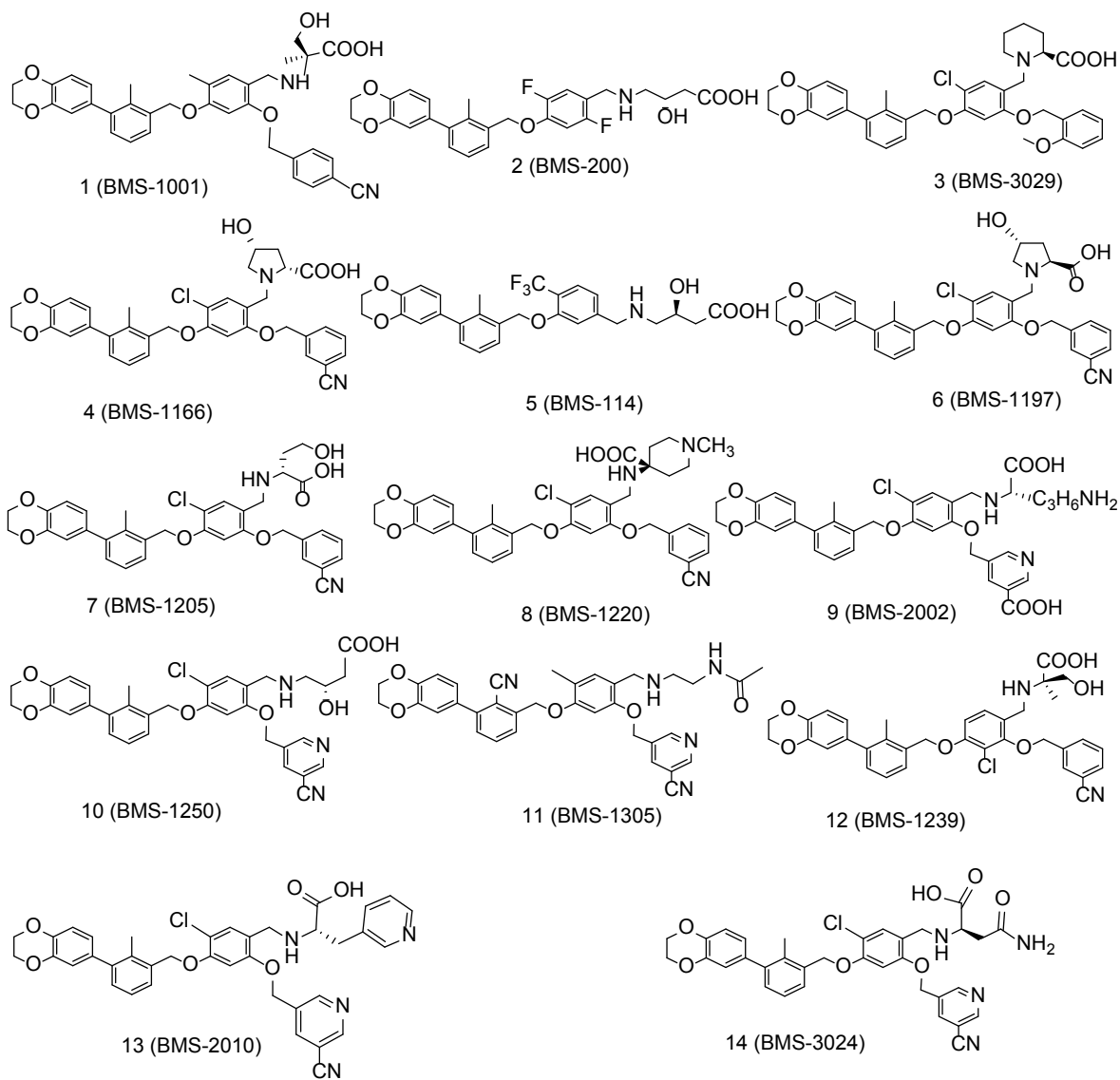
observed in approximately 5% of patients, a phenomenon called hyper-progressive disease (HPD) and it seems to be due to inhibition of both PD-1 and PD-L1.^{40,41}

Therefore, a small molecule inhibitor that binds to PD-L1 only would spare the function of PD-1 and may be an alternative therapeutic approach that may minimize the immune-related adverse effects. Unfortunately, the development of small molecules targeting the PD-1/PD-L1 axis lags far behind the mAb development targeting this pathway. This is due, in part, to insufficient structural information of the PD-1/PD-L1 complex with small molecule inhibitors. The crystal structure of the fully human PD-1/PD-L1 complex (PDB: 4ZQK) was determined in 2015. This crystal structure suggests that there are several binding sites on the PD-1 and PD-L1 that can be targeted to develop small molecule inhibitors.^[42] The crystal structures of PD-L1 complexed with atezolizumab (PDB ID: 3X8L) and durvalumab (PDB ID: 3X8M) were not available until 2017, and they defined the binding site and important residues of the PD-L1 interacting with the mAbs.⁴³ Recently, some new small molecules were identified as PD1/PD-L1 pathway inhibitors with significant inhibitory effects at subnanomolar concentrations.⁴⁴⁻⁴⁵ Besides, the crystal structures of PD-L1 complexed with small molecule inhibitors have been resolved showing that small molecules bind to PD-L1 instead of PD-1, and they inhibit the PD-1/PD-L1 interaction by inducing PD-L1 dimerization through the PD-1 interacting surface site. The binding of small molecules to PD-L1 led to disassociation of the PD-1/PD-L1 complex.⁴⁶⁻

48

Here, we report the structural basis for PD-L1 interactions with the reported BMS inhibitors (Figures 7.1). The docking scores of BMS inhibitors showed that the docking scores in our study are very close to those experimentally observed biological activities.

The binding modes and protein-ligand interaction studies of the PD-L1/BMS inhibitors offer significant structural insight for the design and development of future new and selective inhibitors for the PD-L1/PD-1 complex. We identified residues Tyr56, Asp122, Lys124, Arg125, and Phe19 of PD-L1 as important binding residues for small molecule design as this residue is able to form H-bond interactions. Tyr56, and Asp122 appear to be two most vital residues for interaction with PD1/PD-L1 complex inhibitors.



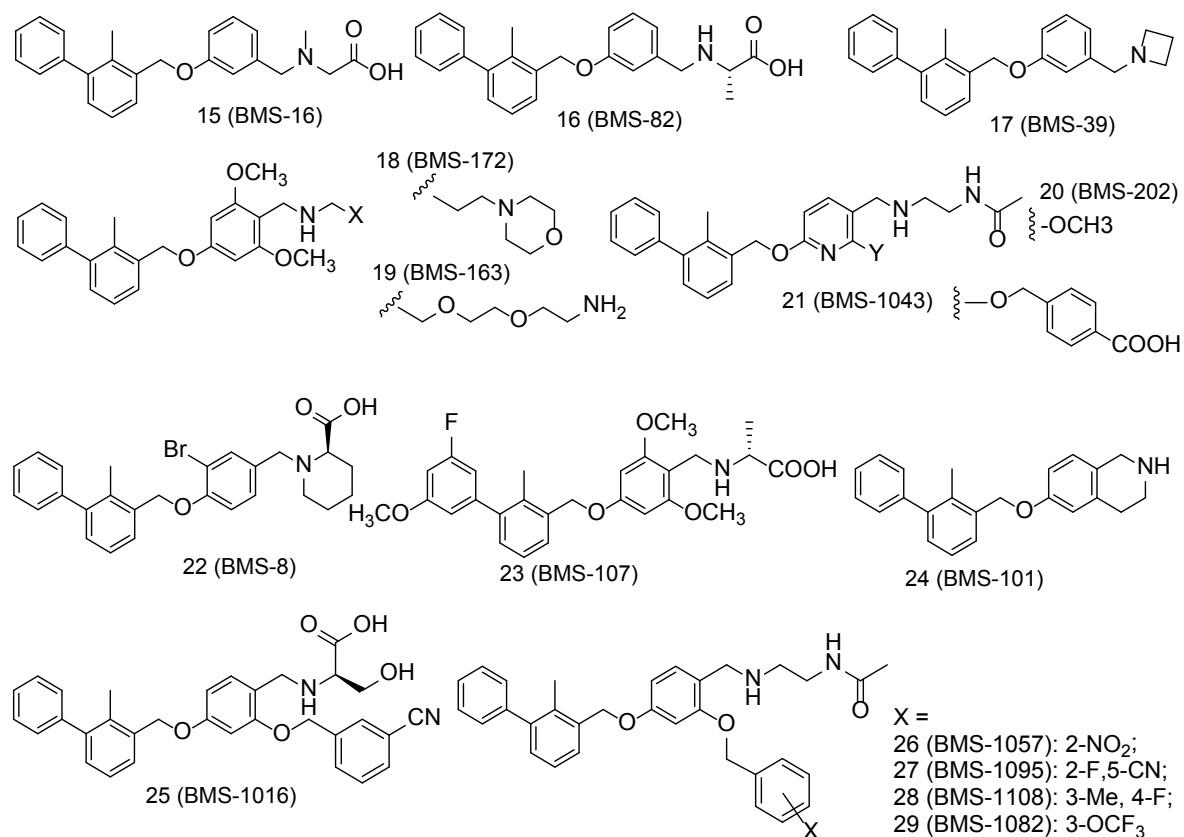


Figure 7. 1. Structures of the PD-1/PD-L1 complex inhibitors (1–14) used in docking studies.

2. Results and Discussion:

2.1. Docking Scores and Validation

To identify amino acids that are essential for small molecule binding, we carried out docking studies of 29 experimentally verified inhibitors of PD-L1/PD-1 complex (Figures 1 and 2). These 29 ligands were docked to two different PD-L1 model proteins (PDBIDs: 5NIU⁴⁸, and 5N2F⁴⁷). The PD-L1/ligand docking scores for these two models are listed in Table 7.1. The docking scores show that the Glide performance was well within the predicted range of the binding affinity (ΔG_{PRED}) of PD-L1/PD-1 complex inhibitors. The comparisons of predicted docking scores to the experimental free energy of bindings, converted from the IC50s show that the docking scores of both models 5NIU and 5N2F are in good agreement with the experimentally observed data, with mean errors of 1.07 and 0.91 kcal/mol, and the root-mean-square errors of 1.66, 1.51 kcal/mol for model proteins 5NIU and 5N2F, respectively. The low standard deviations of 1.29 and 1.22 for model proteins 5NIU and 5N2F, respectively further confirm the validity of the Glide docking method. The more negative the docking score, the more favorable the interaction of the complex. To determine the protonation state of amino groups in compounds outlined in Figures 1 and 2, we carried out computational pKa calculations using EPik program. Table S1 shows that all compounds show pKa around 8 except BMS-1220 (8), which has a high pKa of 10.73. This suggests that the nitrogen atom on most ligands should not be protonated and thus remained neutral whereas BMS-1220 (8) was protonated. In addition to binding affinity, the ligand binding can also be evaluated by binding free energy.

Herein we use a knowledge-based Moveable-Type (MT)-based approach⁴⁹ to estimate the absolute free energy of binding of all 29 ligands using the docked poses

identified in the docking study for two model proteins. The MT-based free energy calculation has been successfully applied to engineering cellular retinoic acid binding protein II ⁵⁰. Table 7.2 shows that the mean errors of predicted free energy of binding from the corresponding experimental values are 0.64, -0.68 kcal/mol, with standard deviation of 1.68, 1.54; and RMSE of 1.77, 1.66 for model proteins 5NIU and 5N2F, respectively. The good agreement between predicted and the experimentally observed values not only proves the validity of the MT-based free energy calculation method, but also further validated the Glide-dock program because the generated docked poses can be used to accurately predict the binding affinity.

There are other methods to validate docking methods.⁵¹⁻⁵² The pose selection is a standard method used whereby docking software is used to dock a ligand with a known conformation and orientation, typically from a co-crystal structure, into the binding site. When the docking software is able to generate a pose for the ligand that is very close to the native conformation in the crystal structure, the docking software is considered dependable when the root mean square deviation (RMSD) value of the superposition of a ligand between the docked pose and the native conformation is low (1.5 or 2 Å depending on ligand size).⁵³ The superposition of the Glide-generated docked pose, and the native conformation in the co-crystal structure (PDB ID: 5NIU) for compound 1 (Figure 7.2) showed that the RMSD between these two poses is 1.04 Å. Therefore, the low RMSD value confirmed that glide dock is able successfully to find the native poses in crystal structures and can be reliably used to define the binding conformations of other ligands.

Table7. 1. The glide docking scores (unit, kcal/mol) of 29 ligands against PD-L1 proteins (5NIU and 5N2F).

Compound	IC50 (nM)	$\Delta G(\text{exp})$	5NIU_Dock	$\Delta\Delta G(5\text{NIU})$	5N2F_Dock	$\Delta\Delta G(5\text{N2F})$
BMS-1001(1, 5NIU)	2.25	-11.80	-11.69	-0.11	-11.60	-0.20
BMS-200 (2, 5N2F)	80	-9.68	-12.06	2.38	-12.18	2.50
BMS-3029 (3)	2350	-7.68	-12.35	4.68	-12.73	5.05
BMS-1166 (4, 5NIX)	1.4	-12.08	-11.08	-1.00	-11.66	-0.42
BMS-114 (5)	43	-10.05	-11.14	1.09	-10.42	0.37
BMS-1197 (6)	1.85	-11.91	-11.15	-0.76	-12.10	0.18
BMS-1205 (7)	2.71	-11.69	-12.14	0.46	-12.14	0.45
BMS-1220 (8)	6.07	-11.21	-14.04	2.83	-10.58	-0.63
BMS-2002 (9)	10	-10.91	-13.04	2.13	-11.63	0.71
BMS-1250 (10)	1.19	-12.17	-12.11	-0.06	-12.64	0.46
BMS-1305 (11)	0.92	-12.33	-11.35	-0.98	-11.34	-0.99
BMS-1239 (12)	148.9	-9.31	-11.10	1.79	-11.19	1.88
BMS-2010 (13)	50	-9.96	-12.00	2.04	-11.93	1.97
BMS-3024 (14)	5.54	-11.26	-12.75	1.49	-11.53	0.27
BMS-16 (15)	1945	-7.79	-9.31	1.52	-8.70	0.91
BMS-82 (16)	3186	-7.50	-9.24	1.74	-9.12	1.62
BMS-39 (17)	4184	-7.34	-8.26	0.92	-8.52	1.18
BMS-172 (18)	107	-9.51	-8.54	-0.97	-9.30	-0.21
BMS-163 (19)	93	-9.59	-10.12	0.53	-10.23	0.63
BMS-202 (20, 5J89)	18	-10.56	-11.22	0.66	-10.34	-0.23
BMS-1043 (21)	239.2	-9.03	-10.51	1.48	-11.33	2.29
BMS-8 (22, 5J8O)	146	-9.32	-11.40	2.08	-10.25	0.92
BMS-107 (23)	329	-8.84	-9.77	0.93	-9.97	1.12
BMS-101 (24)	1076	-8.14	-8.35	0.21	-7.96	-0.19
BMS-1016 (25)	4.55	-11.38	-11.69	0.31	-11.79	0.41
BMS-1057 (26)	985.8	-8.19	-10.31	2.12	-9.66	1.46
BMS-1095 (27)	81.25	-9.67	-9.86	0.18	-11.07	1.40
BMS-1108 (28)	624.2	-8.46	-10.55	2.08	-9.57	1.11
BMS-1082 (29)	828.4	-8.30	-9.66	1.37	-10.68	2.39
Mean Error				1.07		0.91
STDev				1.29		1.22
RMSE				1.66		1.51

Table7. 2. The Moveable-Type-based binding free energy (unit, kcal/mol) of 29 ligands against PD-L1 proteins (5NIU and 5N2F), using docked poses from the Glide dock program.

Title	IC50 (nM)	$\Delta G(\text{exp})$	MT_5NIU	$\Delta\Delta G(5NIU)$	MT_5N2F	$\Delta\Delta G(5N2F)$
BMS-1001(1, 5NIU)	2.25	-11.80	-10.81	-0.98	-9.72	-2.08
BMS-200 (2, 5N2F)	80	-9.68	-11.75	2.07	-9.00	-0.68
BMS-3029 (3)	2350	-7.68	-9.94	2.26	-8.70	1.02
BMS-1166 (4, 5NIX)	1.4	-12.08	-10.99	-1.09	-10.53	-1.55
BMS-114 (5)	43	-10.05	-10.22	0.17	-8.41	-1.64
BMS-1197 (6)	1.85	-11.91	-12.44	0.53	-10.68	-1.23
BMS-1205 (7)	2.71	-11.69	-11.22	-0.47	-9.82	-1.87
BMS-1220 (8)	6.07	-11.21	-12.14	0.93	-10.58	-0.63
BMS-2002 (9)	10	-10.91	-12.56	1.65	-11.57	0.66
BMS-1250 (10)	1.19	-12.17	-11.99	-0.19	-11.58	-0.59
BMS-1305 (11)	0.92	-12.33	-12.29	-0.04	-9.98	-2.35
BMS-1239 (12)	148.9	-9.31	-11.02	1.71	-9.55	0.24
BMS-2010 (13)	50	-9.96	-11.65	1.69	-11.97	2.01
BMS-3024 (14)	5.54	-11.26	-11.37	0.11	-11.84	0.57
BMS-16 (15)	1945	-7.79	-9.25	1.46	-6.93	-0.86
BMS-82 (16)	3186	-7.50	-8.02	0.52	-6.91	-0.59
BMS-39 (17)	4184	-7.34	-8.59	1.26	-6.19	-1.14
BMS-172 (18)	107	-9.51	-6.57	-2.94	-4.99	-4.52
BMS-163 (19)	93	-9.59	-7.34	-2.25	-5.93	-3.67
BMS-202 (20, 5J89)	18	-10.56	-8.89	-1.68	-9.92	-0.64
BMS-1043 (21)	239.2	-9.03	-11.02	1.99	-9.32	0.29
BMS-8 (22, 5J8O)	146	-9.32	-12.35	3.03	-8.94	-0.39
BMS-107 (23)	329	-8.84	-7.73	-1.11	-7.52	-1.32
BMS-101 (24)	1076	-8.14	-8.29	0.15	-6.98	-1.16
BMS-1016 (25)	4.55	-11.38	-10.11	-1.27	-8.98	-2.40
BMS-1057 (26)	985.8	-8.19	-11.84	3.64	-9.88	1.69
BMS-1095 (27)	81.25	-9.67	-11.76	2.09	-9.97	0.30
BMS-1108 (28)	624.2	-8.46	-10.35	1.89	-9.15	0.68
BMS-1082 (29)	828.4	-8.30	-11.71	3.41	-10.29	2.00
MAE				0.64		-0.68
STDev				1.68		1.54
RMSE				1.77		1.66

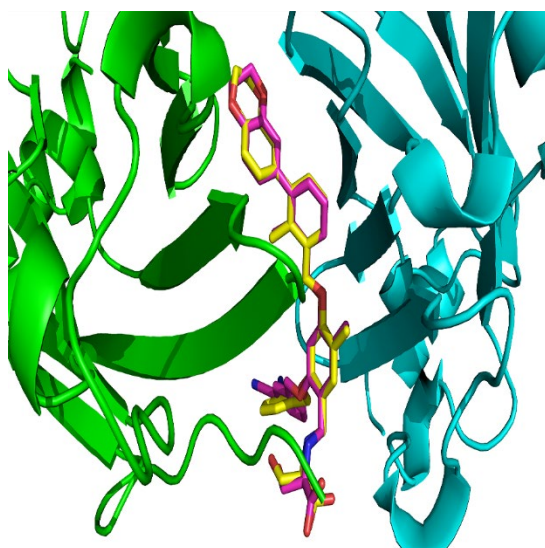


Figure 7. 2. The superposition of the glide-docked generated pose and its native conformation in 5NIU for ligand BMS-1001(1, 5NIU). The native confirmation is in yellow color, and the docked pose is in magenta color.

Binding Interactions of PD-L1/inhibitors

After the validity of the Glide dock method was confirmed by aforementioned methods, we could confidently use the docked poses to identify PD-L1/inhibitors interactions. To design new molecules with desired potency, it is important for the designed molecules to maintain the proper interactions with essential residues in the binding pocket. Thus, it is very important to identify critical binding residues for effective PD-L1 binding.

The PD-L1/PD-1 complex inhibitors bind to PD-L1 through PD-1 interacting surface site inducing PD-L1 dimerization and disassociation of a PD-1/PD-L1 complex. In the crystal structure of 5NIU (PD-L1 dimer/BMS-1001 (1), the 2, 3-dihydro-1, 4-benzodioxine fragment creates $\pi - \pi$ stacking interaction with Tyr56, and the (2R)-2-amino-3-hydroxypropanoic acid moiety formed H-bonds with the carbonyl of Asp122, Tyr123, Lys124, and the main chain carbonyl oxygen of Phe19 (Fig. 7.3). Besides, the 3-cyanobenzyl part creates $\pi - \pi$ stacking interaction with Tyr123, and forms hydrogen bonds with Arg125. The absence of 3- cyanobenzyl group in inhibitor 3 is unable to H-bond with Arg125 and Phe19 (Fig. 7.3), resulting in a much weaker interaction. The IC₅₀s for compounds 1 and 3 are 2.25 and 2350 nM, respectively. Our MT-based binding free energy calculations predicted the ΔG s of -10.81 and -9.94 kcal/mol, respectively, showing a weaker binding in compound 3.

The PD-1/PD-L1 complex inhibitors were run in silico docking using the glide docking method to identify the binding mechanisms of these compounds. The protein/ligand interactions might vary due to the different structural nature of each ligand. To identify residues that are responsible for most ligand binding, we enumerated residues that form H-bonds, or electrostatic interactions or π - π stack interactions with 29 inhibitors.

Table 7.3 shows that residues Tyr56 and Asp122 are two most important residues for ligand binding.

To evaluate the relative importance of active site residues in ligand binding, we enumerate all binding residues for all 29 ligands. Figure 7.4 shows that Tyr56 interacts with all 29 inhibitors and Asp122 forms H-bonds with 26 of those 29 compounds. In addition, Lys124, Arg125 and Phe19 are important residues for ligand binding as they appear in between 30% to 50% compounds binding. The positively charged nature of Lys124 and Arg125 suggests that a negatively charged carboxylate moiety is likely in PD-L1 inhibitors. Please note that to avoid over-exaggeration of the contributions of binding residues, if a residue appears in both chain C and chain D, it is only counted as one. For instance, Tyr56 of chains C and D provide π - π stack interactions with the aromatic rings of ligands but only was counted as once for each entry for compounds **2**, **5**, **6**, **7** and so on. The Arg125 looks to be important for ligand binding. The potency of inhibitors toward the PD-1/PD-L1 complex might be attributed to their ability to interact with Arg125. The majority of potent PD-1/PD-L1 complex inhibitors with IC₅₀ of 100 nM or better tends to show interactions with Arg125, as observed in the potent compound **1**.

Though ligands tend to bind to the interface of dimer Chains C and D, they prefer the binding to one chain over the other; in this case, they show closer interactions with chain D residues as evidenced by Table 7.3 and Figure 7.3. The most frequent residues from chain C is Tyr56, which along with same residue from chain D, form two π - π stack interactions with two aromatic rings of inhibitors. This suggests that there should be two aromatic rings separating by 12 Å away for PD-L1 inhibitors to interact with Tyr56 from both chains.

The electrostatic map of PD-L1/ BMS-1001 (1, 5NIU, Figure 7.5) further confirms that Chain D plays a significant role in ligand binding whereas the role of chain C is much less because the latter has fewer interactions with the PD-L1 inhibitors. The phenol group of Tyr56 is exposed to the binding site generating π - π stacking with the inhibitors. The carboxyl group of Asp122 was positioned toward the ligand binding, having a high concentration of negative charge from the carboxylate group and served as an H-bond acceptor with compound 1. This high concentration of negative charge is visible as red regions in the plot of electrostatic potential (Figure 7.5). The PD-L1 binding sites have a high concentration of positive charge featuring Lys124 and Arg125 that bind compound 1. This high concentration of positive charge is visible as blue regions in the electrostatic potential map (Figure 6). This observation is supported by the high frequency of Lys124 and Arg125 in the protein/ligand interaction map (Fig. 7.5). Therefore, future PD-L1 inhibitor design should consider the residues Tyr56, Asp122, Lys124, Arg125 and Phe19, along with two aromatic rings. The importance of residue Tyr was already observed and reported.[46-48] The finding of Asp122, Lys124, Arg125 and Phe19, and two essential aromatic rings may provide helpful guideline for future PD-L1 inhibitor design.

Table7. 3. The ligand-protein interactions between the PD-1/PD-L1 complex inhibitors and the PD-L1 protein of 5NIU.

Title	IC50 (nM)	Chain C	Chain D
BMS-1001(1, 5NIU)	2.25		Tyr56, Asp122, Lys124, Arg125, Phe19
BMS-200 (2, 5N2F)	80	Tyr56	Tyr56, Ala121, Asp122
BMS-3029 (3)	2350	Tyr56, Gln66	Tyr56, Asp122, Tyr123, Lys124
BMS-1166 (4, 5NIX)	1.4		Tyr56, Asp122, Arg125
BMS-114 (5)	43	Tyr56	Tyr56, Asp122, Arg125
BMS-1197 (6)	1.85	Tyr56	Tyr56, Asp122, Lys124, Arg125, Phe19
BMS-1205 (7)	2.71	Tyr56, Gln66	Tyr56, Asp122, Lys124, Arg125
BMS-1220 (8)	6.07		Tyr56, Asp122, Lys124, Arg125
BMS-2002 (9)	10	Tyr56	Tyr56, Ala121, Asp122, Tyr123, Lys124, Arg125, Phe19
BMS-1250 (10)	1.19	Tyr56	Tyr56, Ala121, Asp122, Arg125, Ala18, Phe19
BMS-1305 (11)	0.92	Tyr56	Tyr56, Asp122, Tyr123, Arg125
BMS-1239 (12)	148.9		Tyr56, Asp122, Lys124
BMS-2010 (13)	50		Tyr56, Asp122, Lys124, Arg125, Ala18
BMS-3024 (14)	5.54	Gln66	Tyr56, Asp122, Arg125, Phe19
BMS-16 (15)	1945	Tyr56, Asn63	Tyr56, Asp122
BMS-82 (16)	3186		Tyr56, Ala121, Phe19, Ala18
BMS-39 (17)	4184	Tyr56	Tyr56, Asp122
BMS-172 (18)	107	Tyr56	Tyr56, Ala121, Asp122, Tyr123
BMS-163 (19)	93	Tyr56	Tyr56, Gly119, Ala121, Asp122, Tyr123
BMS-202 (20, 5J89)	18	Tyr56	Tyr56, Ala121, Asp122
BMS-1043 (21)	239.2		Tyr56, Ala121, Asp122, Tyr123, Lys124, Phe19
BMS-8 (22, 5J8O)	146	Asn63	Tyr56, Lys124
BMS-107 (23)	329		Tyr56, Asp122, Lys124
BMS-101 (24)	1076	Gln66	Tyr56
BMS-1016 (25)	4.55	Tyr56	Tyr56, Asp122, Arg125
BMS-1057 (26)	985.8	Tyr56	Tyr56, Asp122, Lys124, Phe19
BMS-1095 (27)	81.25	Tyr56	Tyr56, Ala121, Asp122, Lys124, Arg125, Phe19
BMS-1108 (28)	624.2	Asn63	Tyr56, Asp122
BMS-1082 (29)	828.4		Tyr56, Ala121, Asp122, Lys124, Phe19

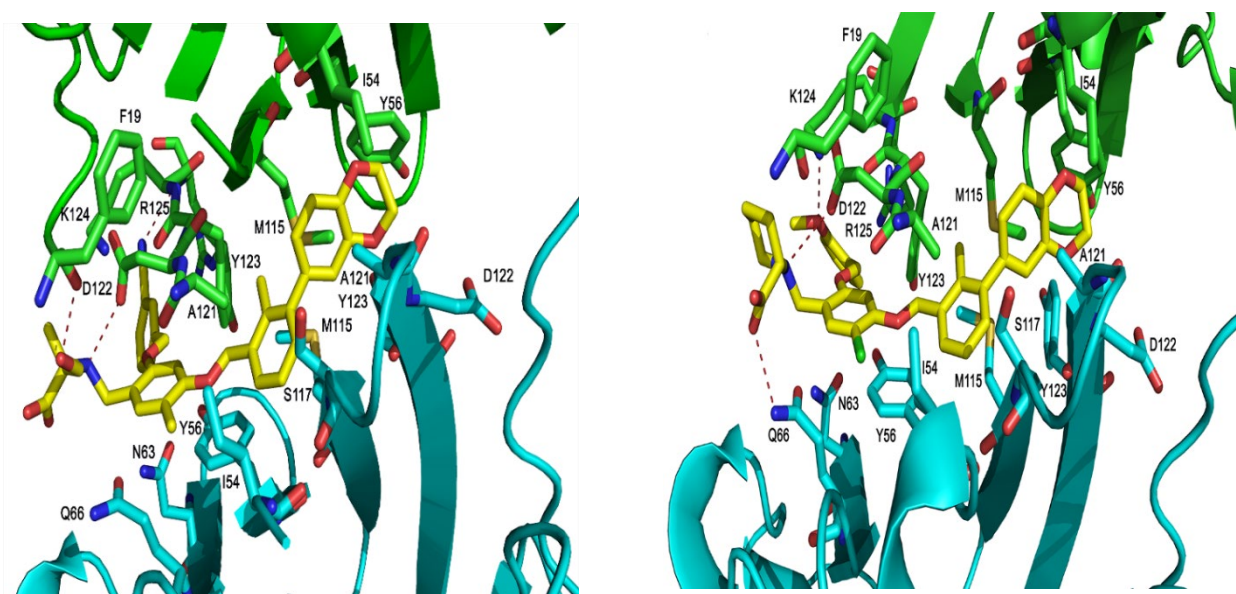


Figure 7. 3. The binding orientation of compound 1 (left), and compound 3 (right) in the PD-L1 protein of 5NIU. The H-bonds is depicted in dark dotted line. Chain D is colored with green secondary structure and atoms whereas Chain C in cyan color.

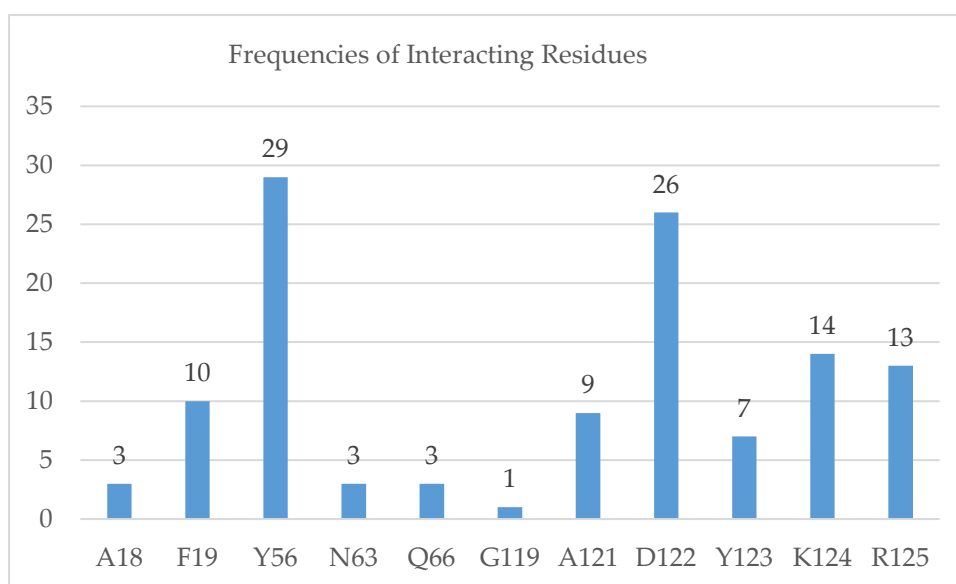


Figure 7.4. Interacting residues of PD-L1 with all 29 different inhibitors.

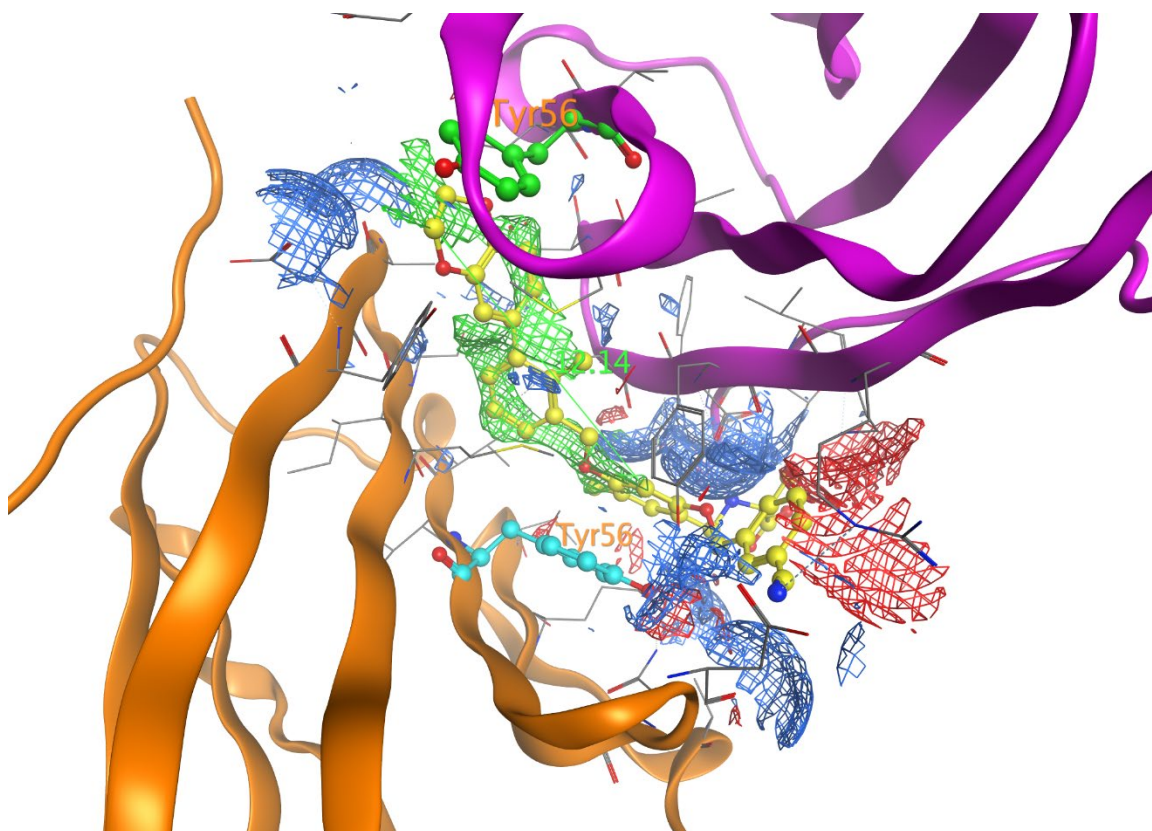


Figure 7.5. Electrostatic surface of the binding pockets of the PD-L1 with BMS-1001 (1, 5NIU). The hydrophobic region is depicted as green; H-bond acceptor, red; and H-bond donor, blue. Chain D is colored with magenta secondary structure whereas Chain C in orange color. Tyr56 of chain C is highlighted in cyan and Tyr56 of Chain D, green. The distance between two aromatic rings interacting with Tyr56 of chain C and chain D is 12.14 Å.

3. Computational Methods:

3.1 Preparation of Protein Structures:

The X-ray crystal structures of the human wild type PD-L1/BMS-1001 (1, PDBID: 5NIU) and the structure of PD-L1/BMS-200 (2, PDBID: 5N2F) were downloaded from the RCSB Protein Data Bank (<https://www.rcsb.org/structure/>). No missing residues were observed in these two crystal structures except a few residues with missing part of side chains. The missing side chains were regenerated during the Protein Preparation step in MOE to correct missing side chains and to optimize the hydrogen bonding network, and to allow protonation be assigned to charged residues and allowing the flipping side chains of Asn, Gln, and His in MOE to maximize H-bond interactions.⁵⁷ 1,2-ethanediol and the water molecules, due to not serving as a bridge between protein and ligands, were deleted in the protein preparation step. Subsequently, the X-ray crystal structure was subjected to energy minimization using the Amber14:EHT force field⁵⁸ in MOE, followed by protein preparation using the Protein Preparation Wizard in the Schrödinger software⁵⁹ to allow the flip of the side-chain of residues of Asn and Gln to maximize H-bond interactions. Then, they were subjected to energy minimization with protein backbone by using the OPLS3 force field in the MacroModel module in the Maestro before docking procedure.

3.2 Preparation of Ligands and Molecular Docking:

We built 29 PD-1/PD-L1 complex inhibitors from different sources based on the crystal structure of 1 in 5NIU as a template using the MOE build panel and all model molecules were subjected to energy minimization using the MMFF94x force field partial charges in MOE.⁶⁰ The minimized ligands were imported to Maestro in Schrödinger software suite

for proper treatment before docking. All inhibitors were minimized by the MacroModel module in the using the OPLS2005 force field.⁵⁹ The pKa calculations of ligands were prepared by using the Epik program in the Schrödinger software.⁵⁹ The Epik calculations calculated the pKa values of all nitrogen atoms in these ligands and if an amine has a pKa greater than 10, that amino group will be protonated. Otherwise, it would be treated as neutral. In our case, only compound BMS-1220 (8) has a pKa of 10.73, which is greater than 10 and thus should be protonated.

To calculate the enrichment factor in order to evaluate the effectiveness of the docking program, we downloaded a database of 260,071 ligands from the National Cancer Institute (NCI) ⁶¹, and this database was converted to 3D structures, and ionic components were removed and the database was further filtered with the Lipinski's rule of five ⁶², and then 261 molecules were randomly selected from this database to assess the enrichment factor and validate our docking study. The selected 261 molecules were subject to energy minimization using the MOE and MacroModel program. The combined database of 29 inhibitors along with 261 randomly drug-like molecules were docked to the PD-L1 binding pockets of model proteins 5NIU and 5N2F.

The compounds were then subjected to energy minimization using the MacroModel module in the Maestro. We used Glide Dock in the Maestro 11.6 for the docking of inhibitors to the PD-L1 proteins. Consequently, we generated a grid file for the crystal structures of 5NIU and 5N2F using the Glide Grid Generation protocol with the bound ligands as centroids of the protein binding pocket. All 29 inhibitors were docked into the grid file, and we later ran docking for the 261 NCI drug-like molecules using the same grid files. During the docking process, the scaling factor for receptor Van der Waals for

the nonpolar atoms was set to 0.8 to allow for some flexibility of the receptor. Besides, all other parameters were used as defaults and the docking procedure established.⁶³ The binding affinity of the PD-L1/ligand complexes was expressed in terms of docking scores. The output docking scores were defined as ΔGPRED . The output ΔGPRED was then related to the experimental ΔGEXP , which calculated from the experimental IC_{50} (nM) using the following equation:

$$\Delta_{\text{EXP}}(\text{kcal/mol}) = RT \ln (\text{IC}_{50} (\text{nM}) \times 10^{-9})/1000$$

Furthermore, we created an electrostatic map for the binding site of PD-L1 to estimate the electrostatically favored locations of H-bond donors, H-bond acceptors and hydrophobic interactions. The electrostatic map was made using the MOE program.

3.3 Binding Free Energy Calculations Using the Moveable-Type (MT)-based

Approach:

After 29 inhibitors were docked to the 5NIU protein, the model protein was saved as pdb format and the 29 ligand each was saved separately in the mol2 file format. The saved protein and ligand files were fed as input files for the Movable-Type (MT) free energy calculation method, an in-house program developed by Prof. Kenneth Merz Jr. at Michigan State University and was generously given to us for complimentary use. The output data of the MT-based method is the absolute free energy of binding, which was used to compare with those experimentally observed values and were listed in Table 2. This method has been proved its reliability by previous publications. [49-50]

4. Conclusion:

The prevalence of the PD-1/PD-L1 complex in several human cancer cells has made the PD-1/PD-L1 complex an attractive target for anticancer drug discovery. The positive results of mAb targeting the PD-1/PD-L1 complex in cancer treatment are boosting and inspiring the design and development of small molecules targeting PD-1/PD-L1 complex. Our studies on the protein/ligand dockings and structural analysis on the docked complexes have suggested that the Glide dock approach and the MT-based free energy calculation method are very dependable in terms of their predictability with low error comparing to those observed values. The low RMS deviations of the docked pose to the native conformation and the very good enrichment factor further confirm the effectiveness of the Glide dock program. The analyses of the protein/ligand interactions reveal that PD-L1 residues Tyr56, Asp122, Lys124, Arg125 and Phe19 may be very important for inhibitor design and that two aromatic rings may be expected in new PD-L1 inhibitors. All these observations will be very useful in the design, development and discovery of the next generation of potent PD-1/PD-L1 complex inhibitors.

References:

1. Pardoll DM. The blockade of immune checkpoints in cancer immunotherapy. *Nat. Rev. Cancer*. 2012;12(4):252-264. doi: 10.1038/nrc3239.
2. Sharpe AH, Wherry EJ, Ahmed R, Freeman GJ. The function of programmed cell death 1 and its ligands in regulating autoimmunity and infection. *Nat Immunol*. 2007;8(3):239-245. doi: 10.1038/ni1443.
3. Nirschl CJ, Drake CG. Molecular pathways: Coexpression of immune checkpoint molecules: Signaling pathways and implications for cancer immunotherapy. *Clin Cancer Res*. 2013;19(18):4917-4924. doi: 10.1158/1078-0432.CCR-12-1972.
4. Mahoney KM, Rennert PD, Freeman GJ. Combination cancer immunotherapy and new immunomodulatory targets. *Nat Rev Drug Discov*. 2015;14(8):561-584. doi: 10.1038/nrd4591.
5. Topalian SL, Drake CG, Pardoll DM. Immune checkpoint blockade: A common denominator approach to cancer therapy. *Cancer Cell*. 2015;27(4):450-461. doi: 10.1016/j.ccell.2015.03.001.
6. Sharma P, Allison JP. The future of immune checkpoint therapy. *Science*. 2015;348(6230):56-61. doi: 10.1126/science.aaa8172.
7. Shin DS, Ribas A. The evolution of checkpoint blockade as a cancer therapy: What's here, what's next? *Curr Opin Immunol*. 2015;33:23-35. doi: 10.1016/j.coi.2015.01.006.

8. Suh W, Gajewska BU, Okada H, et al. The B7 family member B7-H3 preferentially down-regulates T helper type 1-mediated immune responses. *Nat Immunol*. 2003;4(9):899-906. doi: 10.1038/ni967.
9. Greenwald RJ, Freeman GJ, Sharpe AH. The B7 family revisited. *Annu Rev Immunol*. 2005;23:515-548. doi: 10.1146/annurev.immunol.23.021704.115611.
10. Parry RV, Chemnitz JM, Frauwirth KA, et al. CTLA-4 and PD-1 receptors inhibit T-cell activation by distinct mechanisms. *Mol Cell Biol*. 2005;25(21):9543-9553. doi: 10.1128/MCB.25.21.9543-9553.2005.
11. Sharma P, Allison JP. Immune checkpoint targeting in cancer therapy: Toward combination strategies with curative potential. *Cell*. 2015;161(2):205-214. doi: 10.1016/j.cell.2015.03.030.
12. Hoos A. Development of immuno-oncology drugs - from CTLA4 to PD1 to the next generations. *Nat Rev Drug Discov*. 2016;15(4):235-247. doi: 10.1038/nrd.2015.35.
13. Lipson EJ, Drake CG. Ipilimumab: An anti-CTLA-4 antibody for metastatic melanoma. *Clin Cancer Res*. 2011;17(22):6958-6962. doi: 10.1158/1078-0432.CCR-11-1595.
14. Dömling A, Holak TA. Programmed death-1: Therapeutic success after more than 100 years of cancer immunotherapy. *Angew Chem Int Ed Engl*. 2014;53(9):2286-2288. doi: 10.1002/anie.201307906.

15. Powles T, Eder JP, Fine GD, et al. MPDL3280A (anti-PD-L1) treatment leads to clinical activity in metastatic bladder cancer. *Nature*. 2014;515(7528):558-562. doi: 10.1038/nature13904.
16. Hamid O, Robert C, Daud A, et al. Safety and tumor responses with lambrolizumab (anti-PD-1) in melanoma. *N Engl J Med*. 2013;369(2):134-144. doi: 10.1056/NEJMoa1305133.
17. Brahmer JR, Tykodi SS, Chow LQM, et al. Safety and activity of Anti-PD-L1 antibody in patients with advanced cancer. *N Engl J Med*. 2012; 366(26):2455-2465. doi: 10.1056/NEJMoa1200694.
18. Keir ME, Butte MJ, Freeman GJ, Sharpe AH. PD-1 and its ligands in tolerance and immunity. *Annu Rev Immunol*. 2008; 26:677-704. doi: 10.1146/annurev.immunol.26.021607.090331.
19. Francisco LM, Sage PT, Sharpe AH. The PD-1 pathway in tolerance and autoimmunity. *Immunol Rev*. 2010; 236:219-242. doi: 10.1111/j.1600-065X.2010.00923.x.
20. Okazaki T, Honjo T. PD-1 and PD-1 ligands: From discovery to clinical application. *Int Immunol*. 2007;19(7):813-824. doi: 10.1093/intimm/dxm057.
21. Liang SC, Latchman YE, Buhlmann JE, et al. Regulation of PD-1, PD-L1, and PD-L2 expression during normal and autoimmune responses. *Eur J Immunol*. 2003;33(10):2706-2716. doi: 10.1002/eji.200324228.

22. Nishimura H, Nose M, Hiai H, Minato N, Honjo T. Development of lupus-like autoimmune diseases by disruption of the PD-1 gene encoding an ITIM motif-carrying immunoreceptor. *Immunity*. 1999;11(2):141-151. PMID: 10485649.
23. Ansari MJI, Salama AD, Chitnis T, et al. The programmed death-1 (PD-1) pathway regulates autoimmune diabetes in nonobese diabetic (NOD) mice. *J Exp Med*. 2003;198(1):63-69. doi: 10.1084/jem.20022125.
24. Keir ME, Liang SC, Guleria I, et al. Tissue expression of PD-L1 mediates peripheral T cell tolerance. *J Exp Med*. 2006;203(4):883-895. doi: 10.1084/jem.20051776.
25. Phan TG, Long GV, Scolyer RA. Checkpoint inhibitors for cancer immunotherapy. Multiple checkpoints on the long road towards cancer immunotherapy. *Immunol Cell Biol*. 2015;93(4):323-325. doi: 10.1038/icb.2015.12.
26. Herbst RS, Soria J, Kowanetz M, et al. Predictive correlates of response to the anti-PD-L1 antibody MPDL3280A in cancer patients. *Nature*. 2014;515(7528):563-567. doi: 10.1038/nature14011.
27. Wherry EJ. T cell exhaustion. *Nat Immun*. 2011;12(6):492-499. doi: 10.1038/ni.2035.
28. Sakuishi K, Apetoh L, Sullivan JM, Blazar BR, Kuchroo VK, Anderson AC. Targeting tim-3 and PD-1 pathways to reverse T cell exhaustion and restore anti-tumor immunity. *J Exp Med*. 2010;207(10):2187-2194. doi: 10.1084/jem.20100643.
29. Sun S, Fei X, Mao Y, et al. PD-1(+) immune cell infiltration inversely correlates with survival of operable breast cancer patients. *Cancer Immunol Immunother*. 2014;63(4):395-406. doi: 10.1007/s00262-014-1519-x.

30. Muenst S, Soysal SD, Gao F, Obermann EC, Oertli D, Gillanders WE. The presence of programmed death 1 (PD-1)-positive tumor-infiltrating lymphocytes is associated with poor prognosis in human breast cancer. *Breast Cancer Res Treat.* 2013;139(3):667-676. doi: 10.1007/s10549-013-2581-3.
31. Ahmadzadeh M, Johnson LA, Heemskerk B, et al. Tumor antigen-specific CD8 T cells infiltrating the tumor express high levels of PD-1 and are functionally impaired. *Blood.* 2009;114(8):1537-1544. doi: 10.1182/blood-2008-12-195792.
32. Matsuzaki J, Gnjjatic S, Mhawech-Fauceglia P, et al. Tumor-infiltrating NY-ESO-1–specific CD8 T cells are negatively regulated by LAG-3 and PD-1 in human ovarian cancer. *Proc Natl Acad Sci U S A.* 2010 Apr 27;107(17):7875-80. doi: 10.1073/pnas.1003345107.
33. Hawkes EA, Grigg A, Chong G. Programmed cell death-1 inhibition in lymphoma. *Lancet Oncol.* 2015;16(5):234. doi: 10.1016/S1470-2045(15)70103-8.
34. Inman BA, Sebo TJ, Frigola X, et al. PD-L1 (B7-H1) expression by urothelial carcinoma of the bladder and BCG-induced granulomata: Associations with localized stage progression. *Cancer.* 2007;109(8):1499-1505. doi: 10.1002/cncr.22588.
35. Khalil DN, Smith EL, Brentjens RJ, Wolchok JD. The future of cancer treatment: Immunomodulation, CARs and combination immunotherapy. *Nat Rev Clin Oncol.* 2016;13(5):273-290. doi: 10.1038/nrclinonc.2016.25.
36. Baumeister SH, Freeman GJ, Dranoff G, Sharpe AH. Coinhibitory pathways in immunotherapy for cancer. *Annu Rev Immunol.* 2016;34:539-573. doi: 10.1146/annurev-immunol-032414-112049.

37. Farkona S, Diamandis EP, Blasutig IM. Cancer immunotherapy: The beginning of the end of cancer? *BMC Med.* 2016;14:73. doi: 10.1186/s12916-016-0623-5.
- 38 Kruger S, Ilmer M, Kobold S, Cadilha BL, Endres S, Ormanns S, et al. Advances in cancer immunotherapy 2019 - latest trends. *J Exp Clin Cancer Res.* 2019 Jun 19;38(1):268. doi: 10.1186/s13046-019-1266-0.
- 39 Danlos FX, Voisin AL, Dyevre V, Michot JM, Routier E, Taillade L, et al. Safety and efficacy of anti-programmed death 1 antibodies in patients with cancer and pre-existing autoimmune or inflammatory disease. *Eur J Cancer.* 2018 Mar;91:21-29. doi: 10.1016/j.ejca.2017.12.008.
- 40 Ferrara R, Mezquita L, Texier M, Lahmar J, Audigier-Valette C, Tessonnier L. et al. Hyperprogressive Disease in Patients with Advanced Non-Small Cell Lung Cancer Treated with PD-1/PD-L1 Inhibitors or with Single-Agent Chemotherapy. *JAMA Oncol.* 2018, 4, 1543–1552
- 41 Lecis D, Sangaletti S, Colombo MP, Chiodoni C. Immune Checkpoint Ligand Reverse Signaling: Looking Back to Go Forward in Cancer Therapy. *Cancers.* 2019 May 4;11(5). pii: E624. doi: 10.3390/cancers11050624.
42. Zak KM, Kitel R, Przetocka S, et al. Structure of the complex of human programmed death 1, PD-1, and its ligand PD-L1. *Structure.* 2015;23(12):2341-2348. doi: 10.1016/j.str.2015.09.010.
43. Lee HT, Lee JY, Lim H, et al. Molecular mechanism of PD-1/PD-L1 blockade via anti-PD-L1 antibodies atezolizumab and durvalumab. *Sci Rep.* 2017;7(1):5532. doi: 10.1038/s41598-017-06002-8.

44. Chupak LS, Zheng X, inventors; Bristol-Myers Squibb Company, assignee. Compounds useful as immunomodulators. Patent WO2015034820. March, 2015.
45. Chupak LS, Ding M, Martin SW, et al, inventors; Bristol-Myers Squibb Company, assignee. Compounds useful as immunomodulators. Patent WO2015160641. October 22, 2015.
46. Zak KM, Grudnik P, Guzik K, et al. Structural basis for small molecule targeting of the programmed death ligand 1 (PD-L1). *Oncotarget*. 2016;7(21):30323-30335. doi: 10.18632/oncotarget.8730.
47. Guzik K, Zak KM, Grudnik P, et al. Small-molecule inhibitors of the programmed cell death-1/programmed death-ligand 1 (PD-1/PD-L1) interaction via transiently induced protein states and dimerization of PD-L1. *J Med Chem*. 2017;60(13):5857-5867. doi: 10.1021/acs.jmedchem.7b00293.
48. Skalniak L, Zak KM, Guzik K, et al. Small-molecule inhibitors of PD-1/PD-L1 immune checkpoint alleviate the PD-L1-induced exhaustion of T-cells. *Oncotarget*. 2017;8(42):72167-72181. doi: 10.18632/oncotarget.20050.
- 49 Zheng Z, Merz KM Jr. Development of the knowledge-based and empirical combined scoring algorithm (KECSA) to score protein-ligand interactions. *J Chem Inf Model*. 2013 May 24;53(5):1073-83. doi: 10.1021/ci300619x.
- 50 Zhong HA, Santos EM, Vasileiou C, Zheng Z, Geiger JH, Borhan B, Merz KM Jr. Free-Energy-Based Protein Design: Re-Engineering Cellular Retinoic Acid Binding Protein II Assisted by the Moveable-Type Approach. *J Am Chem Soc*. 2018 Mar 14;140(10):3483-3486. doi: 10.1021/jacs.7b10368.

51. Cole JC, Murray CW, Nissink JWM, Taylor RD, Taylor R. Comparing protein-ligand docking programs is difficult. *Proteins*. 2005;60(3):325-332. doi: 10.1002/prot.20497.
52. Jain AN. Bias, reporting, and sharing: Computational evaluations of docking methods. *J Comput Aided Mol Des*. 2008;22(3-4):201-212. doi: 10.1007/s10822-007-9151-x.
53. Hevener KE, Zhao W, Ball DM, et al. Validation of molecular docking programs for virtual screening against dihydropteroate synthase. *J Chem Inf Model*. 2009;49(2):444-460. doi: 10.1021/ci800293n.
54. Bender A, Glen RC. A discussion of measures of enrichment in virtual screening: Comparing the information content of descriptors with increasing levels of sophistication. *J Chem Inf Model*. 2005;45(5):1369-1375. doi: 10.1021/ci0500177.
55. Huang N, Shoichet BK, Irwin JJ. Benchmarking sets for molecular docking. *J Med Chem*. 2006;49(23):6789-6801. doi: 10.1021/jm0608356.
56. Almahmoud S, Wang X, Vennerstrom JL, Zhong HA. Conformational Studies of Glucose Transporter 1 (GLUT1) as an Anticancer Drug Target. *Molecules*. 2019 Jun 7;24(11). pii: E2159. doi: 10.3390/molecules24112159.
57. The molecular operating EnVironment (MOE); Chemical Computing Group Inc.: Montreal, Quebec, Canada, 2019.
58. D.A. Case, V. Babin, J.T. Berryman, et al. AMBER 14, University of California, San Francisco. 2014.

59. Schrödinger, LLC, New York, NY, 2019. Schrödinger suite 2019-1 Protein Preparation wizard, Maestro, Protein Grid Generation, Glide, Macromodel, and Epik.
60. Halgren TA. Merck molecular force field. I. basis, form, scope, parameterization, and performance of MMFF94. *J Comput Chem.* 1996;17(5-6):490-519. doi: 10.1002/(SICI)1096-987X(199604)17:5/63.0.CO;2-P.
61. NCI open database compounds, release 3; national cancer institute, national institutes of health: Bethesda, MD, Sep 2003). Available online at: [Http://Cactus.nci.nih.gov/download/nci](http://Cactus.nci.nih.gov/download/nci) (accessed Aug 18,2008).
62. Lipinski CA, Lombardo F, Dominy BW, Feeney PJ. Experimental and computational approaches to estimate solubility and permeability in drug discovery and development settings. *Adv Drug Deliv Rev.* 2001;46(1-3):3-26.
63. Sabbah DA, Vennerstrom JL, Zhong H. Docking studies on isoform-specific inhibition of phosphoinositide-3-kinases. *J Chem Inf Model.* 2010;50(10):1887-98. doi: 10.1021/ci1002679.

